Dead Sea Workshop

16th- 23rd February 2009

The Dead Sea Rift as a natural laboratory for earthquake behavior: prehistorical, historical and recent seismicity

Organized by
Rivka Amit, Geological Survey of Israel
Alessandro M. Michetti, INQUA Paleoseismology Subcommission

Co-organizers: Amotz Agnon, Ari Matmon, The Hebrew University of Jerusalem

Edited by:
Rivka Amit
Amotz Agnon
Ari Matmon

In collaboration with:

UNESCO
Geological Survey of Israel
Safed Scientific Workshop Program
Hebrew University of Jerusalem
The Israel Geological Society
Israel National Earthquake Preparedness Committee
University of Missouri, Kansas City USA

Acknowledgment:

The field guide was made possible through the financial support of the Geological Survey of Israel. We thank Yoav Nahamias for his outstanding help in the workshop organization. Thanks to Shalev Siman-Tov for his technical assistance and contribution in preparing the figures, Rani Calvo and Shalev Siman-Tov for providing photographs, Rami Madmon, Yaacov Mizrahi and Yaacov Refael for their technical assistance. We specially thank Avner Ayalon for his editorial assistance, Bat-Sheva Cohen, Chana Netzer-Cohen and Nili Almog for their editorial and graphical design of the field guide.

Contents

A r a v a v a l l e y (p a g e s 127-205)

Judean Mountains (p a g e s 207-212)

Introduction - The Dead Sea Fault

Shmuel Marco

The Department of Geophysics and Planetary Sciences, Tel Aviv University.

E-mail: shmulikm@tau.ac.il

The Dead Sea Fault (DSF) accommodates sinistral motion between the Arabia plate and the Sinai subplate since the Middle Miocene, ~20 Ma. The interpretation of 107 km left-lateral slip along the DSF is based on observations from four independent sources: regional plate tectonics, local geology, seismology, and geodesy. The regional tectonics shows that the Red Sea is an incipient ocean, where the Arabian plate has been breaking away from Africa since Late Oligocene-Early Miocene. This motion is transferred to the collision with Eurasia via sinistral shear along the DSF (Courtillot et al., 1987; Freund, 1965; Garfunkel, 1981; Joffe and Garfunkel, 1987; Quennell, 1956). Local geology shows systematic offset of numerous pre-Miocene geologic features by a total of ~107 km (Bartov et al., 1980; Freund, 1965; Quennell, 1956) and fault geometry that indicates left-lateral motion (Garfunkel, 1981). Paleoseismic and archaeoseismic studies show sub-recent activity as sinistral offsets of natural and of manmade structures (e.g., Amit et al., 2002; Ellenblum et al., 1998; Klinger et al., 2000; Meghraoui et al., 2003; Niemi et al., 2001). Focal mechanisms of moderate-to-large earthquakes show sinistral motion along the DSF and generally are in agreement with the location of the active faults, based on geological data (Baer et al., 1999; Hofstetter et al., 2007; Klinger et al., 1999; Salamon et al., 1996). And finally, geodetic measurements are consistent and confirm the left-lateral slip as well as the slip rate from other palaeoseismic evidence of 4±1 mm/yr (Le Beon et al., 2006; Le Beon et al., 2008; McClusky et al., 2003; Reilinger et al., 2006; Wdowinski et al., 2004). This rate, as well as uniform Gutenberg-Richter frequency-magnitude relation, indicate stable tectonic regime in the last 60 ka (Begin et al., 2005; Hamiel et al., 2008).

The complex geometry of the fault is apparent in pull-apart grabens, which are associated with releasing bends, and pressure ridges that formed where restraining bends occur. Garfunkel (1981) maintains that the pull-apart basins are all shorter the total lateral offset because they began to form at a later stage, after some motion had already accrued. This view is supported by seismic surveys that reveal earlier buried basins, which are no longer active (Frieslander, 2000).

The pull-apart basins have acted like sediment traps. Studies of the Miocene to Recent clastic and evaporitic sediments as well as some magmatic sequences that accumulated in the basins have yielded a wealth of information and insight on the history of sedimentological conditions and processes (e.g., Bookman et al., 2004; Frostick and Reid, 1989; Klinger et al., 2003; Sneh, 1981, 1982; Tsatskin and Nadel, 2003), climate (e.g., Bartov et al., 2003; Begin et al., 1974; Frumkin et al., 1991; Stein, 2001), geomagnetic secular variation (Marco et al., 1998), seismicity and deformation (e.g., Agnon et al., 2006; Bartov and Sagy, 2004; El-Isa and Mustafa, 1986; Heifetz et al., 2005; Ken-Tor et al., 2001; Marco et al., 1996; Migowski et al., 2004), fauna and flora (Kislev et al., 1992), humans, and environment (e.g., Braun et al., 1991; Goren-Inbar and Belitzky, 1989; Goren-Inbar et al., 2000; Ron and Levi, 2001).

Several authors noted that the detailed shape of the DSF had changed through time (Garfunkel, 1981; Heimann and Ron, 1987, 1993; Marco, 2007; Rotstein et al., 1992; Shamir et al., 2005; ten Brink et al., 1999; ten-Brink and Ben-Avraham, 1989). The widest zone of about 50 km of distributed faulting is found in the Galilee, where the early-stage (Miocene) faults were associated with formation of basins (Freund et al., 1970; Shaliv, 1991) and with rotation of rigid blocks about sub-vertical axes (Ron et al., 1984). Subsequent post-Miocene deformation took place mostly in the form of normal faulting on E-W trending faults and the transform movement is currently localized in a very narrow zone. The deformation in the south was characterized initially by a 20-30-km-wide zone with primarily strike-slip and some normal slip on faults trending sub-parallel to the main transform fault. It later became localized in the Arava, where a single narrow fault zone offsets the youngest alluvium. In the earliest phase, young faults became active in the Negev, some 20 km west of the Arava (Avni et al., 2000), perhaps indicating another widening phase of the DSF zone (Marco, 2007).

Table 1. Various estimates of the Dead Sea Fault slip rate

Period	Rate mm/y	Data	Reference
Late Pleistocene-Recent	10	Geological	(Freund et al., 1968)
Last 1000 yr	0.8-1.7	Historical	(Garfunkel et al., 1981)

Plio-Pleistocene	7-10	Geological	(Garfunkel et al., 1981)
Last 4500 yr	2.2	Seismicity	(Ben-Menahem, 1981)
Late Pleistocene	6.4±0.4	Seismicity	(El-Isa and Mustafa, 1986)
Plio-Pleistocene	6 (0.283°/ma)	Plate kinematics	(Joffe and Garfunkel, 1987)
Holocene	9	Geological	(Reches and Hoexter, 1981)
Plio-Pleistocene	20	Geological	(Steinitz and Bartov, 1986)
Holocene	>0.7	Geological	(Gardosh et al., 1990)
Plio-Pleistocene	5.4-6.1	Geological	(Heimann, 1990)
Plio-Pleistocene	3-7	Drainage systems, Arava Fault	(Ginat et al., 1998)
Pleistocene	2-6, prefer 4	Alluvial fans, N. Arava	(Klinger et al., 2000)
Pleistocene	4.7±1.3	Alluvial fans, Arava	(Niemi et al., 2001)
Last 2000 yrs	6.9±0.1	Paleo and Archaeoseismology, Missyaf (DSF in Syria)	(Meghraoui et al., 2003)
1996-1999	2.6±1	Geodesy, GPS	(Pe'eri et al., 2002)
1996-2003	3.3±0.4	Geodesy, GPS	(Wdowinski et al., 2004)
25 ka	3.8–6.4	Geological, Lebanon	(Daëron et al., 2004)
Last 5000 yrs	≥3	Stream channel, Jordan Gorge	(Marco et al., 2005)
Survey-Mode GPS	5.6 to 7.5	(from south to north)	(McClusky et al., 2003)
1999-2005	4.9±1.4	GPS	(Le Beon et al., 2008) and thesis
Last 47.5 kyrs	4.7 to 5.1 mm/yr	Offset channels, Jordan	(Ferry et al., 2007) Comment/Reply: (Ferry and Meghraoui, 2008; Klein, 2008)

References

Agnon, A., Migowski, C., and Marco, S., 2006, Intraclast breccia layers in laminated sequences: recorders of paleo-earthquakes, *in* Enzel, Y., Agnon, A., and Stein, M., eds., New Frontiers in Dead Sea Paleoenvironmental Research, Geological Society of America Special Publication, p. 195-214.

Amit, R., Zilberman, E., Enzel, Y., and Porat, N., 2002, Paleoseismic evidence for time dependency of seismic response on a fault system in the southern Arava valley, Dead Sea rift, Israel: Geol. Soc. Am. Bull., v. 114, p. 192-206.

Avni, Y., Bartov, Y., Garfunkel, Z., and Ginat, H., 2000, Evolution of the Paran drainage basin and its relation to the Plio-Pleistocene history of the Arava Rift western margin, Israel: Isr. J. Earth Sci., v. 49, p. 215-238.

Baer, G., Sandwell, D., Williams, S., Bock, Y., and Shamir, G., 1999, Coseismic deformation associated with the November 1995, Mw = 7.1 Nuweiba earthquake, Gulf of Elat (Aqaba), detected by synthetic aperture radar interferometry: J. Geophys. Res., v. 104, p. 25,221-25,232.

Bartov, Y., Goldstein, S.L., Stein, M., and Enzel, Y., 2003, Catastrophic arid episodes in the Eastern Mediterranean linked with the North Atlantic Heinrich events: Geology, v. 31, p. 439-442.

Bartov, Y., and Sagy, a., 2004, Late Pleistocene extension and strike-slip in the Dead Sea Basin: Geological Magazine, v. 141, p. 565-572.

Bartov, Y., Steinitz, G., Eyal, M., and Eyal, Y., 1980, Sinistral movement along the Gulf of Aqaba - its age and relation to the opening of the Red Sea: Nature, v. 285, p. 220-221.

Begin, B.Z., Steinberg, D.M., Ichinose, G.A., and Marco, S., 2005, A 40,000 years unchanging of the seismic regime in the Dead Sea rift: Geology, v. 33, p. 257-260.

Begin, Z.B., Ehrlich, A., and Nathan, Y., 1974, Lake Lisan, the Pleistocene precursor of the Dead Sea: Geol. Surv. Isr. Bull., v. 63, p. 30.

Ben-Menahem, A., 1981, Variation of slip and creep along the Levant Rift over the past 4500 years: Tectonophysics, v. 80, p. 183-197.

Bookman, R., Enzel, Y., Agnon, A., and Stein, M., 2004, Late Holocene lake levels of the Dead Sea: Bull. Geol. Soc. Am., v. 116, p. 555-571.

Braun, D., Ron, H., and Marco, S., 1991, Magnetostratigraphy of the hominid tool bearing Erk el Ahmar formation in the northern Dead Sea Rift: Isr. J. Earth Sci., v. 40, p. 191-197.

Courtillot, V., Armijo, R., and Tapponnier, P., 1987, The Sinai Triple Junction Revisited: Tectonophysics, v. 141, p. 181-190.

Daëron, M., Benedetti, L., Tapponnier, P., Sursock, A., and Finkel, R.C., 2004, Constraints on the post 25-ka slip rate of the Yammouneh fault (Lebanon) using in situ cosmogenic 36Cl dating of offset limestone-clast fans: Earth Planet. Sci. Lett., v. 227, p. 105-119.

El-Isa, Z.H., and Mustafa, H., 1986, Earthquake deformations in the Lisan deposits and seismotectonic implications: Geophys. J. R. Astron. Soc., v. 86, p. 413-424.

Ellenblum, R., Marco, S., Agnon, A., Rockwell, T., and Boas, A., 1998, Crusader castle torn apart by earthquake at dawn, 20 May 1202: Geology, v. 26, p. 303-306.

Ferry, M., and Meghraoui, M., 2008, Reply to the comment of Dr M. Klein on: "A 48-kyr-long slip rate history for the Jordan Valley segment of the Dead Sea Fault": Earth and Planetary Science Letters, v. 268, p. 241-242.

Ferry, M., Meghraoui, M., Abou Karaki, N., Al-Taj, M., Amoush, H., Al-Dhaisat, S., and Barjous, M., 2007, A 48-kyr-long slip rate history for the Jordan Valley segment of the Dead Sea Fault: Earth and Planetary Science Letters, v. 260, p. 394-406.

Freund, R., 1965, A model of the structural development of Israel and adjacent areas since Upper Cretaceous times: Geol. Mag., v. 102, p. 189-205.

Freund, R., Garfunkel, Z., Zak, I., Goldberg, M., Weissbrod, T., and Derin, B., 1970, The shear along the Dead Sea rift: Phil. Trans. Roy. Soc. Lond., v. A. 267, p. 107-130.

Freund, R., Zak, I., and Garfunkel, Z., 1968, Age and rate of the sinistral movement along the Dead Sea Rift: Nature, v. 220, p. 253-255.

Frieslander, U., 2000, The structure of the Dead Sea Transform emphasizing the Arava using new geophysical data [Ph.D. (in Hebrew, English abstract) thesis], The Hebrew University of Jerusalem.

Frostick, L.E., and Reid, I., 1989, Climatic versus tectonic controls of fan sequences: lessons from the Dead Sea, Israel: Jour. Geol. Soc. London, v. 146, p. 527-538.

Frumkin, A., Magaritz, M., Carmi, I., and Zak, I., 1991, The Holocene climatic record of the salt caves of Mount Sedom, Israel: The Holocene, v. 3, p. 191-200.

Gardosh, M., Reches, Z., and Garfunkel, Z., 1990, Holocene tectonic deformation along the western margins of the Dead Sea: Tectonophysics, v. 180, p. 123-137.

Garfunkel, Z., 1981, Internal structure of the Dead Sea leaky transform (rift) in relation to plate kinematics: Tectonophysics, v. 80, p. 81-108.

Garfunkel, Z., Zak, I., and Freund, R., 1981, Active faulting in the Dead Sea rift: Tectonophysics, v. 80, p. 1-26.

Ginat, H., Enzel, Y., and Avni, Y., 1998, Translocation of Plio-Pleistocene drainage system along the Dead Sea Transform, south Israel: Tectonophysics, v. 284, p. 151-160.

Goren-Inbar, N., and Belitzky, S., 1989, Structural position of the Pleistocene Gesher Benot Ya'akov site in the Dead Sea Rift zone: Quaternary Research, v. 31, p. 371-376.

Goren-Inbar, N., Craig, F.S., Verosub, K.L., Melamed, Y., Kislev, M., Tchernov, E., and Saragusti, I., 2000, Pleistocene milestones on the Out-of-Africa Corridor at Gesher Benot Ya'aqov, Israel: Science, v. 289, p. 944-947.

Hamiel, Y., Amit, R., Begin, Z.B., Marco, S., Katz, O., Salamon, A., Zilberman, E., and Porat, N., 2008, The seismicity along the Dead Sea fault during the last 60,000 years: Seismological Society of America Bulletin, v. in press.

Heifetz, E., Agnon, A., and Marco, S., 2005, Soft sediment deformation by Kelvin Helmholtz Instability: A case from Dead Sea earthquakes: Earth Planet. Sci. Lett., v. 236, p. 497-504.

Heimann, A., 1990, The development of the Dead Sea rift and its margins in the northern Israel during the Pliocene and the Pleistocene, Golan Res. Inst. and Geol. Surv. Isr.

Heimann, A., and Ron, H., 1987, Young faults in the Hula pull-apart basin, central Dead Sea transform: Tectonophysics, v. 141, p. 117-124.

—, 1993, Geometric changes of plate boundaries along part of the northern Dead Sea Transform: Geochronologic and paleomagnetic evidence: Tectonics, v. 12, p. 477-491.

Hofstetter, R., Klinger, Y., Amrat, A.Q., Rivera, L., and Dorbath, L., 2007, Stress tensor and focal mechanisms along the Dead Sea fault and related structural elements based on seismological data: Tectonophysics, v. 429, p. 165-181.

Joffe, S., and Garfunkel, Z., 1987, Plate kinematics of the circum Red Sea- a re-evaluation: Tectonophysics, v. 141, p. 5-22.

Ken-Tor, R., Agnon, A., Enzel, Y., Marco, S., Negendank, J.F.W., and Stein, M., 2001, High-resolution geological record of historic earthquakes in the Dead Sea basin: J. Geophys. Res., v. 106, p. 2221-2234.

Kislev, M.E., Nadel, D., and Carmi, I., 1992, Epipalaeolithic (19,000 Bp) Cereal and Fruit Diet at Ohalo-Ii, Sea of Galilee, Israel: Review of Palaeobotany and Palynology, v. 73, p. 161-166.

Klein, M., 2008, A comment on: "A 48-kyr-long slip rate history for the Jordan Valley segment of the Dead Sea Fault" EPSL 260 (2007) 394-406: Earth and Planetary Science Letters, v. 268, p. 239-240.

Klinger, Y., Avouac, J.P., Abou-Karaki, N., Dorbath, L., Bourles, D., and Reyss, J.L., 2000, Slip rate on the Dead Sea transform fault in northern Araba Valley (Jordan): Geophys. J. Int., v. 142, p. 755-768.

Klinger, Y., Avouac, J.P., Bourles, D., and Tisnerat, N., 2003, Alluvial deposition and lake-level fluctuations forced by Late Quaternary climate change: the Dead Sea case example: Sedimentary Geology, v. 162, p. 119-139.

Klinger, Y., Rivera, L., Haessler, H., and Maurin, J.C., 1999, Active faulting in the Gulf of Aqaba: New knowledge from the Mw7.3 earthquake of 22 November 1995: Bull. Seism. Soc. Am., v. 89, p. 1025-1036.

Le Beon, M., Klinger, Y., Agnon, A., Dorbath, L., Baer, G., Meriaux, A.-S., Ruegg, J.-C., Charade, O., Finkel, R., and Ryerson, F., 2006, Geodetic versus geologic slip rate along the Dead Sea, Seismological Society of America Annual Meeting: San Francisco.

Le Beon, M., Klinger, Y., Amrat, A.Q., Agnon, A., Dorbath, L., Baer, G., Ruegg, J.C., Charade, O., and Mayyas, O., 2008, Slip rate and locking depth from GPS profiles across the southern Dead Sea Transform: Journal of Geophysical Research-Solid Earth, v. 113, p. -.

Marco, S., 2007, Temporal variation in the geometry of a strike-slip fault zone: Examples from the Dead Sea Transform: Tectonophysics, v. 445, p. 186 – 199.

Marco, S., Rockwell, T.K., Heimann, A., Frieslander, U., and Agnon, A., 2005, Late Holocene slip of the Dead Sea Transform revealed in 3D palaeoseismic trenches on the Jordan Gorge segment: Earth Planet. Sci. Lett., v. 234, p. 189-205.

Marco, S., Ron, H., McWilliams, M.O., and Stein, M., 1998, High-Resolution Record of Geomagnetic Secular Variation from Late Pleistocene Lake Lisan Sediments (Paleo Dead Sea): Earth Planet. Sci. Lett., v. 161, p. 145-160.

Marco, S., Stein, M., Agnon, A., and Ron, H., 1996, Long term earthquake clustering: a 50,000 year paleoseismic record in the Dead Sea Graben: J. Geophys. Res., v. 101, p. 6179-6192.

McClusky, S., Reilinger, R., Mahmoud, S., Sari, D.B., and Tealeb, A., 2003, GPS constraints on Africa (Nubia) and Arabia plate motions: Geophys. J. Int., v. 155, p. 126.

Meghraoui, M., Gomez, F., Sbeinati, R., derWoerd, J.V., Mouty, M., Darkal, A.N., Radwan, Y., Layyous, I., Najjar, H.A., Darawcheh, R., Hijazi, F., Al-Ghazzi, R., and Barazangi, M., 2003, Evidence for 830 years of seismic quiescence from palaeoseismology, archaeoseismology and historical seismicity along the Dead Sea fault in Syria: Earth Planet. Sci. Let., v. 210, p. 35-52.

Migowski, C., Agnon, A., Bookman, R., Negendank, J.F.W., and Stein, M., 2004, Recurrence pattern of Holocene earthquakes along the Dead Sea transform revealed by varve-counting and radiocarbon dating of lacustrine sediments: Earth and Planetary Science Letters, v. 222, p. 301-314.

Niemi, T.M., Zhang, H., Atallah, M., and Harrison, B.J., 2001, Late Pleistocene and Holocene slip rate of the Northern Wadi Araba fault, Dead Sea Transform, Jordan: Journal of Seismology, v. 5, p. 449-474.

Pe'eri, S., Wdowinski, S., Shtibelman, A., and Bechor, N., 2002, Current plate motion across the Dead Sea Fault from three years of continuous GPS monitoring: Geophys. Res. Lett., v. 29, p. doi: 10.1029/2001GL013879.

Quennell, A.M., 1956, Tectonics of the Dead Sea rift, Congreso Geologico Internacional, 20th sesion, Asociacion de Servicios Geologicos Africanos: Mexico City, p. 385-405.

Reches, Z., and Hoexter, D.F., 1981, Holocene seismic and tectonic activity in the Dead Sea area: Tectonophysics, v. 80, p. 235-254.

Reilinger, R., McClusky, S., Vernant, P., Lawrence, S., Ergintav, S., Cakmak, R., Ozener, H., Kadirov, F., Guliev, I., Stepanyan, R., Nadariya, M., Hahubia, G., Mahmoud, S., Sakr, K., ArRajehi, A., Paradissis, D., Al-Aydrus, A., Prilepin, M., Guseva, T., Evren, E., Dmitrotsa, A., Filikov, S.V., Gomez, F., Al-Ghazzi, R., and Karam, G., 2006, GPS constraints on continental deformation in the Africa-Arabia-Eurasia continental collision zone and implications for the dynamics of plate interactions: Journal of Geophysical Research-Solid Earth, v. 111, p. -.

Ron, H., Freund, R., Garfunkel, Z., and Nur, A., 1984, Block-rotation by strike-slip faulting: structural and paleomagnetic evidence: J. Geophys. Res, v. 89, p. 6256-6270.

Ron, H., and Levi, S., 2001, When did hominids first leave Africa?: New high-resolution magnetostratigraphy from the Erk-el-Ahmar Formation, Israel: Geology, v. 29, p. 887-890.

Rotstein, Y., Bartov, Y., and Frieslander, U., 1992, Evidence for local shifting of the main fault and changes in the structural setting, Kinarot basin, Dead Sea transform: Geology, v. 20, p. 251-254.

Salamon, A., Hofstetter, A., Garfunkel, Z., and Ron, H., 1996, Seismicity of the eastern Mediterranean region: Perspective from the Sinai subplate: Tectonophysics, v. 263, p. 293-305.

Shaliv, G., 1991, Stages in the tectonic and volcanic history of the Neogene basin in the Lower Galilee and the valleys: Geological Survey of Israel - Report (in Hebrew, English abstract), v. 11/91, p. 1–94.

Shamir, G., Eyal, Y., and Bruner, I., 2005, Localized versus distributed shear in transform plate boundary zones: The case of the Dead Sea Transform in the Jericho Valley: Geochemistry Geophysics Geosystems, v. 6, p. -.

Sneh, A., 1981, The Hazeva Formation in the northern Arava: Isr. Jour. Earth Sci., v. 30, p. 81-92.

—, 1982, Quaternary of the northwestern Arava, Israel: Isr. Jour. Earth Sci., v. 31, p. 9-16.

Stein, M., 2001, The sedimentary and geochemical record of Neogene - Quaternary water bodies in the Dead Sea Basin - inferences for the regional paleoclimatic history: Journal of Paleolimnology, v. 26, p. 271-282.

Steinitz, G., and Bartov, Y., 1986, The 1985 time table for the tectonic events along the Dead Sea transform: Terra Cognita, v. 6, p. 160.

ten Brink, U.S., Rybakov, M., Al-Zoubi, A.S., Hassouneh, M., Frieslander, U., Batayneh, A.T., Goldschmidt, V., Daoud, M.N., Rotstein, Y., and Hall, J.K., 1999, Anatomy of the Dead Sea transform: Does it reflect continuous changes in plate motion?: Geology, v. 27, p. 887-890.

ten-Brink, U.S., and Ben-Avraham, Z., 1989, The anatomy of a pull-apart basin: Reflection observations of the Dead Sea basin: Tectonics, v. 8, p. 333-350.

Tsatskin, A., and Nadel, D., 2003, Formation processes at the Ohalo II submerged prehistoric campsite, Israel, inferred from soil micromorphology and magnetic susceptibility studies: Geoarchaeology-an International Journal, v. 18, p. 409-432.

Wdowinski, S., Bock, Y., Baer, G., Prawirodirdjo, L., Bechor, N., Naaman, S., Knafo, R., Forrai, Y., and Melzer, Y., 2004, GPS Measurements of current crustal movements along the Dead Sea Fault: J. Geophys. Res., v. 109, p. 1-16.

Hula Valley

17.2.2009

Field leader

Amotz Agnon

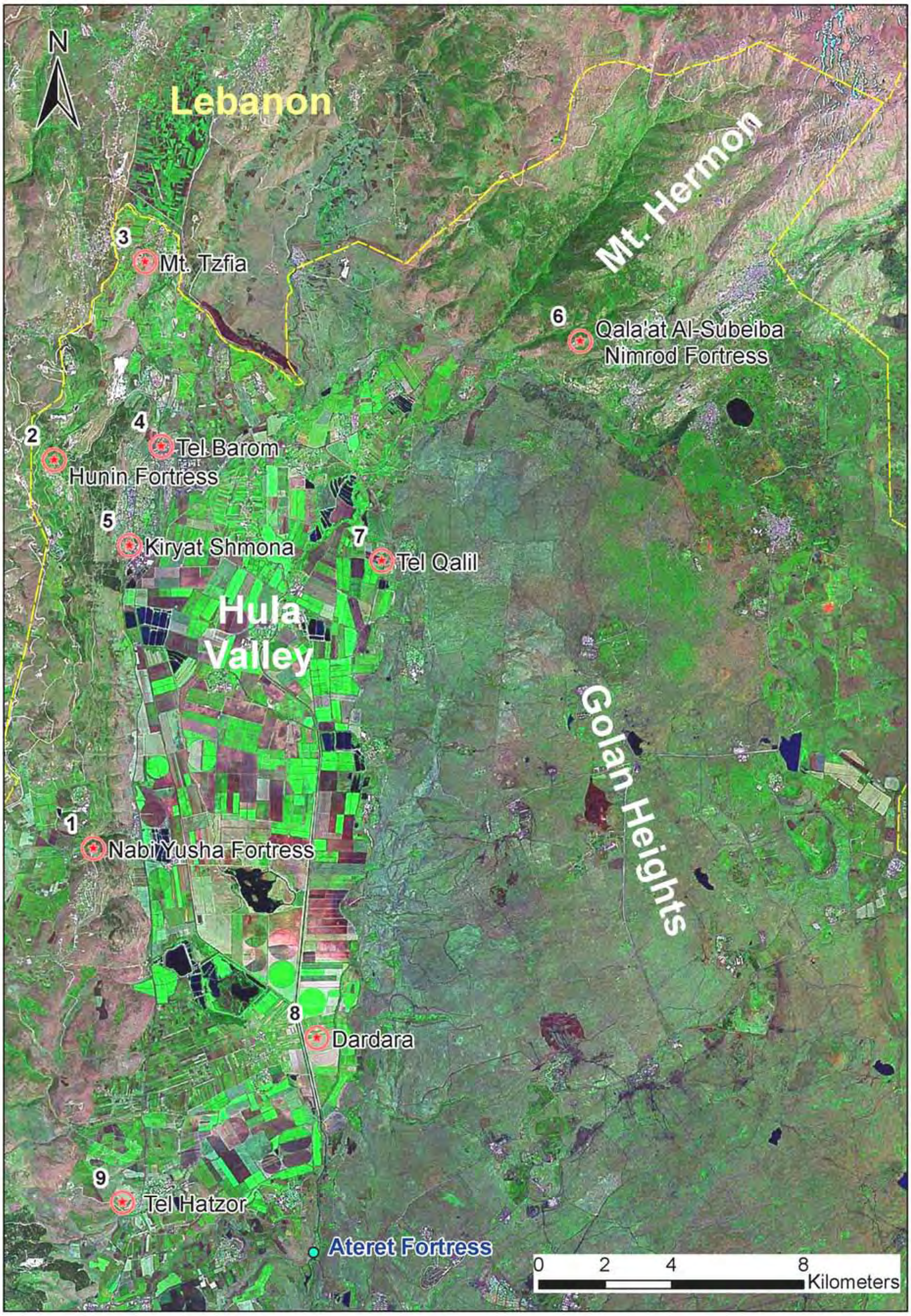
N
Lebanon
Mt. Hermon
3
Mt. Tzfia
6
Qala'at Al-Subeiba
Nimrod Fortress
4
Tel Barom
2
Hunin Fortress
5
Kiryat Shmona
7
Tel Qalil
Hula
Valley
Golan Heights
1
Nabi Yusha Fortress
8
Dardara
9
Tel Hatzor
Ateret Fortress
0 2 4 8
Kilometers

Hula basin

Field guides: Amotz Agnon[1], Hagai Ron[1], Mor Kanari[2], Benjamin Medvedev[3], Moshe Politi[1], Oded Katz[4], Shmuel Marco[2], Rivka Amit[4], Ariel Heimann[5]

[1]Institute of Earth Sciences, The Hebrew University of Jerusalem
[2] Department of Geophysics and Planetary Sciences, Tel Aviv University
[3]The Geophysical Institute of Israel
[4]Geological Survey of Israel
[5]The Davidson Institute of Science Education, Weizmann Institute of Science, Israel

amotz@cc.huji.ac.il

This field-trip will present the following a perspectives on the Hula basin (numbers preceded by # refer to stops given in detail below): the basin as a part of the regional framework, namely a pull-apart basin straddling a major branching point along the transform (#1,#3,#9); intense meso-structures imprinted in the pre-rift carbonates (#2); rockfalls from tectonic scarps (#4); detection of active strands in the shallow subsurface (#5,#8); seismic damage to Medieval Period monuments (#2;#6); subsidiary structures at the margins and trenching results (#7). The route is planned as a clockwise loop.

Background

The Hula and Marj Ayun basins are the northernmost of a string of elongated transform basins along the plate boundary from the Gulf of Aqaba in the south (Fig 1). The stratigraphic section exposed records transition from a carbonate platform on the southern margins of the Neo-Thetys (Jurassic to Paleogene) to a continental margin subject to Neogene to Quaternary rifting and volcanism (Fig. 2). The volcanic plateau field that bounds the Hula valley form east (Golan Heights) is the western edge of the active volcanic field Harrat a Shammah. Neogene to Pleistocene volcanism has affected the Galilee on the western margin of the Hula (Fig. 3) and contributed to the basin fill (Fig. 4). Dating drilled flows has enabled Heimann and Steinitz to constrain the rate of subsidence (Fig. 5). The marginal normal faults east and west of the valley dominate the topography, but a through-going fault is indicated in the short wave content of the gravity field and the epicenter locations (Fig. 6). The stops of the tours (#1 to #9) are shown on Fig. 7.

The Western Margin

We start with a breath taking vista of the Hula basin from the top of the cliff uplifted at the footwall of the western marginal fault (Nebi Yusha / Yesha fortress, #1). The mountain is around 400m above sea-level, whereas the depression below is around 70m (~1000 ft. difference). The shape of the valley contour (contact of fill and bedrock) is a parallelepiped with a sense inverted relatively to the expected for a left lateral transform (Figs. 8 and 10). This may be related to the slip branched to the north east, and possibly to some shear partitioned to the south west. The branching point is hinted on the gravity map (Fig. 6) and old seismic lines are available to test this hypothesis (Fig. 9). Figs. 10 to 13 corroborate Schattner and Weinberger's (2008) suggestion for a through-going transform fault, and also our suggestion for branching close to the depocenter (Politi et al., 2008).

We follow the footwall block to Chastel Neuf / Kal'at Hunin (#2), a Crusader to Ottoman castle, located close on a splay of the Roum fault (a significant branch of the Dead Sea transform from the north-west corner of the basin to the Lebanese coast near Beirut). The castle was demolished three times by large seismic events (1202, 1759, 1837, the last one rupturing the Roum fault). The moat exposes severe tectonic deformation experienced by the bedrock before construction (Ron et al., 1997).

We descend to the valley to Har Tzfiyah (Mt. Vista - stop #3), where we observe the northwestern branching of the main fault to Yammouneh fault (major north-western branch), Roum fault (western north-west branch) and Hasbaya (eastern north-western branch) (Fig. 14).

Then we take a closer look at the transform near Tel Barom (#4), where a fault-zone-wave experiment shows a strong and narrow wave guide along the shallow hundreds of meters along the fault (Figs. 15-17). Fractured basalt exposed on a road cut may comprise the wave guide (Fig. 18). The fault juxtapose the basalt with marl that does not fracture (Fig. 19). We will see a campus constructed recently right on the main fault. Shtivelman et al. (2005) describe this experiment together with two similar surveys taken at Vadum Iacob / Ateret Casle, to be visited the next day, and near Eilat. We will see exposure of intensely fractured basalt that may act as a wave-guide. Tel-Barom turns out to be situated right on the main strand of the fault and a promising site for future archaeosesimic excavations.

The next stop (#5) features earthquake induced rockfalls and their dating, described below by Kanari et al.

The Eastern Margin

We cross the valley to the east passing by numerous archeological sites with their rich archaeoseismic potential yet to be realized (Tel Dan, Tel Banyas, to name the most famous) (Fig. 7). We ascend nearly 700m to Kal'at A-sSubeiba / Nimrod fortress to observe the muslim monuments damaged heavily by the 1759 seismic events (#6). We will study the shifted arches and vaults that record the direction of shaking. On the way south we visit the eastern scarp at the local push-up Tel Qalil (#7), near the paleoseismic trench site of Azaz fault (Zilberman et al., 2000) (Fig. 14).

The Historical Lake and the Southern Depression

Stop #8 is on the lake bed, as testified by the mollusk shells abundant in the agricultural soil. This is the site of a high resolution seismic/gravity study that features a positive flower structure up to several tens meters below the surface (Fig. 20). This survey corroborates the location of the through-going fault suggested by Schattner and Weinberger (2008). A trench excavated lake sediment poor in datable material (Medvedev et al., 2008). Intense fracturing has been identified and future work will focus on finer geophysical imaging and better age control.

Stop #9 will give us a last view of the depression from Tel Hatzor, a biblical ruin of a major city.

References

Belitzky, S., 2002. The morphotectonic structure of the lower Jordan Valley – an active segment of the Dead Sea Rift, EGU Stephan Mueller Special Publications Series vol. 2, pp 95-103.

Freund, R., Garfunkel, Z.,1976. Guidebook to excursion along the Dead Sea Rift. Dept. Geol., Hebrew Univ. Jerusalem, 27 p.

Heimann, A., Ron, H., 1987. Young faults in the Hula pull-apart basin, central Dead Sea transform, Tectonophys., 141, 117-124.

Heimann, A., Ron, H., 1993. Geometric changes of plate boundaries along pat of the northern Dead Sea transform: chronologic and paleomagnetic evidence, Tectonics, 12, 477-491.

Heimann, A., Steinitz, G., 1987. K-Ar dating of the Ramat Korazim basalts, Dead Sea Rift, Israel Geological Society, annual meeting; abstracts, 54-56.

Heimann, A., Steinitz, G., Mor, D., Shaliv, G., 1996. 40Ar/ 39Ar total gas ages of basalts from Notera 3 well, Hula Valley, centrl Dead Sea Rift: stratigraphic and tectonic implications. Isr. J. Earth Sci., 38,173-184.

Medvedev, B., Makovsky, Y., Agnon, 2008a. A.Slip partitioning in the Hula Basin: new evidence from high resolution geophysics, Israel Geological Society, annual meeting; abstracts, 65.

Medvedev B., Makovsky,Y., Bergman, N., Agnon, A., 2008b. Multi-scale fault imaging in the Hula basin, Northern Israel, EOS Trans. AGU, 89,Fall Meet. Suppl.,cAbstract NS13A-1083

Politi, M., Medvedev, B., Shamir, G., Makovsky, Y., Agnon, A, 2008. Branching of the Dead Sea Transform at the Hula Basin; evidence from the sub-surface, srael Geological Society, annual meeting; abstracts, 78.

Ron, H., Shamir, G., Eyal, M. 1997. Deformation of Margaliot block between Roum and Margaliot faults. Isr. Geol. Soc. Annu. Mtg., Kefar Gil'adi, Field trip Guide- book, pp. 33–45 (in Hebrew).

Rybakov, M., Fleischer, L., ten Brink, U., 2003. The Hula valley subsurface inferred from gravity data. Isr. J. Earth Sci., 52, 113-122.

Schattner U., Weinberger R., 2008. A mid-Pleistocene deformation transition in the Hula basin, northern Israel: Implications for the tectonic evolution of the Dead Sea Fault, Geochem. Geophys. Geosyst. 9, Q07009.

Shamir, G., Feldman, L., 1996. Earthquake activity in the Qiryat-Shmemona area, The geophysical Institute of Israel, Rep. # 953/160/96.

Shtivelman, V., Marco, S., Reshef, M., Agnon, A., Hamiel, Y., 2005. Using trapped waves for mapping shallow fault zones, Near Surface Geophys., 3, 95-101

Sneh, A., Weinberger, R. 2004. Geology of the Metulla quadrangle, northern Israel: Implications for the offset along the Dead Sea Rift. Isr. J. Earth Sci. 52, 123–138.

Zilberman E., Amit R., Heimann A., Porat, N., 2000. Changes in Holocene Paleoseismic activity in the Hula pull-apart basin, Dead Sea Rift, northern Israel, Tectonophys., 321,237-252.

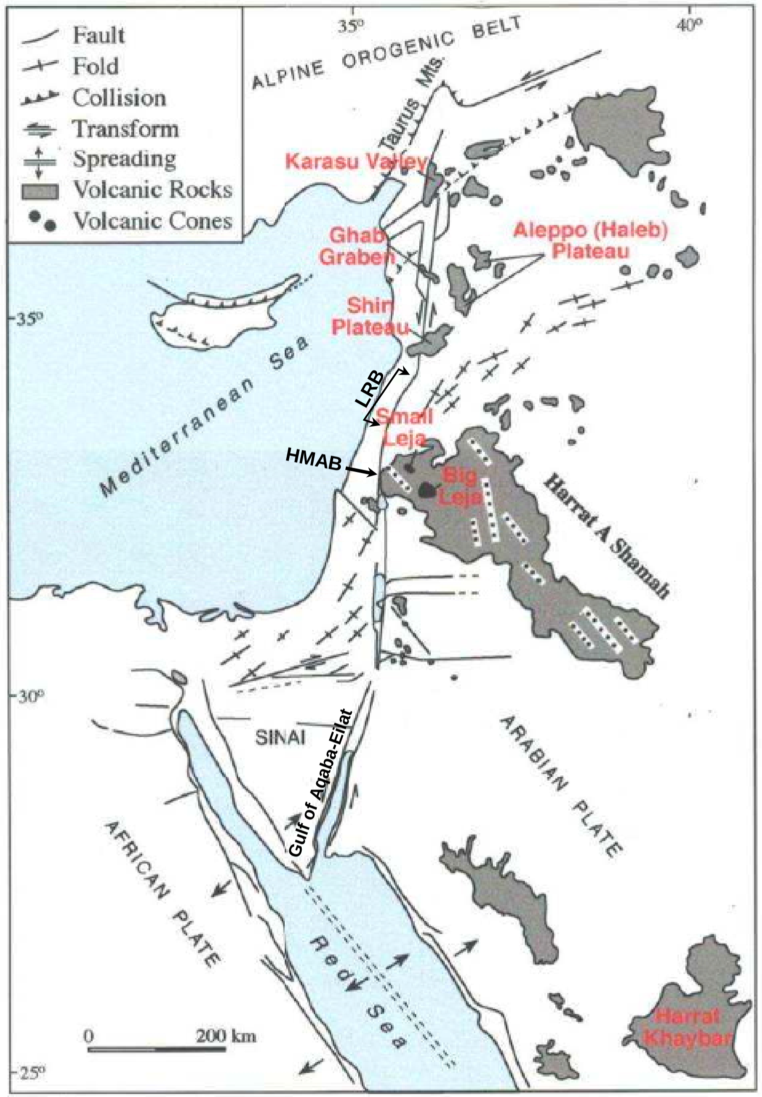

Figure 1: General tectonic setting of Israel and adjacent areas including the volcanic fields (Heimann et al., 1996, after Freund and Garfunkel, 1976). HMAB - Hula - MarjAyun basins. LRB: Lebanon restraining bend.

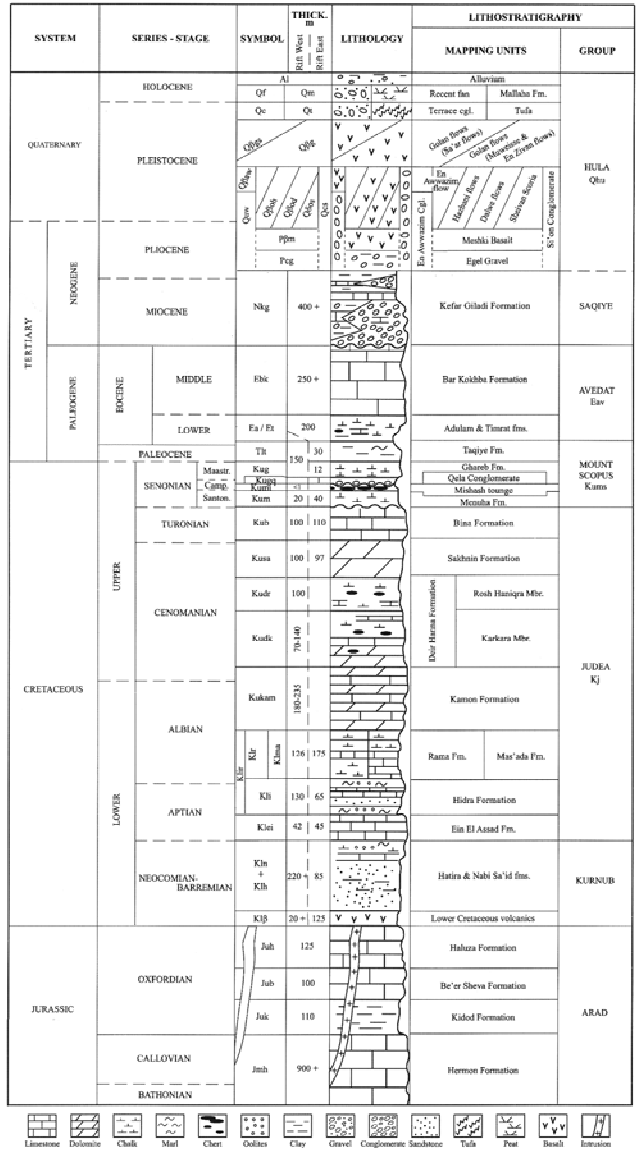

Figure 2: Stratigraphic section of rock units exposed in the Metula quadrangle which straddles the northern Hula valley. Sneh and Weinberger, 2004.

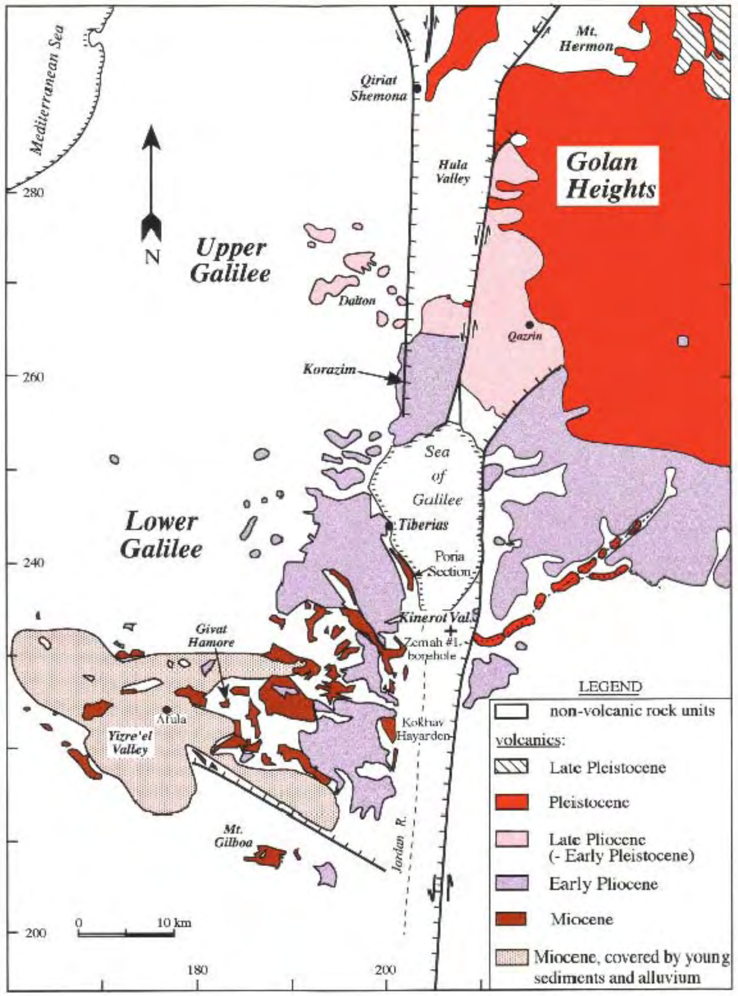

Figure 3: Cenozoic volcanism in the Galilee, northern Dead Sea Transform and the Golan (Heimann et al., 1996).

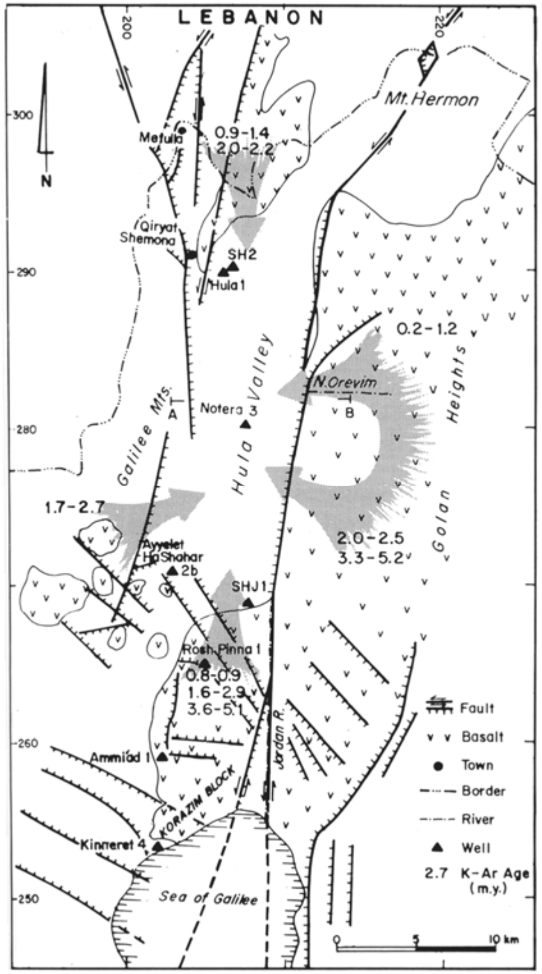

Figure 4: The possible sources of Plio-Pleistocene basalt flows found at the Hula Valley (surface and sub-surface) (Heimann and Steinitz, 1989).

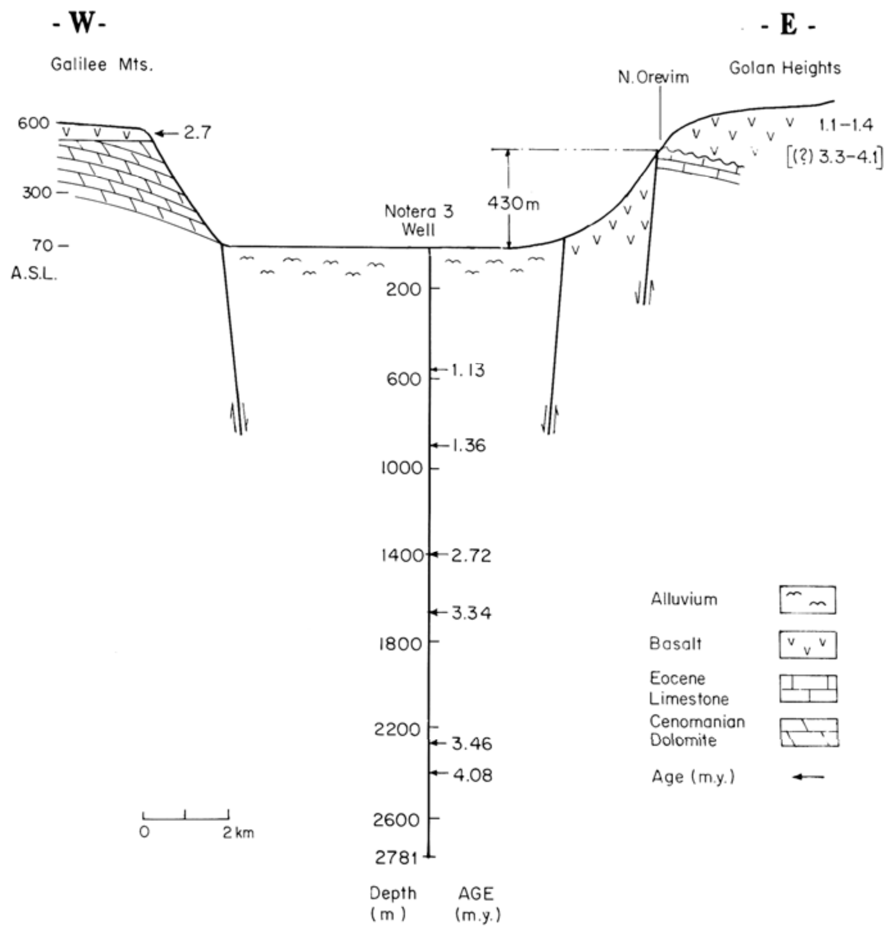

Figure 5: A schematic cross secttion through the Notera-3 well with K-Ar ages of basalt flows (Ma). Calculated subsidence rate are between 0.5 and 0.8 mm/yr (Heimann and Steinitz, 1989).

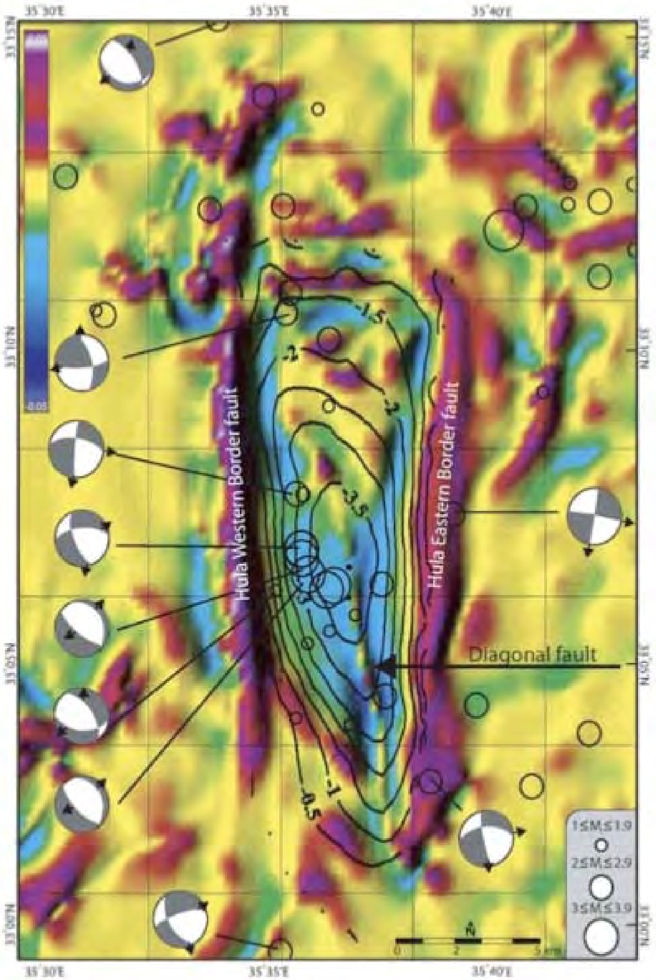

Figure 6: Dip curvature, second derivative of the gravity field superposed by structural 0.5 km contours of the base of the Hula basin fill (after Rybakov et al. 2003). Location of selected seismic events and focal plane solutions of earthquakes recorded between 1982 and 1997 (after Ron et al. 1997) are marked. Schattner and Weinberger (2008) identify the through going lineament with the main active strike-slip strand.

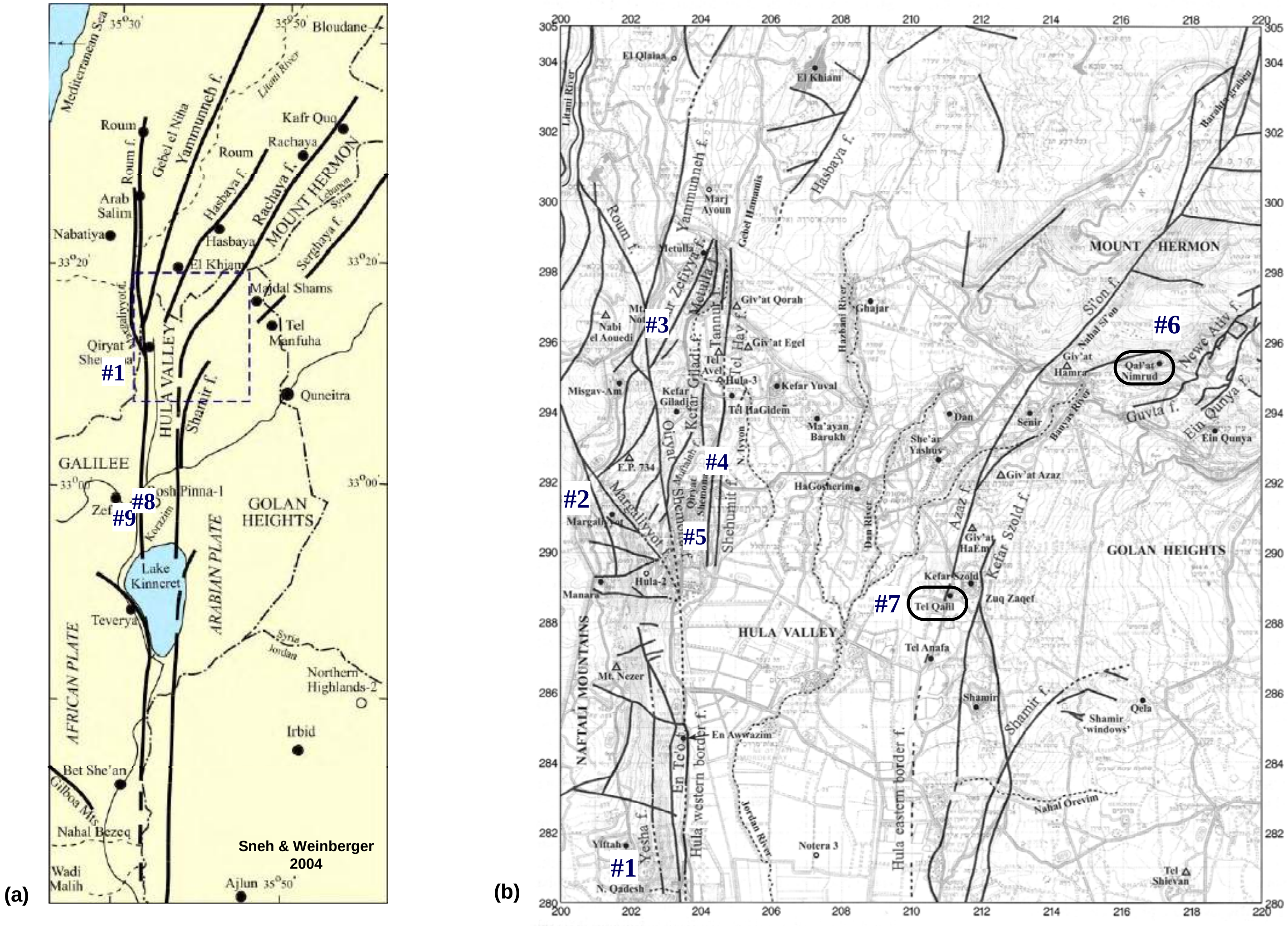

Figure 7: **(a)** A generalized tectonic map of the northern valleys. The first and last stops (#1, #8, #9) are shown. The broken-line quadrangle demarcates the location of the bottom figure.
(b) Excursion stops #2-#7 shown on a detailed fault map of Metulla quadrangle, Geological Map of Israel 1:50,000, GSI (Sneh and Weinberger, 2004).

Geologic map

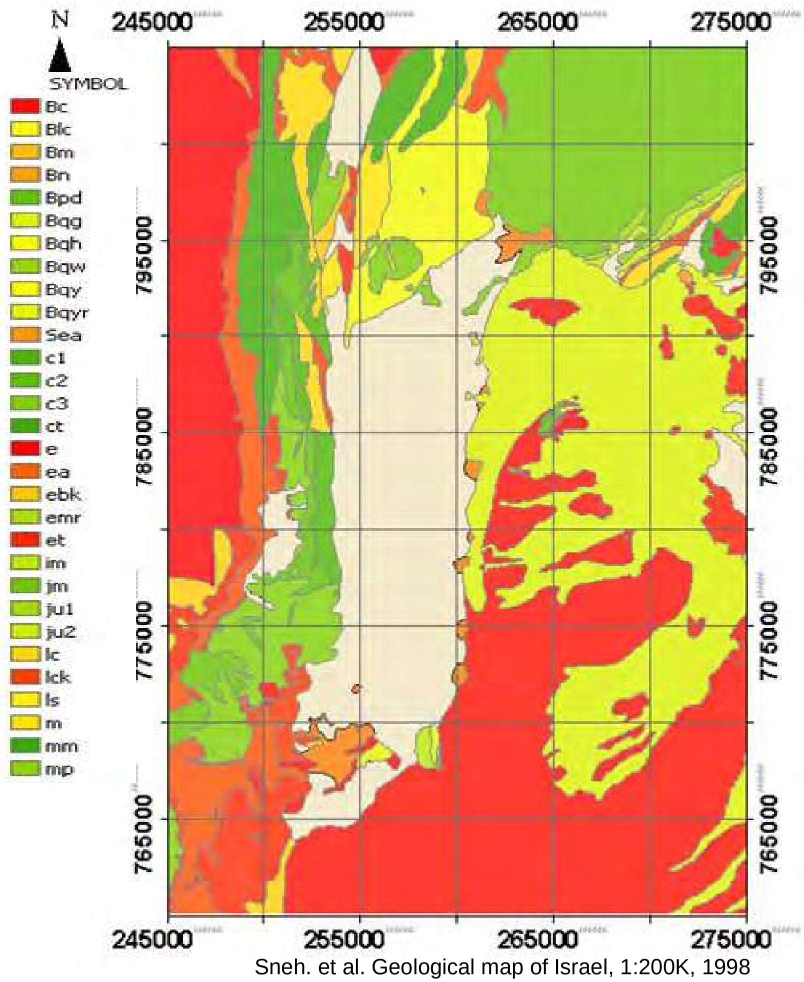

Figure 8: A geological map of the Hula basin. Note the "inverted" parallelepiped shape of the basin fill. Green shades - Upper Cretaceous (shallow marine); Orange - Paleogene (shallow marine); Yellow: Neogene (fluvial); Red: Plio-Pleistocene (volcanic); Grey: Late Quaternary (soil and clastic fill).

Seismic profiles and wells location

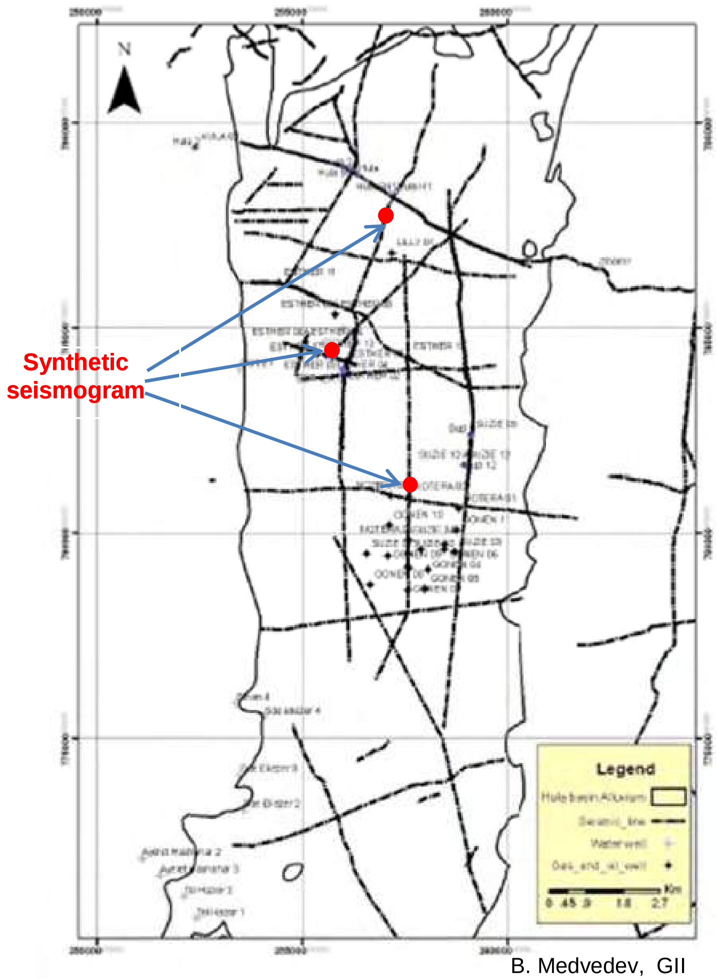

Figure 9: A map of seismic lines and wells in the Hula basin.

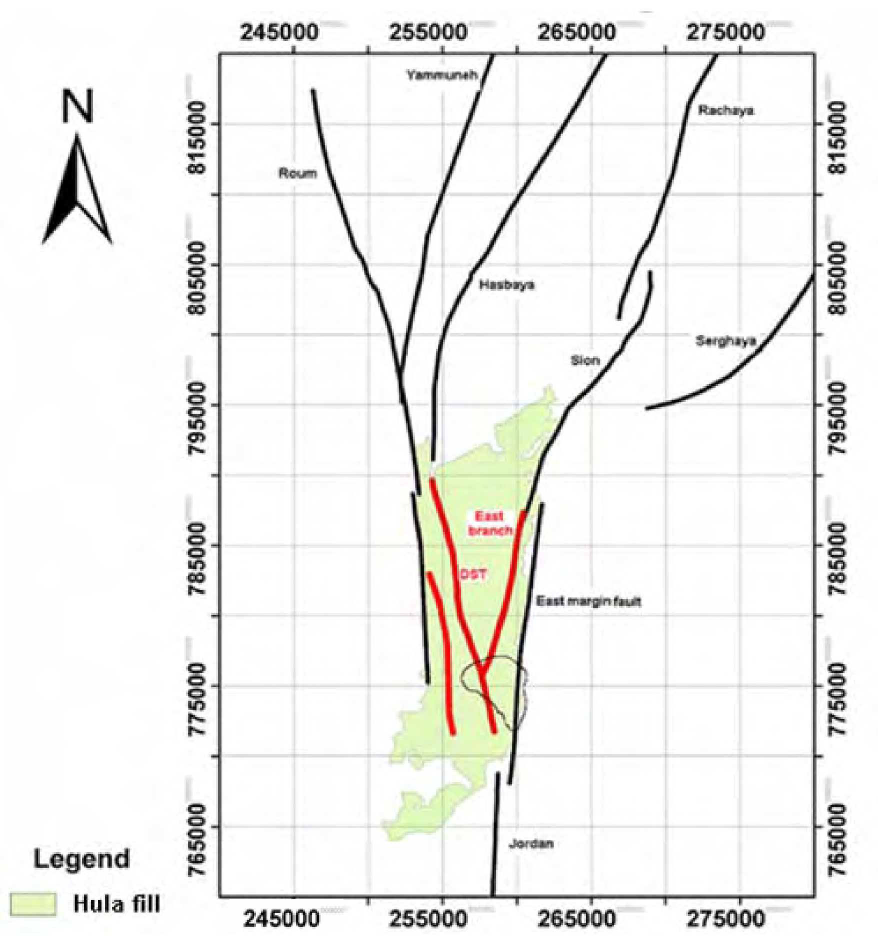

Fig. 10: Branching of DST. Faults – modified after, Heimann and Ron (1993), Shamir and Feldman (1996), Belitzky (2002), Sneh and Weinberger (2004) – Black Faults inferred from seismic – Red Hula basin fill – Green. (“inverted” parallelepiped).

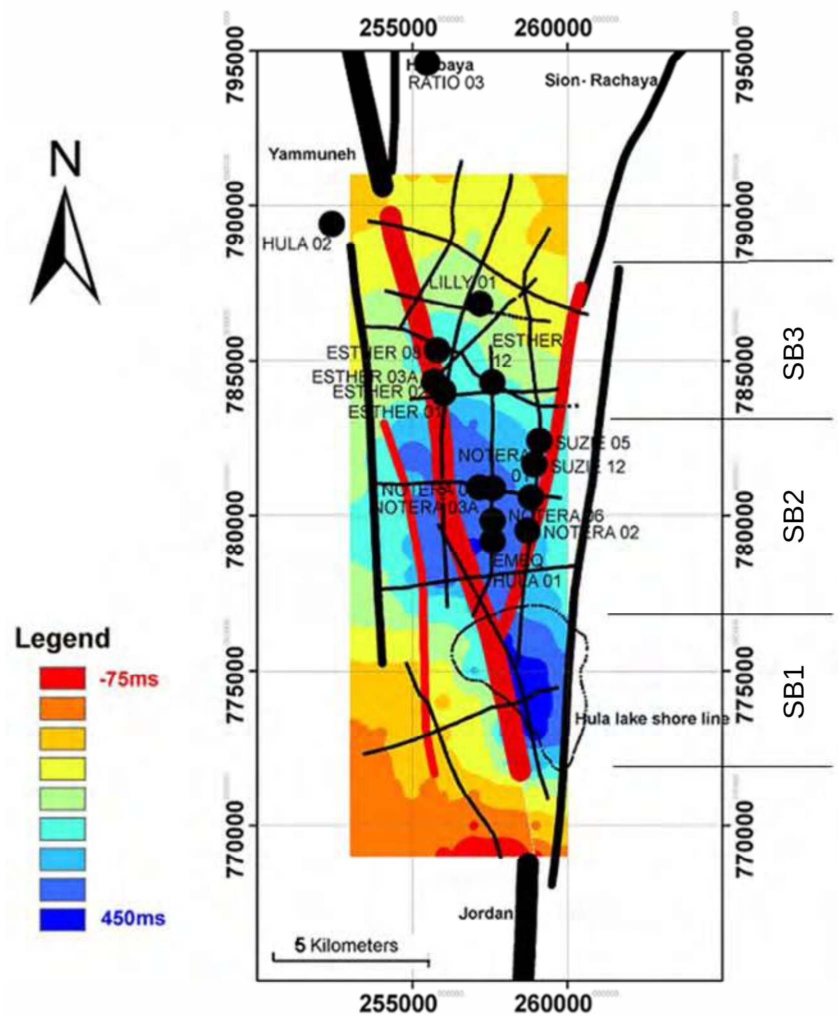

Fig. 11: A structural map (time) on top Ortal flows. An elongated depression along the eastern side of the main fault divided into 3 sub-basins. The sub-basins apparent east of the master fault: SB(1) - the recent depocenter correlating with the historical Hula lake (drained during the early 1950's), SB(2) - a central depression, bounded on either side by two main branches of the rift. SB(3) - a shallow sub-basin. See seismic profiles.

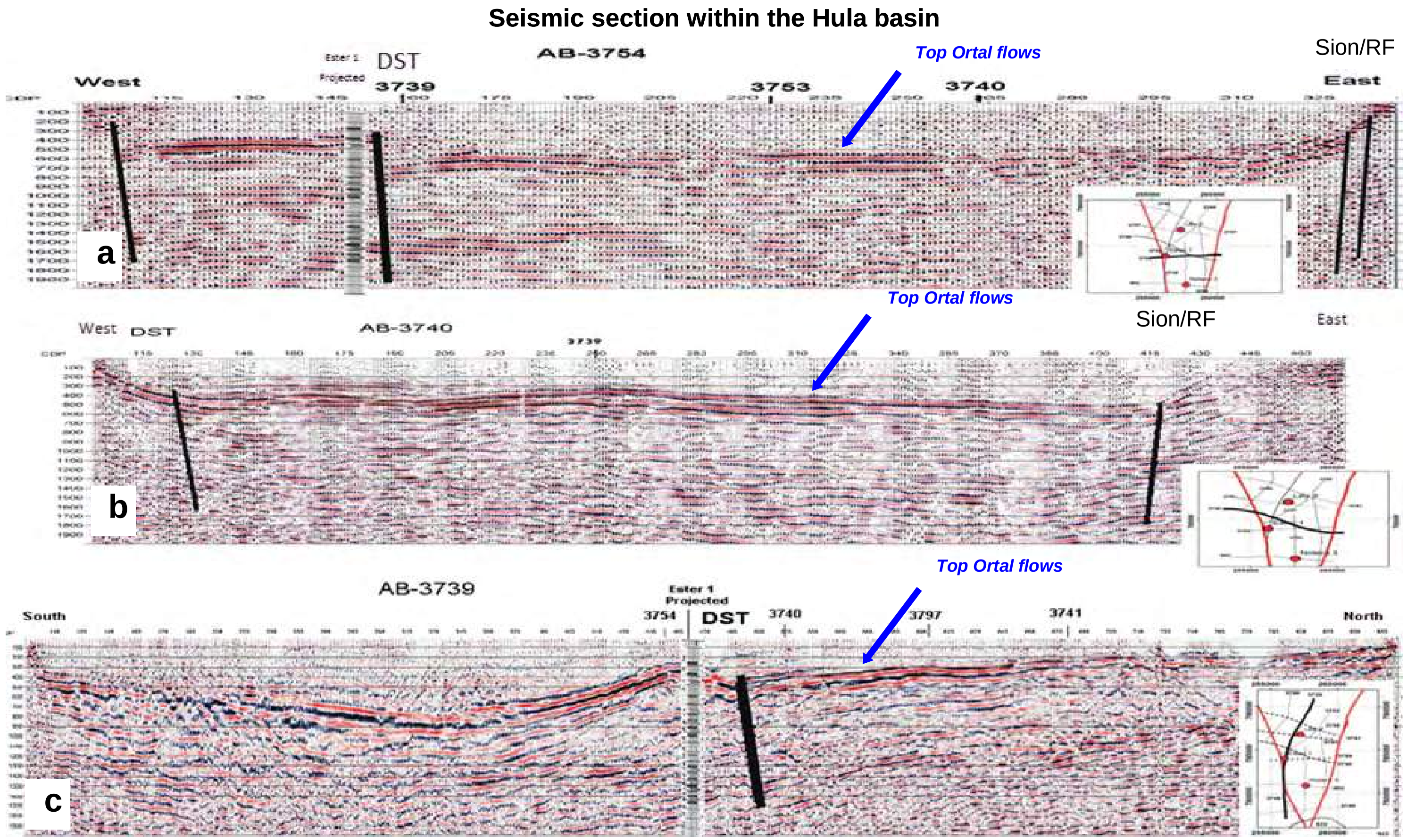

Fig. 12: Reprocessed seismic profiles (stack) after crooked line adjustments (B. Medvedev). Top Ortal basalt flows is prominent regional reflection character and amplitude. Ester 1 control borehole is shown in two of the lines for correlation.

a. 3754 line: E-W profile showing from left to right: (1) The exposed boundary western fault. (2) The master fault near Ester 1 well. (3) an eastern branch, hardly expressed at the surface.

b. 3740 line: E-W profile showing both the master fault and the eastern branch.

c. 3739 line: N-S profile showing the Ester structure near the master fault, Ester 1 borehole and the main depression southward.

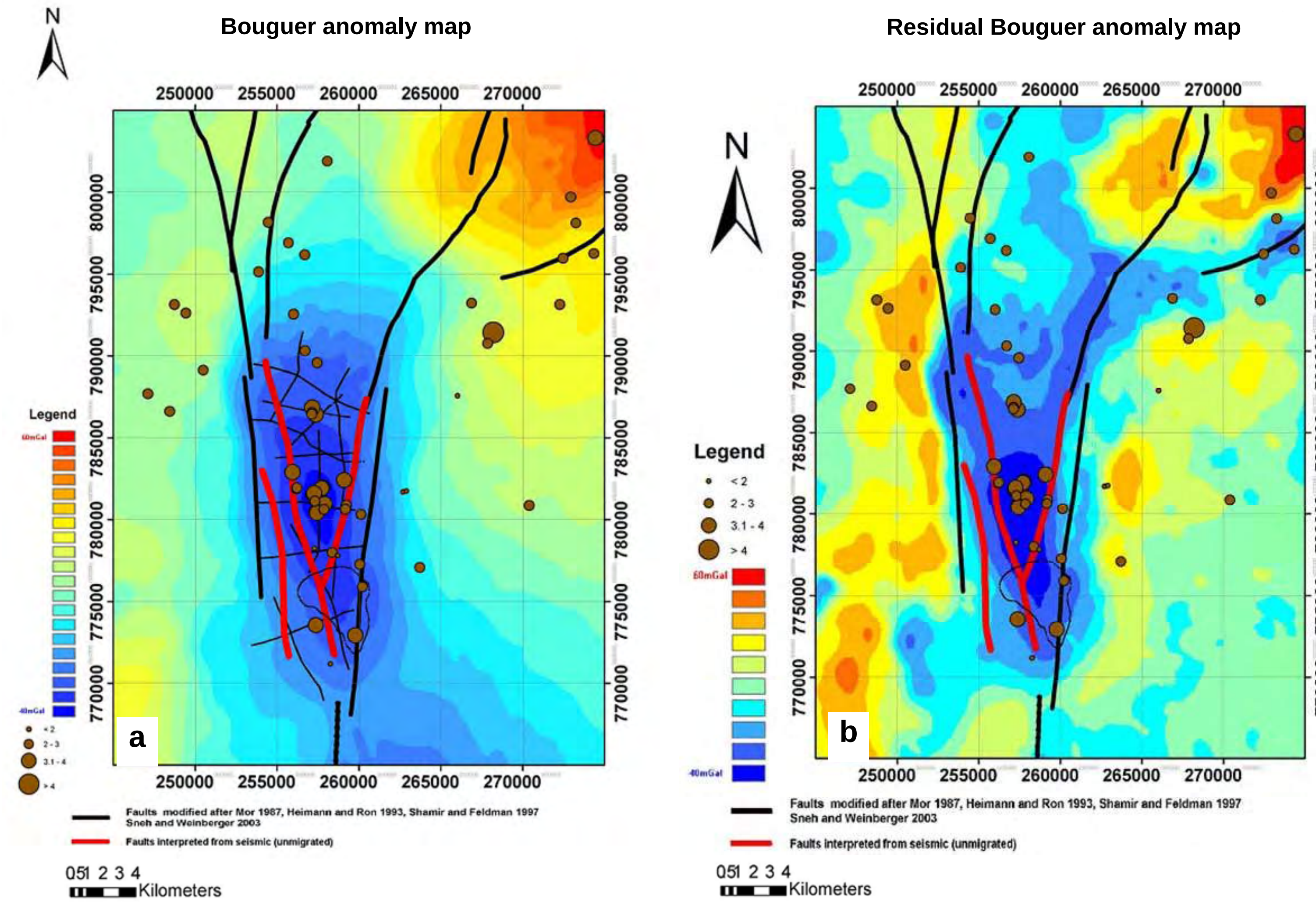

Fig. 13: Gravity maps.

a. Bouguer anomaly map with fault traces and relocated epicenters (courtesy of T. Meirov, GII) and seismic profiles.

b. Residual Bouguer anomaly map showing the main depression and the DST branches.

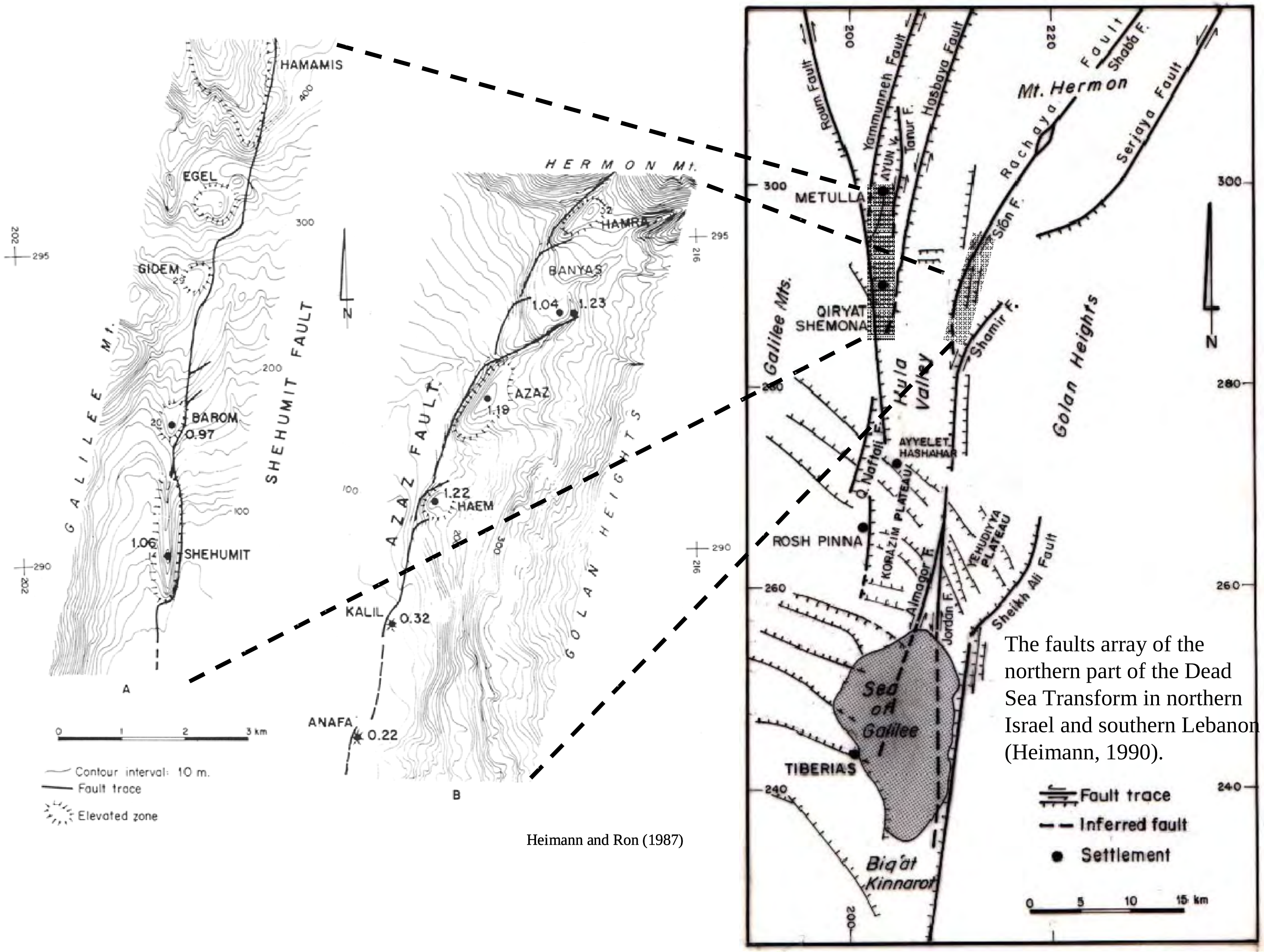

Figure 14: Active strands of the Dead Sea transform and related subsidiary strucures.

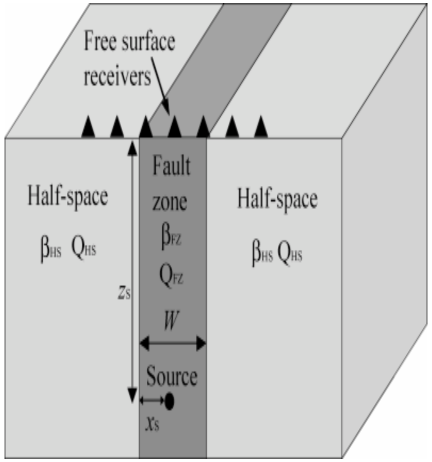

Figure 15: Output of fault-zone wave experiemnt at Tel-Barom (Stop #4). The seismograms show common shot gathers, no gain. Note that some of the shots show distinctive ringing at geophones around #20 after 400 ms. The schematic block on the left, depicts the experimantal layout (Shtivelman et al., 2005).

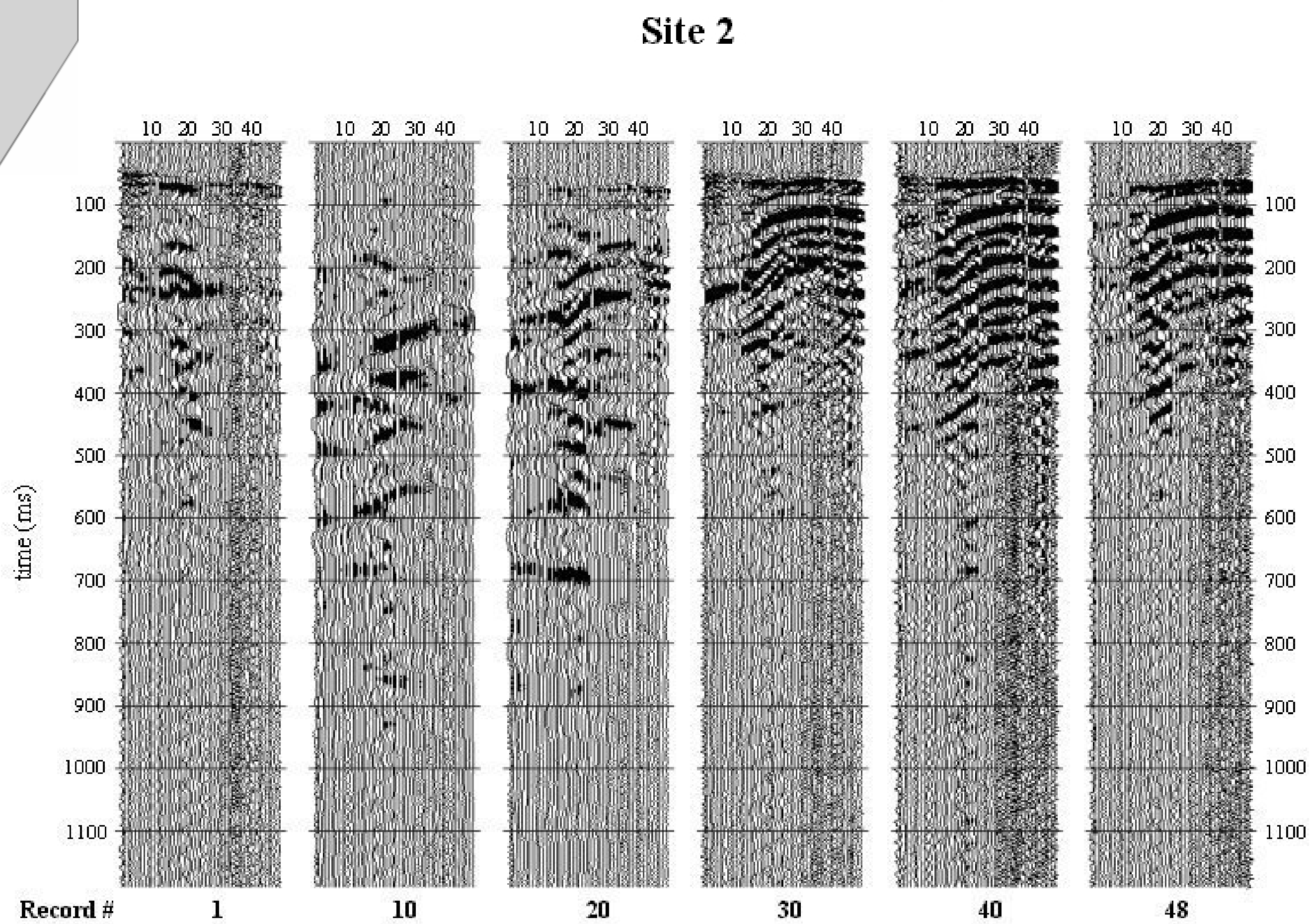

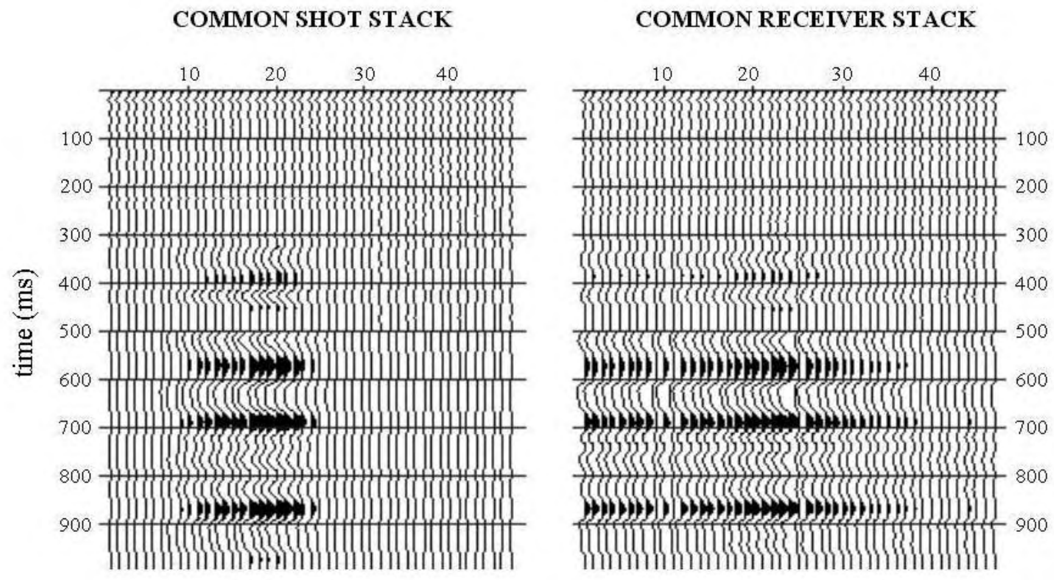

Figure 16: Stacks show cancelation of most of the arrivals before 400 ms, highlighting the fault zone waves. Waves from shots 10-24 (and mostly 15-21) are guided to recievers up to around 30, with a concentration around 20 (Shtivelman et al., 2005)

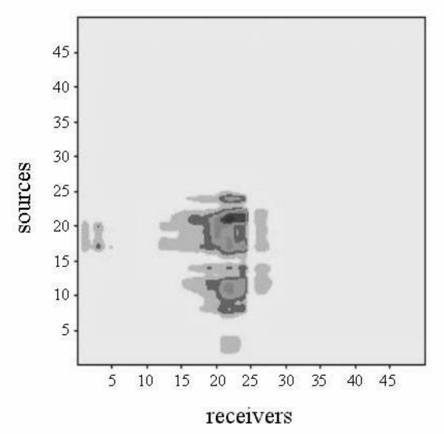

Figure 17: Energy map showing the preferred transfer of seismic energy between shots 16-20 and receivers 20-24, which is were the fault are located (Shtivelman et al., 2005).

Figure 18: A photo showing a Peistocene Basalt exposed at Tel-Brom, several hundred meters due south of the seismic experiment. The Basalt, juxtposed against Paleocene marle, is highly fractured near the fault, with the localized lower seismic speed presumably generating the wave-guide. location marked by star in the adjoined map.

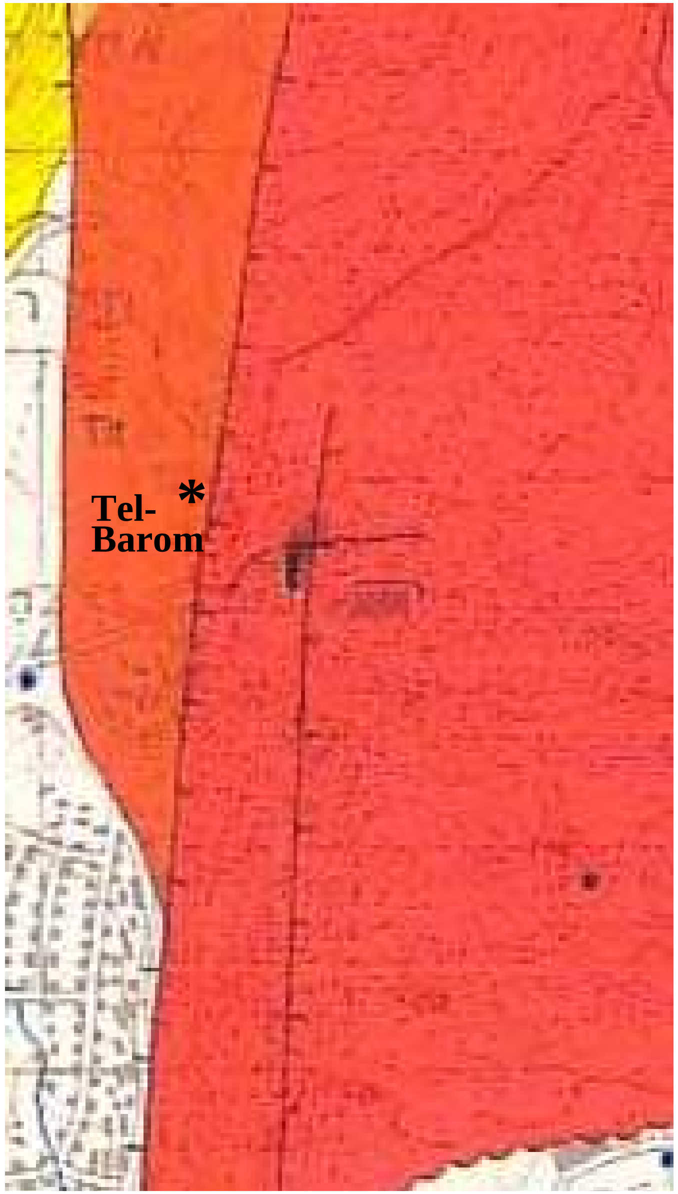

Figure 19: An excerpt from the geological Map of Metulla, Sneh and Weinberger, 2004. Orange - Paleocene Taqiya Formation. Yellow - Neogene Kfar Giladi Conglomerate. Red - Pleistocene Hasbani Basalt The light triangle marks the FZW active seismic experiment.

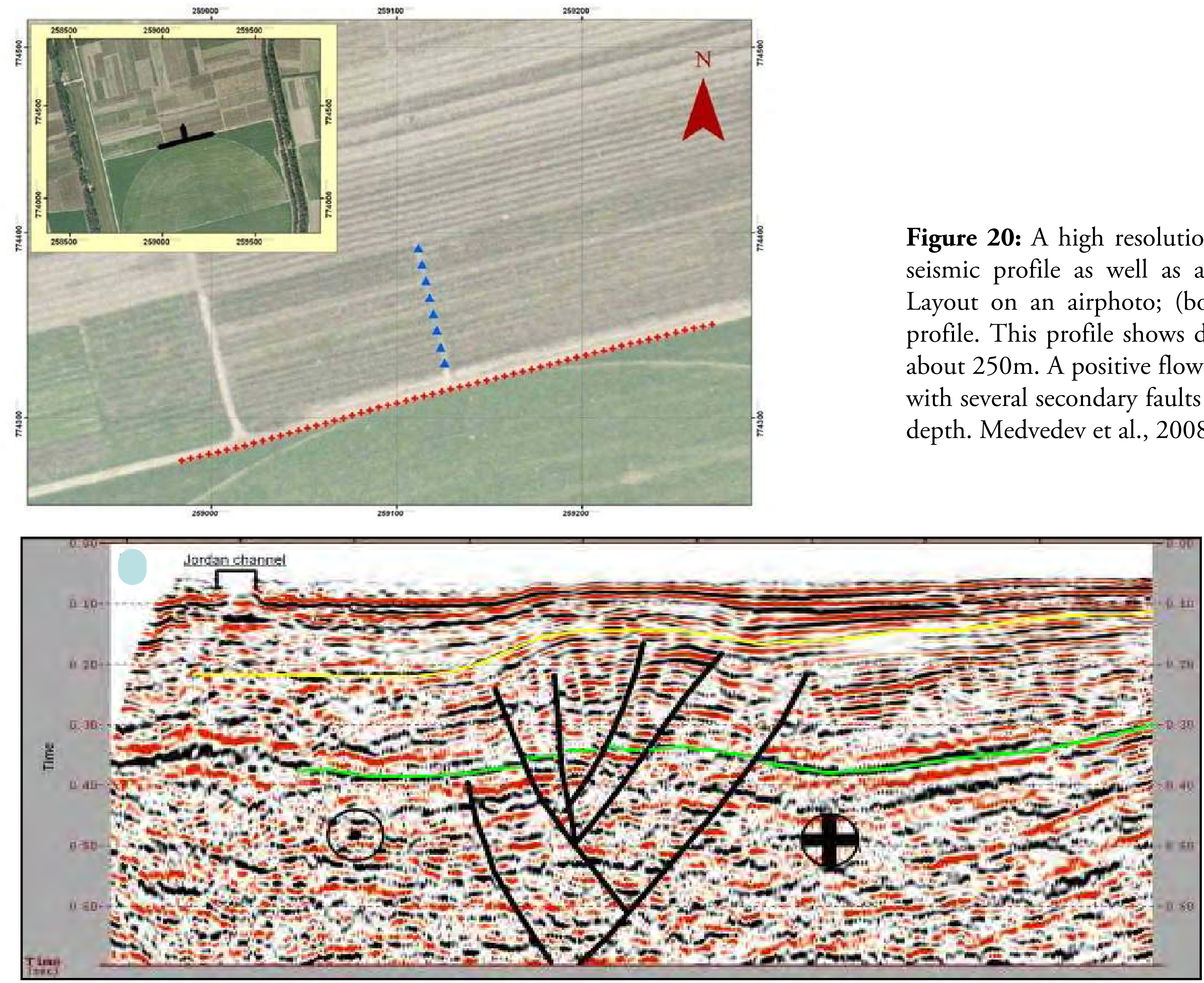

Figure 20: A high resolution geophysical survey (gravity and seismic profile as well as a fan-shooting experiment); (top) Layout on an airphoto; (bottom) A high resolution seismic profile. This profile shows detailed information to a depth of about 250m. A positive flower structure of 120m width is seen with several secondary faults merging to a single major fault at depth. Medvedev et al., 2008.

Evaluation of rockfall hazard to the city of Qiryat Shemona, N. Israel – possible correlation to earthquakes

Mor Kanari[1*], Oded Katz[2], Naomi Porat[2], Ram Weinberger[2], Shmuel Marco[1]

[1] Department of Geophysics and Planetary Sciences, Tel-Aviv University

[2] Geological Survey of Israel

kanarimo@post.tau.ac.il

* Field guide

The study estimates rockfall hazard for the town of Qiryat-Shemona, N. Israel, situated within the Dead Sea Transform fault system, at the foot of the Ramim cliff (Fig.1). The 40-m-thick Ein-El-Assad Formation limestone outcrops provide a source material for rock blocks (Fig. 2). Aerial photos from 1946–1951 show boulders of volume that range in between 1 m^3 and 150 m^3 situated within the now built town premises (Fig. 1). The study examines: (a) what are the properties of the source rock and what is the triggering mechanism? (b) which are the feasible downhill trajectories of the blocks and where do blocks stop? (c) when did rockfalls occur and what is the estimated recurrence interval? (d) what is the rockfall hazard, and what may be recommended as a mitigation design for Qiryat-Shemona?

To answer these questions hundreds of rock-blocks were mapped on the slopes above Qiryat-Shemona using both field surveys and aerial photos and their volume and spatial distributions are analyzed; burial ages of soil samples from beneath large fallen blocks were determined by OSL; rockfall trajectories were simulated using a commercial program (CRSP v4). Hazard evaluation maps for Qiryat-Shemona were compiled from the results of rockfall simulations. Simulated analyses of block velocity and kinetic energy may be used as parameters for the design of mitigation of rockfall damage for Qiryat-Shemona. Rockfall hazard estimation is derived from: a. rockfall recurrence time based on OSL age determinations; b. block size probability derived from block volume distribution.

Results show that the block volume distribution follows an exponential function of the form ax^b with b value –1.17, in agreement with worldwide rockfall inventories. OSL dating of 8 soil samples demonstrate clustering around dates that coincide with known earthquakes, historic and prehistoric (Fig. 3). It is concluded that earthquakes of large magnitudes ($Mw \geq 7$) are the triggering mechanism of rockfalls, yet apparently the rock-mass has to be weakened by joints and fractures to facilitate rockfalls. Maps of maximal downhill block travel distances combined with slope morphological analysis were used to suggest possible trajectories of downhill historical rockfalls. The simulation program variables are calibrated and later used to simulate possible downhill rockfall block trajectories towards the town premises. Simulation results are used to compile the rockfall hazard maps (Fig. 4).

It is concluded that at the south-westernmost part of town, life and property are at rockfall hazard in particular areas. Rockfall recurrence interval and probability of block volumes determined from the volume distribution yield hazard evaluation for the area of Qiryat-Shemona. OSL age analysis of rockfall events (850 years recurrence time and assuming that the last rockfall triggered by the 1202 AD earthquake) lead to a 6.5% probability for the next rockfall to occur within the next 50 years, and a 57% probability within the next 475 years. Evaluated rockfall hazard probability for 50 years is 0.044–0.065, and for 475 years 0.385–0.575, for block sizes or smaller than 10–125 m^3 respectively. Simulated results of block velocity and kinetic energy at specific impact locations on town yield block velocities of 10–15 m/s and kinetic energy of 18,000–45,000 kJ (98% confidence) for block volume of 125 m^3. The recommendation for environmental friendly rockfall damage mitigation design is forestation of the slope.

References

Kagan, E. J., Stein, M., Bar-Matthews, M., Agnon, A., 2007, A tale of two cataclysmic-earthquakes: 39 and 52 kyr BP, DST, Israel; a multi-archive study. AGU, Fall Meeting 2007, San Francisco, Session T12.

Yagoda-Biran, G., 2008, Seismic hazard estimation along the Eastern Margins of Sea of Galilee by back analysis of seismically induced natural and structural failures. MSc Thesis GSI/02/2008 90, p.

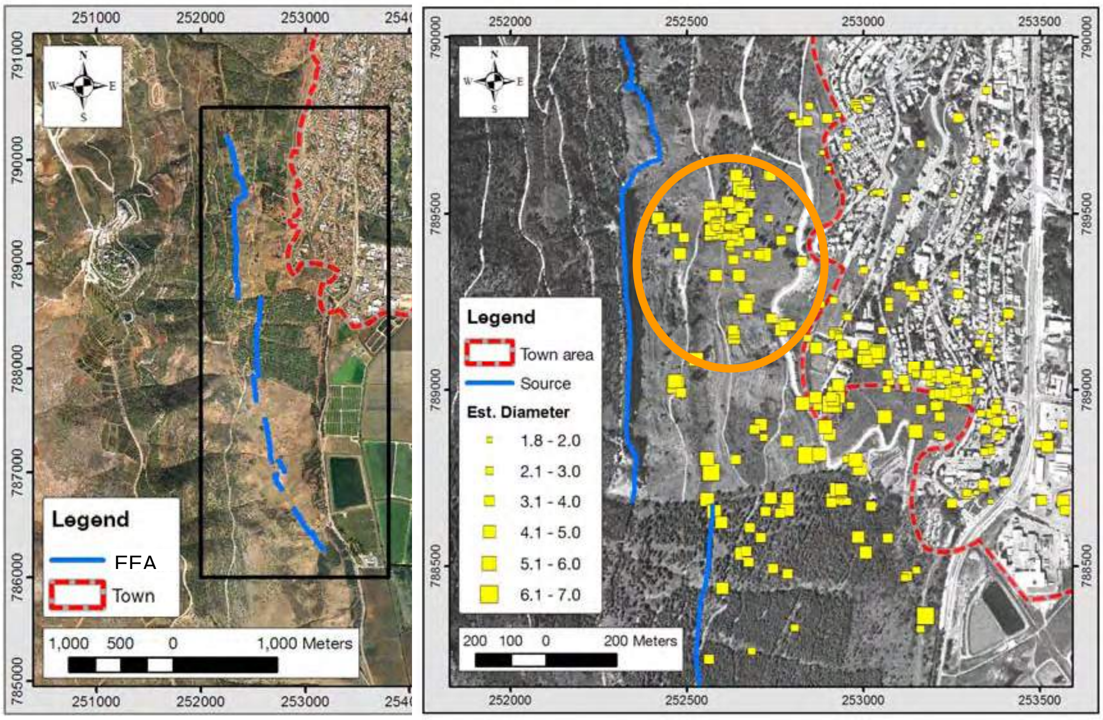

Figure 1: Left: Map of the study area in black rectangle. Ein-El-Assad Formation (EEA) is marked by blue line; town area in red dashed line. Right: location and estimated diameters of non-mappable blocks (located using 1946-51 aerials; blocks in orange ellipse used for the correlation between the sizes of field and non-mappable blocks.

Figure 2: Overview of the study area facing west towards the Ein-El-Assad outcrop. The rockfall talus in front. A normal fault at the rock mass can be observed on the top-right (yellow arrow): the overriding block on the right (north) is lower than the block to the left (south). A scar (yellow ellipse) in the outcrop, possibly the origin of rockfall mass, is clearly visible left (south) to the fault location.

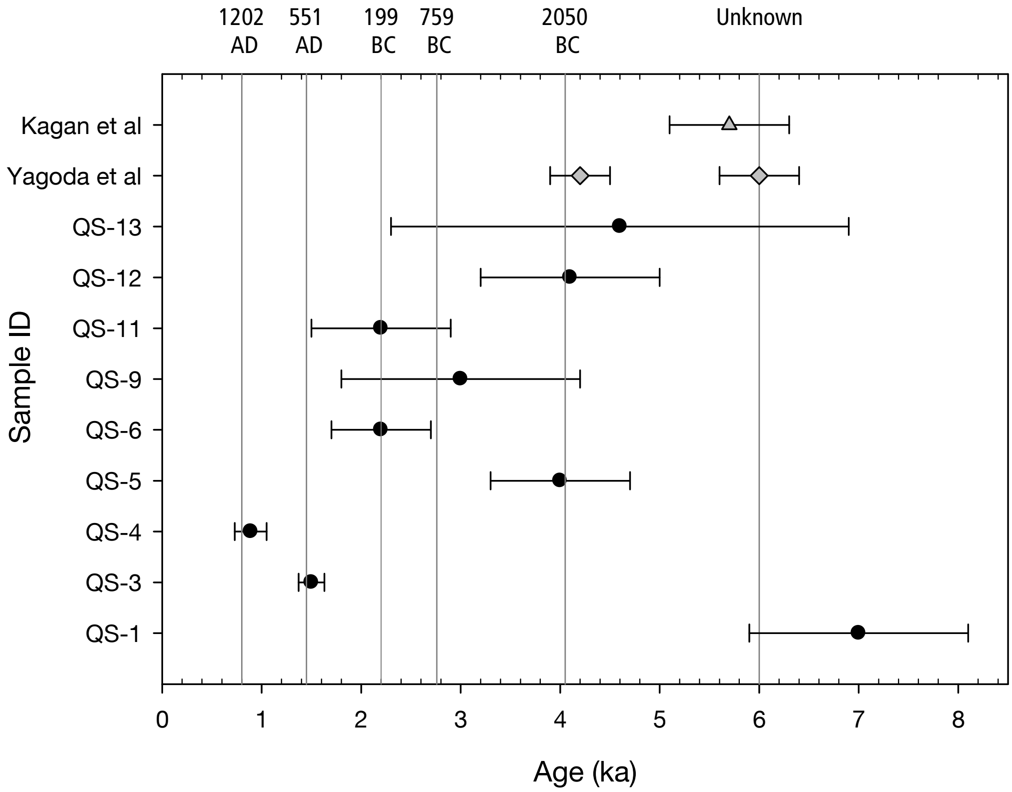

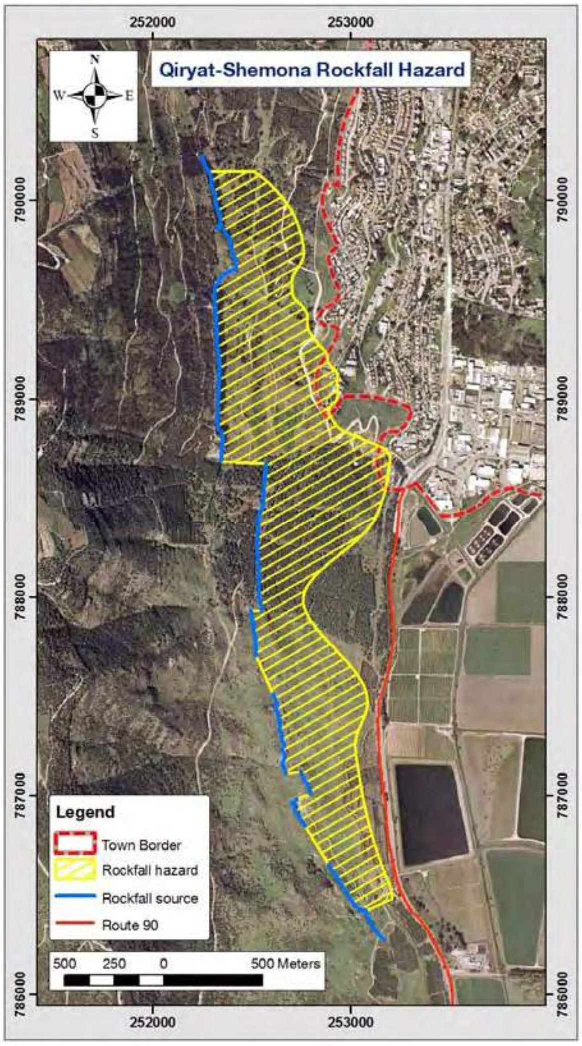

Figure 3 (top): Qiryat-Shemona OSL ages and suggested rockfall triggers. OSL age results for the past 8000 years in black circles with error bars; ages of earthquakes determined by Yagoda et al. (2008) in gray diamonds and by Kagan et al. (2007) in gray triangle; corresponding dates of earthquakes suggested as rockfall triggers in gray lines and labeled at top axis.

Figure 4 (left): Rockfall hazard map of Qiryat-Shemona. Source of rockfall (Ein-El-Assad formation) marked in blue line; area subject to rockfall hazard (from source escarpment to 100% of blocks stop line) dashed in yellow; town border line in red dashed line; Route 90 in orange solid line. Map compiled from maximal travel distance (100% of blocks stop line) of 25 simulation profiles performed using CRSP v4.

Sea of Galilee

18.2.2009

Field leader

Shmuel marco


N
2 Ateret Fortress
1 Safed
Golan Heights
Sea of Galilee
Tiberias
3 Susita
0 2 4 8 Kilometers

Paleoseismic study of earthquake induced landslide hazard in the city of Safed, northern Israel

Oded Katz[1]*

Geological Survey of Israel

odedk@gsi.gov.il

* Field guide

1. Introduction

The field trip focuses on the city of Safed (northern Israel, Fig, 1,which was repeatedly and severely damaged from earthquake induced landslide (EILS) which were triggered by strong-major historical earthquakes (Wachs and Levitte, 1981). The city of Safed is located on an elevated area bordering the tectonically active Dead Sea Transform (DST; Fig. 1). It was settled as early as the Roman times (1st century CE) on a narrow hill, more than 800 m above sea level ('the Citadel', now in the city's center; Fig. 2a). Katz and Crouvi (2007) found that parts of the city are built on a few meters depth of layered anthropogenic material which was deposited as a result of more than 2000 years of human habitation. The anthropogenic material is mechanically weak, susceptible to slope failure and to amplification of seismic shaking.

The field trip follows Katz and Crouvi (2007). It examines field and historical evidence for slope instability in the core city of Safed and evaluates the current EILS hazard using a GIS-based Newmark analysis (Newmark, 1965) following Jibson et al. (2000). It focuses on the significance of the anthropogenic talus/strata as the controlling factor of the slope instability in past disastrous earthquakes and its contribution to the current-hazard in Safed, as well as in similar modern populated centers that share long habitation histories.

Our Results show that earthquakes of magnitudes (MW) 5,6, and 7 at distances of up to 10km,50km and more than 100km, respectively, are likely to induce landslides in the city of Safed. The current engineering status of the city is poor and as a consequence severe damage and loss of life are expected in future earthquakes due to EILS, unless major engineering efforts are made. Comparable cities in the Eastern Mediterranean with long habitation histories (e.g., Jerusalem, Tiberias, Nablus, Amman), are expected to have similar geotechnical problems throughout their old parts. Furthermore, we think that magnitude evaluation of historical-earthquakes based on reported local-damage may yield overestimated magnitude when the damaged site is built on anthropogenic talus (a common setting in the vicinity of the Dead Sea Transform).

2. Field trip stops:

Stop 1: 'The Citadel' area; Geological setting

The bedrock under the built parts of the city consists of Upper-Cenomanian to Eocene dolomite, limestone, chalk, and marl (Fig. 2). Nevertheless, in the frame of the current study we found that most of the core city is built on talus/strata of anthropogenic material up to 10m thick that was deposited on top of the above rock sequence in the course of the long (~2000 years) habitation. The anthropogenic material is typical of an archeological mound 'tell' (Rosen, 1986) and in the studied area it exhibits two types: (1) talus-like inclined (up to 30°) layers of pebbles and pottery embedded in unconsolidated, thin earth-like material (Fig. 3a); this type is exposed mainly around the citadel, and (2) ruins of man-made stone structures filled and covered by reworked sediments (Fig. 3b).

Stop 2: The old city core; Field evidence for slope instability

Tens of sites showing evidence for past and current slope instability were mapped in the studied area (marked by arrows in Fig. 2a, b). This instability is attested in the core city limits by lamp posts based in the anthropogenic talus that are tilted (Fig 4a). Likewise, open cracks, which in some cases approach total structural failure, are common in road pavements, walls, and buildings (Fig. 4b-c). The above field evidence reveals that the anthropogenic talus exposed in the core city is statically unstable and is creeping down slope. This creep shifts the material towards its residual strength and we anticipate that under dynamic earthquake conditions landslides will develop. During the rainy winter season, meter-scale shallow slumps and debris flows are common in the anthropogenic talus (Fig. 4d).

Outside the core city area, within the new city limits, disrupted shallow slides and slumps were found in natural and cut slopes. Rock falls occur where dolomites and limestones are exposed in steep slopes.

Stop 3: Above the old cemetery; EILS hazard analysis

a. Historical evidence for EILS

Historical research indicates that parts of the core city of Safed were repeatedly, and heavily, damaged during earthquakes in the last centuries (M_S ~6.6, Oct. 1759; M_S >7.0, Jan. 1837). We believe that this damage is mainly a result of landslides, considering the steep slopes and the weak geological material the city is founded on. The historical evidence (Thomson, 1873; Ya'ari, 1943; Ben-Horin, 1952; Schiller, 2002; Yizrael, 2002a,b) constrain the limits of the area in which EILS occurred during earthquakes (Fig. 2b). We used these constraints on the areas of the EILS together with the field evidence of slope instability to calibrate the mechanical model of the EILS hazard Newmark analysis.

b. Calibration of the model

Two historical earthquakes that induced landslides in Safed (Oct. 1759 and Jan. 1837) and one earthquake that did not (Aug. 1984, M=5.3; epicenter is shown in Fig. 1) were used for calibration of the mechanical model. By fine tuning of the mechanical model we achieved reasonable similarity (based on visual comparison) between the map of calculated dynamic slope instability in a given earthquake and the field and historical landslides map of the same earthquake (Fig. 5a, b). After calibration, we were able to simulate earthquake scenarios and analyze which of the earthquakes would cause EILS in the Safed.

c. Current EILS hazard in the city of Safed

We calculated slope performance for 24 scenario earthquakes, assumed to be possible along the central part of the DST. Calculations show that magnitude 4 earthquakes at the minimal source distance of 10km will probably not induce landslides in the studied area (Fig. 6). Magnitude 5 earthquakes will induce landslides in Safed at source distance of less than 10km. Magnitude 6 earthquakes will not induce landslides at source distances of more than 50km, but at shorter source distances EILS will be significant. A magnitude 7 earthquake will induce landslides even at distances of more than 100km.

d. Geotechnical consideration of the anthropogenic talus

As discussed above, the anthropogenic talus underlying most of the core city is a major source of EILS hazard in the studied area. This material is apparently a source of additional seismic hazard: the amplification of seismic-shaking. The anthropogenic talus is poorly consolidated and its shear wave velocity is expected to be very low with a velocity contrast with the underlying bedrock. This setting will probably result in amplified seismic shaking that will increase the likelihood of slope failure.

The anthropogenic material is a source of enhanced seismic hazard and a significant contributor to repeated damage due to earthquakes in sites with histories of long human habitation. Each destruction-rebuilding cycle makes the site more vulnerable during the next earthquake.

The nature of the anthropogenic talus may also affect the evaluation of the magnitude of historical earthquakes, if solely based on reported local-damage (e.g., MSK, Bath 1973). Since site amplification is usually not considered in such evaluations (Ambraseys et al., 1994), the assessed historical magnitude may be misleadingly high (relative to a bedrock site). This is especially true for the long record of earthquakes in ancient cities in the vicinity of the Dead Sea Transform.

3. References

Ambraseys, N. N., Melville, C. P., Adams, R. D., 1994. Macroseismic information: The seismicity of Egypt, Arabia, and the Red Sea - A historical review: Cambridge Univ. Press, Cambridge, Mass, 19–110.

Bath, M., 1973. Introduction to Seismology. Birkhauser, 395 p.

Ben-Horin, U., 1952. An official report on the earthquake of 1837. Isr. Exp. J., 2, 63-65.

Jibson, R. W., Harp, E. L., Michael, J. A., 2000. A method for producing probabilistic seismic landslide hazard maps, Eng. Geol., 58, 271-289.

Katz, O., Crouvi, O., 2007. The geotechnical effects of long human habitation (2000< years); earthquake induced landslide hazard in the city of Safed, northern Israel. Engineering Geology, doi:10.1016/j.enggeo.2007.07.008.

Keefer, D.K., 1984. Landslides caused by earthquakes. Geological Society of America Bulletin 95, 406-421.

Levitte, D., 2001. Geological map of Israel, Sheet 2-III: Safed, Geological Survey of Israel. 1 map.

Newmark, M. N., 1965. Effects of earthquakes on dams and embankments. Geotech. 15 (2), 139-160.

Rosen, A. M., 1986. Cities of clay, the geoarcheology of Tells. Prehistoric Archeology and Ecology Series, Karl W. Butzer and Leslie G. Freeman (eds.). Univ.Chicago Press Chicago and London.

Schiller, E., 2002. The 1837 earthquake in Safed. Ariel 157-158, 106-112 (in Hebrew).

Thomson, W. M., 1873. The land and the book. Nelson and Sons, London.

Wachs, D., Levitte, D., 1981. Earthquake induced landslides in the Galilee. Isr. J. Earth Sci., 30, 39-43.

Ya'ari, A., 1943. Letter written by the Jews in Israel to their brothers in the Diaspora from Babylonian Exile to nowadays Zion Return. Gazit, Tel-Aviv, 357-367 (in Hebrew).

Yizrael, R., 2002a. The chronicles of the Jewish quarter in Safed. Ariel 157-158, 203-215 (in Hebrew).

Yizrael, R., 2002b. The old Jewish cemetery in Safed. Ariel 157-158, 216-225 (in Hebrew).

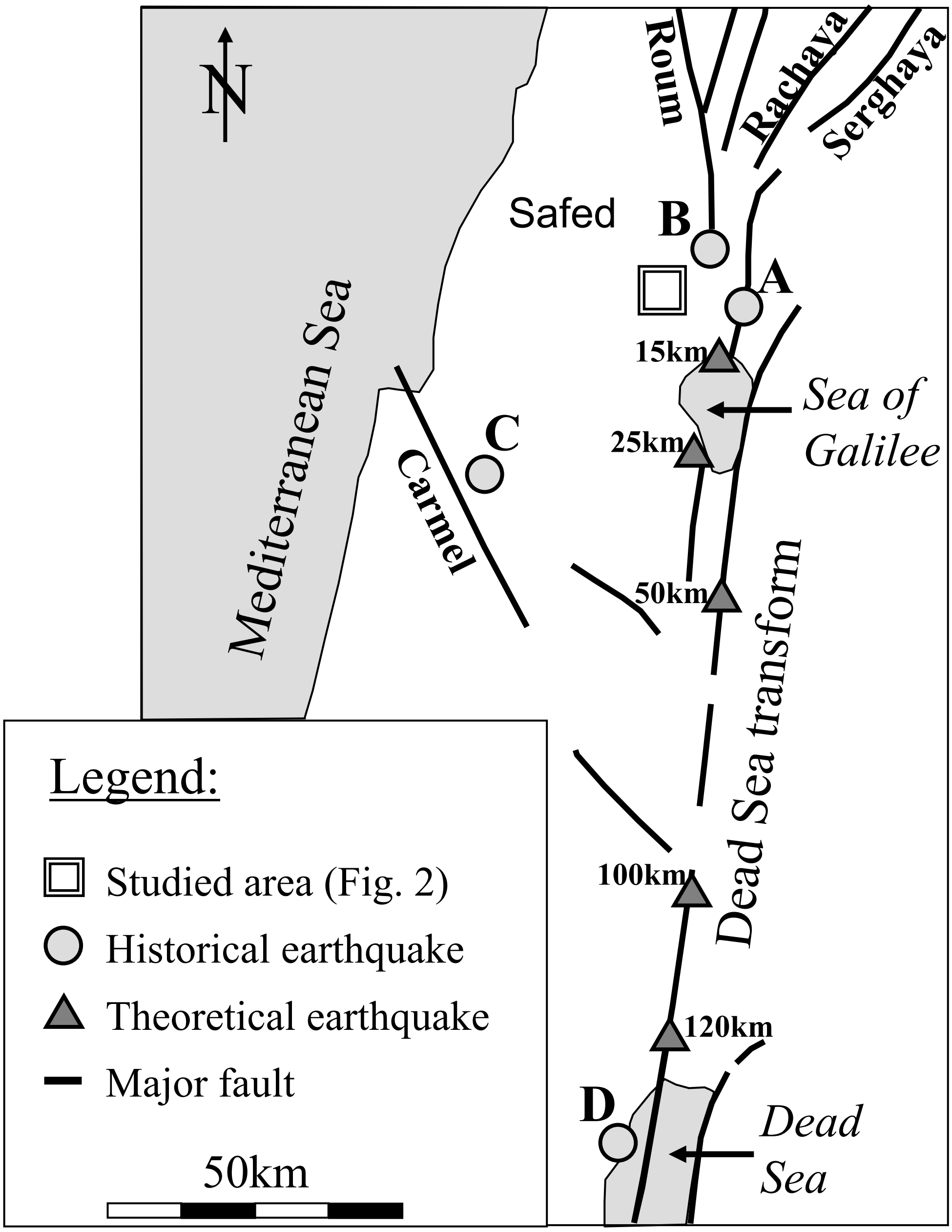

Figure 1: Major fault lines of Dead Sea Rift in the vicinity of Israel. Inferred epicenters of historical earthquakes are marked by gray circles. A is MW = 6, 1759 earthquake; B is MW = 7, 1837 earthquake; C is MW = 5.3, 1984 earthquake; D is MW = 6.5, 1927 earthquake; for details and references see text). Epicenters of scenario earthquakes are marked by gray triangles with distances from the core city of Safed) and are used to analyze EILS hazard in the studied area which is marked by double-line rectangular and shown in detail in Fig. 2.

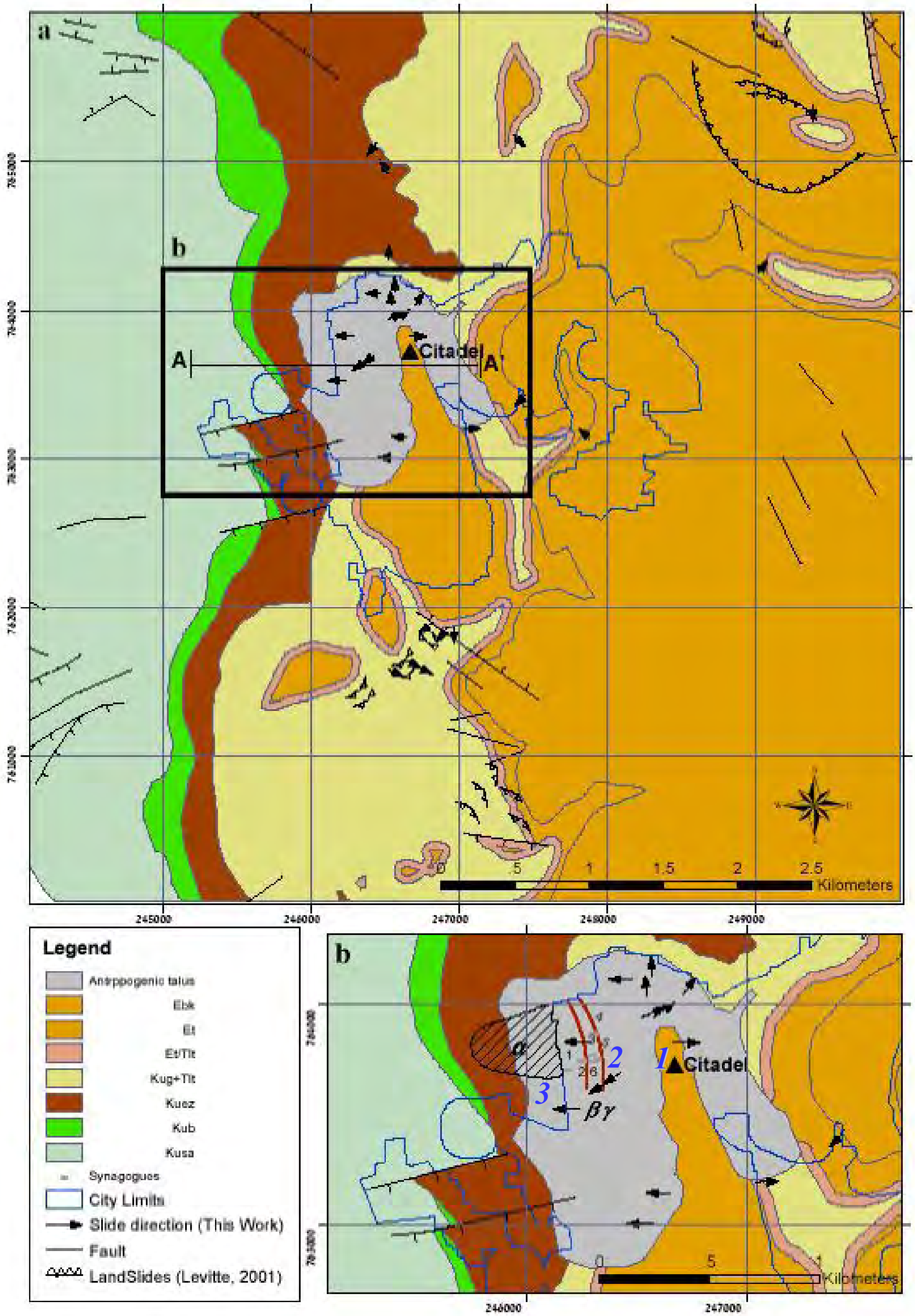

Figure 2: (a) geological map of the studied area (Levitte, 2001; anthropogenic material mapped in Katz and Crouvi, 2007). The current Safed city limits are marked by a blue solid line; (b) the core (historical) city area. The core city extended from the Citadel, westwards to the old cemetery (a). Sites of field-observed slope instability are marked by black arrows. Also shown are upslope limits of EILS area in the 1759 and 1837 earthquakes (b and g, respectively) according to reported damage to synagogues (marked by close squares where 1 is Sefaradic Ari, 2 is Banea, 3 is Hagadol/Abuhav, 4 is Greek pilgrimages/Ashkenazic Ari, 5 is Karo, 6 is Elshiech). Stops of the field trip are marked by italic blue numbers.

Figure 3: Types of anthropogenic material typical of an archeological mound ('tell') outcrop in the core city of Safed: (a) talus-like, inclined (up to 30º) layers of pebbles and pottery embedded in unconsolidated earth-like thin material and (b) ruins of man-made stone structures filled and covered by reworked thin sediments. The current city (shown in the upper part of the picture) is built on top of the ruined structures.

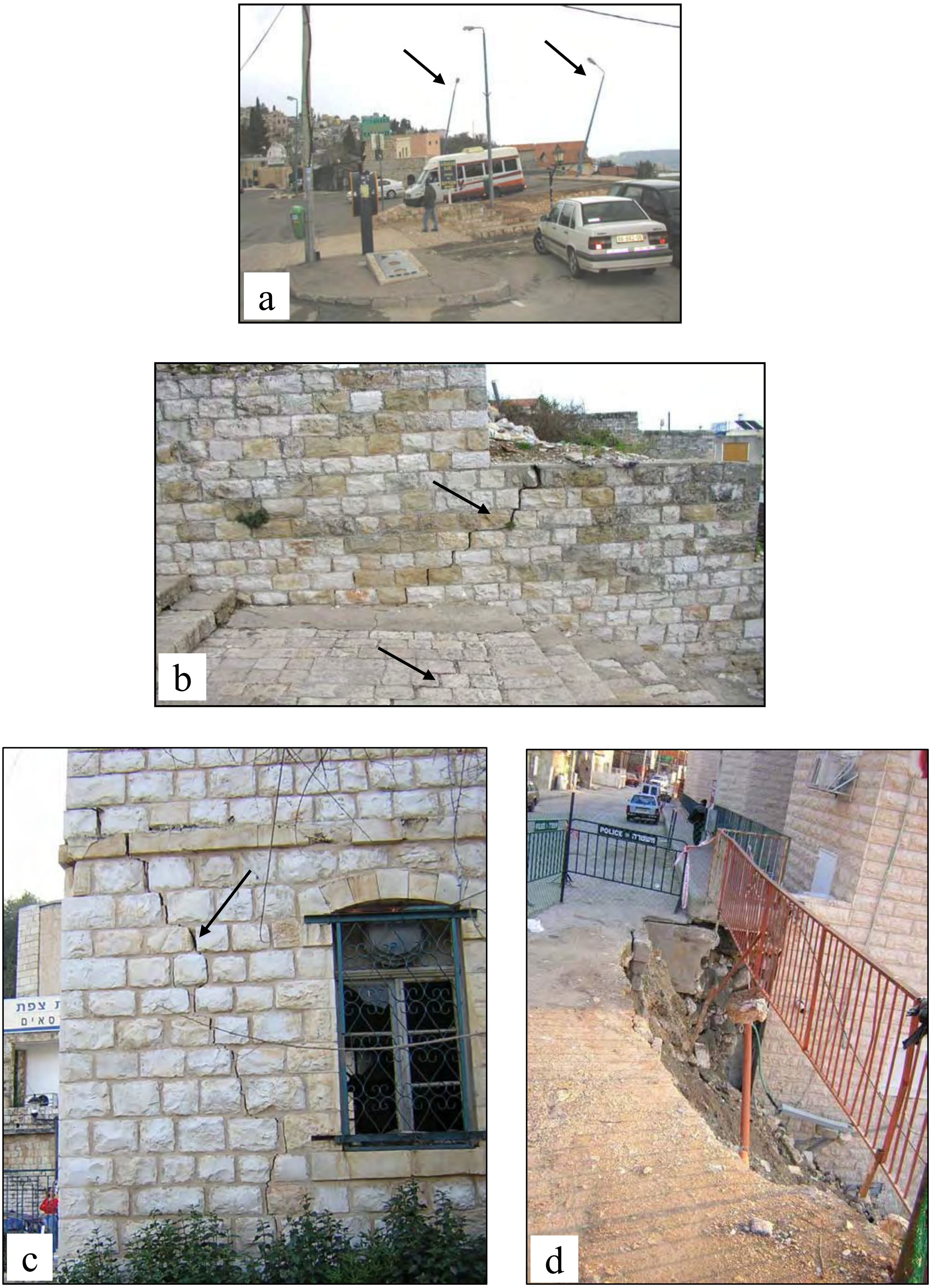

Figure 4: Field evidence for instability of the anthropogenic material slopes.
(a) inclined lamp posts found in the anthropogenic talus (marked by arrows); (b) open cracks (marked by arrows) in retaining wall and (c) in building, both found in the anthropogenic talus; (d) rainy winter-season slump in the anthropogenic talus.

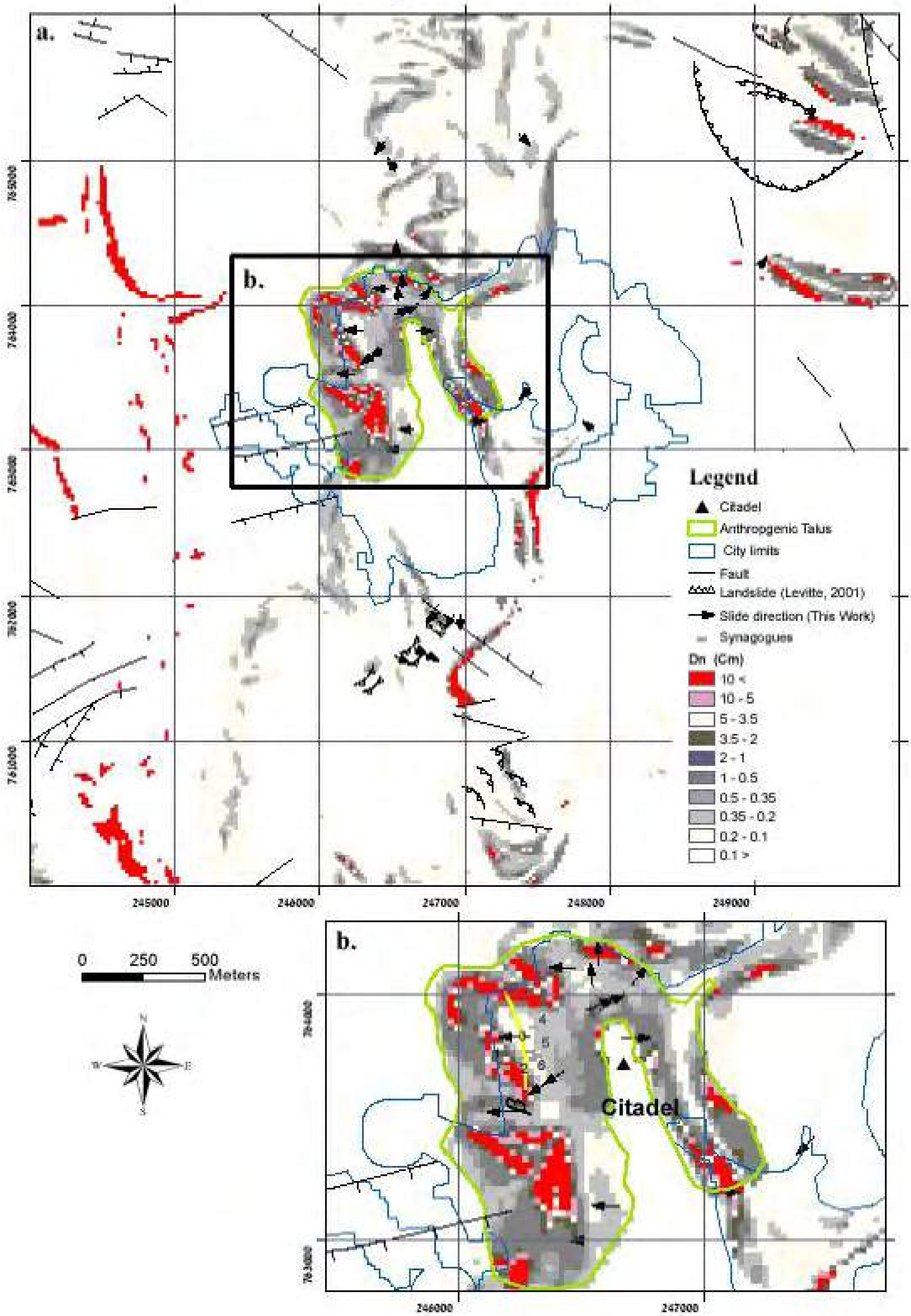

Figure 5: Calculated Newmark displacement maps of two historical earthquakes used to calibrate the mechanical model, (a-b) October 1759 MW=6, R=15 earthquake; (c-d) January 1837 MW=7, R=10 earthquake. For inferred location of epicenter see text and Fig. 1. Also shown are upslope limits of EILS area in the 1759 and 1837 earthquakes (b and g, respectively, see Fig. 2) traced according to reported damage to synagogues (marked by numbered close squares, see Fig. 2).

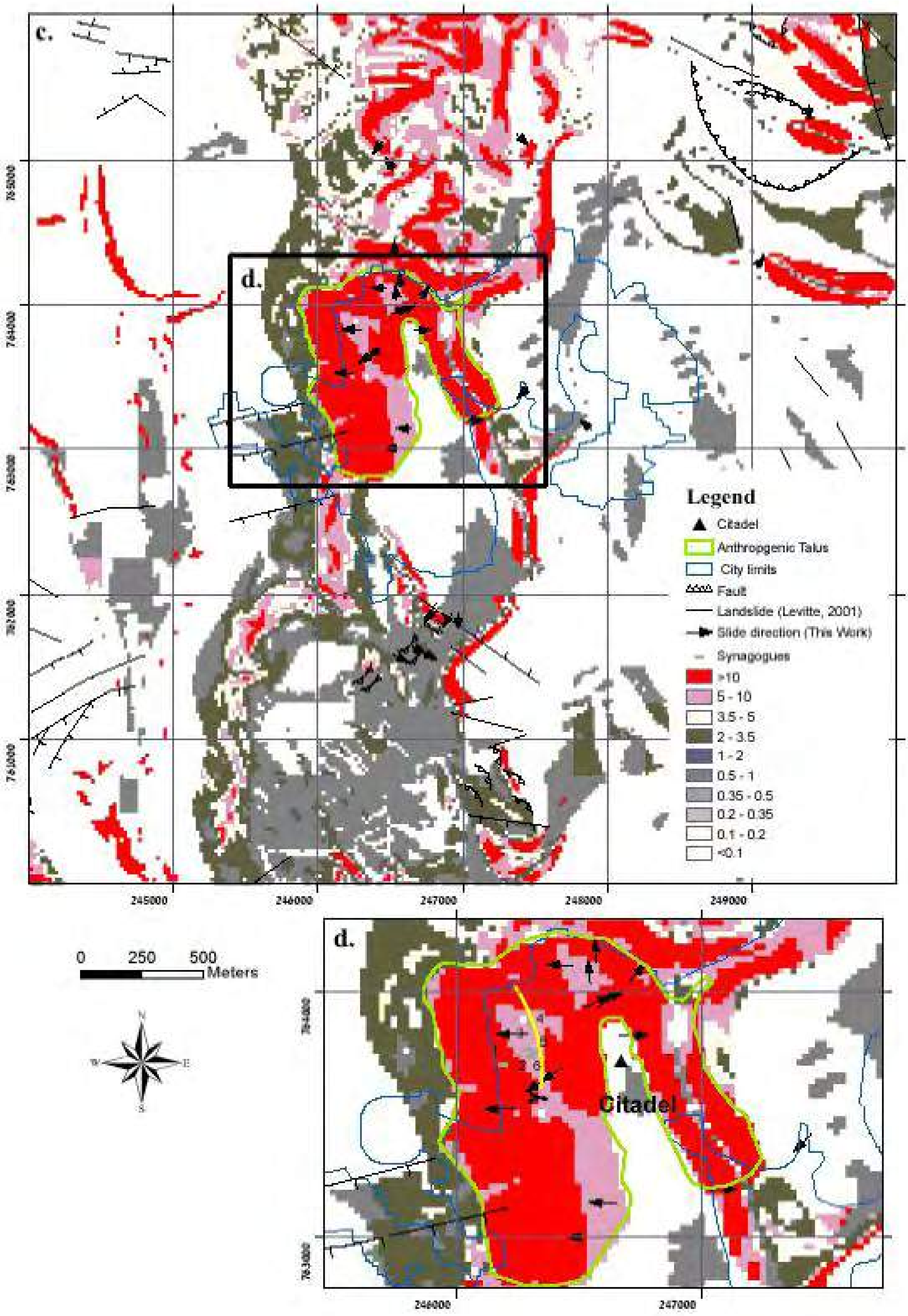

Figure 5: Continue.

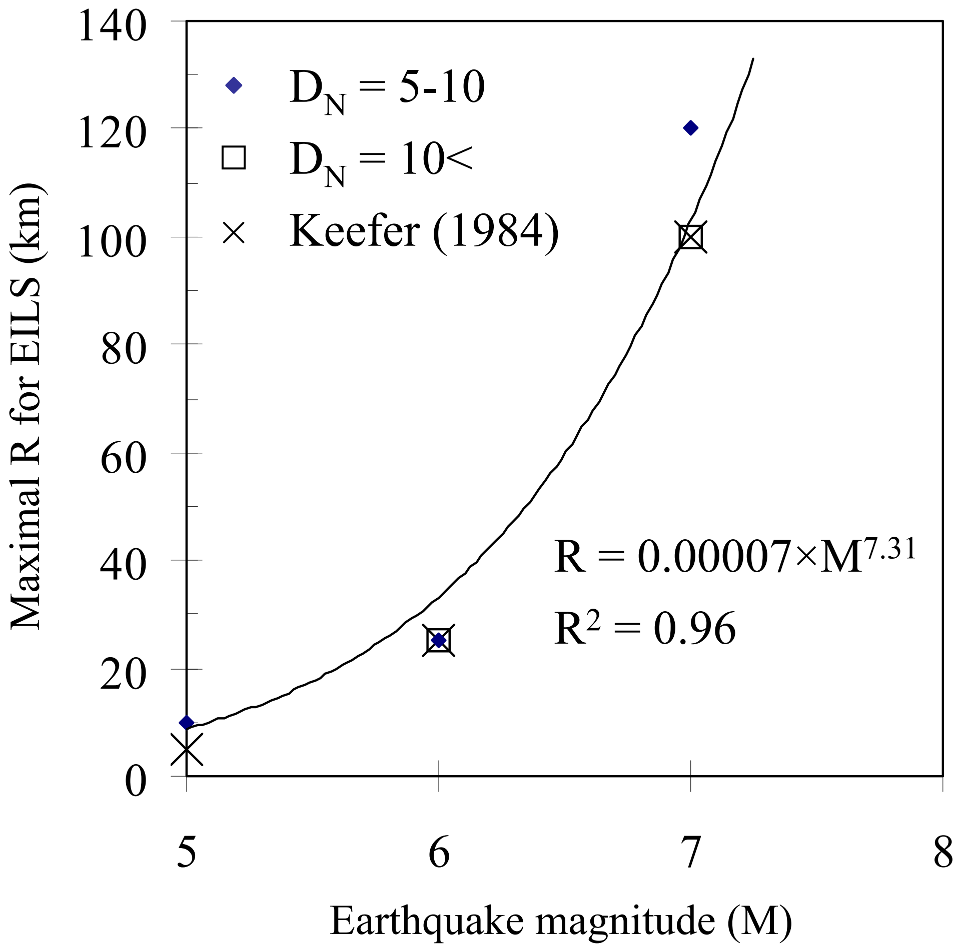

Figure 6: Maximum fault zone distance (R, km) for EILS (threshold DN values are 5-10cm or >10cm, for the conservative cases, respectively) as a function of the triggering earthquake magnitude (MW). Data is from the calculated scenario earthquakes (for location see Fig. 1). Also plotted are the maximum fault zone distances for EILS according to Keefer (1984).

The history of the Frankish Castle of Vadum Iacob

Shmuel Marco[1]*

[1]The Department of Geophysics and Planetary Sciences, Tel Aviv University

shmulikm@tau.ac.il

* Field guide

Source: Ellenblum, R., 1998, Frankish Rural Settlement in the Latin Kingdom of Jerusalem: Cambridge, England, Cambridge University Press, 321 p.

The Frankish Castle of Vadum Iacob [meaning :"Jacobs' ford"], was known also in the 12th century by its Arabic name: Bayt al-Ahzan, [meaning "The House of Grief"] or by its 13th century name of Le Chastelez. Today it is known by the Hebrew name Metzad ‘Ateret [castle of abundance] which is derived from the modern Arabic name Qasr al-‘Atara.

Vadum Jacob dominated the only crossing of the Jordan River south of the Hulah swamps and north of the deep Jordan canyon. The site is a day’s walk from Damascus and half day, according to Al-Muqadasi, from Tiberias or Safad.

The castle was built above the west banks of the River Jordan in the place commonly called “Jacob’s ford”. According to the 13th century Frankish chronicler Ernoul, the place was in the Muslim and not in Frankish territory. The Franks built their castle because they wanted to weaken the most vulnerable part of the Muslim’s frontier

The other possible crossing from Syria to Palestine north of the Sea of Galilee was near the city of Banyas, which was held by the Muslims. It is also possible that Vadum Iacob was even planned to threaten the Muslim center of Damascus.

The King (which king?) made a general call to arms, gathered the whole army in Vadum Iacob and stayed there from the beginning of October, 1178 until the second week of April, 1179. The beginning of the works in October might be attributed to climatic considerations as the heat in the upper Jordan Valley from June to the end of September is unbearable. The temperatures decrease considerably in October. The rainy seasons also starts by the end of October and the rains reach their peak in December, January and February. This schedule left the builders with two months of intensive work in mild weather before the beginning of the rainy season.

William of Tyre stresses that the construction of the castle was already completed when the king left for Jerusalem in the beginning of April, 1179. In other words, he claims that the monumental castle was finished after only six months of work. William was not an eye-witness, since he had left the country several months earlier on his way to Rome, but he also writes that in mid-April 1179, following a battle between Franks and Muslims near Banyas, the Franks carried the dying Constable, Humphrey of Turon, "to the new castle which was still under construction." This statement was interpreted as proof that the castle was not finished when the king left for Jerusalem.

Our excavations reveal that the construction of the castle was not completed at the time of its destruction in August, 1179. Remains of construction works were excavated throughout the castle. We unearthed a complete inventory of medieval working tools: spades, hoes, picks, a wheelbarrow, plastering spoon, scissors, etc. A dramatic find adjacent to one of the gates was a heap of lime with working tools imbedded in it, which was covered by Muslim arrowheads. That clearly demonstrates how the builders where interrupted by the sudden attack.

A similar discrepancy is found in the description of the construction of the castle of Safad, which was built between 1240 and 1260. Benoit, the Bishop of Marseille wrote that when he left the site, after less than six months of work, the castle was already finished, and was in a defensible state. However, when he himself returned there 20 years later, he was impressed by the outer wall, which was added to the castle since his first visit. He himself does not explain how a castle can be "finished and in a defensible state" while the outer wall was only added later.

We can assume that the construction of the inner curtain wall was completed by then, and the four hot months of summer were devoted to improving the conditions of life inside the castle and to preparing for an intensive building season, planned, without doubt, for the cool autumn and winter months.

According to Ibn Abi Tayy, [as quoted by Abu Shama] Salah al-Din tried to buy the castle from the knights Templars and negotiated possible terms. The Franks, so it seems, were willing to consider the destruction of the castle if the Muslims paid the estimated cost of its construction. The Sultan offered 60,000 dinars and was even willing to offer 100,000 dinars because "the Templars provided it generously with garrison, provision and arms of all kinds". Salah al-Din promised his men to destroy the castle by himself, once it was taken.

It seems that Salah al-Din was reluctant to challenge the entire Frankish army and dared to attack only when the army was no longer present. He visited the site immediately after the departure of the king in April 1179, accompanied by a representative of the Khalif, Qadi al-Fad'il. He probably considered the advance of the works, weighing the possibilities of taking it by force, or buying it. Immediately after the failure of the negotiations, in May 16th 1179, Salah al-Din attacked the site for the first time. He stayed there for five days and failed to take it by surprise.

The decisive attack on the castle commenced on Saturday, 19th Awal, 575\August 24th 1179, the Muslim forces being commanded by Salah al-Din himself and his best generals. Salah al-Din realized that it will be difficult to take the castle by assault and opted for digging under the walls. The result of the first attempts was very poor. The tunnel was 30 feet in depth and 3 feet in width, whereas the width of the wall was 12 feet. The timber that supported the tunnel was set on fire but the wall did not collapse. Salah al-Din was in a hurry; he could not wait for the fire to be extinguished gradually. He therefore promised a dinar for every skin full of water, which will be poured onto the flames.

When the fire was extinguished and the sappers dug to a deeper and wider tunnel, which they set on fire once again on Wednesday. Finally, on sunrise, Rabi' I 575 [=29 August 1179], the Muslim sappers succeeded in breaking through the walls which collapsed to the applause of the Muslims. The Franks erected a temporary timber wall, but strong wind strengthened the flames and the tents, timber and many of the Frankish warriors caught fire. The Muslim sources describe in amazement how the commander of castle jumped into the flames. The rest of the Franks asked for surrender terms.

The Muslim armies entered the castle killing many of the Frankish marksmen and taking many captives. Saladin took the armors of about 1000 knights and sergeants, 100,000 weapons and many animals as booty. The captives were led to Damascus.

The Muslim soldiers then destroyed the castle and threw the corpses of the defenders into a deep cistern. This last careless operation was probably the cause of a plague, which started within 3 days of the conquest. Saladin and his men left the site on their way to Damascus. The Frankish army in Tiberias saw their fortress caught ablaze and covered with deep smoke.

The Earthquake ruptures

The Crusader castle of Vadum Iacob (Fig. 1) was deformed by destructive earthquakes triggered by motion along the Dead Sea Transform. This is evident in the 2.1 m offset of the E-W-striking walls on the south and on the north. The first time was an M>7 earthquake at the dawn of 20 May 1202. It offset the castle walls by 1.6 m. The earthquake of 25 October 1759 accounts for the remaining 0.5 m out of a total 2.1 m of offset (Ellenblum et al., 1998).

In the last phase of excavations in Vadum Iacob we unearthed parts of a large Hellenistic compound, which we identify as a fortified settlement, built on the same strategic point on the main road between the Galilee and Syria. The Hellenistic structures complete a 23-century long record of slip. Abundant ceramics and C14 ages confirm the identification of Hellenistic buildings in the northern part of the Crusader fortress, north of the mosque and south of the southern Crusader wall outside the fortress. In both locations the Hellenistic walls are truncated by the fault. The correlation between the walls on the west and on the east is clear only in the south, where a 5.7-m-offset is inferred (Fig. 2). Crosscutting Hellenistic walls of different styles and different offsets may be explained by an earthquake in the end of the second century BCE, after which the site was rebuilt. Some supporting evidence is found in nearby archaeological sites and in a rather vague written record about an earthquake in 198 BCE (Guidoboni et al., 1994). Unfortunately there are no structures between the Hellenistic and the Crusader periods, apparently the site was abandoned. The 3.6 m displacement in this period may have been associated with one or more earthquakes.

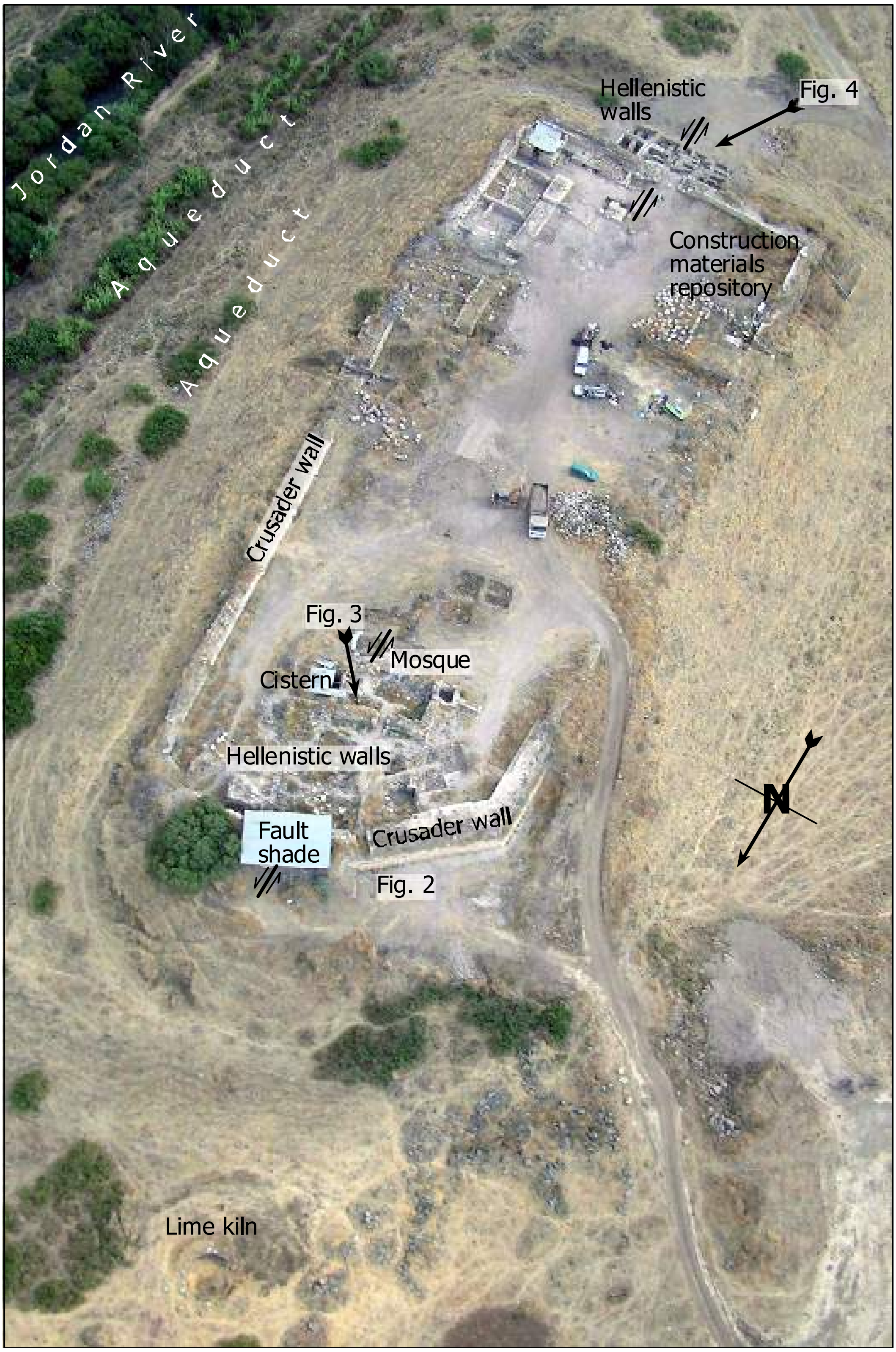

Figure 1: Oblique airphoto of the Vadum Iacob (Ateret) fortress.

Figure 2: Northern Crusader defense wall built of meticulously hewn ashlars from a quary on the hill to the west. On the left side is the construction ramp, which was used for hauling the blocks up to the high levels of the wall. The wall was actually buried as its construction advanced.

Figure 3: Faulted wall of the Ottoman mosque. Picture taken in 1994, before the excavation.

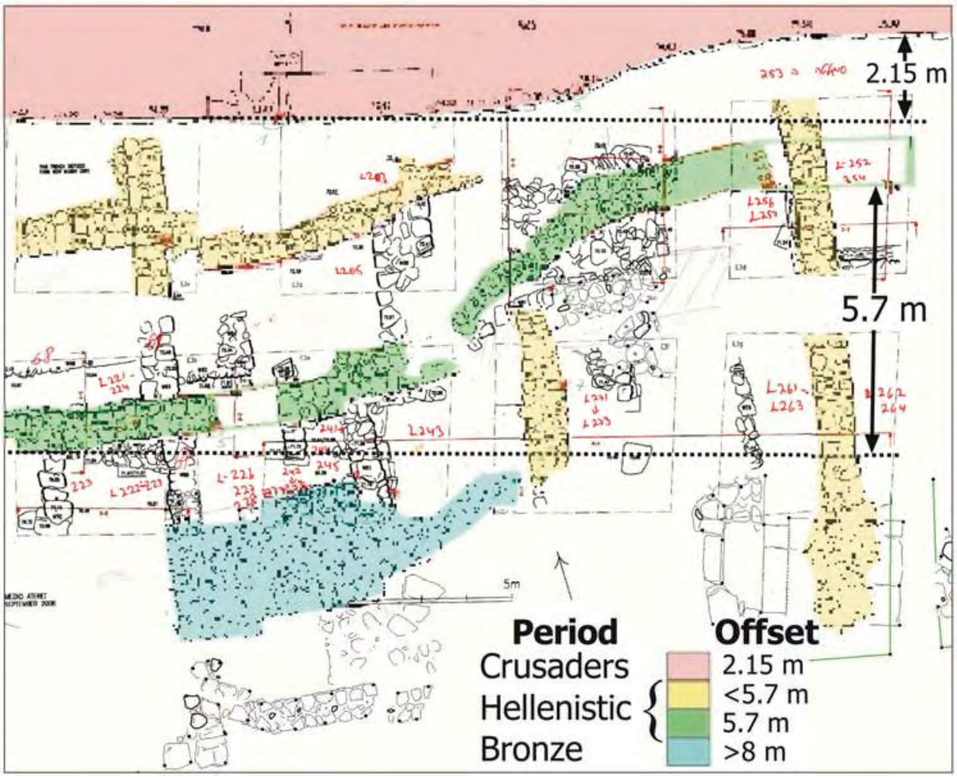

Figure 4: Two different styles of Hellenistic walls are found south of the Crusader fortress. The older walls (green) are about 60-80 cm thick, made of local basalt and limestone cobbles without cement. Their foundations are found at shallow depth of up to 1 m below the modern surface. Some of them are damaged, with the upper parts collapsed, and fallen stones are lying on the floor near them, burying whole ceramic artifacts. The artifacts are identified as 3rd century BC candles, jars, and cooking pots. The E-W trending Hellenistic walls are sheared and offset left-laterally. The location of the fault is 2-3 m west of where the Crusader wall is faulted. The second type of Hellenistic walls is made of the same materials but the cobbles are cemented, their foundations are over 1.5-2 m below the modern surface, and their width is 50 cm. They are associated with artifacts from the late 2nd and early 1st century BC. The present stage exposed primarily N-S-trending walls of this kind, which truncate the former E-W-trending walls. The fault-parallel trend of these walls does not provide any measurable for slip.

The types and the arrangement of the walls are interpreted as two construction periods separated by a destruction event, most probably associated with the left-lateral displacement of the older walls. We therefore attribute the termination of the older phase to an earthquake that occurred after the 3rd century BC and before the late 2nd century BC.

References

Ellenblum, R., 1998, Frankish Rural Settlement in the Latin Kingdom of Jerusalem: Cambridge, England, Cambridge University Press, 321 pp.

Ellenblum, R., Marco, S., Agnon, A., Rockwell, T., and Boas, A., 1998, Crusader castle torn apart by earthquake at dawn, 20 May 1202: Geology, v. 26, p. 303-306.

Guidoboni, E., Comastri, A., and Traina, G., 1994, Catalogue of Ancient Earthquakes in the Mediterranean Area up to the 10th Century: Bologna, Istituto Nazionale di Geofisica, 504 p.

Paleo PGA estimates around the Sea of Galilee from back analysis of old landslides and structural failures in historic monuments

Gony Yagoda-Biran [1*], Yossef H. Hatzor[1], Rivka Amit[2*] and Oded Katz[2*]

[1] Dept. of Geological and Environmental Sciences, Ben-Gurion University
[2] Geological Survey of Israel

yagoda@bgu.ac.il

*field guide

1. Motivation and Rationale

The estimated peak ground acceleration (PGA) for a specific region can not always be determined reliably from compilation and statistical analyses of instrumental data acquired in specific regions, because of the relatively short time window available for such an approach, typically up to 100 years of instrumentation .

In this project, we estimate paleo-PGA values on the eastern and western margins of the Sea of Galilee (Lake Kineret) using two different approaches: 1) Backward limit equilibrium analyses of ancient, seismically induced, slumps in natural rock slopes, and 2) Backward dynamic analysis of seismically driven toppling of columns at the south-eastern church of Susita, believed to have been destroyed by an earthquake dated to 749 AD. We believe that Paleo-PGA values thus obtained may constrain modern PGA estimates for the region that are based on the instrumental record only.

2. Research Methods and Preliminary Results

2.1 Backward limit equilibrium analyses of ancient landslides

Two ancient landslides are analyzed: 1) The *Ein Gev* landslide – located on the eastern margins of the Kineret, 2) The *Fishing Dock* landslide – located on the western margins of the lake.

Both slides are back-analyzed using the Morgenstern-Price Method of Slices, using the commercial software package SLOPE/W 2004. The geometry of the slope profile, ground water table level, material properties, and assumed location and geometry of the failure surface are used as input for the code. The geometry of the slope is defined using a 1:50,000 topographical map. The ground water table level is estimated on the basis of field observations. The material properties for the rock mass are determined using laboratory tests. For the Ein Gev landslide we performed direct shear tests at the rock mechanics laboratory in Ben-Gurion University. For the Fishing Dock landslide material properties are selected from data reported by Dr. Uzi Saltzman. The exact location and geometry of the sliding surfaces are assumed on the basis of field observations and borehole data.

2.1.1 The Ein Gev landslide – preliminary results

Geometrical comparison between the slumped and intact slope profiles

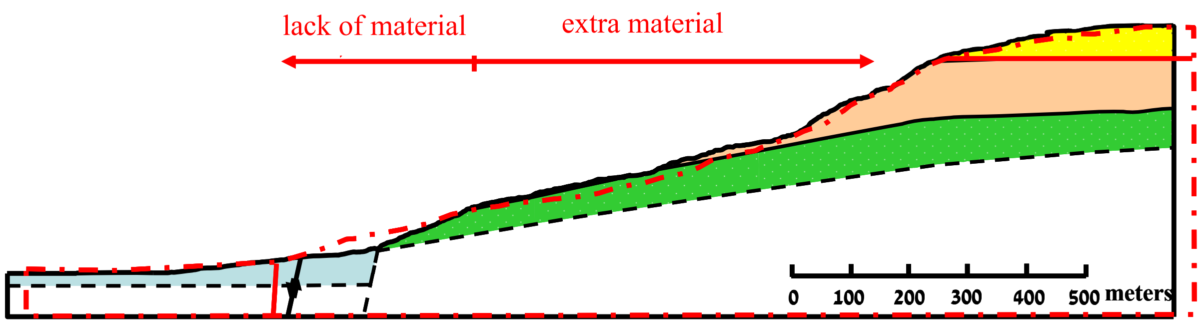

Geological section of the southern, intact, slope (colored). The profile of the slumped slope is superimposed (red dashed line). The geometrical comparison reveals lack of material in the middle section of the slumped slope, and extra material in the lower section of the slumped slope, as would be expected in a typical slump configuration.

The modeled profile of the landslide for backward analysis with Slope/W

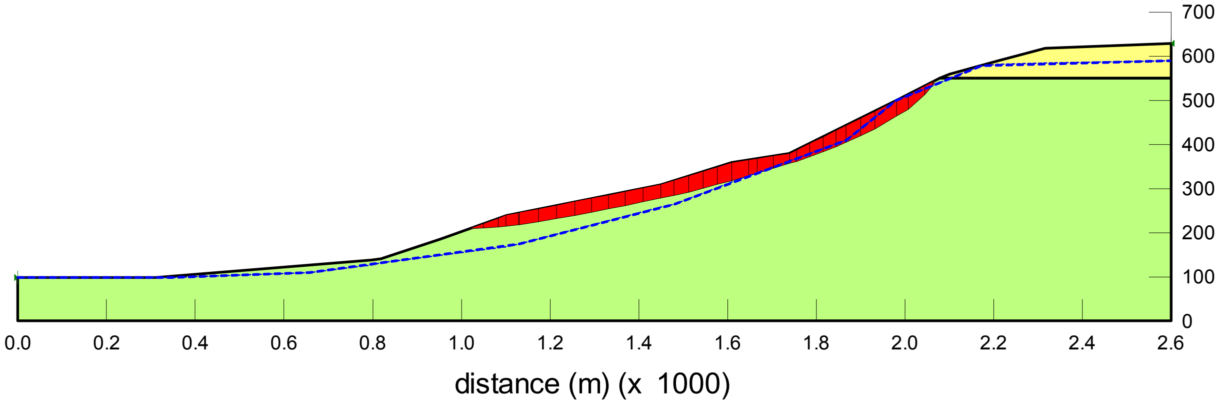

Modeled landslide profile in Slope/W. Legend: Green region - defined by the experimentally obtained material properties for the Ein Gev sands formation (= 43°, c = 370 KPa), Yellow region - undisturbed Cover Basalt formation, Red - the modeled slump, Dashed blue line - assumed ground water table level.

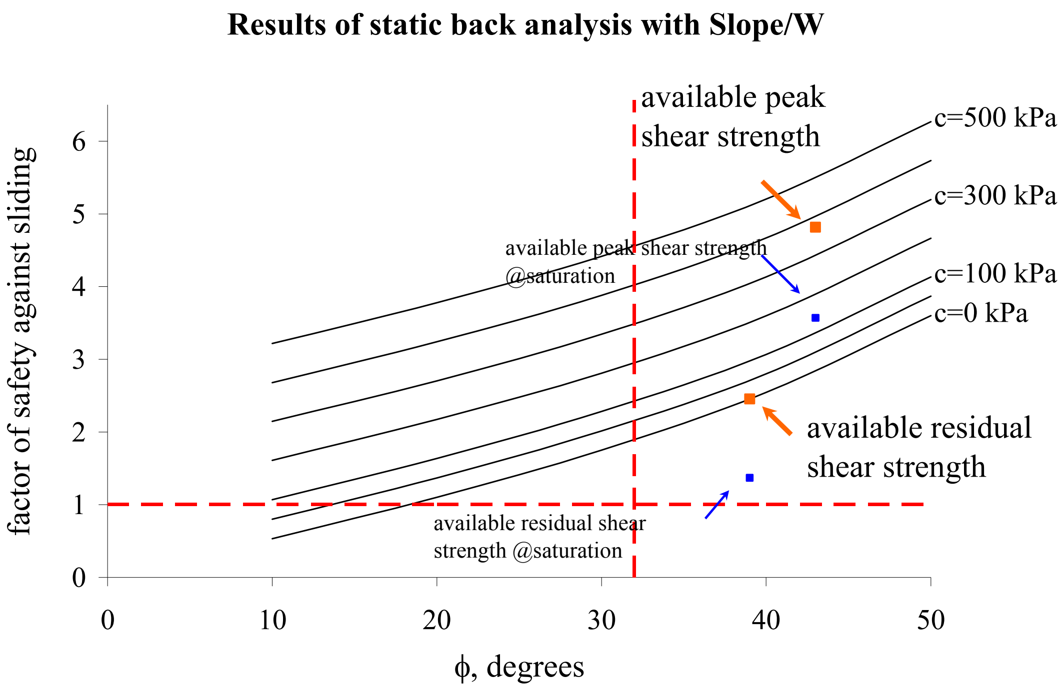

Factor of safety for static loading conditions as a function of cohesion (c) and friction angle ( ).Most results are well above the F. S. = 1 line, implying a stable slope under static loads.

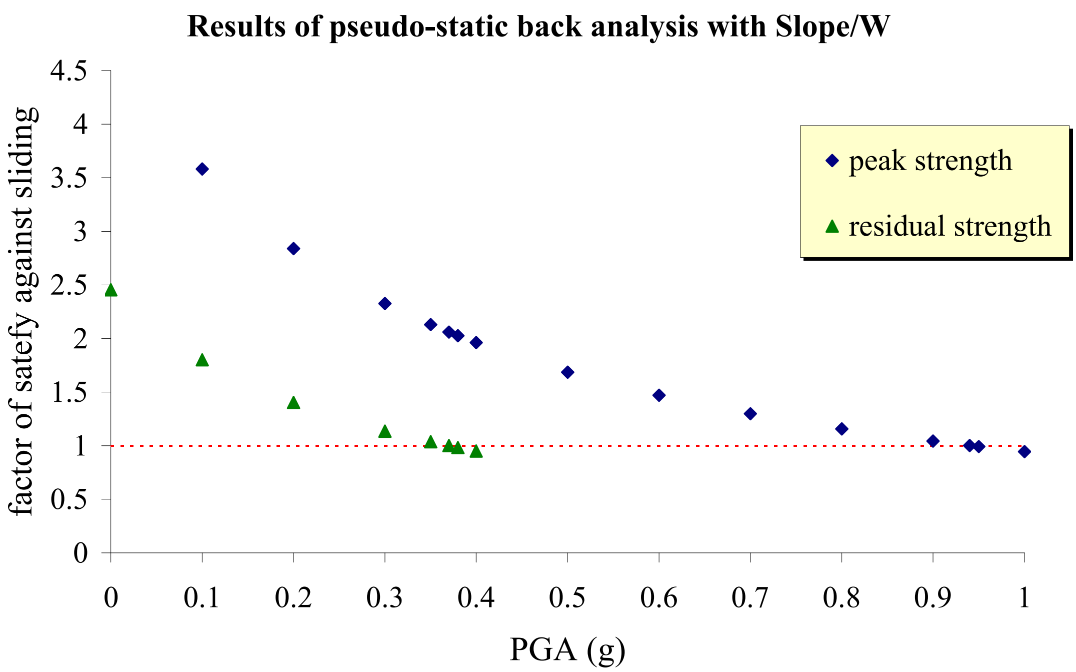

Factor of safety vs. pseudo-static horizontal force expressed in terms of horizontal PGA. The shear strength parameters are = 43°, c = 370 kPa for peak strength, and = 38°, c = 0 for residual strength. Note that with the available peak shear strength slope failure requires a PGA of 0.95 *g*. With residual strength slope failure is obtained with PGA = 0.37 *g*.

Results of a seismic reflection survey

A

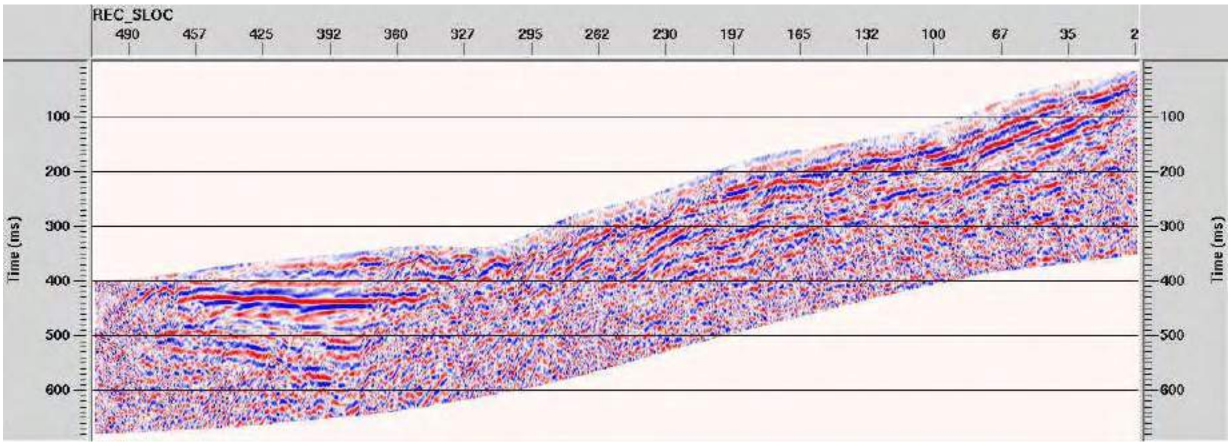

B

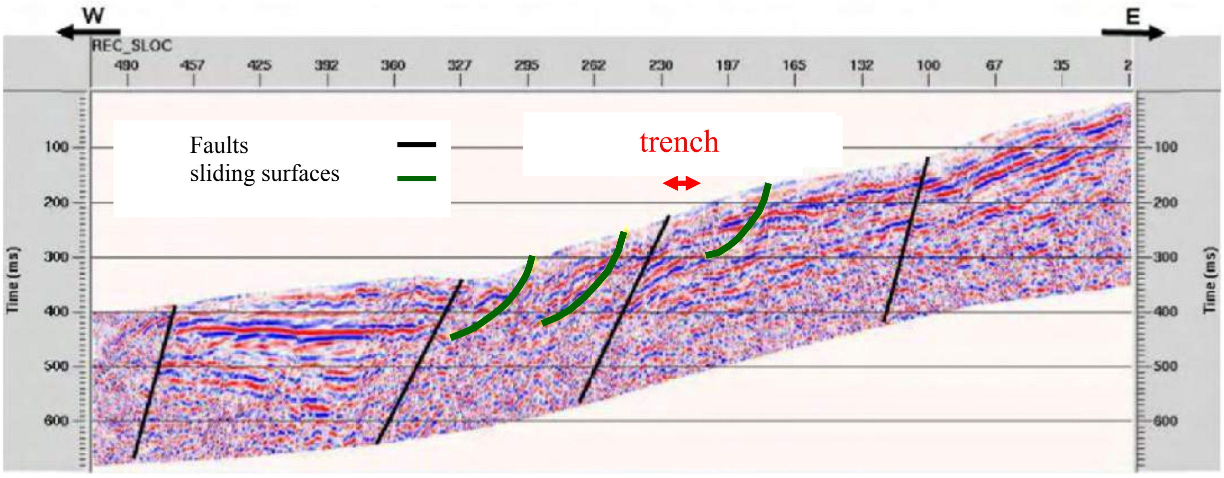

Seismic reflection survey of the slump: A) Un interpreted cross section, B) Interpreted cross section. Black lines - delineate discontinuities interpreted as faults, Green lines – delineate discontinuities interpreted as possible sliding surfaces.

2.1.2 The Fishing Dock Landslide – preliminary results

Material properties used for back analysis (Data from U. Saltzman)

Test date	Drill #	Test type (*)	Depth (m)	Lithology (**)	Cohesion (KPa)	Friction angle	Comments	Average
June, 1995	1	CD-DS	15	CH	400	46	Natural conditions	c=400 ϕ=46
Jan, 1999	1	CD-DS	24	CH	45	21	Saturated conditions	c=35 ϕ=42
Jan, 1999	2	CD-DS	16	CH	10	36	Saturated conditions	
2003	1	CD-DS	8-9	CH	0	65	Saturated conditions	
2003	1	CD-DS	11-12	CH-CL	100	47	Saturated conditions	
2003	7	CD-DS	14	CH	20	42	Saturated conditions	

Test date	Drill #	Test type (*)	Depth (m)	Lithology (**)	Cohesion Total	Cohesion effective	Friction angle Total	Friction angle effective	Comments	Average
May, 1996	1	CU-TX	15	CL	400	350	16	23	Saturated conditions	c_T=86 ϕ_T=33
May, 1996	1	CU-TX	19	CL	50	0	44	48	Saturated conditions	
May, 1996	3	CU-TX	20	MH	20	36	10	46	Saturated conditions	
Jan, 1998	3	CU-TX	5	MH	25	5	32	36	Saturated conditions	
Jan, 1998	3	CU-TX	3	CH	25	10	39 (res)	33 (res)	Saturated conditions	
2003	2	CU-TX	12	CH	0	10	24	31	Saturated conditions	

Modeled profile of the Fishing Dock landslide for backward analysis with Slope/W

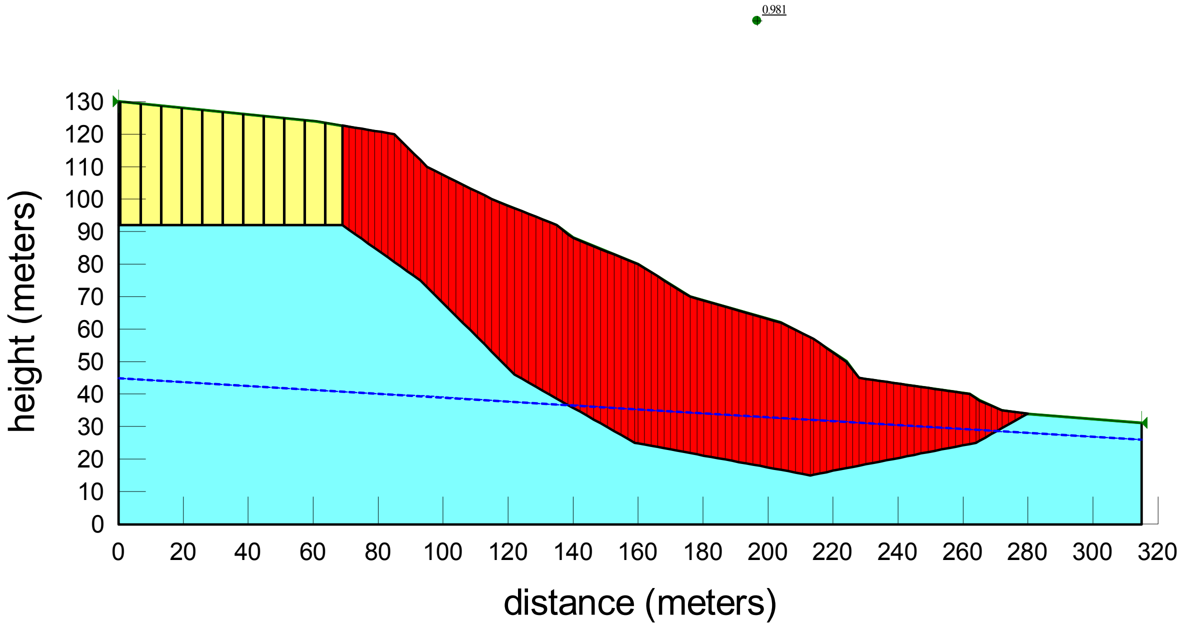

The modeled profile in Slope/W. Legend: Blue - material properties compiled from Saltzman's data, Yellow – Cover Basalt, Red – slump, Dashed blue line – assumed GWT.

Concentrated limit equilibrium analysis results - the Fishing Dock landslide

Run #	Ground water table	Material strenth	Static Factor of Safety	Pseudo-Static PGA (g)
1	recent	Natural, drained	4.9	1.61<
2	recent	Saturated, drained	2.8	0.85
3	at surface	Saturated, drained	1.52	0.28
4	recent	Saturated, undrained, total	2.3	0.5
5	at surface	Saturated, undrained, total	1.35	0.15

2.2 Backward dynamic analysis of the toppled columns at Susita with the numerical DDA method

The dynamic analysis was performed using the DDA (Discontinuous Deformation Analysis) method - an implicit discrete element method. DDA models a discontinuous material as a system of individually deformable blocks that move independently with minimal amount of interpenetration. The formulation is based on dynamic equilibrium that considers the kinematics of individual blocks as well as friction along the block interfaces.

The DDA needs as input the geometry of the column and its physical properties (density, friction angle, Young's modulus), as well as some numerical parameters.

2.2.1 The modeled cathedral column at Susita – preliminary results

The modeled column in DDA

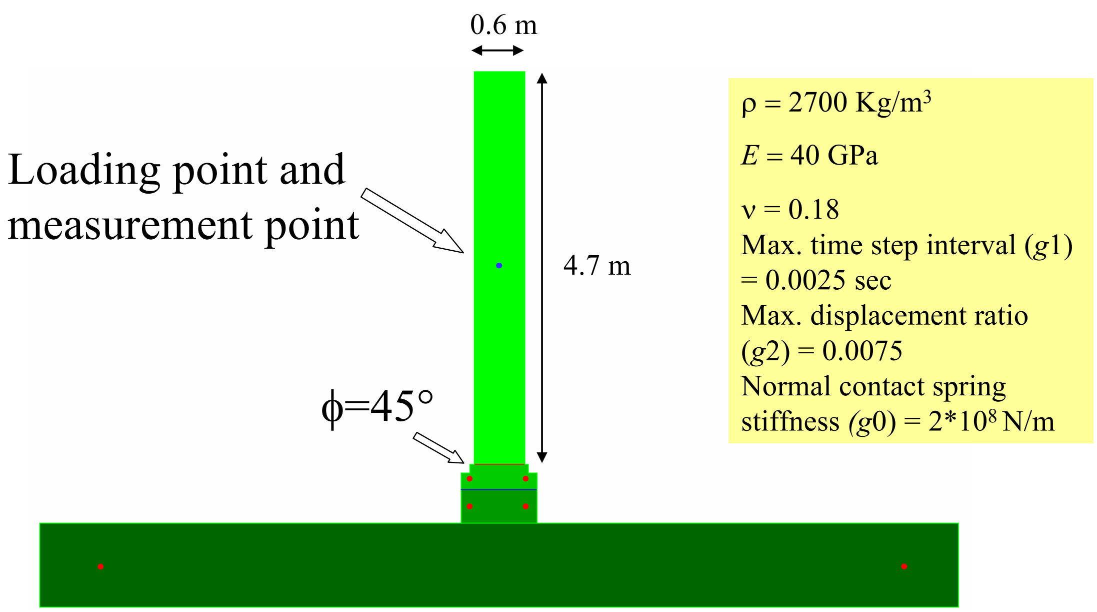

Concentrated results for DDA simulations with different earthquakes as input

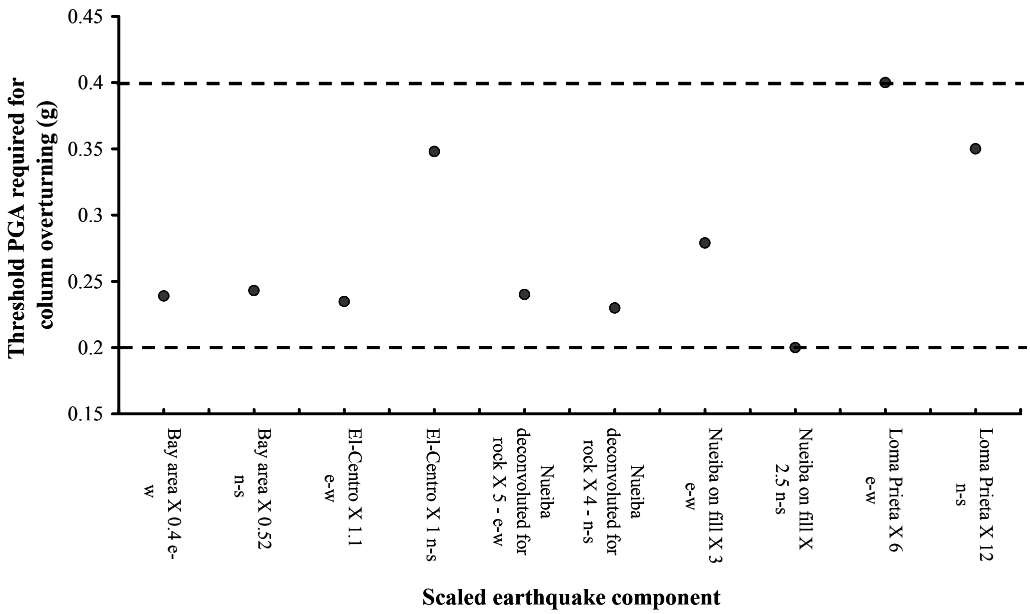

Threshold PGA values required to topple the modeled column with DDA, using different earthquake records as input acceleration. Five different earthquakes are used: the Nuieba 1995 as recorded in Eilat, the Nueiba 1995 record deconvoluted for rock response, a San Francisco Bay area design earthquake (synthetic), the Loma Prieta 1989 record measured on rock, and the Imperial Valley 1940 record measured on fill. Each record is used twice: 1) N-S + vertical component, and 2) E-W + vertical component, resulting in 10 records. The records were either up-scaled or down-scaled to obtain the threshold PGA required for toppling. Note that although the records are from different fault systems, measured on different subsurface conditions, and have different frequency contents, the obtained range of threshold PGA values required for column toppling is rather narrow: between 0.2 and 0.4 *g*.

Paleoseismology of the Eastern Sea of Galilee

Rivka Amit[1*], Oded Katz[1*], Gony Yagoda-Biran[2,1*], Yossef H. Hatzor[2]

[1]Geological Survey of Israel

[2]Dept. of Geological and Environmental Sciences, Ben-Gurion University

rivka@gsi.gov.il

* Field guide

The study site is located between the western slopes of the Golan Heights and the eastern coast of the Sea of Galilee (Fig1) in a seismically active area as part of the Dead Sea Rift (DSR). In this area landslides and faulted and tilted blocks shape the steep, 600 m high slopes of the southern Golan Heights. The Miocene–to-Quaternary sequence which is exposed on these slopes is composed of sedimentary rocks such as marls, sand, fluvial sediments, lake sediments and basalts of Pliocene-Pleistocene age. This geological setting and lithology enhance development of compound landslides of several kinds (e.g. earth flow, slump, creep) with slide units comprising, in places, complete rock sequences. The faulting, the westward dipping strata and the steep slopes play significant roles in the sliding process, resulting in a terraced morphology of these steep slopes.

Three trenches were opened crossing three of the mapped N-S oriented normal faults composing 800 m wide fault zone (Fig 1). These faults are ~ 200 m apart from each other, crossing a series of tilted blocks .

TEG –A (Fig 2a)

A normal fault displacing the slope of one of the tilted blocks. This tilted block is composed mainly of intercalation of chalky limestone (slightly sandy) of the Maresha Formation (Middle Eocene). The fault scarp is partly covered by colluvial material towards the top and part of the scarp has a free face exposing the chalky limestone of the Maresha Formation. The paleoseismological analysis revealed that the fault is a multiple type with two identifiable faulting events. The age of the faulted slope is between 47±8 ka and 3.5±1.4. The slope which was stable during the upper Pleistocene was faulted twice during the Holocene with one event during the early Holocene (~ 11 ka) displacing ~ 1m (colluvial wedge 3) and another event during the late Holocene (~ 3.5 ka) displacing ~80 cm (colluvial wedge 4). The fresh rocky free face, which is exposed more to the north along the fault trace, might suggest that an additional faulting event occurred later than the last dated event (< 3.5±1.4 ka).

TEG - B (Fig 2b)

A normal eastern fault crossing a tilted block is displacing the Hordos and En Gev formations. The faulted slope has a minimal age of 78.6±13 ka.
Three events were identified; two that occurred close in time (during the late Pleistocene) and one that occurred during the Holocene after a long quiescence of about 35 ky. The last event, which occurred ~ 5.7±2.2 ka, displaces the slope by ~ 40 cm and was also detected in trench TEG – A, a parallel fault line located more to the west (Fig1).

TEG – C (Fig 2c)

A fault displacing the toe of the two landslides in the study site was trenched (Fig 1). The trench was opened along the southern margin of the southern landslide (Fig 1). The trenched area is composed mostly of colluvial material (unit 3) partly derived from the white-yellowish sandstone of the En-Gev formation exposed at the upper part of the slope (unit 5) and partly composed of limestone and chert lithoclasts. The colluvium is mostly rock supported with large angular rock blocks, some of which reach 50 cm, and gravel ~ 15 cm. The matrix is composed of unsorted coarse silt, sand, grit and granules. Calcic soil developed in this unit. The calcium carbonate envelopes the gravel and is disseminated in the sandy matrix. The soil reached stage II-III. At the fault zone, which is ~ 1 m wide, the colluvial unit 3 and 1 are intensely cracked and jointed (between 1–2 mm and 5-10 cm wide joints) (Fig 2).

Phase 1: Displacement of unit 3 by about 1.60 m which occurred ~ 37±3 ka (at TEG - C ~ 36 ka). The faulted unit is composed of sand (coarse and fine) with small amounts of silt and gravel of 3-4 cm size. The gravel is composed of sandstone, limestone and chert. Calcic soil developed in this unit and reached stage II-III with calcium carbonate enveloping the gravel and disseminated in the sandy matrix. The age of this unit in the downthrown block is 255±19 ka (Fig 2c; TEG-45). At the fault zone (Fig 2c; TEG-43) and in the upthrown block close to the surface (Fig 2c; TEG 46) the age of unit 3 is 97±18 and 99±12 ka, respectively. The colluvial unit 2 which is deposited on top of unit 3 on the downthrown block is composed of massive clay-silty colluvium mixed with small gravel (3-5 cm). A calcic soil developed in this unit and reached stage II-III. Most of the calcium carbonate is deposited in the upper 1 m of the unit, with decreasing amounts downward. Orthic and disorthic calcium carbonate nodules are scattered in the fine matrix, most of them ~ 2 mm. Some of the gravel is coated with calcic crust. The disorthic nodules and the coated clasts scattered in the colluvium are the result of soil erosion and deposition on the downfaulted block. The orthic calcic nodules were formed during the quiescence in between the tectonic events.

Phase 2: The second tectonic event occurred ~ 9 ka ago (Fig 2c), displacing the slope by ~40 cm. As a result, colluvial unit 1 was deposited on the downthrown block and covered the whole slope. This colluvial unit (unit 1) is composed of unsorted gravel which ranges between 20 cm, the largest, and 3 cm, the smallest. In addition, granules of the size of 0.5 – 1 cm are also scattered in the matrix. The matrix is composed of silt and fine sand and a high amount of organic material. A weak clayey-gypsic soil developed continuously along the slope and integrated into the calcic soil at unit 2.

Two events were identified in this trench. One occurred at ~ 37 ka (Fig.2c ;TEG-42: 37±3) and another occurred ~ 9 ka ago (TEG- 44; 9.2±1.9). The well-developed soil in unit 2 and the weak soil profile in unit 1 point to a long quiescence between events.

Summary

The oldest event occurred ~ 37 ka ago and was detected in two of the trenches, TEG-B and TEG-C. Another event occurred ~ 11 ka ago and was detected in all three trenches studied. The youngest event was detected in TEG-A and occurred ~3 ka ago.
A magnitude of Mw 6.6 was estimated. The calculated magnitude ranges between Mw 6.3 and Mw 6.8 and was estimated as Mw 6.6. The recurrence time of large earthquakes on this segment is ~ 9 ky.

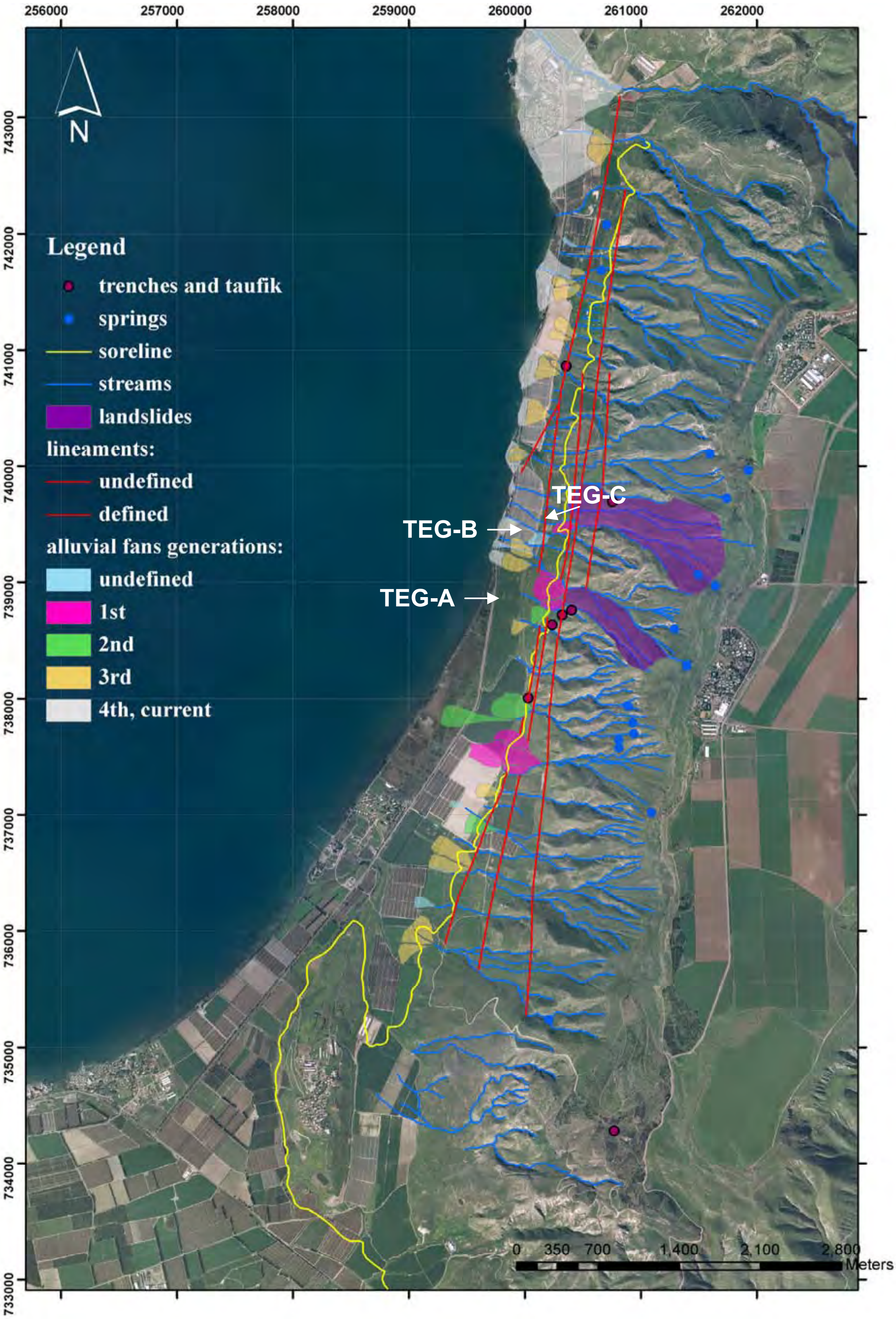

Figure 1: Morphotectonic map of the Eastern Sea of Galilee

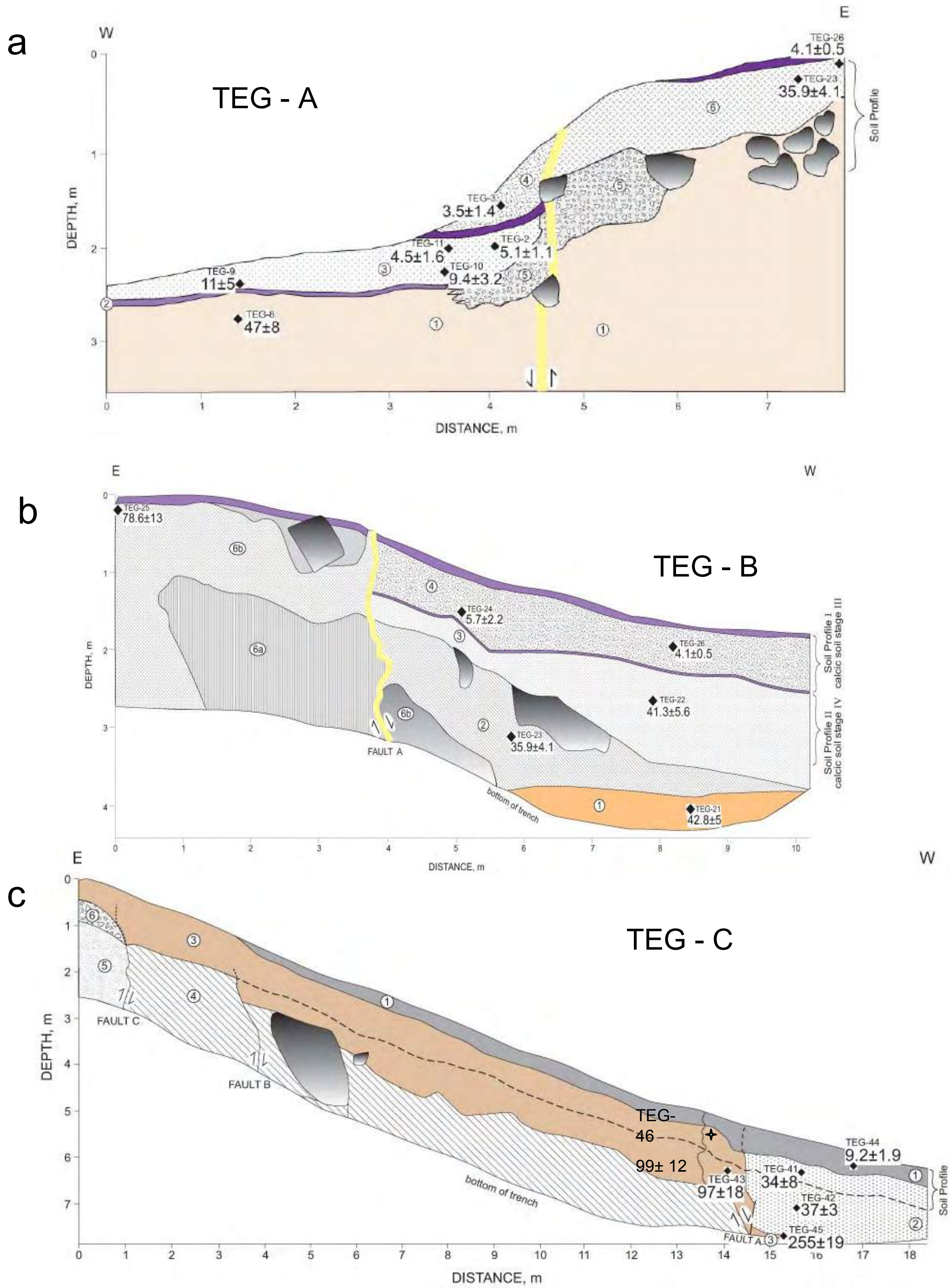

Figure 2: Paleoseismic trenches: (a) Two events: ~ 11ka and ~ 4ka; (b) two events: ~ 40ka and ~ 4 ka; (c) Two events: ~ 40ka and ~ 10ka

Dead Sea

19-20.2.2009

Field leaders

Meir Abelson

Amir sagy

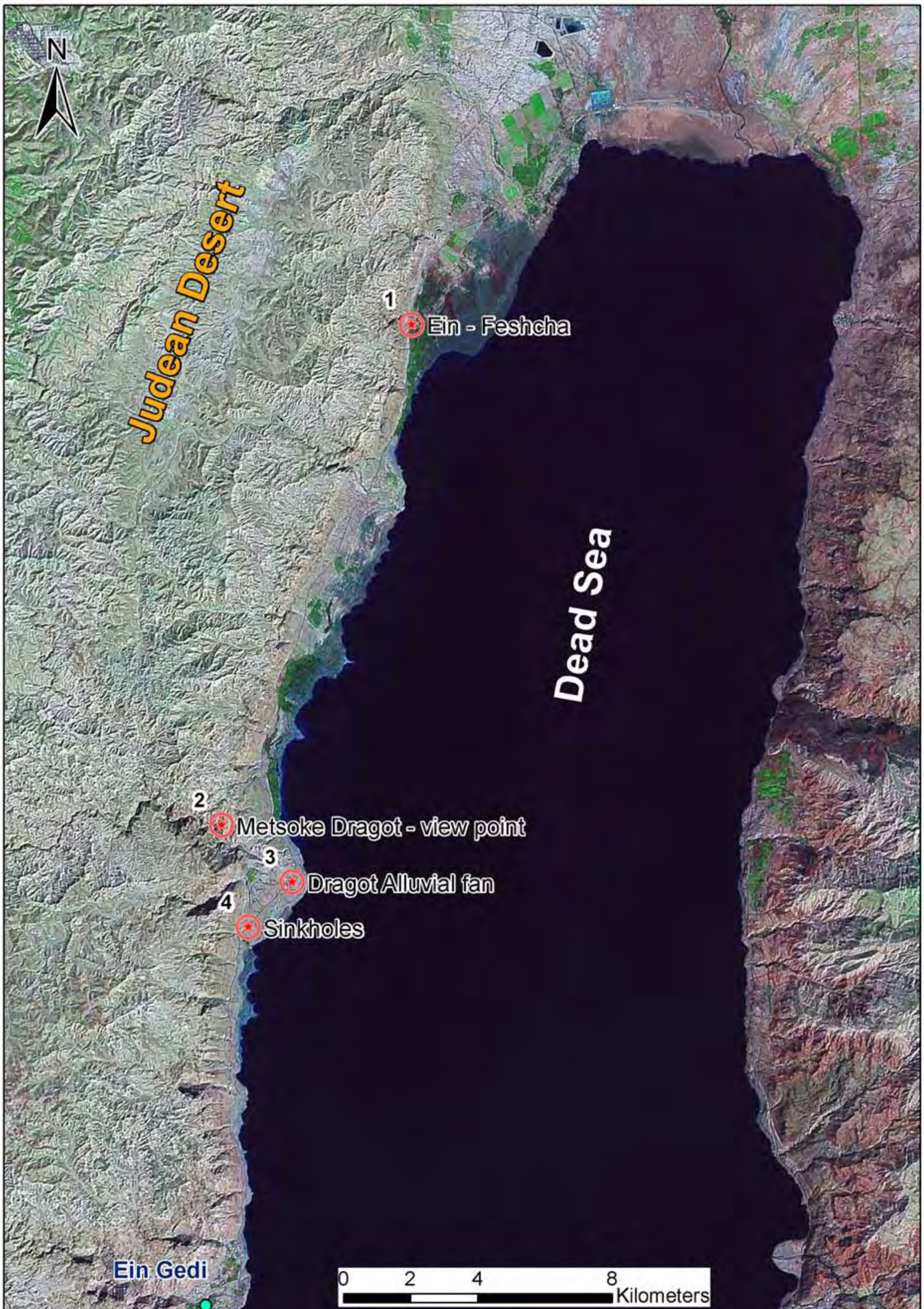
N
Judean Desert
Dead Sea
1
Ein - Feshcha
2
Metsoke Dragot - view point
3
Dragot Alluvial fan
4
Sinkholes
Ein Gedi
0 2 4 8
Kilometers

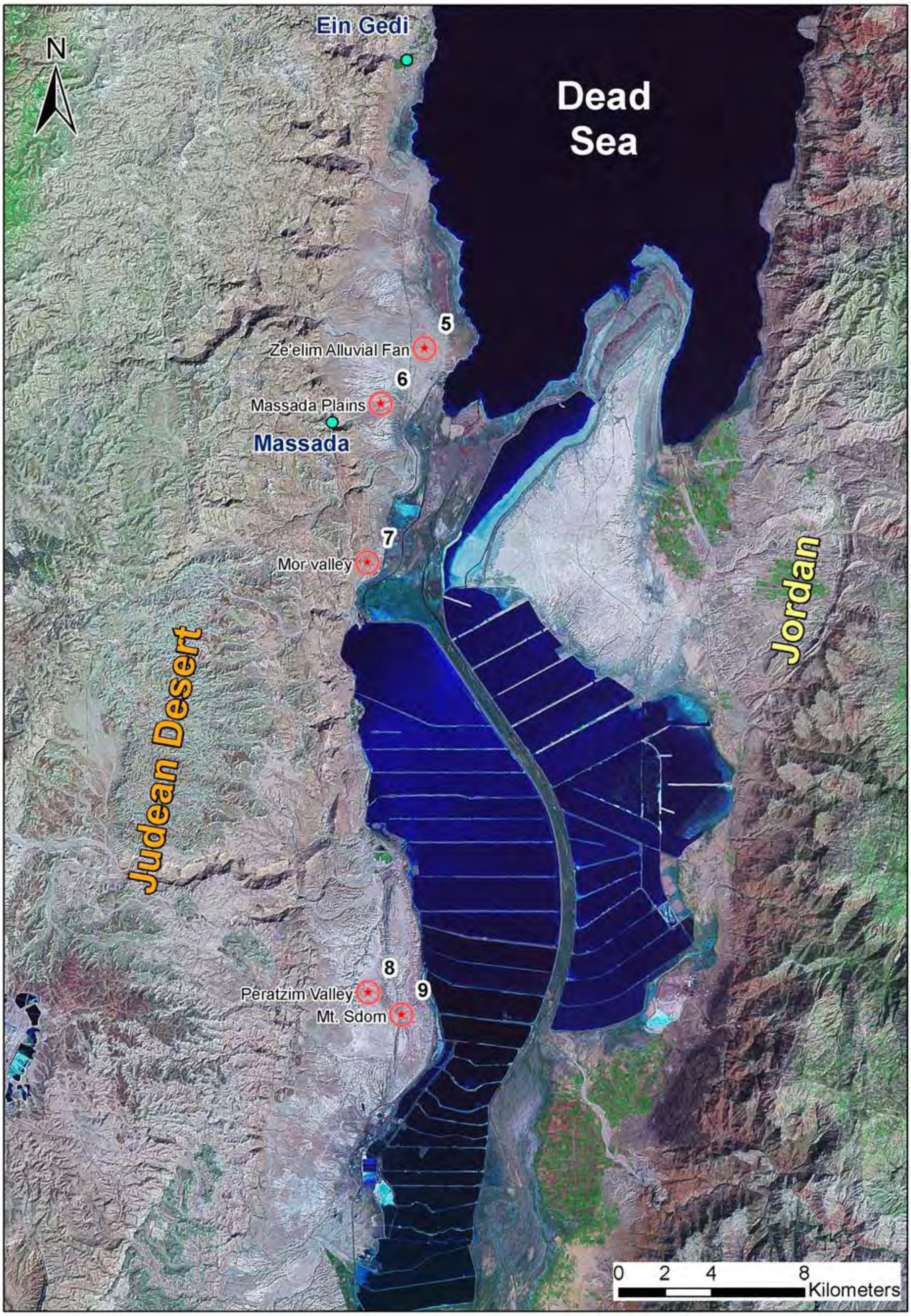
Ein Gedi
N
Dead Sea
5
Ze'elim Alluvial Fan
6
Massada Plains
Massada
7
Mor valley
Judean Desert
Jordan
8
Peratzim Valley
9
Mt. Sdom
0 2 4 8
Kilometers

Radon signals in geogas of the upper crust – The Enot Zuqim sector, NW Dead Sea

Gidi Steinitz[1*]

[1]Geological Survey of Israel

Steinitz @gsi.gov.il

*Field guide

Radon (^{222}Rn) is a radioactive inert gas formed by disintegration from ^{226}Ra as part of the ^{238}U decay series. It occurs at varying concentrations in geological environments. The combination of its noble gas character and its radioactive decay make it a unique ultra-trace component for tracking temporally varying natural processes in subsurface systems. Using nuclear techniques the measurement sensitivity for radon in the subsurface geogas is extremely high and can be performed with a time resolution in the order of 1 hour or less. The application of stress to rocks is thought to enhance the exhalation of radon from the solid mineral phase, rendering radon a potential sensitive tracer of geodynamic processes in the upper crust. Transport of radon in soil and water has been investigated as a tool for monitoring volcanic activity and the proposition that radon may serve as a useful proxy for seismic activity has been repeatedly raised. Radon is viewed in these scenarios as a highly sensitive tracer of secondary geodynamic processes – mainly mechanical and thermal. Despite the presumed advantages of radon as a geophysical proxy, the utilization of radon in geodynamics has been hampered by the complex patterns of the measured signals.

The research team at the Geological Survey of Israel is addressing, since 1990, the temporal variations of radon and its geophysical significance in geogas in upper crustal rocks in the frame of the Israel Geophysical Radon Project (IGRnP. Intensive high-time resolution (<1 hour) monitoring of Rn is being performed since 1995 in upper crustal rock systems, along the western margin of the Dead Sea transform (DST). Presently radon is being monitored in a 200 km segment along the western boundary fault of the DST, from the Dead Sea to the Gulf of Aqaba. Several arrays of stations, spanning 0.5 to 20 km, consist each of several monitoring sites (Table 1). The Rn signals are characterized by: a) unambiguous temporal signature types (Steinitz et al., 1992; Steinitz et al., 1996; Steinitz et al., 1999, Balogh and Steinitz, 2004); b) recurrence at the different locations within the same geologic unit; c) similar features recorded in diverse geographic, geological and geodynamic situations.

A large regional (20 km) and most intense (high level) radon flux anomaly is developed along the western fault scarp of the DST, in the Enot Zuqim (EZ) segment in NW sector of the Dead Sea. The anomaly occurs in the unconsolidated gravel from the fault scarp eastwards, to the shore of the Dead Sea. Several radon monitoring sites, spanning +15km and utilizing 15-minute sampling, are operative in the EZ. Site 17, situated along the active fault site and operative since 1995, is a world scale key locality in terms of the intensity of the recorded radon signals.

Temporal variations and signals of radon occur at the EZ sites. The signals are classified based on the temporal scale of the variation, as follows: a) Seasonal variation of radon (SR), periodic at 1 cycle/yr; b) Multi-Day (MD) signals, lasting 2-20 days, which are non-periodic; c) Diurnal Radon (DR) signals, which have typical periods of 24-, 12- and 8-hours (S1, S2, S3). Indicative gravity diurnal periodic constituents (M1, O1) are clearly lacking in the radon time series. This is interpreted to indicate that the DR signal (S1, S2, S3 constituents) is driven by a solar tide related process.

Using an 8-year record of Rn, obtained next to a major active boundary fault of the DST, a statistically significant relation between multi-day Rn signals and earthquakes in the nearby sector of the DSR was demonstrated by Steinitz et al. (2003). In these works the establishment of the geodynamic nature of the signatures and signals is based on negation of atmospheric influence, analyzing radon signatures in the geological, spatial, time and frequency domains and, primarily, on correlating radon with geophysical phenomena, and specifically the correlation to earthquakes (Steinitz et al., 2003; Begin and Steinitz, 2005).

Recent advance in the understanding of these radon phenomena is demonstrated by using the geophysical approach as applied for analysis of radon signal in the Elat Granite (by Steinitz et al., 2006, 2007). A new geophysical framework for the temporal patterns of radon is obtained by: i) applying advanced time series methods and signal processing approaches in the time and frequency domain to long (multi-year) and high-resolution (< 1 hour) radon time series for the extraction and description of the superimposed signals; ii) the analysis of the environmental and geophysical influences on radon time series; and iii) both multi-site and multi-parameter analysis of radon phenomena and other geophysical phenomena. The primary outcomes concerning the radon signal in the subsurface are: a) the compound variation is composed of a periodic Seasonal Radon (SR) signal, a periodic Daily Radon (DR) signal containing diurnal (24-hour) and semi-diurnal (12-hour) periods, and non-periodic Multi-Day (MD) signals; b) the MD signals may be representing transients of a mechanical affiliation; c) the SR and especially the DR signals are probably generated in the subsurface by a solar irradiance related process.

Table 1: Monitoring sites of the IGRnP, north to south along 200km sector of the DST

Region/Array (extent in km)	Site	Elev. (m)	Depth (m)	Geology Age	lithology	Structural and tectonic situation
Enot Zuqim (EZ), NW Dead Sea (20 km)	19W	-388	2	Recent	Gravel	Along and next to active main western fault of the central segment of the DST
	19E	-368	2			
	17W	-373	2			
	23W	-381	2			
	23C	-364	2			
	23E	-364	2			
	21W	-364	2			
Ramon (GAV) (0.1 km)	GAV1.2	470	1.2	Lower Cretaceous	Syenite	Intraplate
	GAV85		85			
Southern Arava (0.1 km, each]	BGO	220	~ 80	Precambrian	Granite	Uplifted structural blocks along the western margin of the southern segment of the DST.
	RODED	285	10		Meta diorite	
Elat Granite (ELTGR) (1 km)	E1	29	10		Granite	
	E2	27	4			
	E3	53	53			
Gulf of Elat (0.1 km)	IUI	-1.5		Recent	Gravel, Seawater	Active main western fault of the DST

References

Balogh, B. and Steinitz, G., Radon monitoring at the Gavnunim site, Makhtesh Ramon. Interim Report. Isr. Geol. Surv. Tech. Rep. TR-GSI/22/04, 17p., 2004.

Barbosa, S. M., G. Steinitz, O. Piatibratova, M. E. Silva, and P. Lago, Radon variability at the Elat granite, Israel: Heteroscedasticity and nonlinearity, Geophys. Res. Lett., 34, L15309, 2007. doi:10.1029/2007GL030065.

Begin, Z.B. and Steinitz, G., Temporal and spatial variations of micro-earthquake activity along the Dead Sea Fault, 1984-2004. Israel Jour. Earth Sci., 54, 1-14, 2005.

Steinitz, G., Begin, Z.B. and Gazit-Yaari, N., A Statistically Significant Relation between Rn Flux and Weak Earthquakes in the Dead Sea Rift Valley. Geology, 31, 505-508, 2003.

Steinitz, G., O. Piatibratova, and S. M. Barbosa, Radon daily signals in the Elat Granite, southern Arava, Israel, J. Geophys. Res., 112, B10211, 2007. doi:10.1029/2006JB004817

Steinitz, G., Piatibratova, O., and Malik, U., Radon signals in the Elat Granite pluton, southern Arava, Israel. Geol. Surv. Rep. GSI/18/06, 53p., 2006.

Steinitz, G., Vulkan, U., Lang, B., Gilat, A. and Zafrir, H., Radon emanation along border faults of the Rift in the Dead Sea area. Israel Jour. Earth Sci., 41, 9-20, 1992.

Steinitz, G., Vulkan, U. and Lang, B., Monitoring of the tectonically related radon flux in Israel. Isr. Geol. Surv., Current Res., 10, 148-153, 1996.

Steinitz, G., Vulkan, U., Lang, B., The Radon flux at the northwestern segment of the Dead Sea (Dead Sea Rift) and its relation to earthquakes. Israel Jour. Earth Sci., 48, 283-299, 1999.

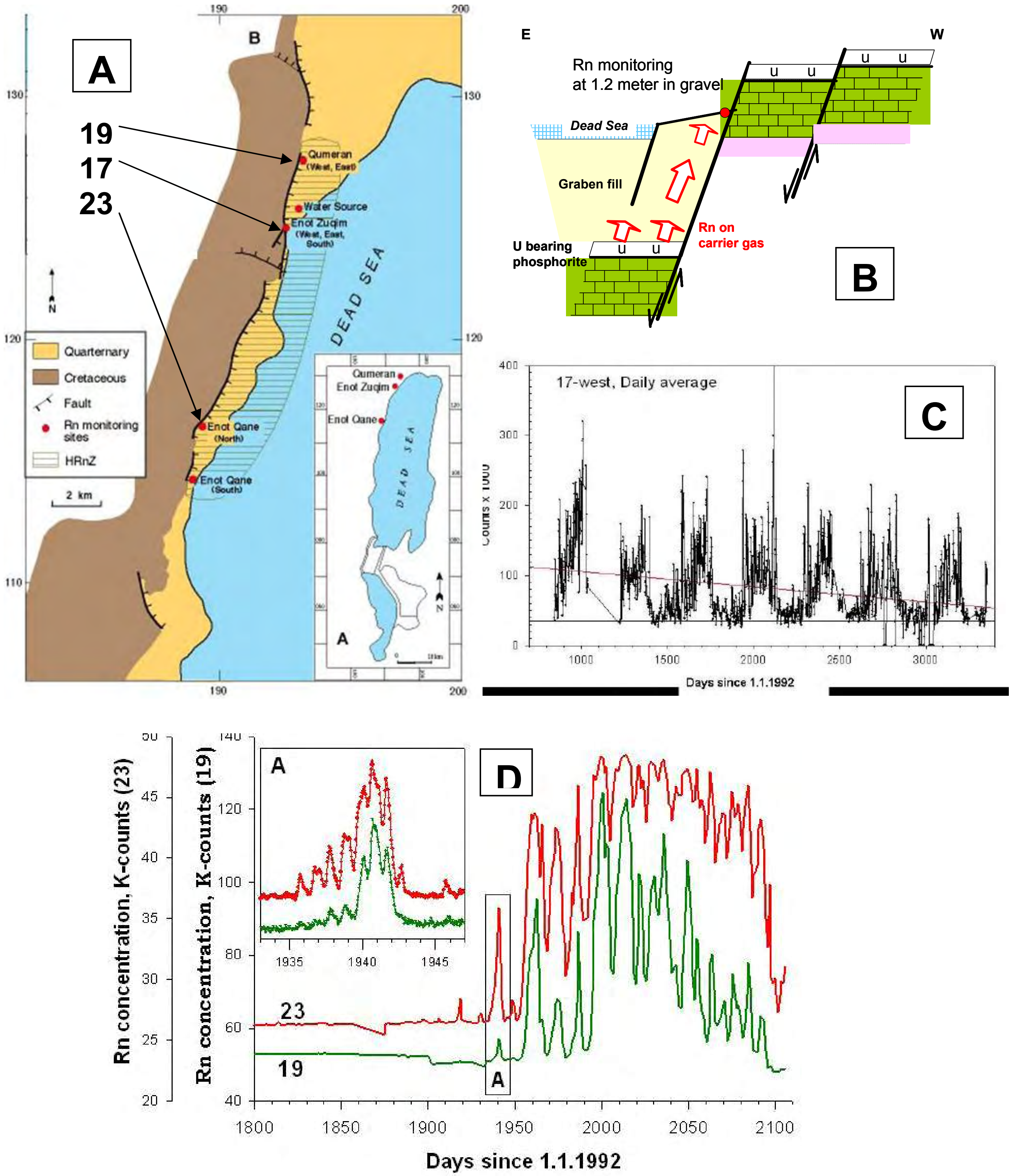

A – Regional radon anomaly along the fault scarp of the western boundary fault of the DST and location of radon high-time resolution monitoring sites in the unconsolidated gravel.

B – Schematic cross section, at the primary monitoring site 17W, presenting a possible model for the local radon flux regime.

C – Long term monitoring (+7 years) at site 17 showing: 1) a long term variation; 2) periodic annual radon signal, and 3) superimposed non periodic multi-day radon signals.

D – Radon time series at sites 19 & 23 showing regional correlation of: 1) annual radon signal; 2) superimposed non periodic multi-day radon signals, and 3) periodic diurnal signals (inset).

Active tectonics in the Nahal Darga Fan-Delta

Yehouda Enzel[1]*, Yehuda Eyal[2], Galit Kadan[2],

[1]The Hebrew University of Jerusalem
[2]Ben Gurion University of the Negev

yenzel@cc.huji.ac.il

* Field guide

In this site we will see large exposures into the Holocene fan-delta of Nahal Darga that is deposited on top one of the major faults in the western Dead Sea basin according to available data. Holocene and late Pleistocene fan-deltas are common features along the western margins of the Dead Sea (e.g., Sneh, 1979; Bowman, 1974; Manspeizer, 1985; Kadan, 1997; Bartov et al., 2006). Such fan-deltas can record the areal and temporal distribution of significant earthquakes (Sims, 1975; Dunne and Hempton, 1984; Allen, 1984). As the Darga fan is one of the largest and situated farther to the east than most other fans in the western margin, it probably forming over a major structure, at least as the faults are mapped (Fig. 1). Its very steep delta front and the nearby bathymetry support this association. In this station we will show evidence for diverse deformations in fine-grained lacustrine alternating with coarse-grained delta and fan. When we begun the work in Nahal Darga fan in early 1990s, this type of information on paleoseismicity, tectonic deformation, and lake level reconstruction was yet untapped in Israel. Then, and for several years, the sedimentary sequence of the Nahal Darga fan-delta was the best exposed in the Dead Sea area (and probably far beyond) as a very large flood in early January 1992 cleared the deeply incised banks to produce a remarkable natural trench walls (Fig. 2). From many aspects this fan delta is still a source of new data as incision continues to expose deeper sections with Dead Sea level continuing to drop at ~1 m/yr. Stratigraphically, the Darga's is the best-documented fan-delta in this tectonically active basin (Kadan, 1997; Enzel et al., 2000; Eyal et al., 2002). We specifically aimed at the detailed stratigraphy and age of the deformed beds within the Holocene fan-delta of Nahal Darga but also to understand the sedimentology that later served other researchers in the basin, especially those interested in lake level reconstructions. We stress that the exposure is still better than can be achieved through trenching.
We conducted two complimentary studies here: the subsurface and the exposures.

Shallow High-Resolution Seismic Study

High-resolution seismic profiles were acquired for the shallow subsurface in the Nahal Darga fan-delta (Figs. 3 and 4). Profiles 1, 2, and 3 are along the southern bank, the stream channel, and the northern bank, respectively and Profile 4 actuates as it follows the Dead Sea shoreline in 1996. The methods used can be found in Eyal et al, 2002 and in references therein. The lines below of high-resolution seismic lines intrude east into the northern Dead Sea basin on land and are connected well to the exposed stratigraphy.

We present here only the results of the reflection wave profiles, although exact determination of fault location within the profile is also based on diffraction waves. Usually the detection of faults on seismic sections is solved by visual interpretation of stacked sections. However, when detecting faults with a vertical displacement of less than the wavelength, a more sophisticated method must be used. To obtain reliable information about possible structural/ lithological discontinuities from seismic data, a procedure utilizing certain features known to be associated with the presence of such discontinuities is desirable. One such specific feature demonstrating the presence of faults on a seismic section is associated with the presence of diffracted waves in the vicinity of the discontinuity location. These waves can serve as a good indicator for fault detection. We extracted diffractions from the unmigrated stacked sections and used this information for identifying real discontinuities in the subsurface. The seismic interpretation is based on the presence of reflection horizons which, most probably but not necessarily, imply stratigraphic correlation. The time is given in seconds by Two Way Time (TWT). Based on a priori information (see details in Eyal et al., 2002) average velocity in the investigated area is about 2000–2500 m/s, so the maximal information depth achieved by these seismic profiles is about 400 m.

<u>Profile 1</u> is obviously disturbed in its central part due to its proximity to the steep southern wall of the stream channel. Nevertheless, in its western part the bedding dips gently eastward and one normal fault can be interpreted. This fault is located underneath the exposed eastern part of the western deformation zone (see Fig. 5 at about 50 and 100 m at the northern and southern walls, respectively). At the eastern part of this profile (S.P. 137–150) two normal faults are defined below the area in which the large-scale deformations are exposed at the surface (see below).

<u>Profile 2</u> was measured in the middle of the Nahal Darga channel and, therefore, can be related to both channel walls. The western termination of this seismic line lies approximately at the eastern part of the western deformation zone. No overlap exists between these two because an cement in the road prevented installation of the geophysical equipment further to the west. Therefore, the faults of the western deformation zone could not be detected in this seismic profile. The subsurface bedding dips gently toward the east as expected of eastward draining delta. An overall subsurface positive flower structure, comprised of a major reverse fault associated with a cluster of minor normal faults and a gentle fold, is evident. The location of these subsurface faults is below the area of the large scale deformations and the deformed blocks in the northern wall. At S.P. 140 a normal fault is observed in the subsurface extending almost to the surface. This fault is located east of the eastern deformation zone and underneath the surface area in which the bedding and cross-bedding become steep. Development of steeply dipping cross sets is commonly associated with deposition in deep water and, therefore, the existence of deep-seated normal faults beneath these sets may suggest deepening of the basin near the coast due to down faulting. It should be mentioned that earlier studies (e.g., Neev and Emery, 1967) used the steep bathymetry of the delta (yes, all the area you were waling on were under water 45 years ago) as indicator of the location of the fault. At S.P. 65–80 and 0.06–0.1 s (TWT) a

concave unconformity, probably the trace of an old small channel is observed. This is similar to small erosional channels exposed today or to the surface slumps.

<u>Profile 3</u> is characterized by intensive normal faulting, which at S.P. 45–80 forms a flower structure pattern with a gentle fold between the secondary faults at S.P. 80, 0.1 s TWT. The main subsurface fault, at S.P. 50, overlaps the intensively faulted area of the western deformation zone along the northern channel wall. Actually, this subsurface fault is found along the continuation of a surface fault that exhibits the largest observed vertical displacement in this fan-delta. At the eastern part of the profile a large reverse fault (its upper part at S.P. 138, and lower at 157), which forms the western boundary of a gentle anticline (its hinge at S.P. 160 and 0.07 s TWT) is observed. This reverse fault is located just underneath the eastern deformation zone in the northern bank of the channel (Fig 5). A 25m wide, bowl shaped unconformity is observed at S.P. 170 and 0.1 s (TWT) representing either an old buried channel or another large scale deformation.

<u>Profile 4</u> was measured along the Dead Sea shoreline in 1996 and shows (a) flat bedding and a few normal faults its southern part (up to S.P. 70), (b) from S.P. 70–190 a pattern of a positive flower structure with many normal faults intensively deforming the strata and also a few reverse faults and folds, (c) S.P. 195–305 is characterized by continuous bedding gently dipping southeastward. At S.P. 255 and time 0.1 s (TWT) the strata are discontinuous and the bowl shape of the discontinuity is similar to the cross section of the exposed large scale deformations of the eastern deformation zone (e.g. Fig. 5) or an erosional channel. An unconformity, including stratigraphic reduction of the thickness between two markers is observed between S.P. 190–300 and time 0.1–0.12 s (TWT).

There is a general consistency between the structures around the intersection points of line 4 with lines 1, 2, and 3.

2. The Exposed Stratigraphy and Deformation

Fig. 5 shows the exposed stratigraphy in the southern and northern banks of the incised Nahal Darga as was documented in 1995-1996. It should be noted (a) the original mapping of the exposures was carried out in more details at sites needed for both paleoseismology and lake level fluctuations and delta sedimentology. (b) The current exposure is not were we documented over a decade ago: stream meandered and walls collapsed but what is more interesting incision deeper into section, provides additional information.

<u>Faults</u>

Most faults and visible displacements are associated with two deformation zones; only a few occur outside these two zones (Fig. 5- Northern Wall). The faults are normal, and striations on some of the fault planes suggest dip–slip displacements; on a few faults, a small component of left-lateral slip was observed. Dips of the faults cluster in two main trends, ESE and WNW (Fig. 6). The faults from the respective deformation zones differ mainly in vertical displacement, in our ability to identify a specific fault in both walls, and in evidence for multiple displacements.

The normal faults in the western zone (Figs. 7 and 8) reveal multiple events that intersect almost the entire exposed section. Vertical components of displacement along these faults range from a few centimeters to 2 m. Examination of individual faults and beds in Fig. 8 indicates progressively larger offsets of older units, which in turn indicate multiple displacements. Along some faults, three discrete displacements were observed, whereas along other faults only one or two events were identified. It is difficult to determine which of the displacements on one fault affected nearby faults. Please not that the most spectacular faults are west-block down faults with minor displacements whereas the largest vertical displacement is on less clear fault. The youngest deformation in this western zone we can detect, is revealed in the northern wall of Nahal Darga. Between meters 15 and 30 m (Fig. 5), faults reach the surface. The age of the last activity on these faults is <2225±50 yr B.P., which is the age of the youngest deposit stratigraphically beneath the youngest faulted units (Fig. 5, meter 250 and follow units into meter 30). This age of faulting is supported by the youngest possible age of the faulted beach gravel that underlies the surface at the fault line and gently climes west to ~370 m; the last time a lake level reached 370 m below sea level to deposit such gravel was before 4000 yr ago (Kadan, 1997; Ben-David Novak, 2004). The earlier displacements observed on these faults is 9600–7000 yr B.P. (not calibrated; see Enzel et al, 2000 for calibration of Darga ages).

The faults in the eastern deformation zone (meters 255–320, Fig. 5) are confined to three layers and most clearly appear in a sandy layer bearing ripple marks. The vertical displacements along these faults are small and do not exceed 10 cm; no evidence for multiple movements was identified. The age of this "faulting", according to dated displaced strata, is <2400 yr B.P. No field evidence directly connects these minor faults with other tectonic structures. However, they are spatially associated with what we termed "allochthonous tectonic slumps" (see Large-scale deformation section below) to avoid any clarity as we have ideas what are they but no solution-field discussions are welcomed). To examine the possibility that the exposed faults are expressions of shallow gravitational movement, we acquired the above four high-resolution seismic profiles (Kadan, 1997; Eyal et al., 2002). These profiles demonstrate that large deep-seated subsurface faults exist below the two relatively narrow deformation zones.

<u>*Deformed Beds and Paleoearthquakes*</u>

Another field discussion…

At least 11 horizontal beds revealing internal deformation were observed in the stratigraphic sequence. Table 2 in Enzel et al (2000) lists the stratigraphic units in which these beds are located, their estimated ages, and the detailed stratigraphy and the thickness of the deformed bed, and the morphology of the major deformation observed in the specific bed. Most beds are sandy and were deposited in a near-shore environment (Kadan, 1997) and you will see many exposures of them. A few beds contain more silt and/or clay and evidently were deposited in a less energetic setting (Kadan, 1997). Beds that contain silt and clay are deformed into 'convolute lamination' whereas the pure sand layers are deformed into 'ball and pillow' and "flame" and "dike" structures (Sims, 1975; Hempton and Dewey, 1983; Allen, 1984; Maltman, 1994). The "ball and pillow" structures occur commonly in the section. Generally the deformed beds have: (a) horizontal and sub-horizontal layering, (b) a thin cover of sediments with thickness ranging from a few centimeters to a maximum of 0.5 m, (c) random (but also some orientated) direction of the internal folds and other soft-sediment deformational structures, and (d) field relations indicating that the deformation occurred when the sediments were at the surface or very near the ground surface.

Most of the beds overlying these structures are deformed only at their lower contact, if at all, even if they are composed of similar or identical material. Some of the deformed beds can be traced for more than 100 m and are even recognized on both sides of the channel. Other deformed beds are truncated; these are only a few tens of meters long and are found only on one side of the channel. In some beds, the internal deformation disappears laterally as the layer thins and deformation reappears when the layer returns to its more characteristic thickness. This may imply (but not much data was collected) that there is a critical thickness at which a layer is affected by, and thus records, an earthquake. The vertical spacing of the deformed beds in the stratigraphic section is uneven. The proximity of these deformed layers may imply a

Large-Scale Deformations

The next section was written 10 years ago. Purposely I leave it unchanged.

In both walls of the channel, in the same stratigraphic position, there is an intensively deformed zone several meters thick (meters 260–320 in Fig. 2A and meters 280–350 in Fig. 2B). This zone is characterized by deformation of alluvial gravel, near-shore sands with ripple marks, and laminated lacustrine clays and silts with occasional aragonites. Each of these large scale deformations is composed of a zone of beds that are intensively deformed including vertical and overturned beds and folds. They exist at the same stratigraphic position in both walls, with no deformed beds above or below. When occasional floods erode the gravel that covers the floor of the 1996-7 channel, these large-scale deformations are also exposed in the stream bed between the two exposures at the walls. The slumps in these exposures are probably along a fault trending subparallel to the trace of the Jericho fault. Analysis of the high resolution seismic profiles (Eyal et al., 1997; 2002; see below) indicates that this elongated deformation is situated directly above a deeply seated flower structure that almost reaches the surface. We then were not sure about the origin of this large, stratigraphically well defined, linear zone of large-scale, soft-sediment deformation. We hypothesized that it is related to seismic activity along the Jericho fault located directly beneath it (Fig. 1). We suggested that if our hypothesis is correct, these slumps represent another style of deformation caused by a medium to large earthquake that affects fan-delta, perhaps saturated, deposits. Perhaps such slumping represents a larger earthquake than the earthquakes that caused liquefaction. The stratigraphy and radiocarbon ages help in narrowing the age range of this large deformation. The deformed beds within the slumps are bounded at their base by a bed dated at 2400 yr B.P. A piece of wood from the undulating plane that marks the base of the slump has an age of 2115±50 yr B.P. Two radiocarbon ages posdating the deformation are 1440±110 and 1315±90 yr B.P. Stratigraphically, the deformation is also older than 1500 yr B.P., which is the age of the unconformity that truncates sediments that were deposited above the deformed material (Kadan, 1997). Therefore, the slump occurred sometime between 2400 and 1500 yr B.P., and probably after 2100 yr B.P.

Figure 9 shows the two situations; at the lower photograph you can see the 1999 first exposure of the large-scale deformation in the channel. Last year after incision but also stream self cleaning a new exposure shows that as the geophysics suggested and many hand dug holes did not, under the eastern deformation zone there is a fault and all the deformations on top of it could have been soft deformation responses to tectonic activity below. Some suggest that these deformations are sinkholes. We agree that two or three of them (will be shown in the field) resemble sinkholes but most not. These deformations have pushed up depositional units.

References

Allen, J. R. L. (1984). Sedimentary structures, their character and physical basis. *In* "Developments in Sedimentology **30**," Vol. II, Elsevier, Amsterdam.

Bartov, Y., Bookman, R., and Enzel, Y., (2006). Current depositional environments at the Dead Sea margins as indicators of its past levels. In: Enzel, Y. Agnon, and M. Stein, (eds.)., New Frontiers in Dead Sea Paleoenvironmental Research. Geological Society of America Special Paper 401, p. 127-140.

Ben David-Novak, H., Morin, E., and Enzel, Y., (2004). Modern extreme storms and the rainfall thresholds for initiating debris flows on the hyperarid western escarpment of the Dead Sea, Israel. Geological Society of America Bulletin. v. 116 (5-6): 718-728

Bowman, D. (1974). "River Terraces in the Dead Sea Area—Morphological Aspects." Unpublished Ph.D. dissertation, Hebrew University of Jerusalem (in Hebrew with English Abstract).

Dunne, L. E., and Hempton, M. R. (1984). Deltaic sedimentation in the Lake Hazar pull-apart basin, sout-eastern Turkey. *Sedimentology* **31**, 401–412.

Enzel, Y., Kadan, G., and Eyal, Y. (2000). Holocene Earthquakes in the Dead Sea Graben from a Fan-Delta Sequence, Quaternary Research, 53, 34–48,.

Eyal, Y., Bruner, I., Kadan, G., Enzel, Y., and Landa, E. (1997). "Association of Surface and Subsurface Tectonic Structures at the Holocene Fan-Delta of Nahal Darga, Dead Sea Israel." Holon, Israel. The Geophysical Institute of Israel Report No. 704/150/96.

Eyal, Y., Brunner, I., Kadan, G., Enzel, Y., and Landa, E. (2002). High-resolution seismic study of the Nahal Darga fan-delta, Dead Sea, Israel, with the aim to relate the surface and subsurface tectonic structures. European Geophysical Union Stephan Mueller Special Publication Series, 2, p. 21-33.

Kadan, G. (1997). Evidence for Dead Sea Lake-Level Fluctuations and Recent Tectonism from the Holocene Fan-Delta of Nahal Darga, Israel, Unpublished M.Sc. thesis, Ben Gurion University of the Negev (in Hebrew with English Abstract).

Maltman, A. (1994). "The Geological Deformation of Sediments." Chapman & Hall, London/New York.

Manspeizer, W. (1985). The Dead Sea Rift: Impact of climate and tectonism on Pleistocene and Holocene sediments. *In* "Strike-Slip Deformation, Basin Formation and Sedimentation" (K. T. Biddle and N. Christie-Black, Eds.). *Society for Economic Paleontology and Mineralogy Special Publication* **37**, 143–158.

Neev, D., and Emery, K. O. (1967). The Dead Sea, depositional processes and environments of evaporites. *Geological Survey of Israel Bulletin* **41**.

Niemi, T., and Ben Avraham, Z. 1994. Evidence for Jericho earthquakes from slumped sediments of the Jordan river delta in the Dead Sea. Geology, v.22, 395-398

Shapira, A., Avni, R., and Nur, A. (1993). A new estimate for the epicenter of the Jericho earthquake of 11 July 1927. *Israel Journal of Earth Sciences* **42**, 93–96

Sims, J. D. (1975). Determining earthquake recurrence intervals from deformational sructures in young lacustrine sediments. *Tectonophysics* **29**, 141–152.

Sneh, A. (1979). Late Pleistocene fan deltas along the Dead Sea rift. *Journal of Sedimentary Petrology* **49**, 541–552.

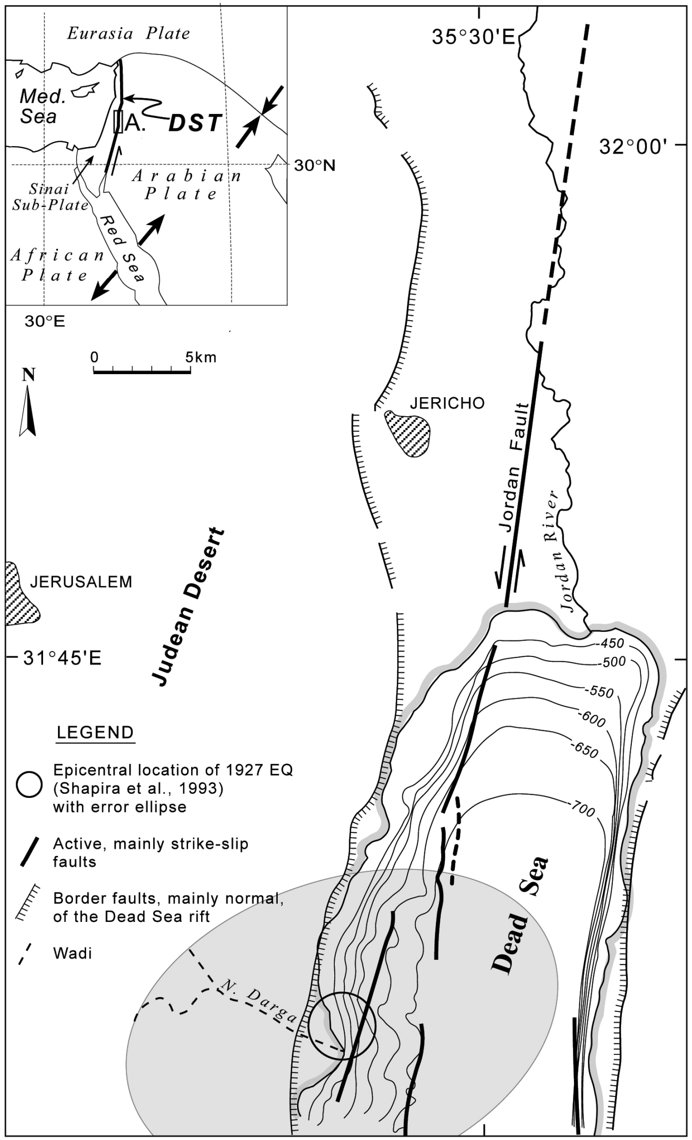

Figure 1: General location map and the general tectonic setting of the northern part of the Dead Sea (after Niemi and Ben-Avraham, 1994). The epicenter location of the Jericho 1927 earthquake (Shapira et al., 1993) is about 2 km northeastward of the Nahal Darga fan-delta. The contour lines are the bathymetric contours of the Dead Sea.

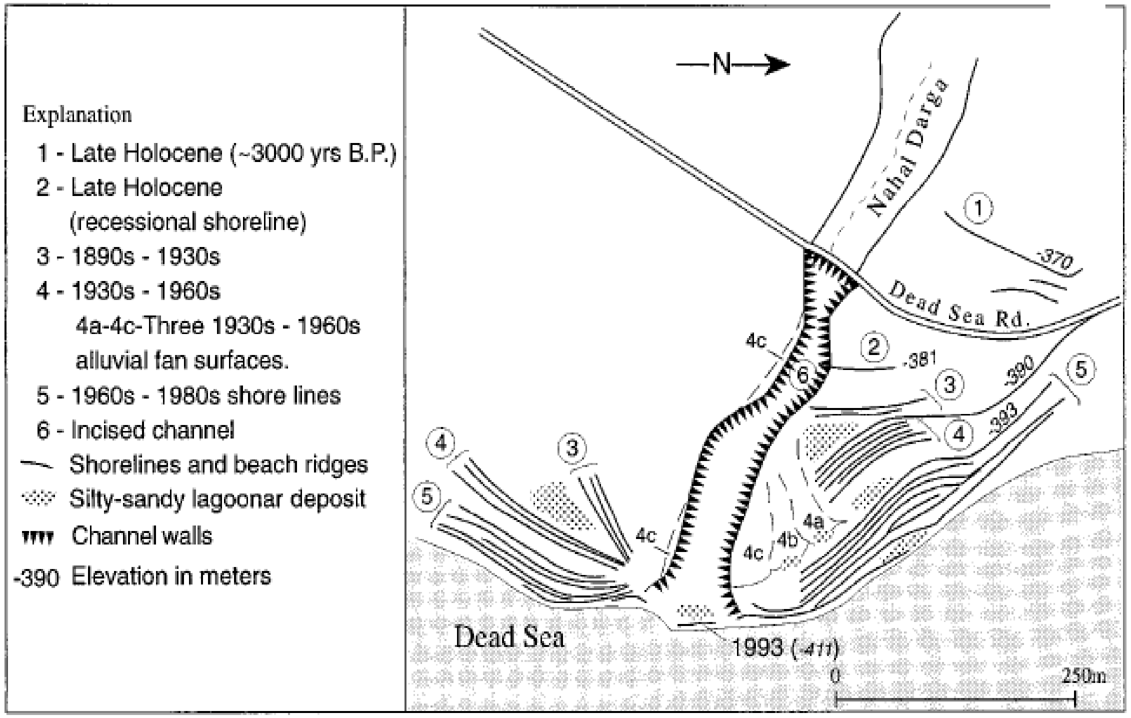

Figure 2: Shorelines of the Dead Sea on late Holocene fan-delta surfaces of Nahal Darga. (from Enzel et al., 2000).

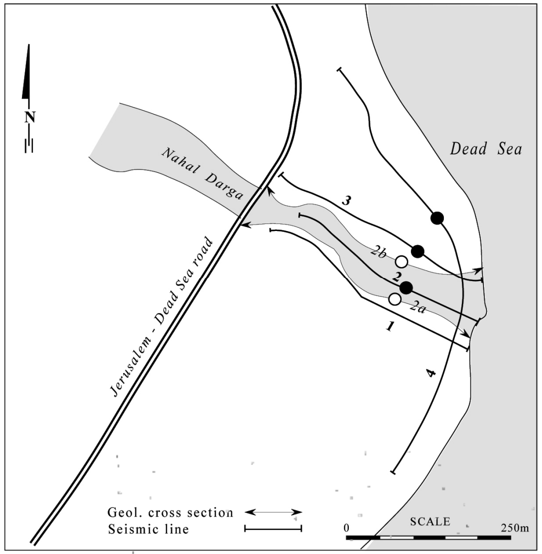

Figure 3: The outline of the seismic profiles lines 1 to 4 . 2a and 2b are the southern and the northern geologic cross section exposed along the channel walls. The open circles mark the center of the location of the exposed heavily deformed sediments (in 1997). The solid circles on the seismic profiles represent the first appearance, from west, of the large subsurface reverse faults and flower structures, probably representing the western boundary of the eastern deformation zone (S.P. 100, 140 and 190 in profiles 2, and 3, and 4, respectively).

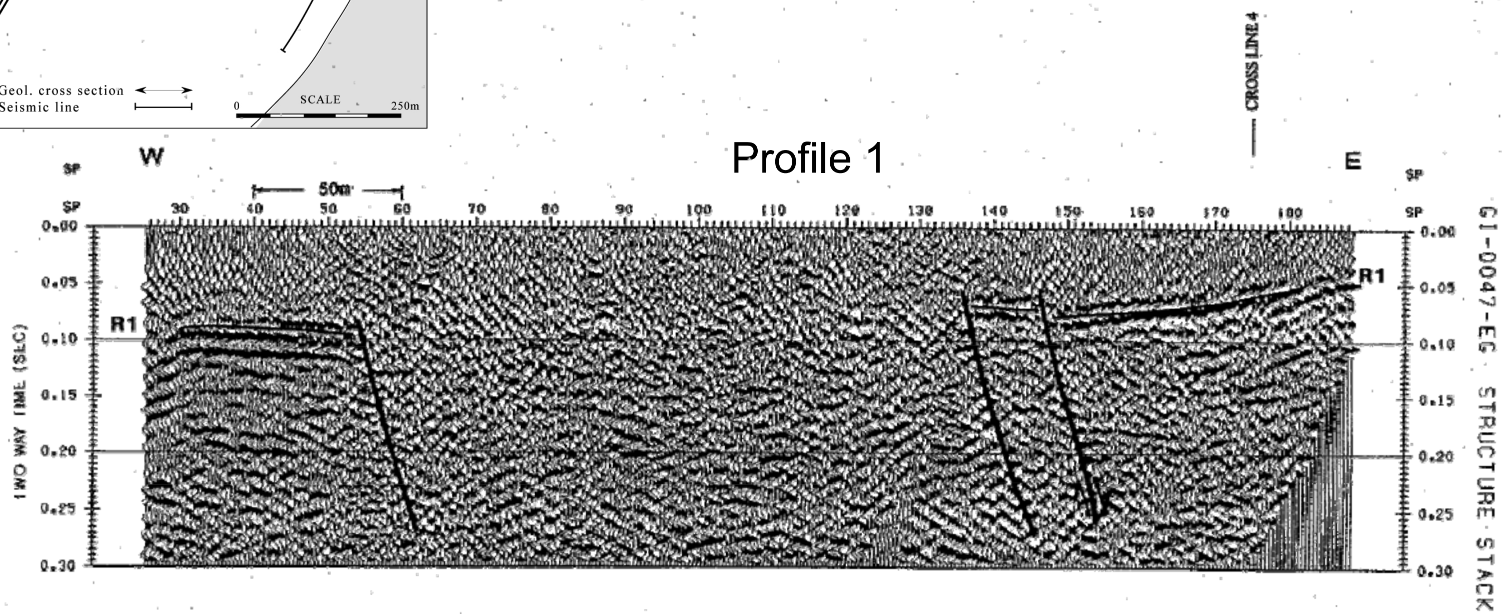

Figure 4: Interpreted multichannel high-resolution seismic profiles from the Nahal Darga fan-delta. The locations of these profiles are shown in Fig. 3. The interpreted seismic markers do not have any stratigraphic correlation. The exact determination of fault location within the profile is also based on diffraction waves. The time is given in seconds by Two Way Time (TWT). The vertical lines above the seismic profiles in each of the profiles relate to the crossing location of seismic profiles. For example, the vertical line at the eastern part of profile 1 is the location where profile 4 crosses profile 1. The three vertical lines above profile 4 are the locations where, from left to right, profiles 3, 2 and 1 cross profile 1 respectively.

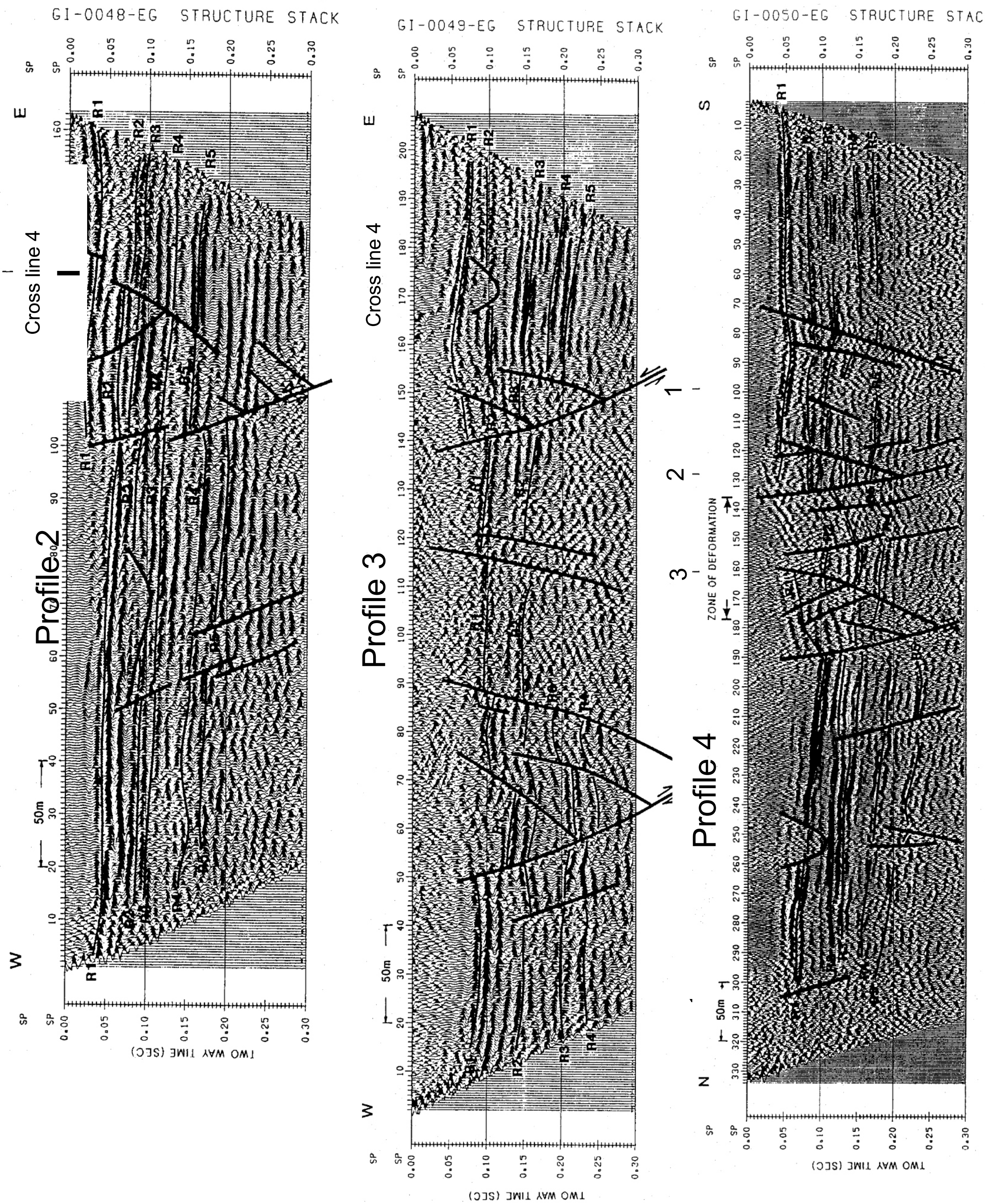

Figure 5: figure caption next page

Figure 5:
The stratigraphy of the southern wall and the northern wall of the incised channel (Fig. 1) of Nahal Darga in 1996. No vertical exaggeration. The scale at the base of each section is in meters along the base of the section and therefore it somewat longer from the shortest distance from highway to shore. The left end of each of the five sections is connected to the right end of the section below. Numbers in circles are easily identified field stratigraphic units; each may contain a few to many beds and more than one lithology. The main lithology is marked. See Table 1 in Enzel et al.(2000) for details and calibration of these ^{14}C BP ages. Lithologies: 1, fluvial gravel; 2, near-shore sand with frequent ripple marks; 3, well-bedded to laminated clay silt with occasional aragonite; 4, well-to medium sorted coarse sand, pebbles and cobbles in sets of the delta front; 5, well-sorted prograding beach deposits with lenses of clay–silt lagoonal deposits; 6, the major unconformity in the section; its age is roughly estimated at approximately 4000 yr B.P. (Kadan, 1997).

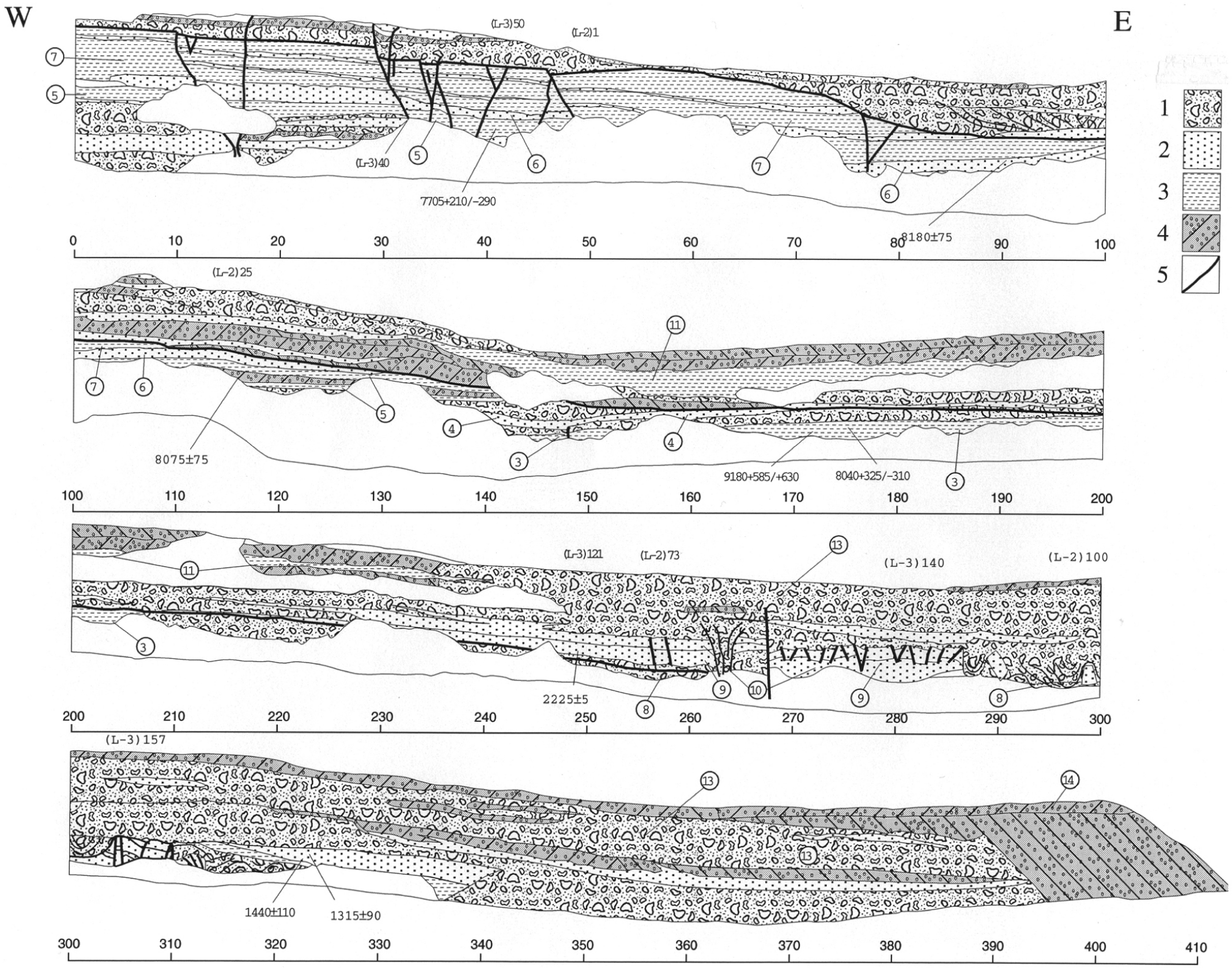

Figure 5: Southern wall in 1996

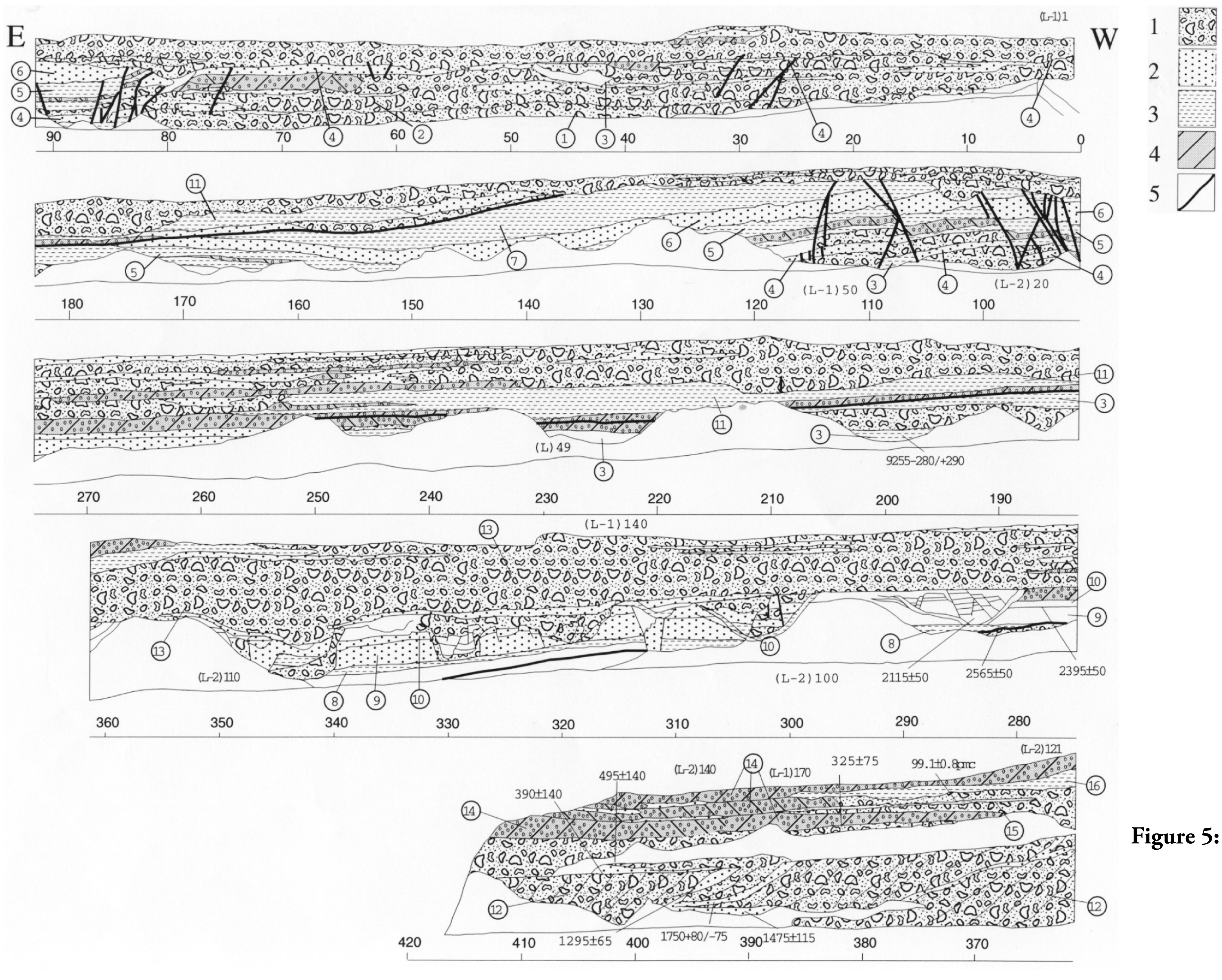

Figure 5: Northern wall

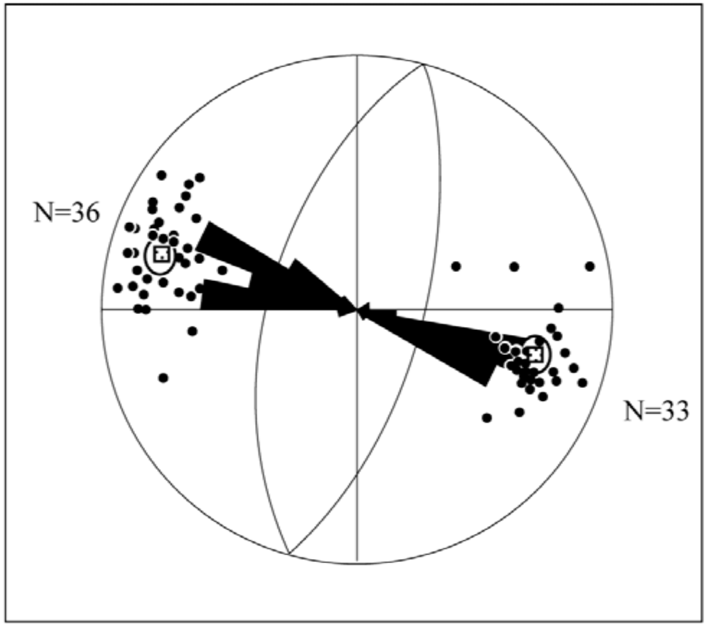

Figure 6: Stereographic projection, lower hemisphere, of 99 poles (dots) to fault planes from Nahal Darga. The great circles are the mean fault planes of the two groups of faults striking NNE-SSW with dips to WNW and ESE. The small circles outline the 95 range.

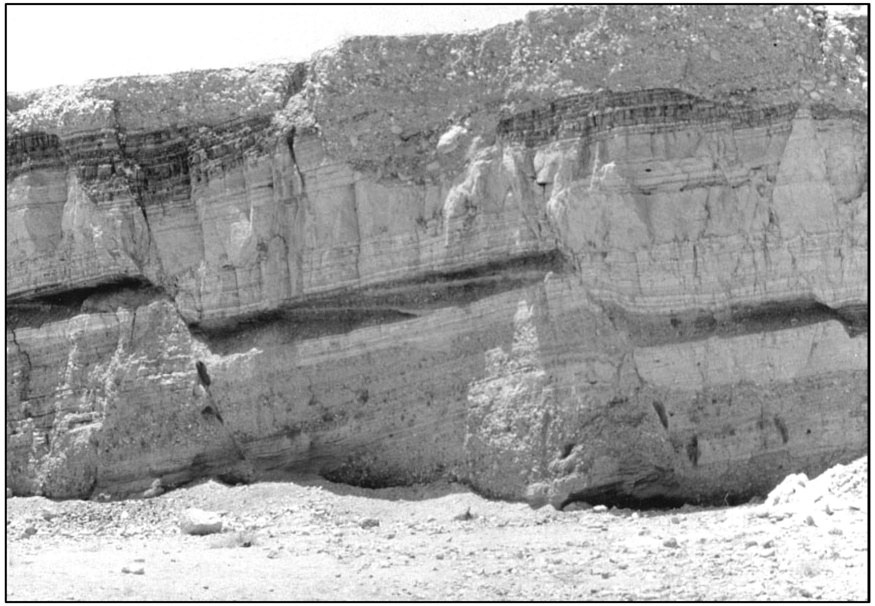

Figure 7: A photograph showing faults A and B of Figure 8 exposed at the southern wall. See Figure 4 for scale and explanations. Note the tilted lacustrine and fluvial deposits with well-pronounced prograding beach ridge deposits in the middle of the section. The erosional channel parallels the faults and was filled with coarse sandy gravel of unknown age and was truncated and covered again by a very thin (0.5 m) 1960s alluvial-fan deposits.

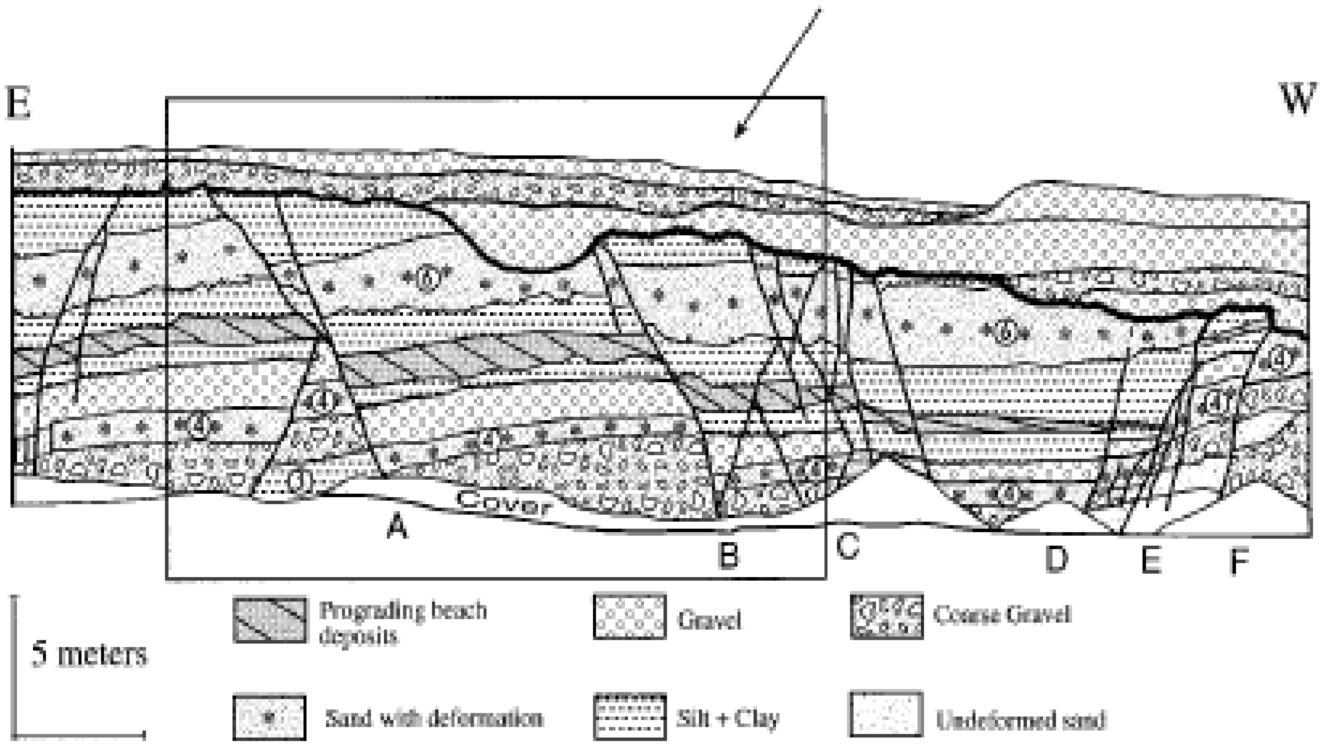

Figure 8: Detailed map of the western faulted zone at the southern wall of Nahal Darga. They were probably experienced three distinct displacements. Total vertical displacement of unit 4 on faults D–F is approximately 4.5 m. When displacement is measured from the two ends of the figure and unit thickness changes are accounted for, the total displacement is 3.5 m. The prograding beach deposits are displaced approximately 3.5 m by faults D–F but with lower total displacement in the entire zone. The units underneath the erosional unconformity (marked as a dark solid line) are 7000 yr B.P. Most of these units grade into sand a few tens of meters to the east. The age of the erosional channel and its associated deposits directly above the unconformity is not clear. The age of the unconformity itself is probably 4000 yr B.P. (Kadan, 1997). The top gravel unit is a historical alluvial-fan, which was active since the early 1900s but here we think it is of the late 1960s. Only minor fractures without any observed displacement cross the unconformity; none reach the surface.

When in the field and visit this exposure, it is time to turn around and watch the northern wall.

Figure 9:

November 2007 photograph during documentation of the exposed fault and deformations following 4+ meters of incision of channel bed

Photograph in 1998

Large scale deformation exposed in channel bed after a flood, in-between the deformation in the two walls

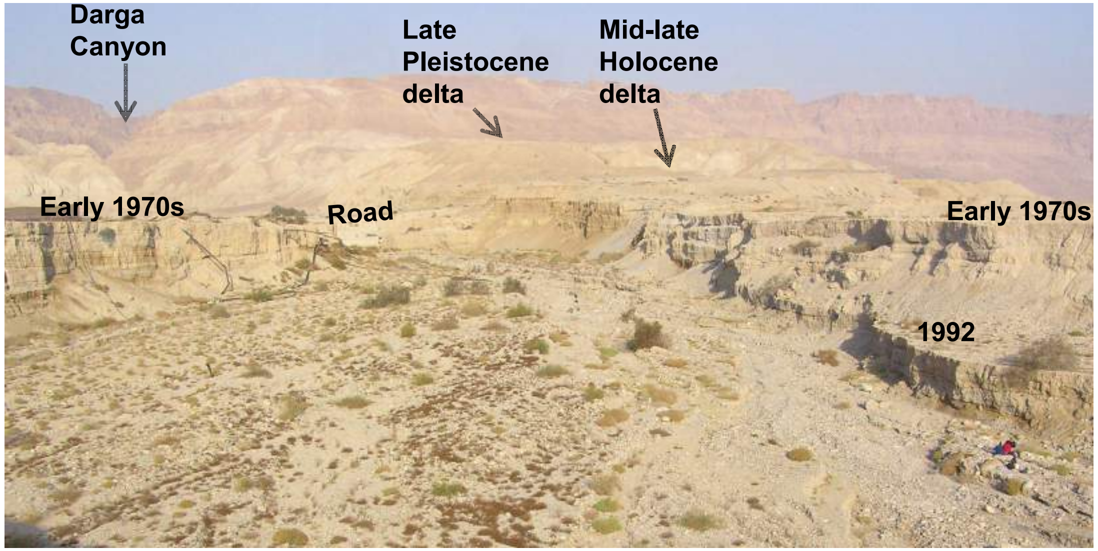

Figure 10A: Nahal Darga, view to the west\upstream in 2007. Note the deep incision since the late 1960s and the early 1970s. The channel is maintained in because of the artificial cement knickpoint at the road (see Ben Moshe et al., 2008, *Geomorphology*). During our Mid-1990s work the channel bed was at about the level of the 1992 terrace.

Figure 10B : Nahal Darga, view to the west\upstream in 2007. The students stand next to a new exposure.

Collapse-sinkholes near Mineral Beach - Do sinkhole clusters reveal active faults buried within the sediments of the Dead Sea basin?

Meir Abelson[1*], Gidon Baer[1], Yoseph Yechieli[1], Eyal Shalev[1], Vladimir Shtivelman[2]

[1]Geological Survey of Israel

[2]Geophysical Institute of Israel

meira@gsi.gov.il

* Field guide

Since the early 1980s, more than 2000 sinkholes have developed along the western coast of the Dead Sea (DS). All sinkholes are concentrated within a narrow strip with a width of tens meters to <1 km (Figs. 1-2). More than 75% of the sinkholes occurred in the last decade, in a rate of 150-300 sinkholes per year (Fig. 3). This highly dynamic phenomenon occurs due to dissolution of a salt layer buried between 20 – 70 m (depth to layer top), which in turn forms cavities causing the collapse of the overlying sediments (Fig. 4). The whole process is triggered by the rapid decline of the DS level and by eastward migration of its coastline. The eastward migration of the DS coastline is accompanied by the eastward migration of groundwater brine and intrusion of groundwater undersaturated with respect to halite. The undersaturated groundwater dissolves the salt layer, hence forming the underground cavities (Yechieli et al., 2006; Shalev et al., 2006).

Sinkhole lineaments along cryptic, likely active, young faults

The sinkholes around the DS cluster in more than 40 sites, where each site includes from 1 to more than 100 sinkholes. Almost all sinkhole clusters display a clear linear shape. Comparison between the trends of the sinkhole lineaments, the exposed faults, and the zigzagging rift wall segments shows a striking similarity (Fig. 5a and 5b). All features show a predominantly bimodal distribution with NE and NW principal directions (Fig. 5b). No relationships are found between sinkhole lineaments and other surface features such as ancient or current DS shorelines, or alluvial fans. These observations suggest that sinkhole formation is controlled by faults concealed within the rift fill.

To confirm this linkage between buried faults and sinkhole lines we conducted 10 profiles of seismic reflection across and along sinkhole lines in six different sites (Figs. 5-6). In the examined sites the sinkhole lineaments were found to overlie prominent discontinuities. For instance, profiles across the sinkhole lines in the Neve Zohar and Hever-south sites (Fig. 1) display clear discontinuities interrupting the reflectors beneath the sinkhole lines (Figs. 5c,d and 6) that offset young sediments several thousands of years old. In the Hever-south site layers shallower than 20 m are offset beneath the sinkhole line (Fig. 5d). ^{14}C dating of the salt layer at depth of 27 m (sampled from a borehole in this site) indicates 10 kyr (Fig. 5d), suggesting that the offset layers are younger than 7500 years. This implies that the faults are young and likely active, but bear no surface manifestation other than the sinkhole lineaments.

Radar interferometry, land subsidence, and young faults

Subtle land subsidence along the DS coast was recently detected by InSAR [*Baer et al.*, 2002]. Sixteen SAR scenes obtained by the European Remote Sensing satellites ERS-1 and ERS-2 during 1992 to 1999 were analyzed, spanning periods of 2 to 71 months. Gradual subsidence features, a few hundred meters to a few kilometers long, with subsidence rates of 0-20 mm/yr, were found in association with most sinkhole sites. This subsidence was attributed to the consolidation of the clayey (and/or silt) layers within the alluvial fill due to the drop in level of the DS and the associated drop of groundwater level [*Baer et al.*, 2002].

Sinkhole lines occur either within the subsiding areas, or along the boundaries of these areas (Fig. 7). For example, in the En-Gedi south area, a sinkhole line oriented 062° (Fig. 7) is located within the subsiding area sub-parallel to its straight northwestern boundary; the southwestward continuation of the sinkhole line coincides with another straight boundary further to the west (Fig. 7). This configuration is interpreted as two sub-parallel ENE trending faults, suggesting that both sinkhole lines and linear boundaries of the subsiding area reflect buried faults.

Role of faults and land subsidence in the formation of the DS sinkholes

The appearance of the fault-related sinkholes, combined with the linear boundaries of subsiding areas observed by InSAR, complement our view of the tectonic structure buried in the alluvial fill. In the En-Gedi area, for example, the InSAR and sinkhole lineaments suggest two sets of faults (Fig. 7). The strikes of one set are between 347°-360°, in agreement with the common direction of the rift-margin faults. This is also the most common trend of the sinkhole lines in the entire area. A zigzag pattern is formed by an additional, secondary group of lines oriented ~60°.

Considering all the observations mentioned above, we suggest a mechanism that combines gradual land subsidence with the formation of the DS sinkholes (Fig. 8). The trigger for both phenomena is the drop in the DS level and of the surrounding groundwater levels. This drop decreases the pore pressure in the aquifer system and increases the effective stresses in the rock column [*Terzaghi*, 1925; *Galloway et al.*, 1998; *Amelung et al.*, 1999]. Consequently, areas of higher clay content are differentially compacted [*Baer et al.*, 2002]. The decline of the DS level also leads to eastward migration of the saline-fresh water interface, bringing water under-saturated with respect to halite towards the buried salt layer, causing salt dissolution and formation of cavities. This notion is strongly supported by the finding of undersaturated water below and above the salt layer in boreholes near the sinkhole site of En-Gedi plantations (see Fig. 1 for location). Several-meter-thick aquiclude layers above and below the salt layer (as indicated in several boreholes [*Yechieli et al.*, 2006; *Abelson et al.*, 2006], Fig. 2d) may restrict access of the sub-saturated water to the salt layer. However, differential compaction could generate and localize shear strain within the clayey layers along or parallel to pre-existing faults. These faults may then serve as conduits for the sub-saturated water to percolate to the salt layer (Fig. 8b) and promote the development of sinkholes (Abelson et al., 2003). The ascent of sub-saturated water is possible due to overpressure in the confined aquifers below the salt and clayey layers, which was found to be higher than the upper phreatic aquifer in the boreholes along the DS coast (*Yechieli et al.*, 2006). We therefore propose that sinkhole distribution and gradual land subsidence features are controlled by, and reflect the young and possibly active faults concealed within the fill of the DS basin. It appears that sinkhole lines and subsidence features can serve as a useful tool for mapping active faults in this seismically active region. We speculate that a strong earthquake may open these faults through the aquiclude layers which in turn may promote flow of undersaturated groundwater towards the salt layer, hence catalyzing sinkholes formation.

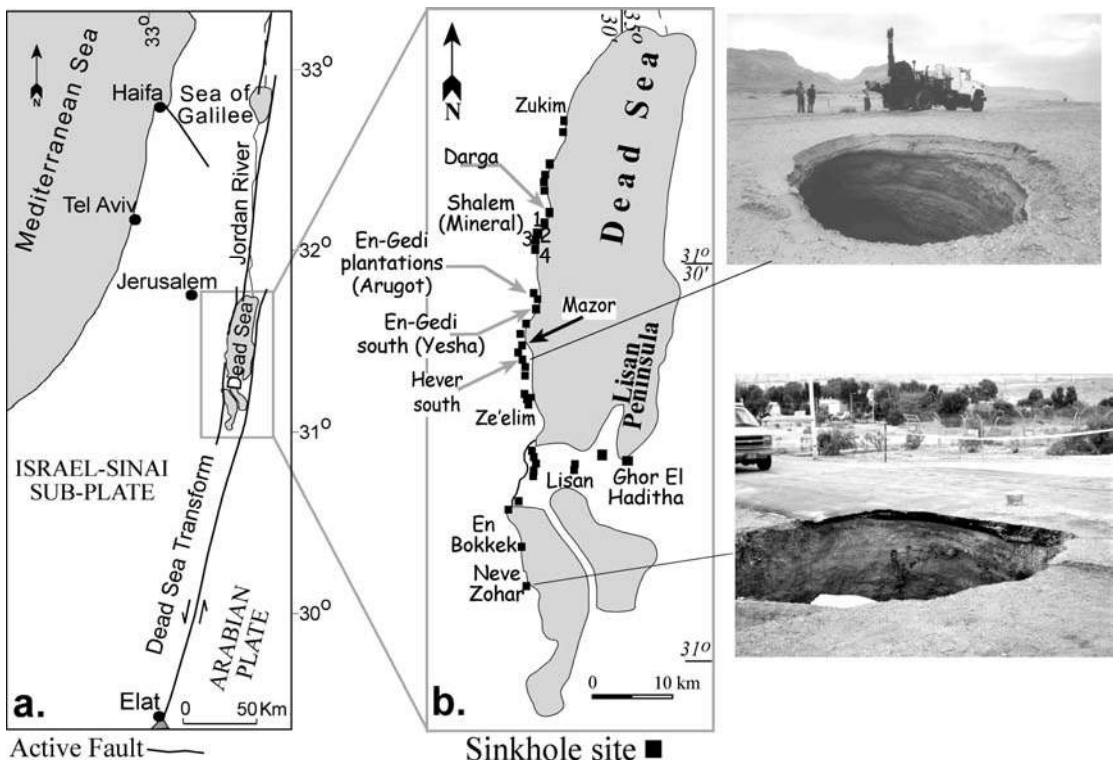

Figure 1: (a) Location map showing the Dead Sea pull-apart basin along the Dead Sea Transform. (b) Distribution of sinkhole sites along the Dead Sea coast and two examples of sinkholes.

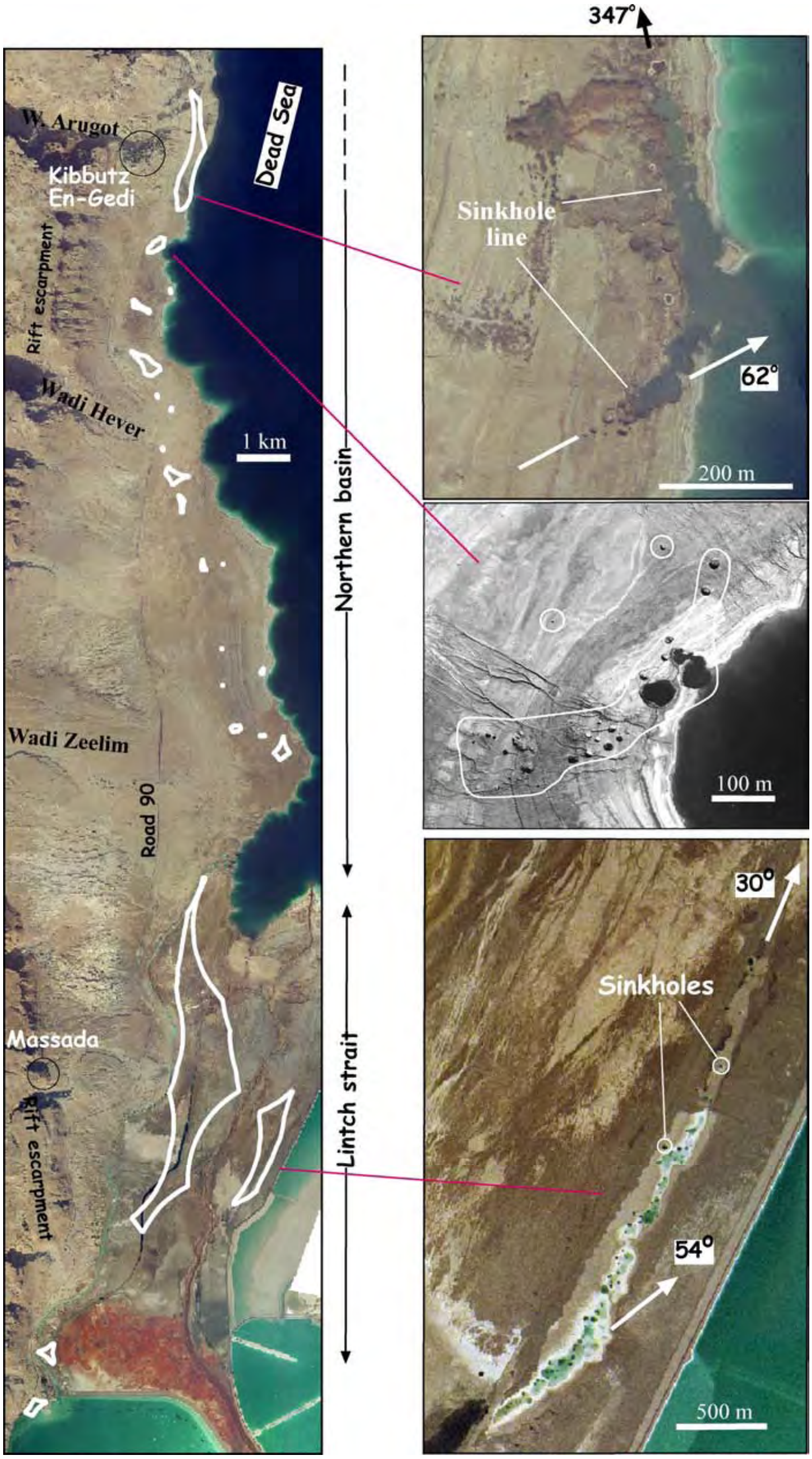

Figure 2. Rectified aerial photograph along the Dead Sea coast (a) between Lynch Strait and En-Gedi (see Fig. 1 for location) (Yechieli et al., 2006). White polygons denote sinkhole sites. Road 90 is the main road running through the Dead Sea rift valley. The figure displays the widest part, ~1 km, of the strip where more than 2000 sinkholes have developed since the early 1980s. Three aerial photographs show a closer view of three sinkhole sites (b-d). Note the preferred orientation of sinkhole clusters which follow concealed tectonic lineaments.

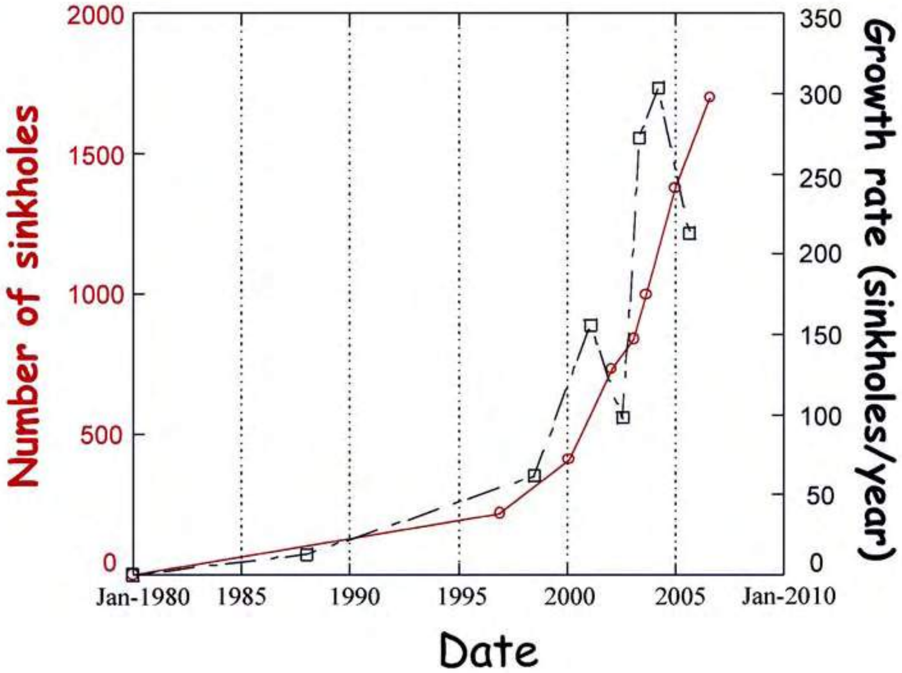

Figure 3: Rate of sinkholes growth since the early 1980s. Number of sinkholes (red) and growth rate (black) are presented versus the calendar year (Abelson et al., 2006).

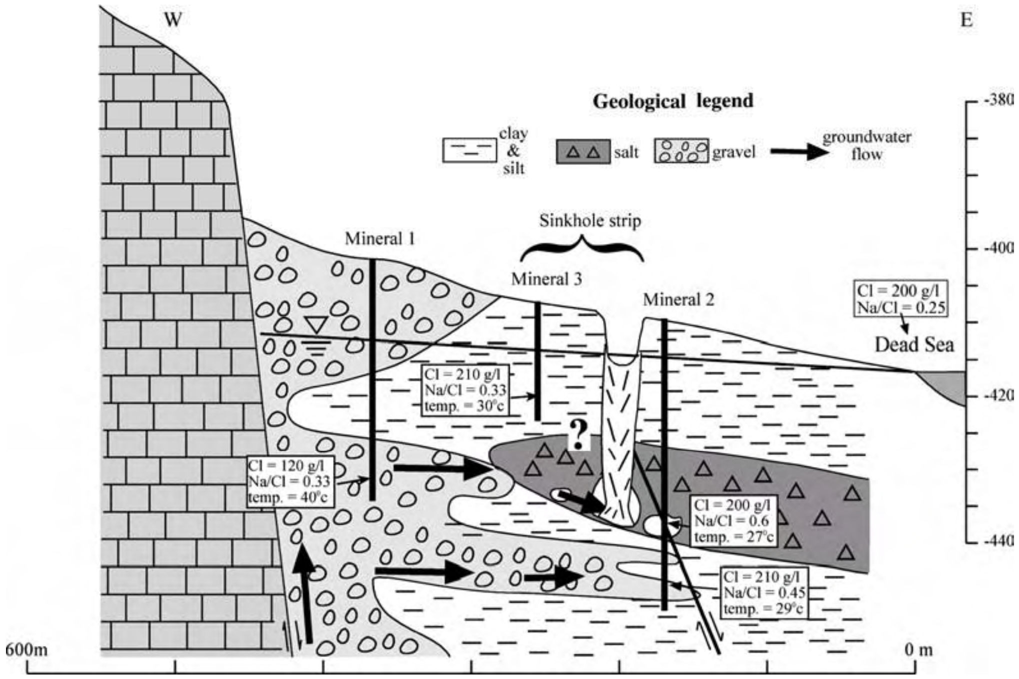

Figure 4: A hydrogeological schematic section across the elongated swarm of sinkholes in the Shalem-2 site (see Fig. 1 for location) (after Yechieli et al., 2006). The Mineral-2 borehole penetrated a cavity in the salt layer with water that exhibits a clear signal of salt dissolution (Na/Cl=0.6). Much less saline water (Cl=120 g/l, unsaturated with respect to halite) and also lower Na/Cl values (0.33) was found in the nearby Mineral-1 borehole. The sinkholes which develop along a lineament are found close to the western margin of the salt layer distribution.

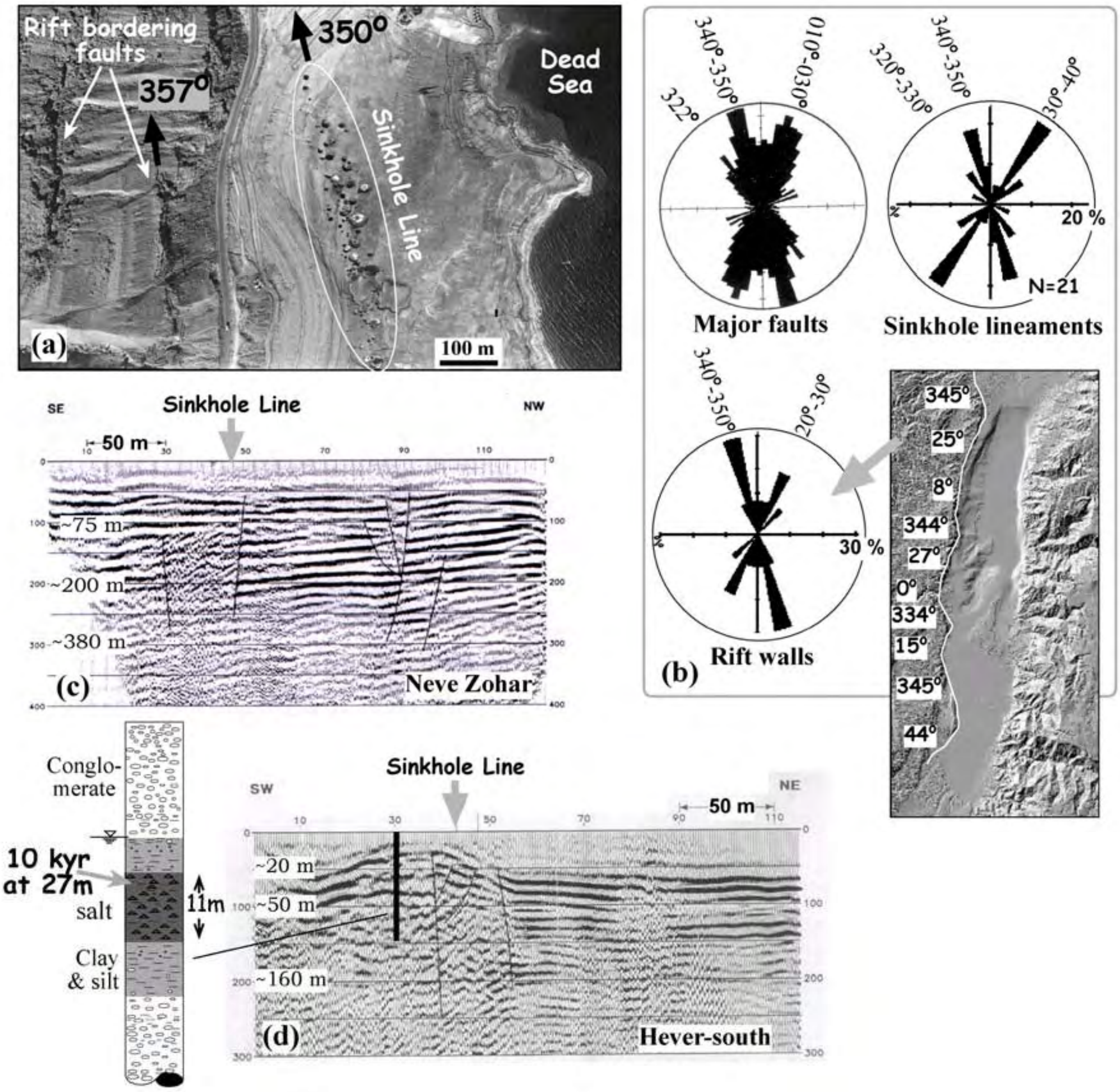

Figure 5: Sinkhole lineaments and buried faults (after Abelson et al., 2003). (a) A rectified air photograph from 1999 showing the sinkhole site of Hamme Shalem (Fig. 1). The sinkholes are aligned sub-parallel to the local rift-margin faults. (b) Area weighted, rose-diagrams of strikes of major faults on the western margin of the DS rift [*Sagy et al.*, 2002] (cumulative length 322 km), sinkhole lines, and strikes of the western rift wall segments displayed on a digital shaded-relief map [*Hall*, 1994]. Note the similar bimodal distribution of the various populations, implying a tectonic control on the sinkhole lines. (c) and (d) Seismic reflection profiles across the Neve Zohar and Hever-south sites (see Fig. 1 for location) showing prominent discontinuities beneath the sinkhole lines. In Neve Zohar (c), a sequence of disturbed layers is bounded by the two discontinuities interpreted as faults. The northwesterly discontinuity is beneath the sinkhole line. A seismic reflection profile parallel to the sinkhole line at this site shows no discontinuity, suggesting that the buried discontinuities/faults are parallel to the sinkhole line. A summary of borehole findings (80 m deep) from Hever-south site is presented in (d); ^{14}C dating from a 27m-deep clay horizon within the salt layer indicates age of 10,000 years, suggesting that the observed offsets shallower than 20 m are younger than 7500 years.

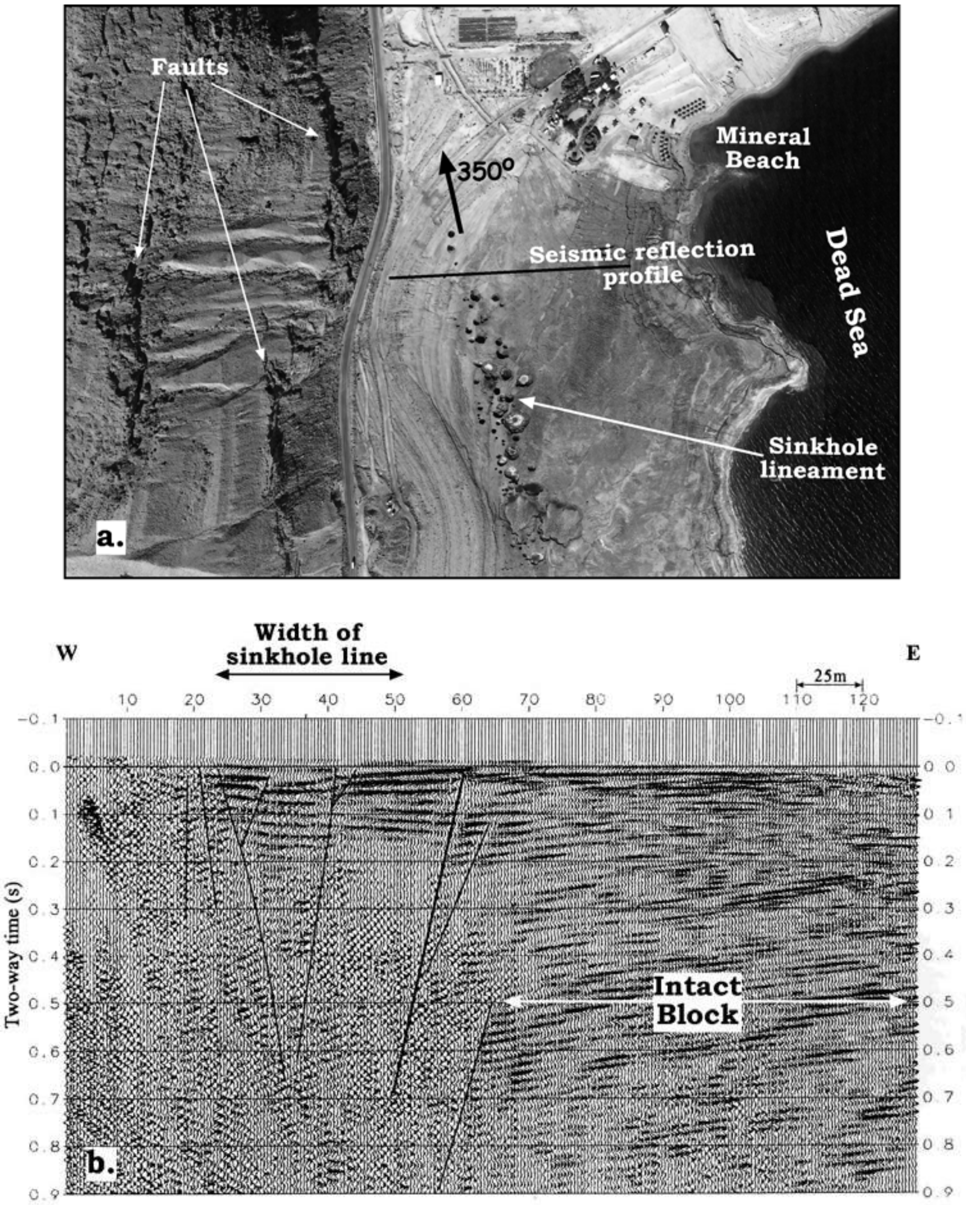

Figure 6: Sinkhole lineament and buried faults at the sinkhole site near Mineral beach (after Abelson et al., 2006). (a) A rectified air photograph from 2001 showing one of the sinkhole sites – Shalem site (Fig. 1 for location). The sinkholes are aligned sub-parallel to the local rift-margin faults. (b) Seismic reflection profile across the sinkhole line (profile location is marked in (a)) showing prominent discontinuities beneath the sinkhole lineament interpreted as faults, and intact structure of reflectors away from the sinkhole lineament.

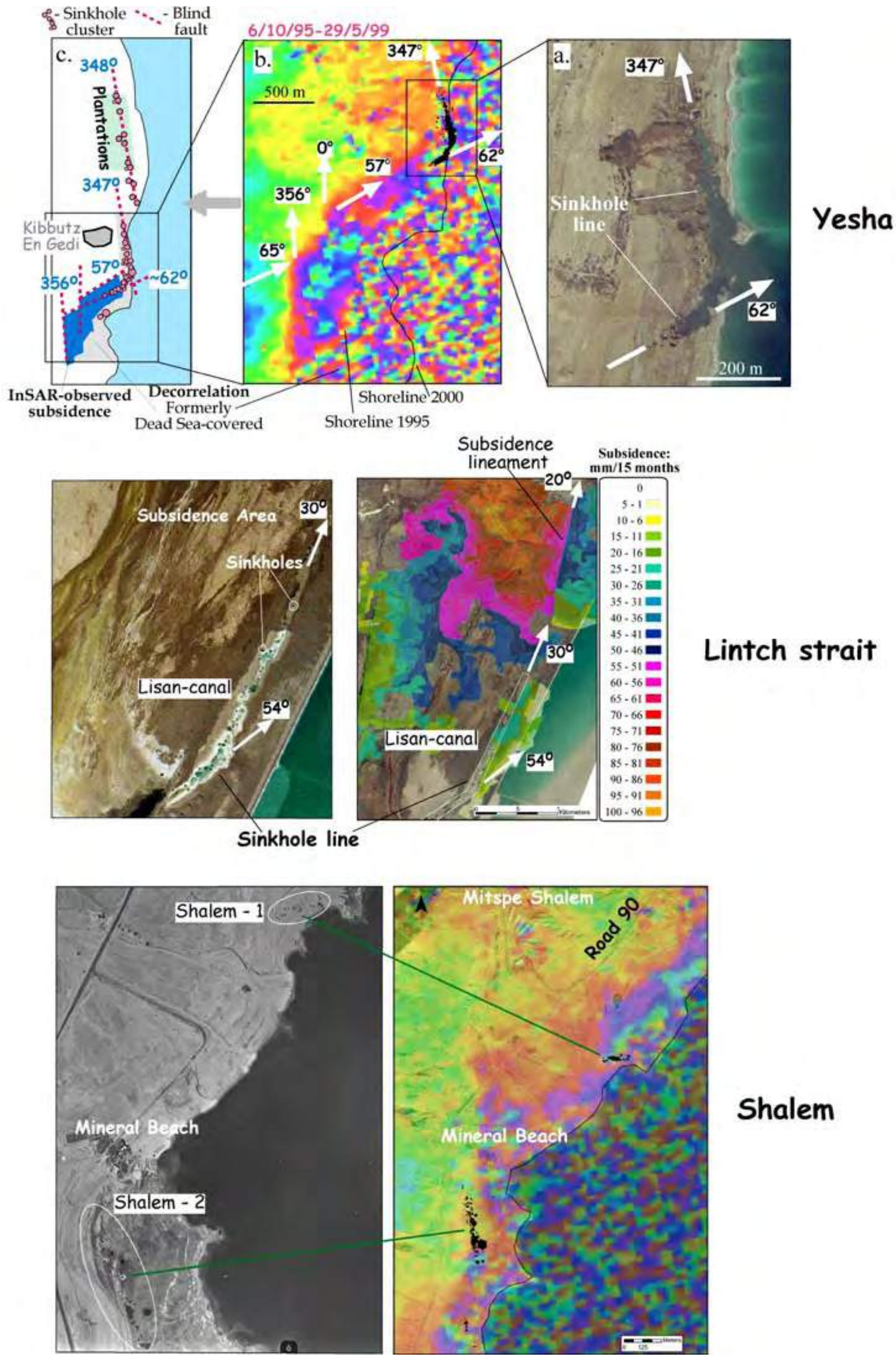

Figure 7: The buried tectonic fabric as revealed by sinkhole lines and InSAR-detected gradual subsidence in three various sinkhole sites (after Yechieli et al., 2004). *Upper panel*: (a) A rectified aerial photo showing a sinkhole site with two main linear segments. (b) A rectified interferogram displaying a subsiding area with straight boundaries suspected to be faults. The color fringe pattern in the interferogram reflects ground subsidence, where one fringe cycle represents ~31 mm of vertical displacement [*Baer et al.*, 2002]. (c) A schematic sketch showing our interpretation of the concealed tectonic fabric as inferred by the sinkhole lines and InSAR. Note that the straight borders of the subsidence area are sub-parallel to the sinkhole lines, and the N62°E striking sinkhole line is at the continuation of the step-shaped border of the subsiding area. This geometry is observed in all pairs of interferograms of this area (see Fig. 6 of *Baer et al.* [2002]). *Middle panel*: A sharp lineament partitions two areas of different subsidence rate calculated from the InSAR (right). This lineament is at the continuation and the same orientation of a 2 km long sinkhole-lineament. Both lineaments are probably surface expression of hidden faults. *Lower panel*: Parallelism between two sinkhole lineaments near Mineral beach and linear boundaries of a subsiding area.

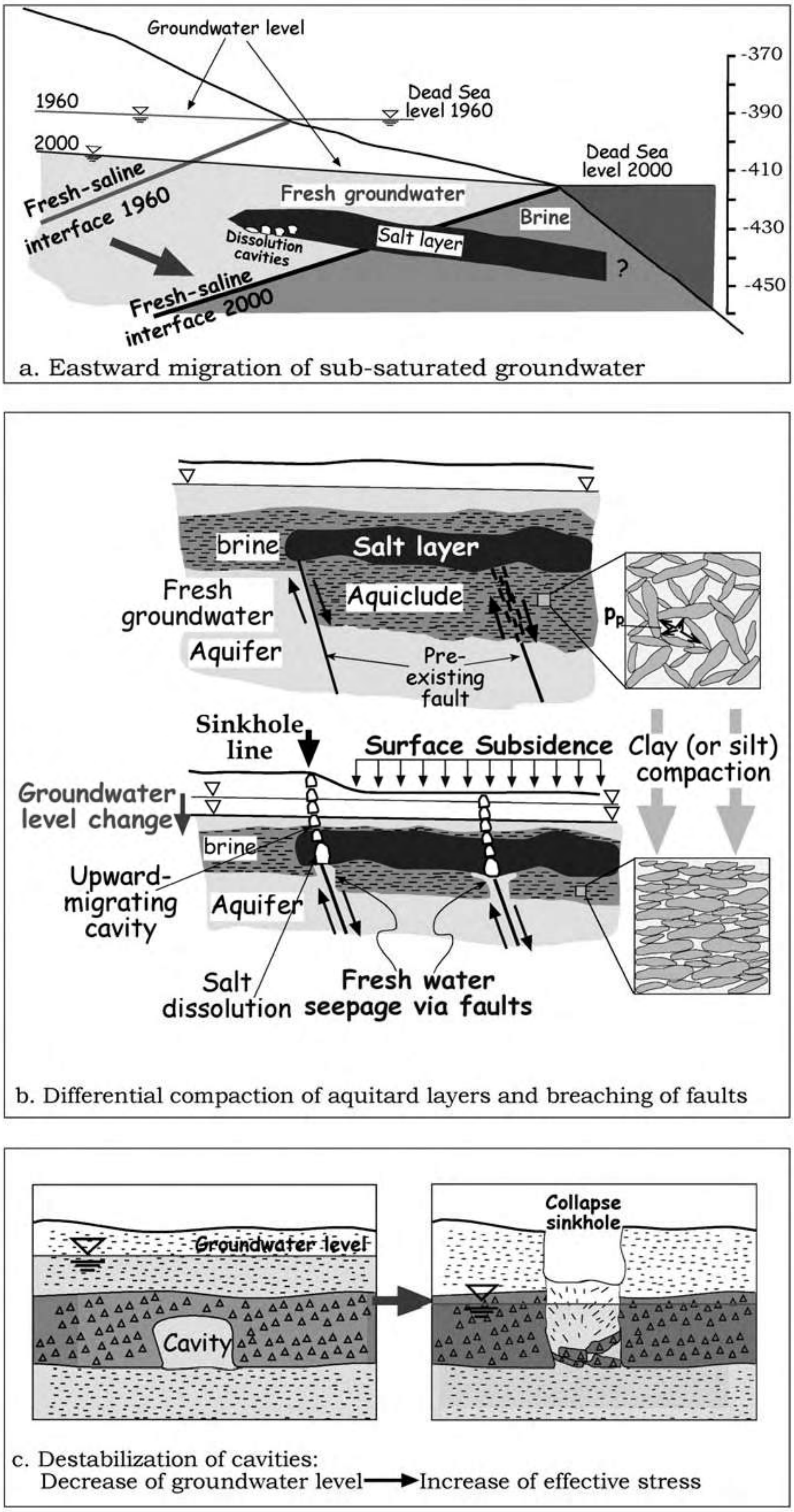

Figure 8: The triple effect of the decline of the Dead Sea level (After Abelson et al., 2006). Effects (a) and (b) cause cavity formation, while (c) is a catalyst for cavity collapse.

Figure 9: Two aerial photographs of the sinkhole sites near Mineral beach (Shalem-2) taken in January 2005 and December 2008. White arrow in both photos marks the northern tip of the sinkhole lineament in January 2005, and black arrow marks the northern tip in December 2008. The site growth was by development of sinkholes by lineament prolongation northward, and with some widening eastward. The sinkhole lineament lies above the western boundary of the salt layer (Fig. 4), where further salt dissolution forming more caverns causes the lineament widening eastward. Exposed fault escarpments are marked, and are oriented parallel to the sinkhole lineament (Fig. 6).

References

Abelson, M., Baer, G., Shtivelman, V., Wachs, D., Raz, E., Crouvi, O., Kurzon, I., and Yechieli, Y., 2003, Collapse-sinkholes and radar Interferometry reveal neotectonics concealed within the Dead Sea basin, *Geophysical Research Letters*, 30, v. 10, 1545, 52(1-4).

Abelson, M., Yechieli, Y., Crouvi, O., Baer, G., Wachs, D., Bein, A., and Shtivelman, V., 2006, Evolution of the Dead Sea sinkholes, in "New Frontiers in Dead Sea Paleoenvironmental Research", eds. Y. Enzel, A. Agnon, M. Stein, *Geological Society of America, Special Paper*, 401, 241-253.

Amelung, F., D.L. Galloway, J.W. Bell, H.A. Zebker, and R.J. Laczniak, 1999, Sensing the ups and downs of Las Vegas: InSAR reveals structural control of land subsidence and aquifer-system deformation, *Geology*, *27* (6), 483-486.

Baer, G., Schattner, U., Wachs, D., Sandwell, D., Wdowinski, S., and Frydman, S., 2002, The lowest place on Earth is subsiding - An InSAR (interferometric synthetic aperture radar) perspective, *Geological Society of America Bulletin*, 114 (1), 12-23.

Hall, J., (1994) Digital shaded map of Israel, Israel Geological Survey.

Galloway, D.L., K.W. Hudnut, S.E. Ingebritsen, S.P. Phillips, G. Peltzer, F. Rogez, and P.A. Rosen, 1998, Detection of aquifer system compaction and land subsidence using interferometric synthetic aperture radar, Antelope Valley, Mojave Desert, California, *Water Resour. Res.*, *34*, 2573-2586.

Sagy, A., Reches, Z., Agnon, A., 2003. Hierarchic three-dimensional structure and slip partitioning in the western Dead Sea pull-apart. Tectonics. V. 22 1004, doi:10.1029/2001TC001323

Shalev, E., Lyakhovsky, V., and Yechieli, Y., 2006, Salt Dissolution and Sinkhole Formation along the Dead Sea Shore, *J. Geophys. Res.*, 111, doi: 10.1029/2005JB004038.

Terzaghi, K., 1925. Principle of soil mechanics, V - Settlement and consolidation of clay, *Engineering News-Record*, *95*, 874-878.

Yechieli, Y., Abelson, M., Bein, A., Stivelman, V., Crouvi, O., Wachs, D., Baer, G., Kalvo, R. and Lyakhovsky, V., 2004. Formation of sinkholes along the shore of the Dead Sea – summary of finding from the second stage of research: Geological Survey Report GSI/41/2004 (in Hebrew), 34 p.

Yechieli, Y., Abelson, M., Bein, A., Crouvi, O., Shtivelman, V., 2006, Sinkhole "swarms" along the Dead Sea coast: Reflection of disturbance of lake and adjacent groundwater systems, *Geological Society of America Bulletin*, v. 118, 1075-1087.

Ze'elim Gully - a high –resolution lacustrine paleoseismic record of the late Holocene Dead Sea basin

Elisa Kagan[1,2*] Revital Bookman[3*] Moti Stein[2*] Amotz Agnon[1]

1 Institute of Earth Sciences, The Hebrew University of Jerusalem
2 Geological Survey of Israel
3 Charney School of Marine Sciences, University of Haifa

elisa.kagan@mail.huji.ac.il

*Field guide

Introduction

During the last decades the Dead Sea has retreated from around 400 to around 430 m below MSL (BSL). The dramatic (mainly man–made) retreat has lead to the formation of new erosional gullies within the shore terraces, where the lacustrine sections of late Holocene Dead Sea are exposed, interfingered with fluvial and shoreline deposits. The sediments, composing the top of the Ze'elim Formation, contain deformed sequences (breccias and liquefied sands) that are interpreted as seismites. The seismites can be dated by radiocarbon to produce a chronology of seismic events in the region. This record is compared and combined with the historical record of earthquakes in the region, producing a high resolution paleoseismic record of the late Holocene time, which is used to constrain temporal and spatial occurrence patterns of earthquakes in the region. In this field trip we will see the deformation within the lacustrine sediments, present their dating, and discuss historical correlation. The landscape in this arid environment is responding rapidly to the developing base level and stations 2-5 described below represent a highly ephemeral setting.

Station 1 – Ze'elim Plain

We will stand on the margins of the Ze'elim Wadi fan-delta on sediments that emerged since the 1960s. This location was underwater for long periods of time during the Holocene, recording the lake's paleolimnological history. Ongoing erosion processes exposed the lacustrine sections that are currently more than 10 m thick and cover more than the past 5000 years (fig. 1).

The benefits of this location include relatively high sedimentation rates and abundant organic debris present in the sediments; both of which are favorable for high-resolution chronological and paleoseismological studies.

Station 2 – Gully B, southern wall

The gully wall (gully B, (Ken-Tor et al., 2001) is composed of fine grained to pebble units that indicate variations in the Dead Sea level in the past. Towards the east the facies become finer, representing a deeper off-shore depositional environment.

Deformation in a sandy unit indicates liquefaction during an earthquake event (fig. 2). Remains of the original bedding are visible. The deformation thins out to the west and eventually disappears. A thin undeformed layer separates two seismic events. In places the older event is "masked" by the younger one. This phenomenon points to the incompleteness of the record. Detection resolution for consecutive events is given by Tres=Hb/Rs, where Tres is the temporal resolution of individual earthquakes, Hb is the thickness of the breccia formed by the younger earthquake, and Rs is the rate of sedimentation (Agnon et al., 2006).

Organic debris deposited within the sediments before deformation were used for radiocarbon dating. Transport time of fine debris as small branches, stalks, and seeds into the lake with the seasonal flash floods is conceivably short; hence they can be used to date the seismic event. Most of the correlated historical earthquakes fall well within the 1σ error envelope of the seismite radiocarbon age (Ken-Tor et al., 2001; Agnon et al., 2006).

Station 3 – Gully B, northern wall

The uppermost section includes the youngest reported earthquakes in the region. The two seismites recognized in the exposure are separated by a few centimeters of lacustrine aragonite sediments that are correlated with the Dead Sea high stand of the late 19th century (when the lake rose to 392 m BSL). Radiocarbon dating, stratigraphic considerations, and historical documentation lead to the conclusion that these seismites record the 1834 and 1927 earthquakes.
Historical evidence for damage indicates the 1834 event epicenter was probably south of the Dead Sea. Alternatively, the M7.0 1837 earthquake from the Roum Fault in southern Lebanon (Ambraseys, 1997; Nemer and Meghraoui, 2006) could have re-disturbed the sediments. The M6.2 1927 earthquake was the first large seismic event to be recorded instrumentally. Its epicenter was re-located at the northern basin of the lake (Avni et al., 2002).

Station 4 - Gully A, Southern wall

Two nearby outcrop sections (western: ZA-1, Ken-Tor et al, 2001a and eastern: ZA-2, (Kagan et al., 2006) were described and 14C dated (34 radiocarbon ages) allowing the compilation of a relatively highly detailed paleoseismic record that was correlated to historical earthquakes. The sediments were deposited mostly in the lacustrine environment with occasional shore deposits (sandy units, aragonite crusts, and shore ridges) indicating lake level drops. The seismites here are mostly brecciated lacustrine laminae (fig. 3). The western section includes several depositional hiatuses. Missing earthquakes according to the historical record are correlated to the time intervals of these hiatuses. Indeed, where the lacustrine record is more complete, e.g. in the Ein Gedi, Ein Feshkha, and the recently studied east Ze'elim section, most of the historical records are well correlated with the seismites (Migowski et al., 2004; Neumann et al., 2007; Kagan et al., in preparation)
The more eastern section was dated by radiocarbon ages of organic debris by accelerator mass spectrometry (AMS) (Neumann et al., 2007). Modeling was carried out by Bayesian statistical methods using the OxCal-04 program (Bronk-Ramsey, 2008) for a depositional model (Kagan et al., in preparation). Six radiocarbon ages (no outliers) are available from ~1000 BC to 1500 AD (fig. 4).

Ten seismite ages were interpolated from the model based on their depths. Historical earthquakes were assigned to each of the seismites and fit within their 1σ age range.

Station 5 – Near the widening of Gully B, southern wall

Here we documented the famous 31 BC earthquake described in the Jewish wars of Flavius. The seismite comprises brecciated clayey detrital laminae, where 20 meters to the west it undergoes a facies change and is visible as liquefied sand. This earthquake was documented by other paleoseismic studies elsewhere along the DST (Reches and Hoexter, 1981; Migowski et al., 2004).

References

Agnon, A., Migowski, C., and Marco, S., 2006, Intraclast breccia layers in laminated sequences: recorders of paleo-earthquakes, in Enzel, Y., Agnon, A., and Stein, M., eds., New Frontiers in Dead Sea Paleoenvironmental Research, Geological Society of America Special Paper 401, p. 195-214.

Ambraseys, N.N., 1997, The earthquake of 1 January 1837 in Southern Lebanon and Northern Israel: Annali di Geofisica, v. XL, p. 923-935.

Avni, R., Bowman, D., Shapira, A., and Nur, A., 2002, Erroneous interpretation of historical documents related to the epicenter of the 1927 Jericho earthquake in the Holy Land: Journal of Seismology, v. 6, p. 469-476.

Bookman (Ken-Tor), R., Enzel, Y., Agnon, A., and Stein, M., 2004, Late Holocene lake levels of the Dead Sea: Geol Soc Am Bull, v. 116, p. 555-571.

Bronk-Ramsey, C., 2008, Deposition models for chronological records: Quaternary Science Reviews, v. 27, p. 42.

Kagan, E.J., Stein, M., Agnon, A., and Neumann, F., 2006, New observations from paleoseismic records across the Dead Sea and Jordan valley basins during the last 70,000 years, Geological Society of Israel annual meeting: Bet-Shean.

Ken-Tor, R., Stein, M., Enzel, Y., Agnon, A., Marco, S., and Negendank, J.F.W., 2001, Precision of calibrated radiocarbon ages of historic earthquakes in the Dead Sea Basin: Radiocarbon, v. 43, p. 1371-1382.

Migowski, C., Agnon, A., Bookman, R., Negendank, J.F.W., and Stein, M., 2004, Recurrence pattern of Holocene earthquakes along the Dead Sea transform revealed by varve-counting and radiocarbon dating of lacustrine sediments: Earth and Planetary Science Letters, v. 222, p. 301.

Nemer, T., and Meghraoui, M., 2006, Evidence of coseismic ruptures along the Roum fault (Lebanon): a possible source for the AD 1837 earthquake: Journal of Structural Geology, v. 28, p. 1483-1495.

Neumann, F.H., Kagan, E.J., Schwab, M.J., and Stein, M., 2007, Palynology, sedimentology and palaeoecology of the late Holocene Dead Sea: Quaternary Science Reviews, v. 26, p. 1476.

Reches, Z., and Hoexter, D.F., 1981, Holocene seismic and tectonic activity in the Dead Sea area: Tectonophysics, v. 80, p. 235.

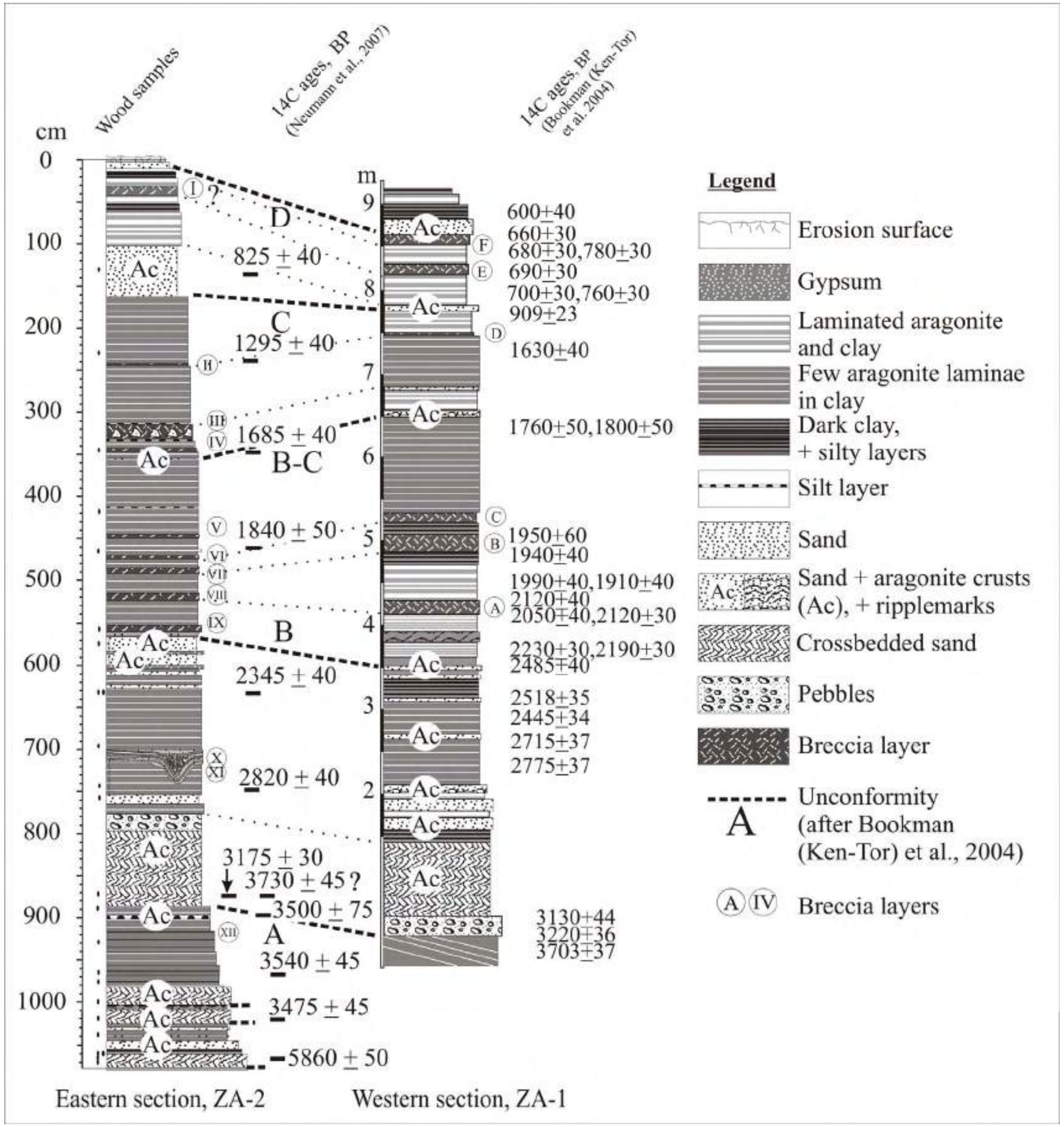

Figure 1: Eastern (left) and western (right) Ze'elim gully sections (diagram modified after Neumann et al., 2007). Radiocarbon ages (uncalibrated), seismites, and sedimentary unconformities are marked.

Figure 2: Photograph of liquefied sand from Ze'elim Gully B.

Figure 3: Photograph of intraclast brecciated layer, Ze'elim Gully A. Note dark grey matrix with broken fragments of aragonite laminae. Dated to the 31BC earthquake documented by Flavius.

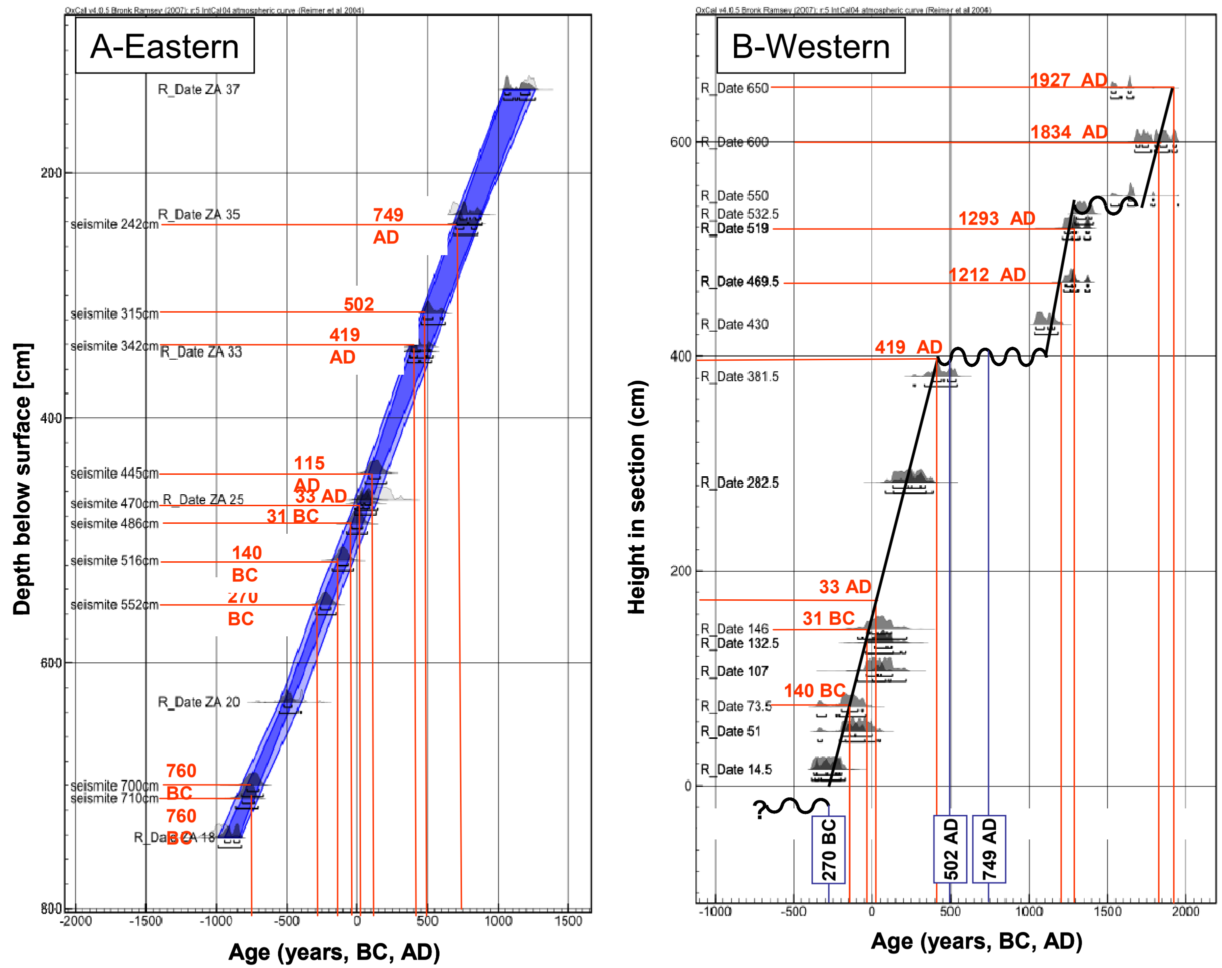

Figure 4: Age-depth models of Ze'elim sections. (a) ZA-2, eastern section, deposition model according to OxCal04 P_sequence. Outer (light blue) range gives 2s, inner (dark blue) range gives 1s model ages. Date histograms indicate calibrated and modeled ages of radiocarbon samples. Seismite histograms from marked depths (i.e. seismite 552cm) indicate model ages of seismites. (b) ZA-1, radiocarbon data and historical correlation, modified after Ken-Tor et al. (2001) and Agnon et al. (2006). Diagonal black lines define periods of deposition. Horizontal curvy lines define depositional hiatuses, which correlate to lake level drops. Blue lines and dates at X-axis are earthquakes which occurred during depositional hiatuses and are missing in the western record but appear in the eastern record.

High-resolution stratigraphy reveales repeated earthquake faulting in the Masada Fault Zone, Dead Sea Transform

Shmuel Marco[1]*, Amotz Agnon[2]

[1]Department of Geophysics and Planetary Sciences,Tel Aviv University, Israel

[2]Institute of Earth Sciences, The Hebrew University of Jerusalem

amotz@cc.huji.ac.il

*Field guide

A syndepositional fault zone east of Masada provides an example for fundamental characteristics of earthquakes, such as long term temporal clustering, repeated faulting on the same planes for a limited time of the order of a few thousands of years, and the formation of subaqueous breccia layers interpreted as seismites. The MFZ was studied in outcrops of Lake Lisan sediments, dated by the Uranium series to 70-15 ka (Schramm et al., 2000). Detailed columnar sections on both sides of well-exposed faults show that each individual fault exhibits a cluster, up to 4 kyr long, with 3-5 slip events on the same plane. Each slip event is associated with the formation of widespread layers exhibiting soft sediment deformation, which are interpreted to be seismite layers. The uppermost part of the Lisan section, about 5 m, is not faulted, hence the last cluster of slip events, ended about 25 kyrs ago. The clusters of activity of individual faults coalesce to form larger clusters. These are evident in the distribution of seismite layers throughout the entire Lisan section which shows earthquake clustering during periods of ~10 kyr. The clusters are separated by relatively quiescent periods of comparable duration (Agnon et al., 2006; Marco and Agnon, 2005; Marco et al., 1996).

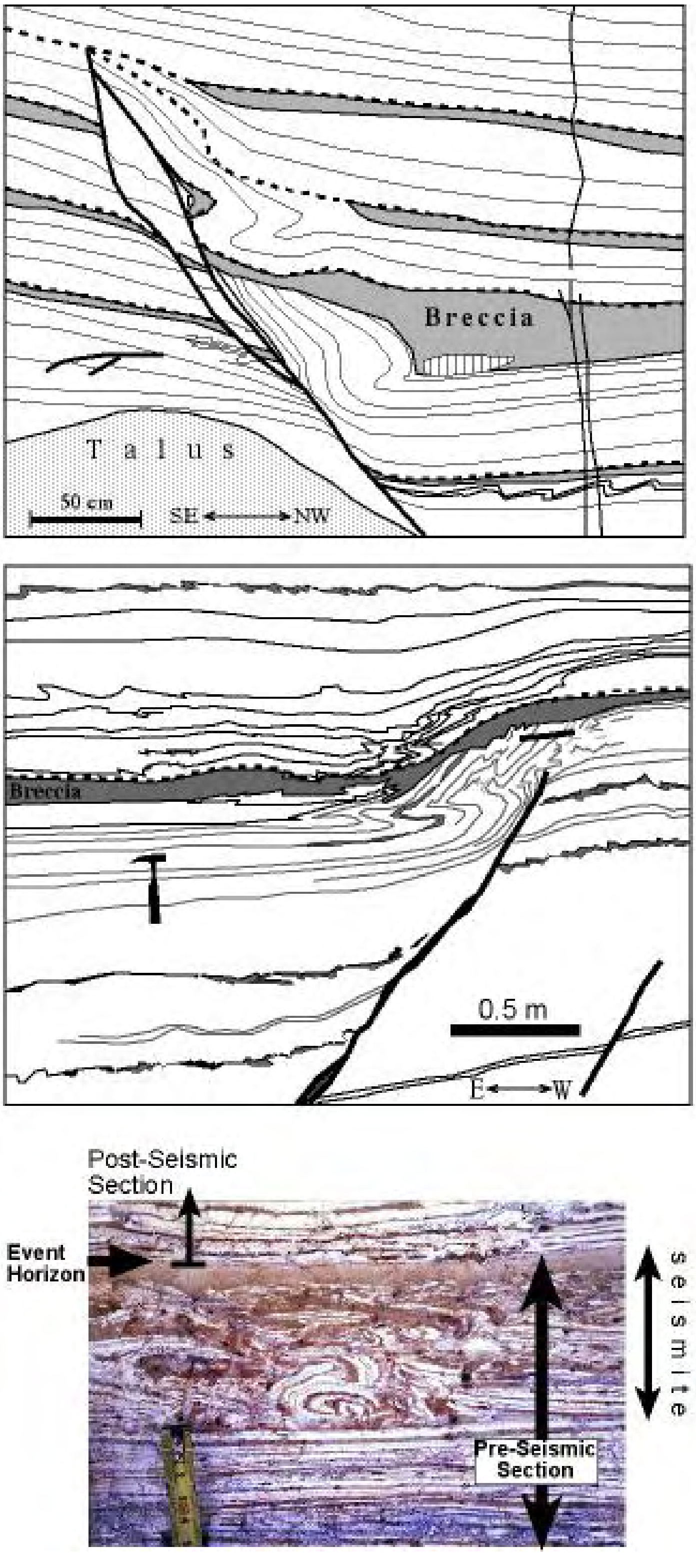

Figure 1: Typical syndepositional fault exposures. Top two: Line drawings are traced from photographs, emphasizing bedding, breccia layers (gray), and fault planes (solid lines). The association of faults and breccia layers indicates that the latter formed when slip occurred on the fault. Dashed thick lines are traces of the surfaces immediately after slip events, i.e., event horizons. One of the breccia layers in exposure 16 contains an embedded intraclast with vertical laminae. It probably fell from the adjacent fault scarp. Photograph at bottom shows a 7-cm-thick breccia layer exhibiting large fragments of former laminas at the

bottom and upward decrease of fragment size. The top of the breccia layer is made of pulverized laminae. We interpreted such layers as seismites, which have been formed by fluidization of upper part of the sediment at the bottom of the lake during strong earthquake shaking (Marco and Agnon, 1995).

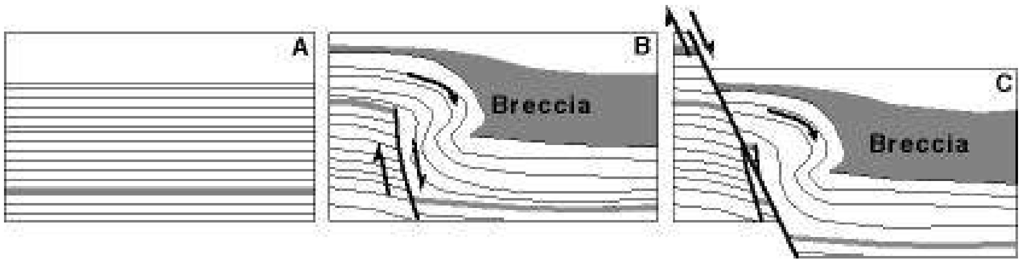

Figure 2: A model of subaqueous faulting that explains the observed faults. **A.** Horizontal laminated sediment at the bottom of the lake. **B.** Faulting forms a scarp (solid line) and the shaking triggers the formation of a breccia layer composed of a mixture of laminated fragments at the top of the sediment. The breccia layer is thicker in the hanging wall. Reclining folds in the hanging wall form coseismically when uppermost poorly consolidated layers slump down the fault scarp. **C.** A second slip event.

References

Agnon, A., Migowski, C., and Marco, S., 2006, Intraclast breccia layers in laminated sequences: recorders of paleo-earthquakes, *in* Enzel, Y., Agnon, A., and Stein, M., eds., New Frontiers in Dead Sea Paleoenvironmental Research, Geological Society of America Special Publication, p. 195-214.

Marco, S., and Agnon, A., 1995, Prehistoric earthquake deformations near Masada, Dead Sea graben: Geology, v. 23, p. 695-698.

Marco, S., and Agnon, A, 2005, High-resolution stratigraphy reveals repeated earthquake faulting in the Masada Fault Zone, Dead Sea Transform: Tectonophysics, v. 408, p. 101-112.

Marco, S., Stein, M., Agnon, A., and Ron, H., 1996, Long term earthquake clustering: a 50,000 year paleoseismic record in the Dead Sea Graben: J. Geophys. Res., v. 101, p. 6179-6192.

Schramm, A., Stein, M., and Goldstein, S.L., 2000, Calibration of the ^{14}C time scale to 50 kyr by ^{234}U-^{230}Th dating of sediments from Lake Lisan (the paleo-Dead Sea): Earth Planet. Sci. Lett., v. 175, p. 27-40.

Mor structure: example for Late Pleistocene north-south extension in the Dead Sea basin

Amir Sagy[1]*, Yuval Bartov[2]

[1]Geological Survey of Israel
[2] I.E.I Ltd.

asagy@gsi.gov.il

*Field guide

The Dead Sea basin

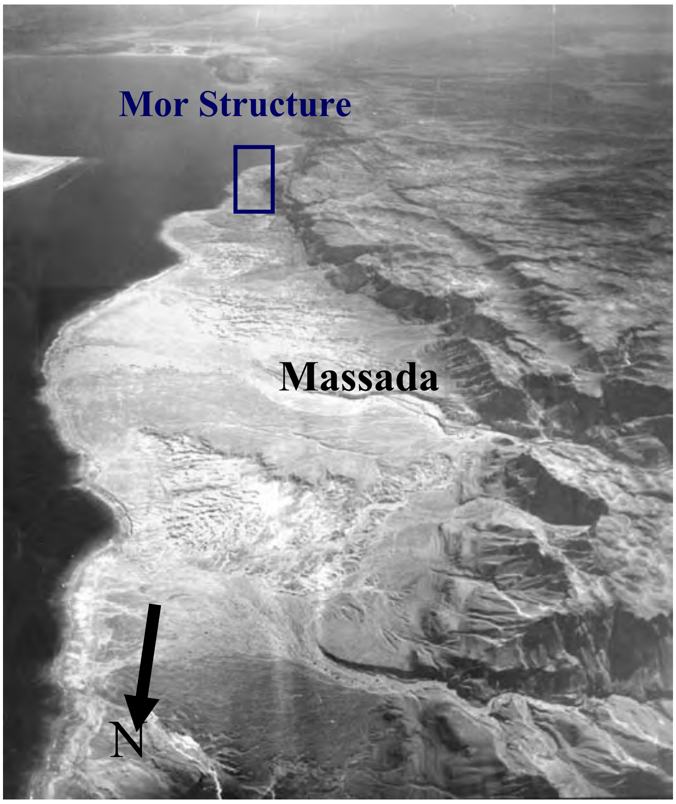

The Mor structure is a deformed zone located in the Dead Sea basin. Faults that are exposed in this location were active from Late Pleistocene times to the present. The structure includes E-W trending normal faults that are bounded and crossed by N-S trending faults. The well exposed fault system and the precise chronology of the regional Late Pleistocene deposits (Schramm, Stein & Goldstein, 2000; Bartov et al. 2002) have been used to calculate the amount, timing and rate of extension of the structure over the last 50 ka (Bartov & Sagy, 2004).

Mor structure: Stratigraphic section

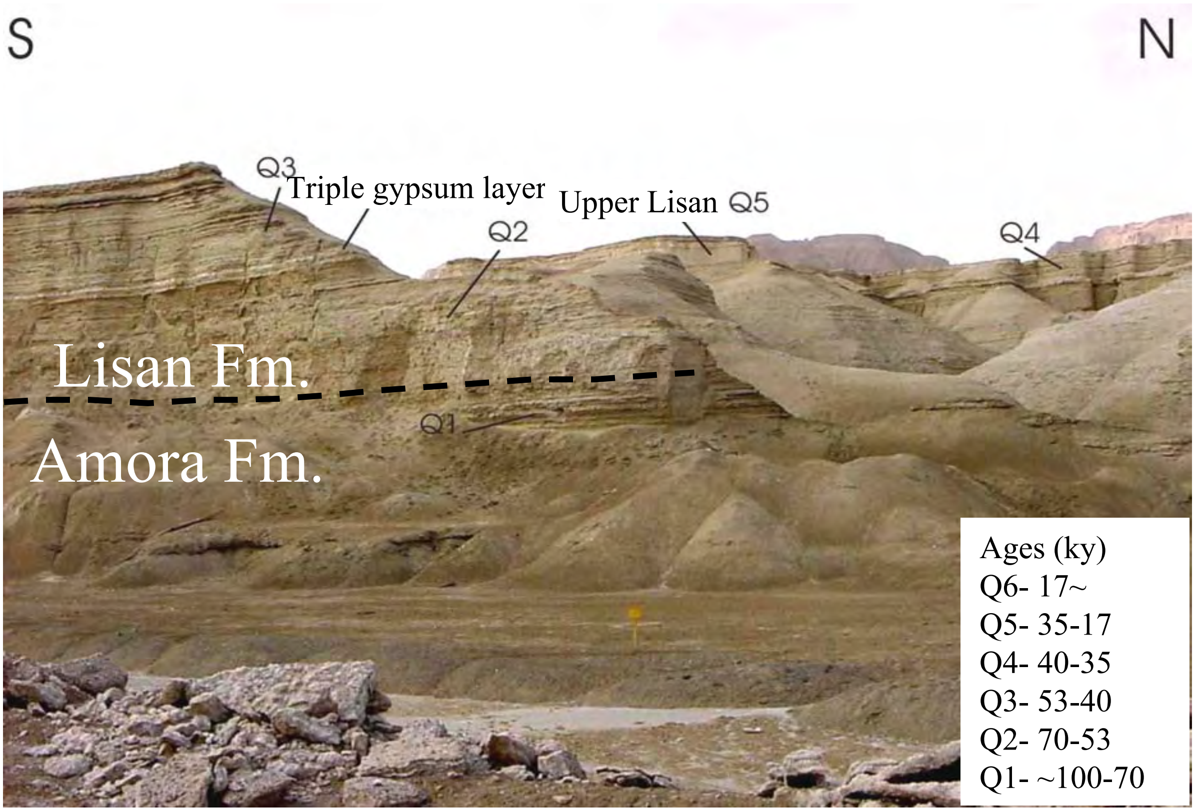

The Dead Sea Basin hosted a number of lacustrine water bodies since the Pliocene time (Stein, 2001). The exposed sedimentary sequences are mostly the remnants of Late Pleistocene to Holocene lakes (Amora, Lisan and Ze'elim), that are chronologically well constrained (Kaufman, Yechieli & Gardosh, 1992; Schramm, Stein & Goldstein, 2000; Waldman, 2002). The Mor structure is located at the distal part of the small Mor Valley fan delta. This geographic position produces a relatively continuous record of deposition interrupted by episodic low-lake levels that are expressed by distinct unconformities. The stratigraphic sequence consists of 37 m of laminated aragonite, silts and gypsum that interfinger with coarse clastic deposits transported from the western shores by streams. These deposits are of the Upper Amora (<120–70 ka) and Lisan formations (70–15 ka) and are partly covered by a thin transgressive Holocene unit (<6 ka). The local section is divided into six mapping units that are well correlated with high-resolution U–Th dated sections (Schramm, Stein & Goldstein, 2000; Bartov et al. 2002).

Mor Structure: Geological map

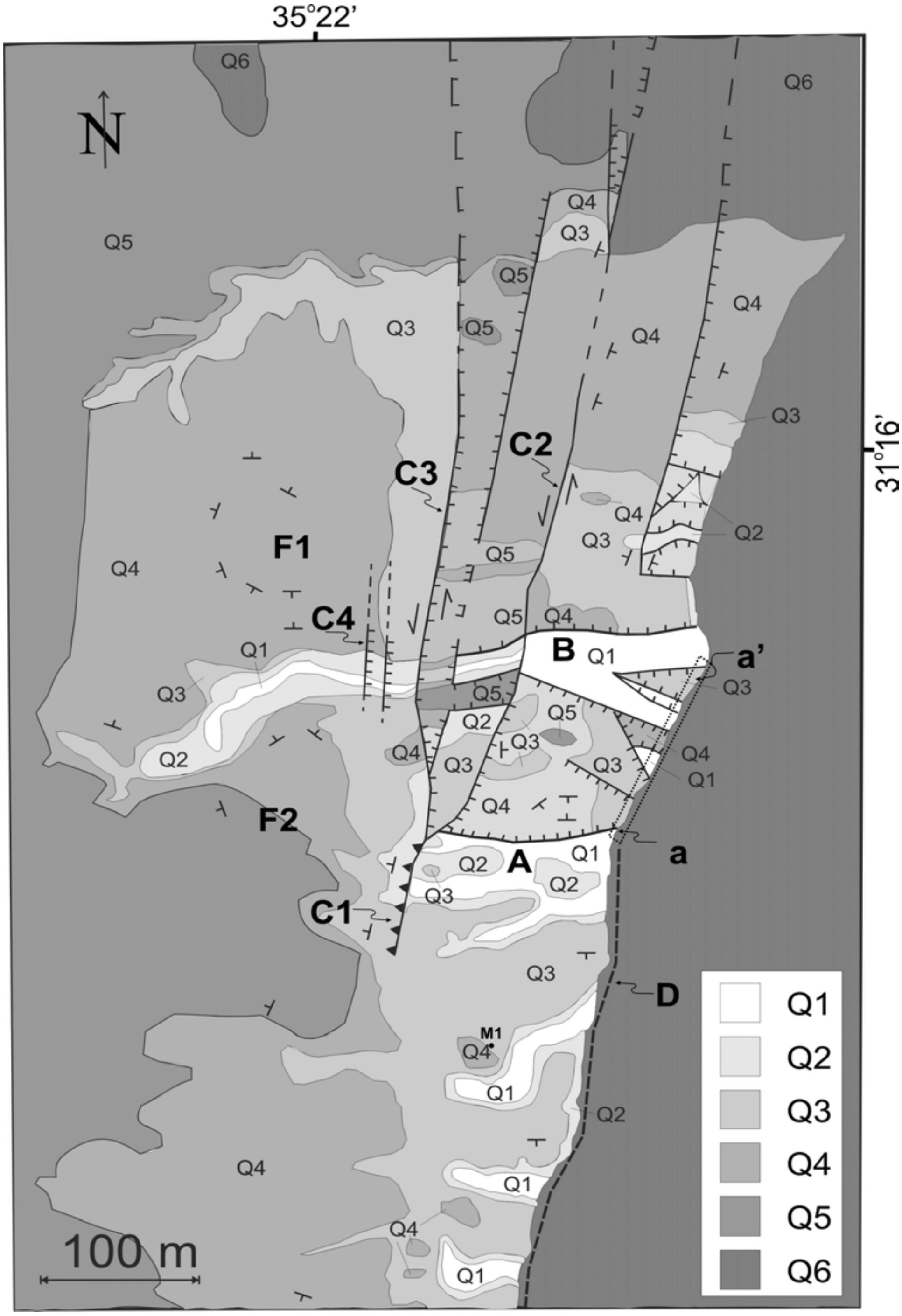

The Mor structure is bounded by N–S-trending faults, and cross-cut by low-angle, E–W-trending normal faults. The continuing deformation in this structure is evident by the observation of at least three deformation episodes between 50 ka and the present. The calculated extension is 3.5 mm/yr over the last 30 000 years.

Field observations: High and low angle normal faults

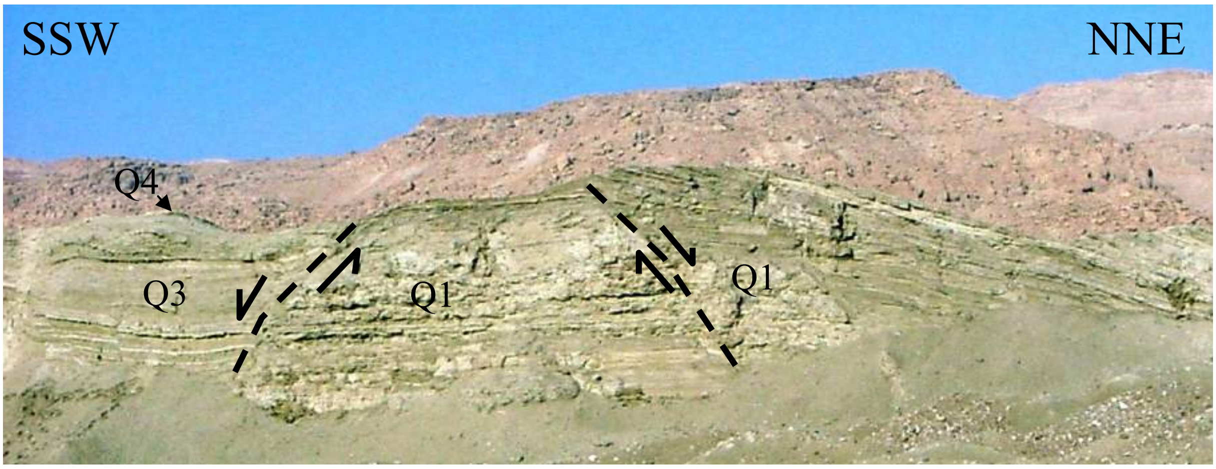

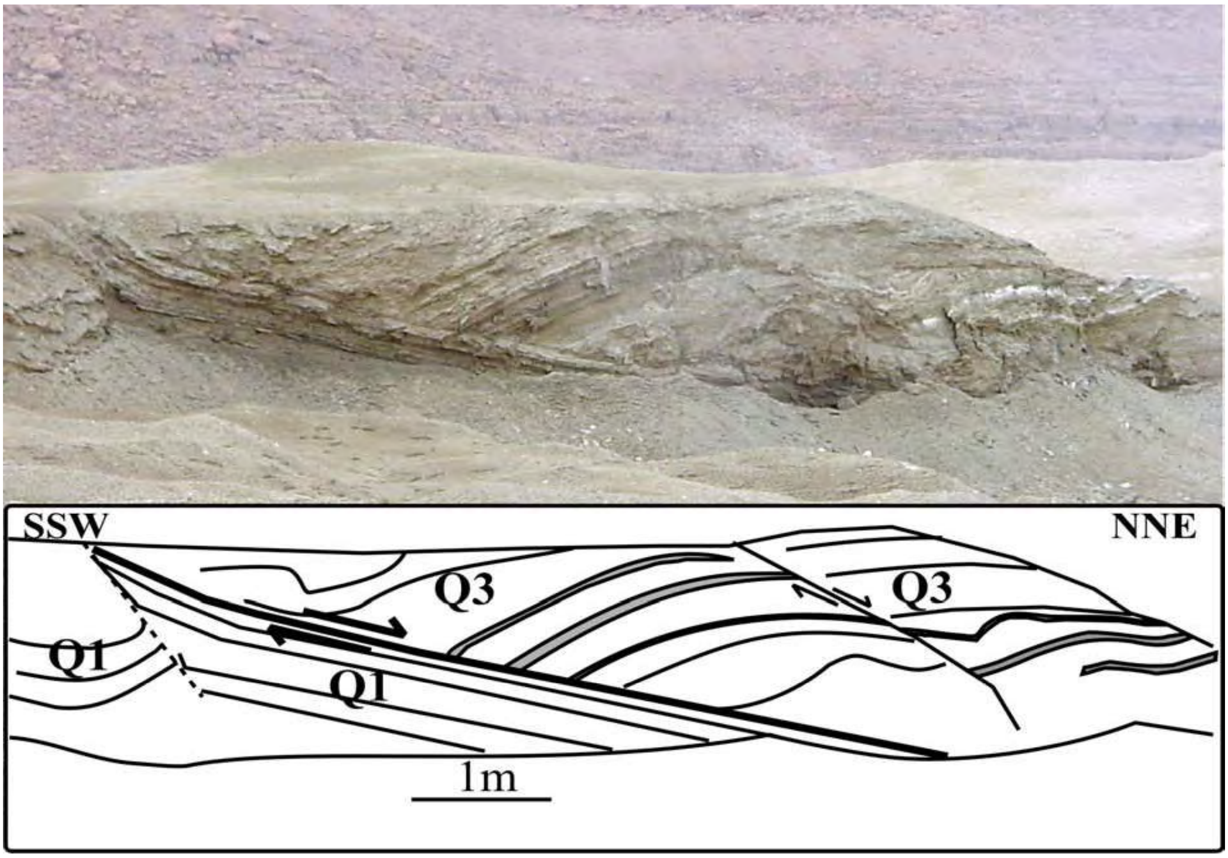

Faulting and ductile deformation on N-S trending faults

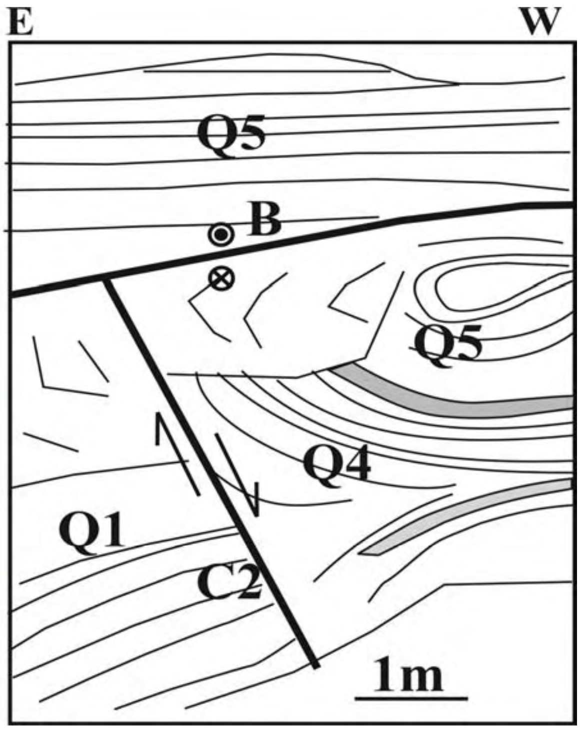

Elongated structural dome

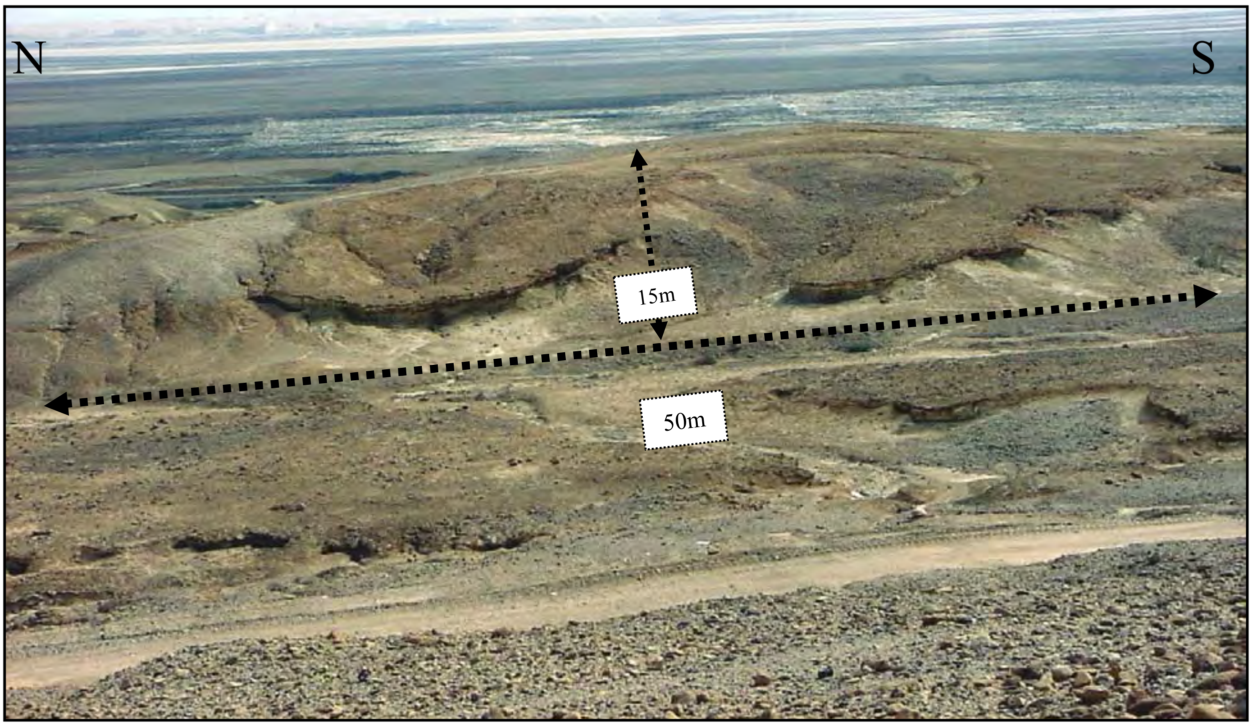

Mor structure: Interpretation

The N-S extension along the Mor structure is orthogonal to the dominant E–W extension within the western margins of the Dead Sea Basin (Sagy, Reches & Agnon, 2003), and thus it is best interpreted as associated with strike-slip motion along the N-S trending faults. Furthermore, a sinistral sense of motion along system C is indicated by: (1) a thick pebbly layer locally observed west of fault C in the dome's area is concealed at the southeastern part, and is exposed again some 70 m to the northeast of fault C; (2) the penecontemporaneous growth of the structural uplift west of the boundary longitudinal fault is consistent with observations in experiments of pull-apart development in ductile materials (Reches, 1988).

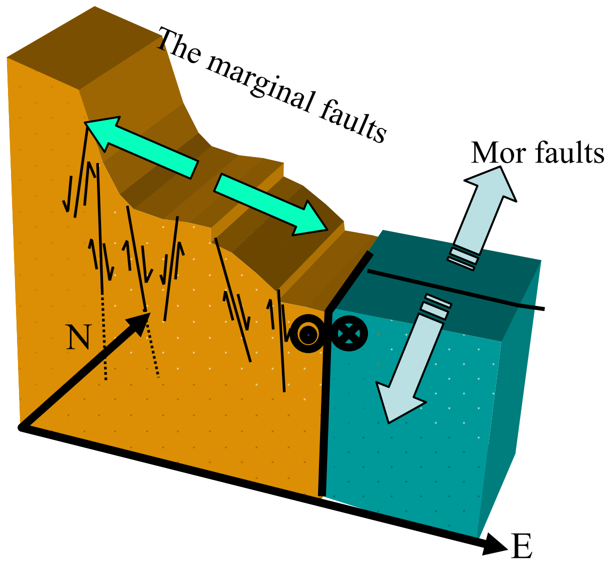

(3) recent seismic activity in the Dead Sea Basin indicates that four sinistral events occurred in the immediate proximity of the Mor structure over the past decade (Hofstetter et al., 2007).
The relationship between longitudinal faults and E–W normal faults suggests that the horizontal motion along the two stepped N–S strike slip faults is transferred from one to the other by the extension associated with the normal faults. Such relation lead us to interpret the structure as a small pull-apart in a strike slip system.

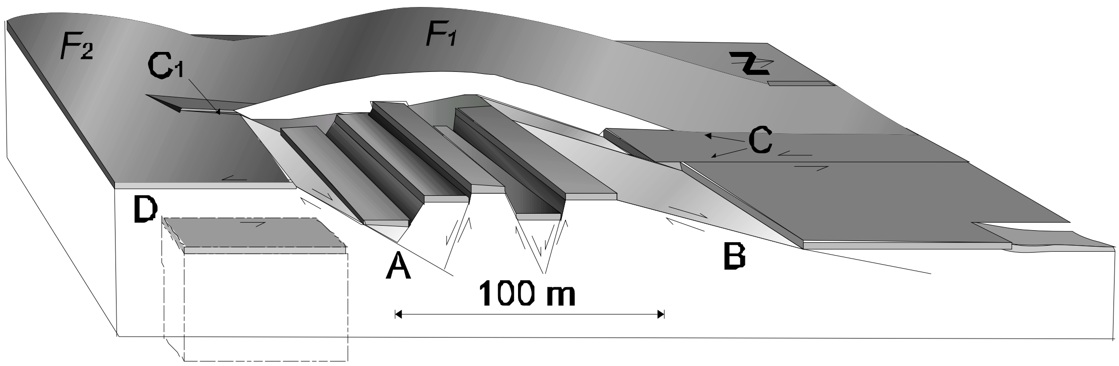

References

Bartov, Y., Stein, M., Enzel, Y., Agnon, A. & Reches, Z. 2002. Quaternary Research 57, 9–21.
Bartov, Y. & Sagy, A. 2004. Geological. Magazine. 141, 565–572.
Haase-Schramm, A., Goldstein, S. L. & Stein, M. 2004. Geochimica et Cosmochimica Acta 68, 985–1005.
Hofstetter R., Klinger Y., Abdel-qader A., Rivera L., & Dorbath L., 2007. Tectonophysics 429, 165-181.
Reches, Z. 1988. Tectonophysics 145, 141–56.
Sagy, A., Reches, Z. & Agnon, A. 2003. Tectonics 22.
Schramm, A., Stein, M. & Goldstein, S. L. 2000. Earth and Planetary Science Letters 175, 27–40.
Stein, M. 2001. Journal of Paleolimnology 26, 271–82.
Waldman, N. 2002. M.Sc. thesis, Hebrew Univ. Jerusalem,

Emplacement mechanism and fracture mechanics of clastic dikes

Tsafrir Levi[1]*, Ram Weinberger[1], Yehuda Eyal[2], Tahar Aïfa[3], Vladimir Lyakhovsky[1], Naomi Porat[1], Shmuel Marco[4], Eyal Heifetz[4]

1. Geological Survey of Israel
2. Department of Geological and Environmental Sciences, Ben Gurion University of the Negev
3. G´eosciences-Rennes, CNRS UMR6118, Universitee´ de Rennes l, Campus de Beaulieu, France
4. Department of Geophysics and Planetary Sciences, Tel Aviv University, Israel

tsafrir@gsi.gov.il

*Field guide

Clastic dikes are discordant, sub-vertical sheets of sediment within a host rock. While the common final geometry of these structures is everywhere similar and well defined, their mode of formation is ambiguous. This ambiguity arises because the sediment comprising the dikes may accumulate either 'passively' (depositional dikes) by deposition of clastic materials into preexisting fissures or 'dynamically' (injection dikes) by fracturing the country rocks and injection of clastic materials during overpressure buildup. Many studies of clastic dikes deal with the possible source rocks of the dike fill, but usually their determinations are either tentative or unequivocal. Only a few studies deal with the emplacement mechanism of the clastic dikes, but commonly without integrating the issues of fracturing with flow mechanics of clastic material and direction of flow.

To complete the paleoseismic record, all structures in seismically active zones that were induced by relative strong earthquakes should be identified. Of these structures injection dikes are probably the most impressive liquefaction-fluidization features that occur during relative large earthquakes (M>6.5). Hence, understanding the processes involved in dynamic clastic dike emplacement is of interest beyond the context of clastic transport. The present study focuses on the mechanisms of clastic-dike formation within the seismically active Dead Sea Fault (DSF) zone. The study area is located within the Ami'az Plain and Nahal Perazim area where hundreds of dikes cross-cut the late Pleistocene lake sediments of the Lisan Formation.

To understand the processes of clastic dike emplacement mainly two aspects were studied in the frame of the present work: (1) the transportation mechanism of the clastic material comprising the dikes; and (2) the fracture mechanics of the evolving dikes that enabled the injection of the clastic material into the host rock. In this study, independent techniques were used to differentiate between depositional dikes and injection dikes. One technique is based on Anisotropy of Magnetic Susceptibility (AMS) of the dike's fill. The AMS was applied here to detect the origin and shed light on the transportation of the clastic infill. The second technique used here was the Optically Stimulated Luminescence (OSL) dating method to distinguish between the depositional dikes and the injection dikes and to suggest reasonable interval ages for the clastic dikes' emplacement. The third technique applied the Elastic Crack Theory (ECT) and the channel flow theory to the clastic dikes to understand the fracturing and the dynamics that took place during the dike emplacement. The fourth issue, though not one of the main issues of this study, is to understand the fracture mechanism of the clastic dikes by using the relations between the fracture apertures and the fracture heights (*A-H*) in 3-D and the sizes of the Elongated Tip Zone (ETZ) and comparing them with the Linear Elastic Fracture Mechanics (LEFM) theory (and other fracture mechanic theories).

In the present study the anisotropy of magnetic susceptibility (AMS) of clastic dikes of known origin was analyzed and the characteristic AMS signatures of depositional or injection filling was defined. The passively filled dikes, comprising brownish silt that resembles the local surface sediments, are characterized by an oblate AMS ellipsoid and vertical minimum susceptibility axis V_3. The dikes comprising green clayey sediment, which is connected to a mineralogically identical detrital layer in the Lisan Formation, are characterized by a triaxial AMS ellipsoid, well-grouped sub-horizontal and parallel to the dike walls' maximum susceptibility axis V_1, and sub-vertical intermediate susceptibility axis V_2. Field evidence and AMS analysis indicate that these dikes were emplaced by injection probably due to seismically triggered fluidization-liquefaction.

Detailed analyses of the magnetic fabric indicate that the clastic dikes formed by simultaneous fracture propagation and injection of clastic material into the fractures as a result of high pressure buildup in the source layer. The AMS results supported by field evidence indicate that the injection of clay-rich sediment is characterized by: (1) Vertical flow characterized by subvertical V2 axes, indicating the flow directions during fast flow, and subhorizontal V1 and V3 axes. and (2) Subvertical V3 axes characterizing horizontal slow flow, and subhorizontal V1 and V2 axes. A streaked AMS pattern mainly comprised of V2 and V3 axes represents a turbulent flow that generated local eddies during the clastic material transport. The AMS parameters along the dikes and possible grain imbrications along the dike walls support preferred orientation of grains under high strain rates. This novel application of the AMS provides a petrofabric tool for distinguishing passively filled dikes from injection dikes and identifying the latter as seismites.

The quartz single aliquot OSL ages of both depositional and injection dikes are between 15 and 7 ka, younger than the Lisan host rock. The highly scattered distribution of single grain ages of depositional dikes suggests several episodes of infill. The latest Pleistocene to Holocene single grain ages of the injection dikes results from the resetting of OSL signals because they do not contain recently bleached grains that infiltrated from above. The resetting occurred at the time of fluidization–liquefaction and buildup of fluid pressure within the injection dikes. If this resetting mechanism has a physical basis, then OSL dating is an important tool for constraining the ages of earthquake-induced injection dikes.

Two analytic models were examined based on field observations and experimental viscosity tests: (A) a channel flow for upward injection of a clay–water mixture; and (B) a profile of fracture dilation based on the elastic theory analysis. These two models predict that high pressures, between 1-10 MPa, were generated in the dikes and source layer during the last stage of the injection process. The model of channel flow predicts that the injection velocity can reach tens of meters per second, and the emplacement time of the clastic dikes is on the order of a few seconds. The emplacement of the shallow clastic dikes in the Dead Sea basin could not have been driven by buoyancy. It is suggested that the high pressure values may result from the seismic waves which passed through the solid medium. The predicted high pressure values indicate that the clastic dikes were emplaced very close to an active segment of the Dead Sea Fault. The high pressures that lead to the injection process could also have caused the resetting of OSL ages as suggested above.

The present study suggests, based on field measurements and analysis of fracture geometry, that the small-scale fractures (clastic dikes) (height<1m), extensively developed in the upper Lisan Formation, belong to the last stage of the dynamic fracturing process. It is suggested that these fractures developed under deceleration conditions and have propagated at a post dynamic fracturing stage. Plotting the apertures and the fracture heights (*A-H*), measured in 3-D from different outcrops strongly indicate power-law relations. The present study shows that these power-law relations form only because fractures whose heights are less than 0.1m indicated a non constant aspect ratio (*A/H*). Because in these fractures the *A/H* is not constant, the LEFM theory in such fracture sizes can no longer hold and other fracture mechanic theories such as Elastic Plastic Fracture Mechanics (EPFM) should be used. The relative increase of the ETZ height may bring to increasing the resistance to fracturing. Since at this stage the ETZ height is relatively long, the stress intensity is estimated under an Elastic Plastic condition (Anderson, 1995). This condition lowers the stress intensity magnitudes and consequently the velocity is lowered as well. Based on the above, it is suggested that the formation of the ETZs may also play an important role in dynamic fracturing during the deceleration process; this must be further verified in the future.

References

Levi, T., Weinberger, R., Aïfa, T., Eyal, Y. & Marco, S., 2006a. Earthquake-induced clastic dikes detected by anisotropy of magnetic susceptibility: *Geology*, **34**, 69-72, doi: 10.1130/G-22001.1

Levi, T., Weinberger, R., Aïfa, T., Eyal, Y. & Marco, S., 2006b. Injection mechanism of clay-rich sediments into dikes during earthquakes. *Geochem. Geophys. Geosyst.*, **7**(2) 1–20, Q12009, doi:10.1029/2006GC001410.

Levi, T., Weinberger, R., Eyal, Y., Lyakhovsky, V., Heifetz, E &., 2008. Velocities and driving pressures of clay-rich sediments injected into clastic dykes during earthquakes: *Geophys. J. Int.*, 1-13, 10.1111/j.1365-246X.2008.03929.x.

Porat, N., Levi, T. & Weinberger, R., 2007. Possible resetting of quartz OSL signals during earthquakes—Evidence from late Pleistocene injection dikes, Dead Sea basin, Israel. *Quatern. Geochron.*, **2**, 272-277.

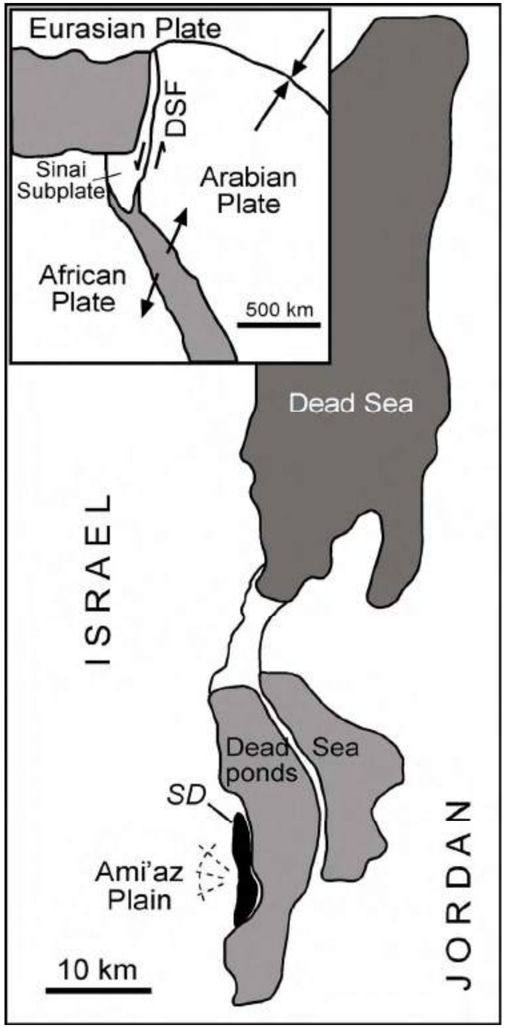

Figure 1: Location maps of the study area. The regional setting of the Dead Sea Fault (inset) and the Ami'az Plain with the clastic dikes marked schematically by dashed lines. DSF, Dead Sea Fault; SD, Sedom Diapir. The rocks exposed in the Ami'az Plain belong to the late Pleistocene Lisan Formation, which consists mostly of lacustrine laminae of aragonite and fine detritus, dated between ca. 70 and 14 ka (Haase-Schramm et al., 2004, and references therein). About 250 clastic dikes were mapped in the Ami'az Plain by means of aerial (after Levi et al., 2006a).
photographs and field surveys (Marco et al, 2002, Levi et al, 2006a).

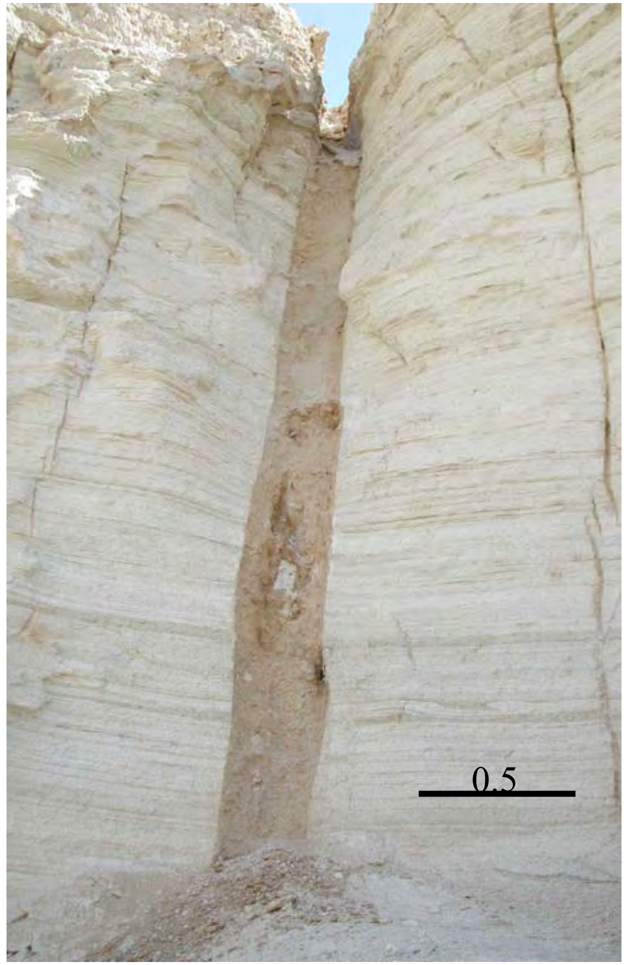

Figure 2: Clastic dike, sub-vertical, sheets of sediment within a host rock. While the common final geometry of these structures is everywhere similar and well defined, their mode of formation is ambiguous.

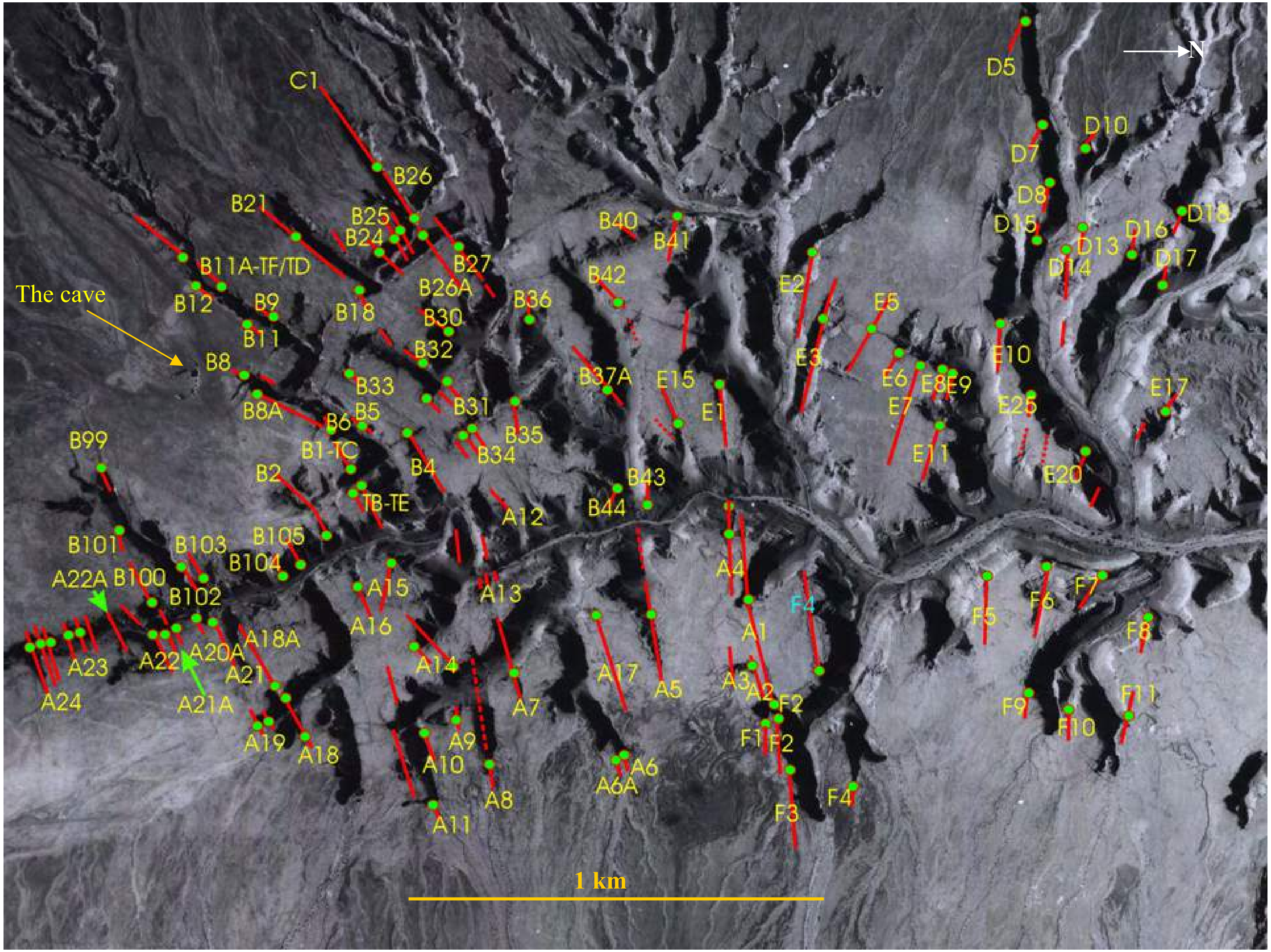

Figure 3: Location and geometry map of the clastic dikes that are arranged mainly in semi radial geometry (Marco et al 2002) in Ami'az Plain. The letter code denotes the dikes (after Levi et al., 2006a).

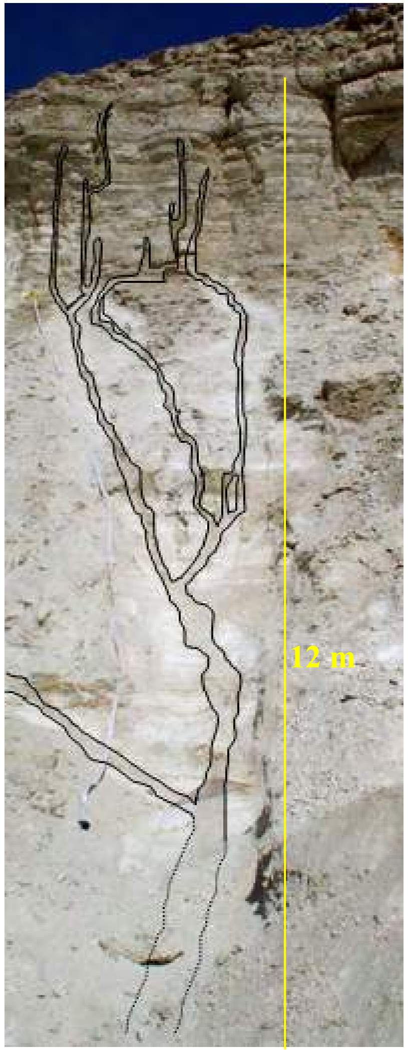

a) In injection dike

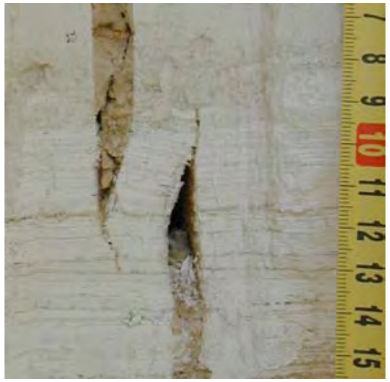

b) Segmented dike

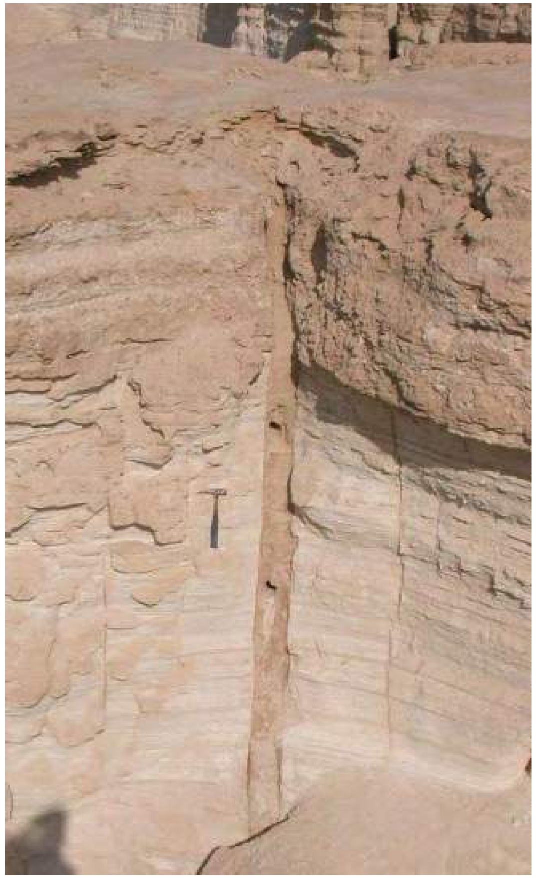

c) Sedimentary dike

Figure 4: Different transportation mechanism and fracturing style, during the clastic dike emplacement. a) Dike architecture resembles that of bifurcated dynamic fracture during upward propagation. b) Two disconnected, partially overlapping dike segments in the upper section of the Lisan Formation. Similar to magmatic dikes, this geometry hints at the role played by internal pressure during dike emplacement and horizontal transport of clastic material into the evolving dikes. Lisan laminae are not displaced along the dike walls, indicating that clastic dikes are extensional fractures. Note that because the dike segments are not physically connected to the surface, the flow within it had a lateral component. c) Wide (~0.4 m) sedimentary clastic dike open at surface filled with brownish silt. Source of fill is veneer of eolian and fluvial sediments, which cover Ami'az Plain (after Levi et al., 2006a).

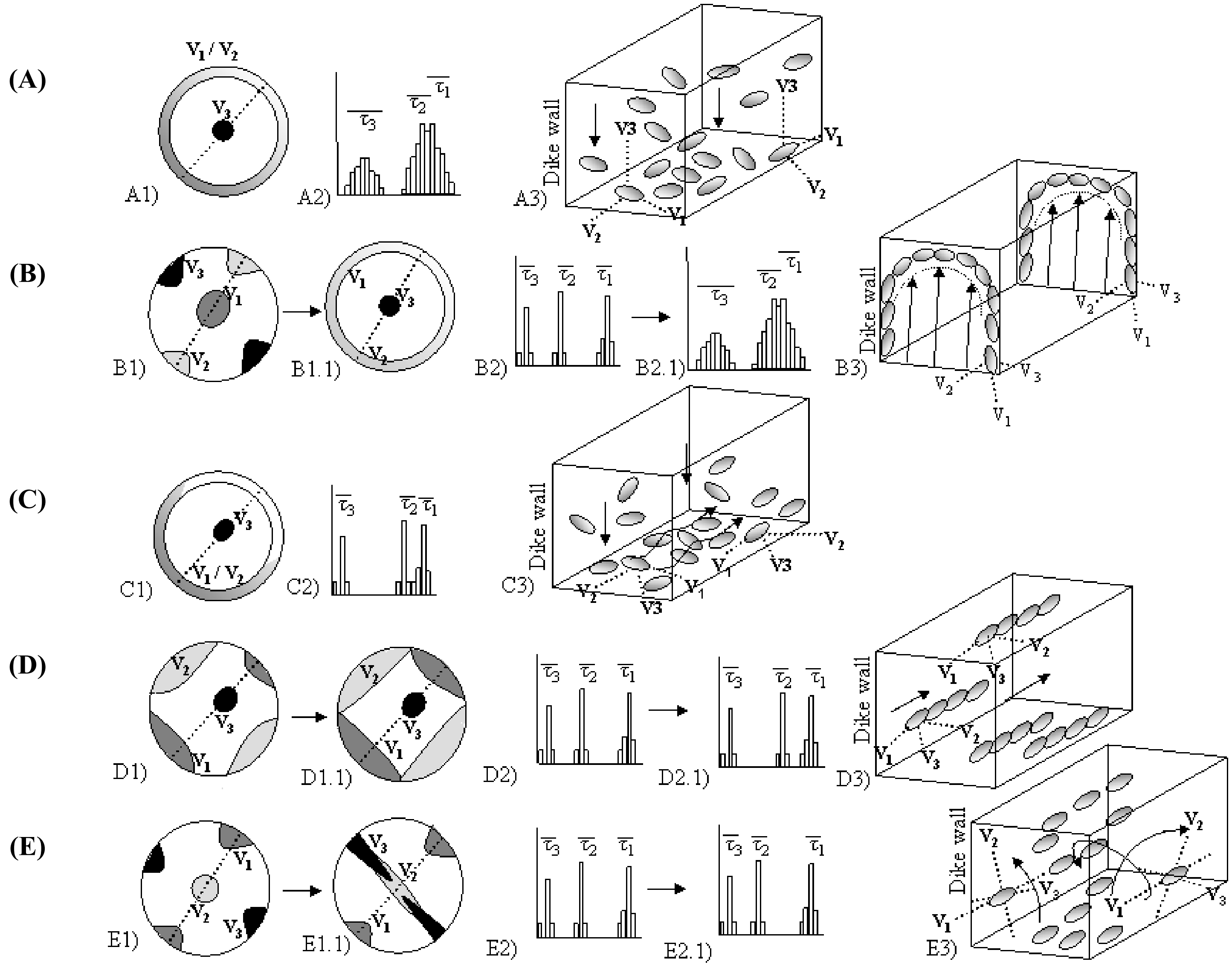

Figure 5: AMS for clastic dikes (synthetic models) that were emplaced under different conditions (after Levi et al, 2006b). (A) Sedimentary (oblate) AMS fabric in depositional dikes. (B) Flow AMS fabric developed during injection of viscous Newtonian fluid and characterized by imbrications along the dike's walls. (C) Low-energy flow fabric of oblate to weak triaxial AMS ellipsoids. (D) Moderate energy flow fabric of triaxial. (E) High-energy flow fabric of triaxial. The principal axes are either grouped (E1) or streaked (E1.1) due to rotation of particles during turbulent flow.

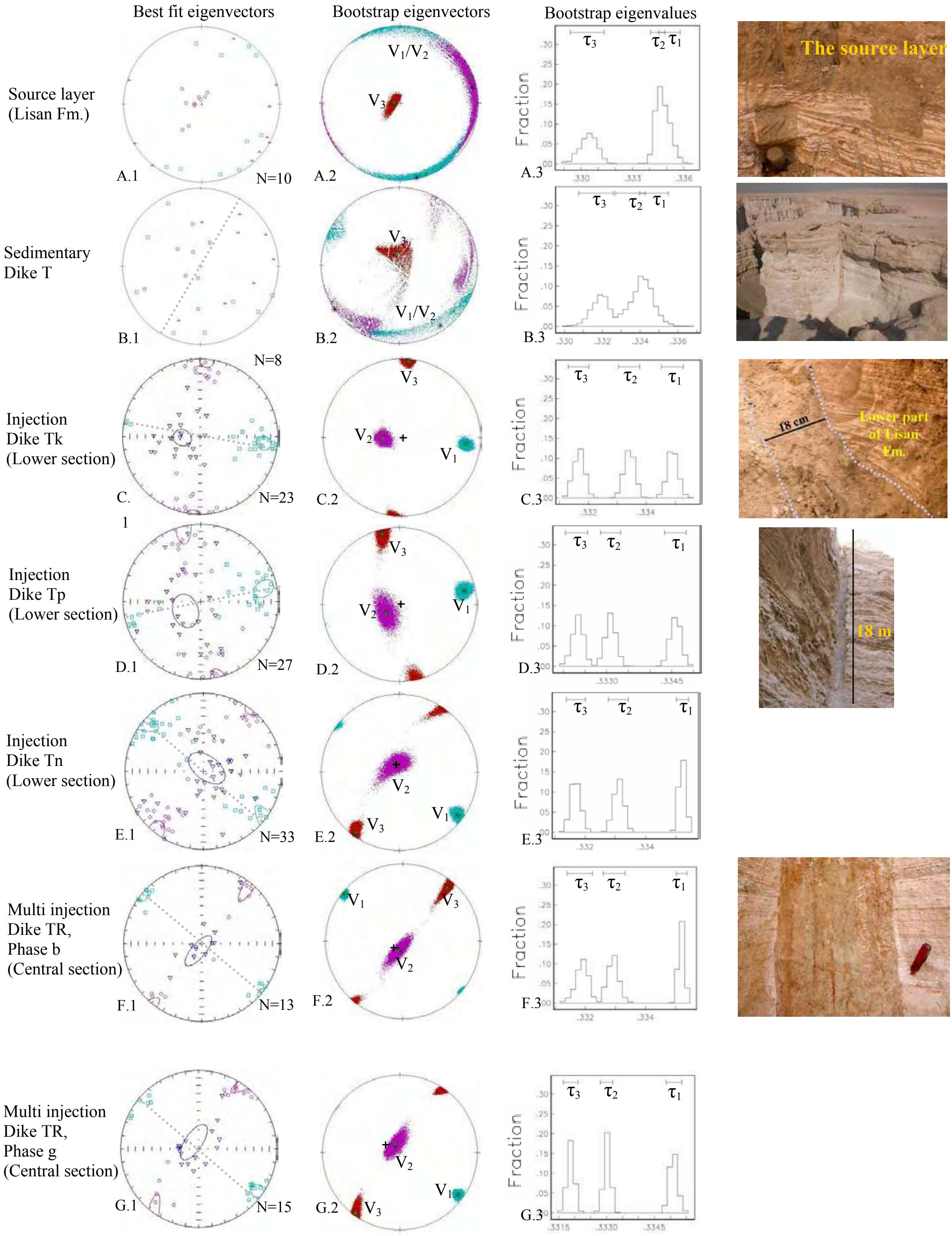

Figure 6: AMS of the source layer, sedimentary dike (Dike To, A) and five injection dikes (Dikes Tk, Tp, Tn, Tp, and TR). A1–G1: Lower-hemisphere, equal-area projections of AMS principal axes and the 95% confidence ellipses; squares represent V1 axes, triangles represent V2 axes, and circles represent V3 axes. A2–G2: Lower-hemisphere, equal-area projections of AMS principal axes analyzed by the bootstrapping method. A3–G3: Principal values distribution with 95% confidence bounds. Dashed lines mark the dike strike (after Levi et al., 2006a,b).

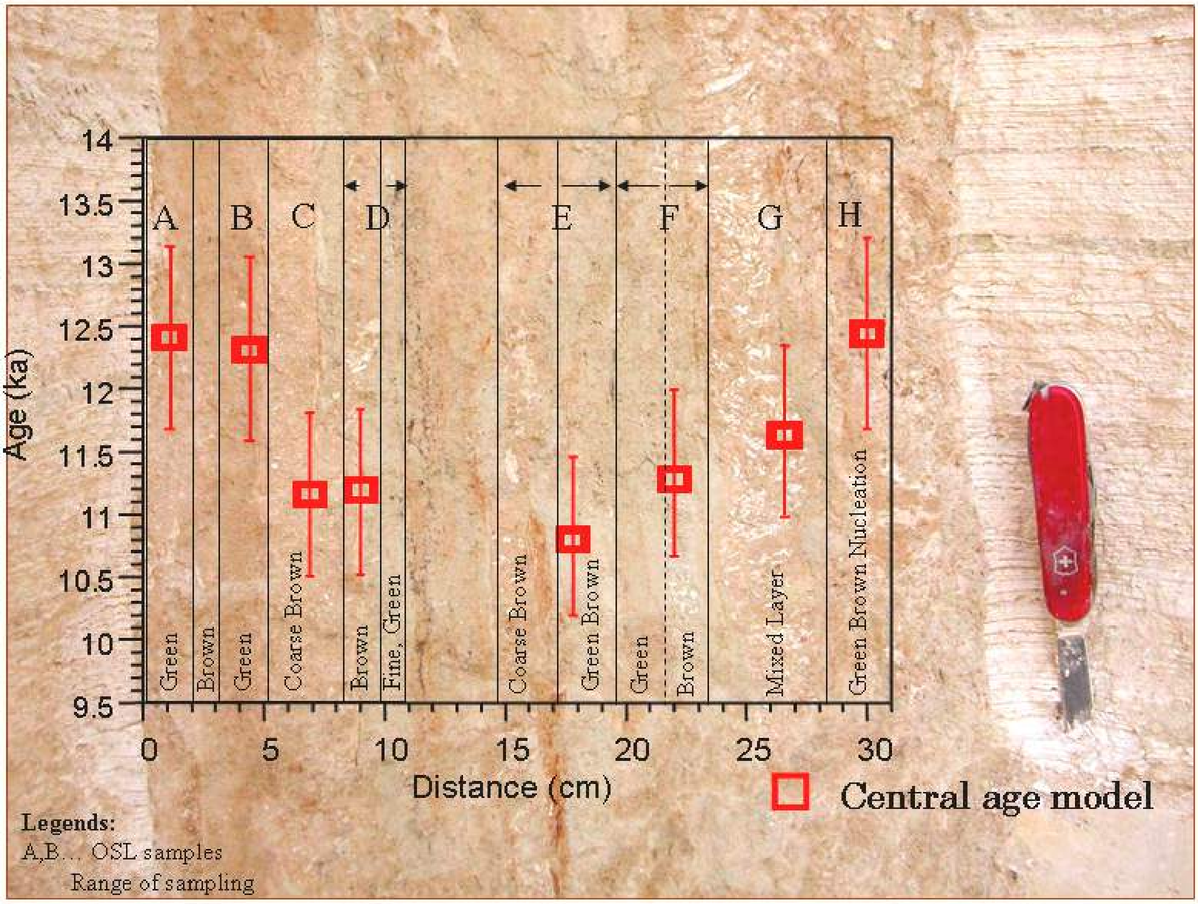

Figure 7: A multi-phase dike composed of 11-12 adjacent vertical sheets of sediment that can be differentiated based on their color and texture. We interpreted these sheets as discrete and separate episodes of injection phases, and hypothesized that the older phases would be closer to the dike margins. Eight individual phases and samples (A-H) are shown schematically. Note that some samples include more than one phase. The age for each sample is plotted as a function of distance from the left wall of the dike. Errors were calculated using the central age models. The uncertainties on the ages are large and all the ages overlap. The ages range between 12.3±1.1 ka and 10.9±0.9 ka indeed decrease towards the center of the dike. At least four injection episodes can be clearly distinguished, with only several hundred years difference between them (after Porat et al., 2007).

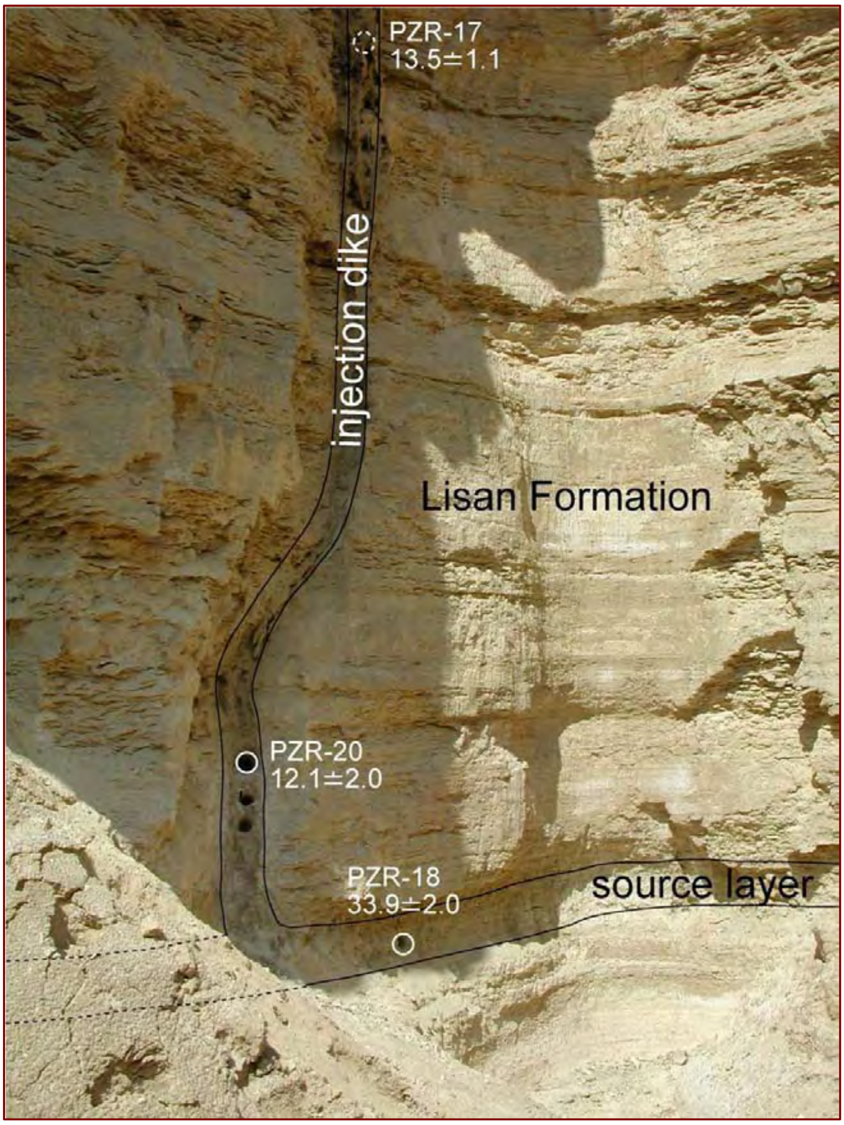

Figure 8: A source horizontal layer and a connected vertical injection dike sampled for OSL dating. Sample numbers and ages (in ka) are indicated. Upper sampling hole (broken line) is projected from a sampling site located ~30 m away along the dike strike. Width of sampling holes is ~ 8 cm. The age of the source layer agrees with U-Th ages for the Lisan Fm. However the OSL ages in the dike are much younger, indicating resetting of the OSL signal during injection (Porat et al., 2007).

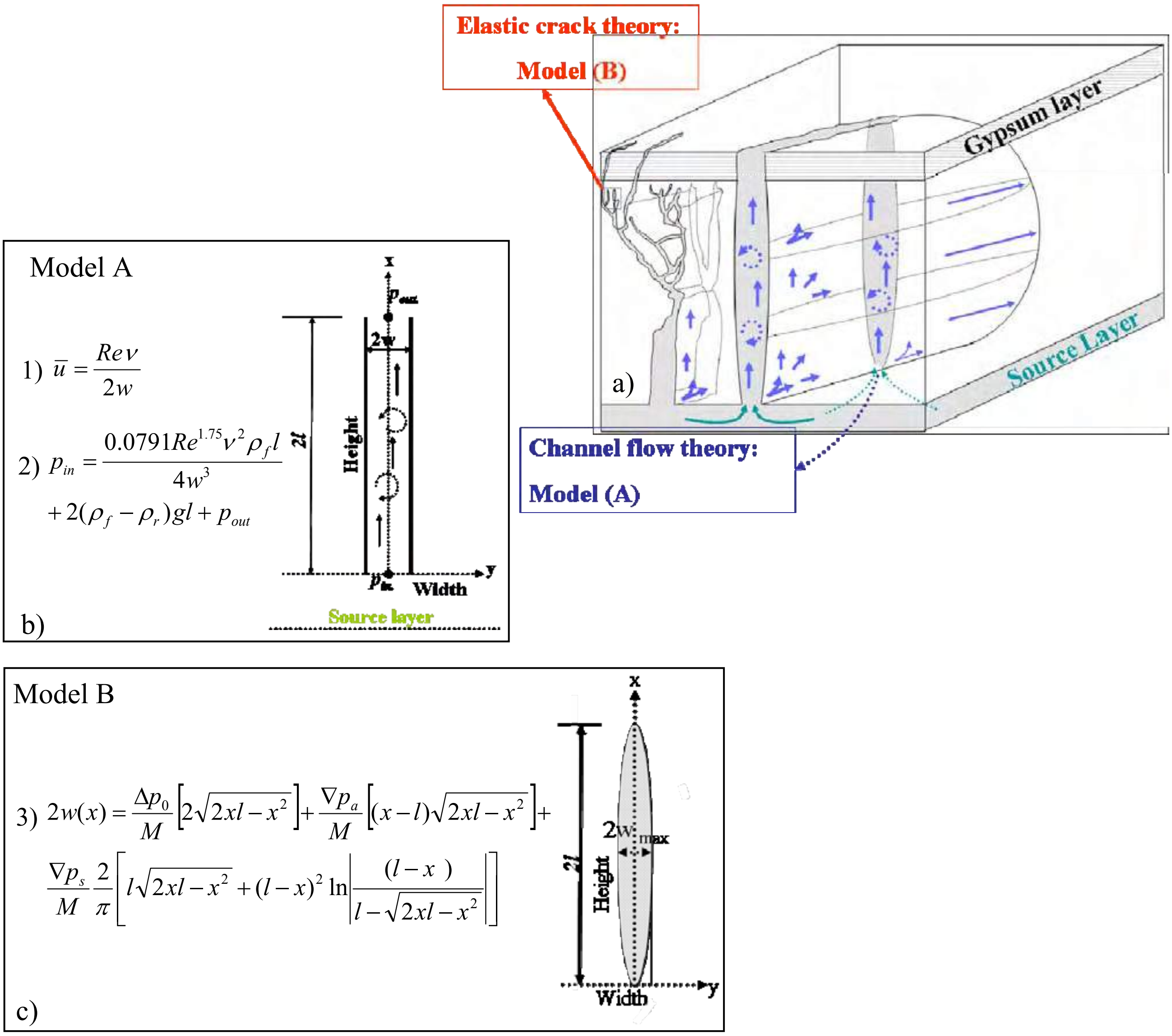

Figure 9: (a) Schematic representation of the two types of dikes: a blade-like dike with a cross section resembling a channel and a branching dike and its associated dikelets (left-hand panel). Some dikes/dikelets cross the upper stiff gypsum layer and some do not. (b) Model (A), showing upward flow along the *x*-axis under turbulent flow conditions. (c) Model (B), showing dilation profile of a representative dikelet. In Eq. (1) $\bar{u}$ is the mean velocity, *Re* is the Reynolds number,   is the kinematic viscosity and *2w* is the dike width. In Eq. (2) P_{in} is the pressure at the source layer, $_f$ is the fluid density, $_r$ is the host rock density, *g* is the constant of gravitational acceleration and *l* is the half dike height. In Eq. (3), the general dilation profile solution, Δp_0 is the uniform normal stress, p_a is the asymmetric linear stress gradient, p_s is the symmetric linear stress gradient and *M* is the elastic stiffness (after Levi et al., 2008).

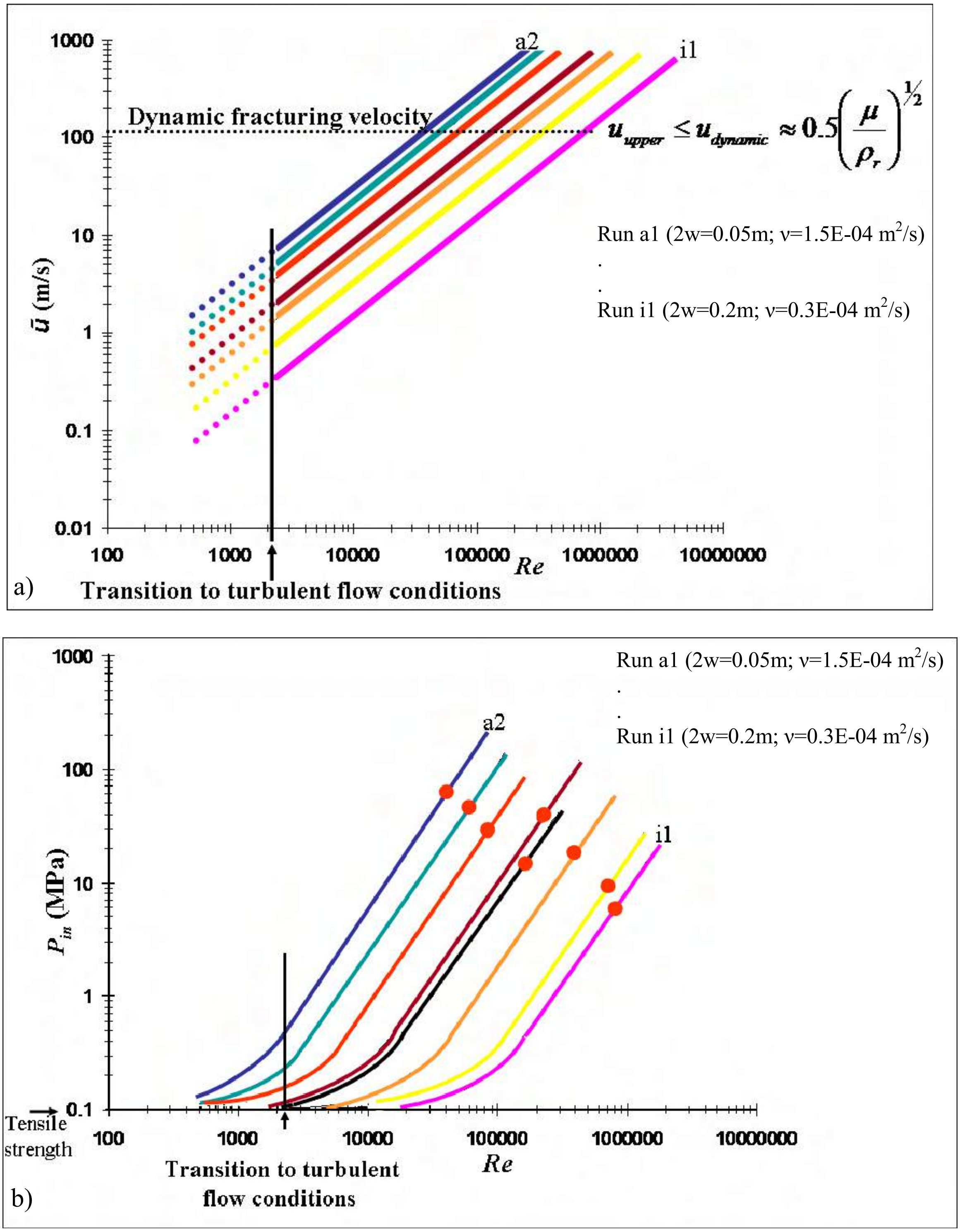

Figure 10: a) Results of model (B), showing the mean injection velocity as a function of *Re* plotted on log-log graph. b) Results of model (A), showing pressure at the source layer as a function of *Re* plotted on log–log graph. The red filled circles denote the possible upper pressures calculated by using the Reynolds numbers that are related to the high velocity values (after Levi et al., 2008). High velocity values, comparable to the dynamic fracture velocity.

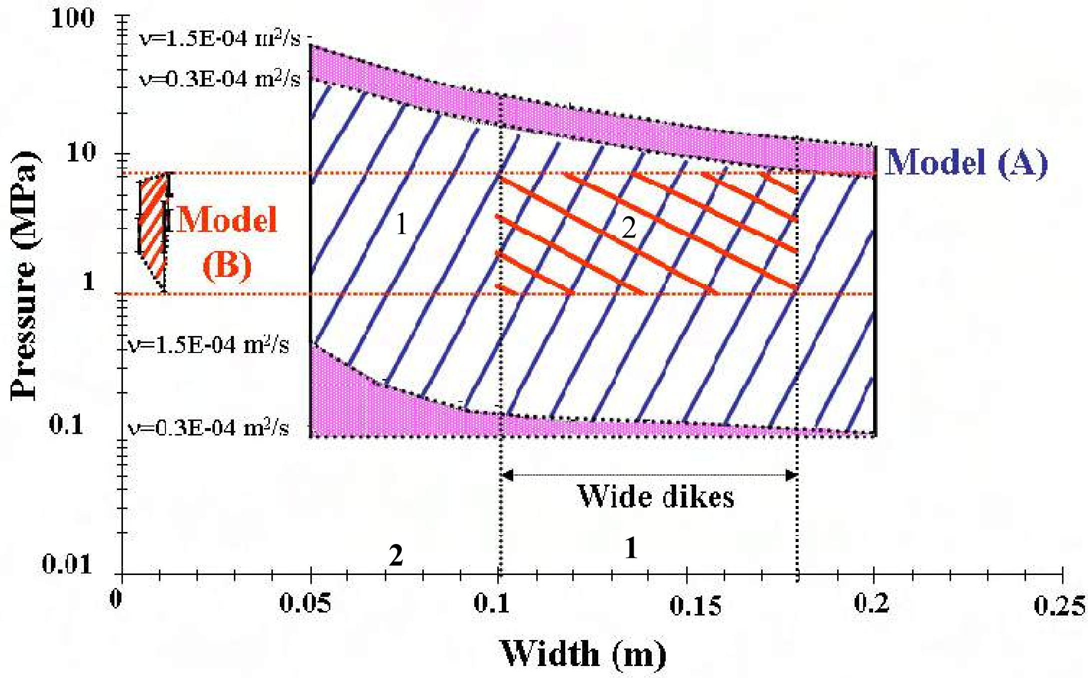

Figure 11: Range of possible pressures in the source layer versus the width of the clastic dikes calculated by coupling model (A) and model (B). The pink polygons mark the minimal and maximal pressures calculated using model (A) with kinematic viscosity v = 0.3E – 04 m^2 s–1 and v = 1.5E – 04 m^2 s–1. Bars correspond to the pressure range for each dikelet calculated using model (B). The polygon bounding these bars defines the estimated pressure range based on model (B). Polygons #1 and #2 represent the most probable range of driving pressures for wide and narrow dikes estimated by integrating models (A) and (B). The overlapping driving pressures of the two models are between 1 and 10 MPa. Based on the lower value of the driving pressure (1 MPa), the associated *Re* numbers were derived from Fig. 10b and, consequently, substituted them in Fig. 10a to obtain a lower value for the injection velocity of ~10 m/s. It is most likely that wider dikes, associated with large elastic deformations, were emplaced under higher driving pressures, probably generated by stronger seismic events or due to more efficient local pressure build-up in the source layer (after Levi et al., 2008).

Petra

21.2.2009

Field leader

Tina M. Niemi

Paleoseismology and archaeoseismology of sites in Aqaba and Petra, Jordan

Tina M. Niemi*[1]

[1]Department of Geosciences, University of Missouri - Kansas City

NiemiT@umkc.edu

*Field guide

QUATERNARY GEOLOGY OF AQABA

Aqaba, Jordan is built predominantly on alluvial fan sediment derived from the adjacent mountain ranges to the east (Fig. 1). The drainage basin of the Wadi Yutim reaches far into the eastern plateau and covers a minimum area of 1100 km^2. It is the largest drainage system in the southern ‘Arabah valley and flows into the 'Ain Defiya depression in Eilat. Several branches of the Wadi Yutim flow southwestward toward the Gulf of Aqaba. The Aqaba Regional Authority has constructed flood control measures to divert runoff away from the city of Aqaba.

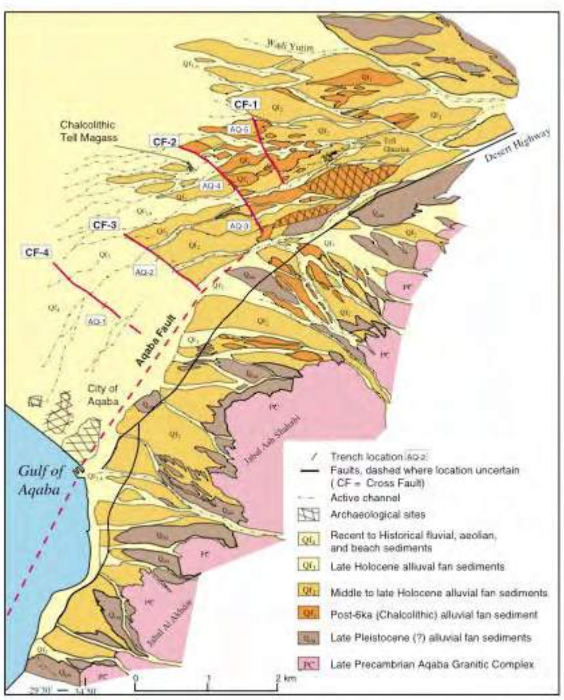

Figure 1. Geologic map of the Aqaba region based on interpretation of 1:25,000 scale airphoto from 1953. Cross fan faults (CF 1-4) are mapped as continuous lines even though these features are eroded by wadi washes. These cross faults formed as normal to oblique-slip faults associated with a left stepover in the Dead Sea Transform. Locations AQ 1-3 mark the sites of exploratory trenches excavated across the NW-trending faults. A high concentration of archaeological ruins in the Aqaba area provide age constraints on surface deformation and provide a unique record of damage from past earthquakes (modified from Niemi and Smith, 1999).

Niemi and Smith (1999) divided the alluvial fan sequence in the Aqaba region into five mappable fan units (Q_{oa}, Qf_1, Qf_2, Qf_3 and Qf_4). Remnants of a Pleistocene alluvial fan sequence, designated Q_{oa}, located near the mountain front, may correlate to the Upper Pleistocene fan surfaces mapped on the Shehoret alluvial fan sequence west side in Israel. The oldest Holocene alluvial fan surface (Qf_1) is distinguished by a moderately developed desert varnish. It overlies archaeological artifacts from the Chalcolithic period (Tell Magass and Tell Ghuzlan) dated to 5-6 ka. The Qf_2 fan surface is slightly inset into or buries the Qf_1 surface. The age of the Qf_2 fan surface is unknown. The young alluvial fan deposits are generally incised across older fan surfaces and include the active channel deposits and distal fan sediments. The youngest unit also contains aeolian and beach sediment within the coastal zone.

PALEOSEISMOLOGY

Airphoto interpretation of the Aqaba regional surficial geology (Fig. 1) suggests that a strike-slip fault emerges from the gulf and that slip is transferred to cross faults. This geometry constrains the location of the Aqaba fault to lie east of the cross faults and west of alluvial fan surfaces that contain no north- to northeast-striking fault lineaments. The location of the Aqaba fault is therefore believed to lie within a 500-m swath that is covered by the modern city (Fig. 1). It appears that the Aqaba fault follows a recent wadi that has obliterated its active fault morphology. A ground-penetrating radar survey in the city confirmed the location of a portion of the Aqaba fault (Slater and Niemi, 2003; Abueladas, 2005; Abueladas *et al.,* in prep).

The Aqaba fault apparently trends northeast with increasing curvature as it dies out toward the northeast. This bending to the northeast of the eastern bounding fault of a pullapart has been noted for other large pullapart basins along the Dead Sea Transform including the Dead Sea and the Sea of Galilee (Garfunkel *et al.*, 1981; Garfunkel, 1981). Reches (1987) showed using clay model experiments that that faults initially bend away from each other at a dilational jog in ductile materials. This geometry led Reches (1987) to conclude that the Arabian plate was thickening by ductile deformation. The Aqaba fault should therefore have a reverse component to its motion. New GPR data across the fault confirm this prediction (Abueladas *et al.,* in prep; Fig. 2).

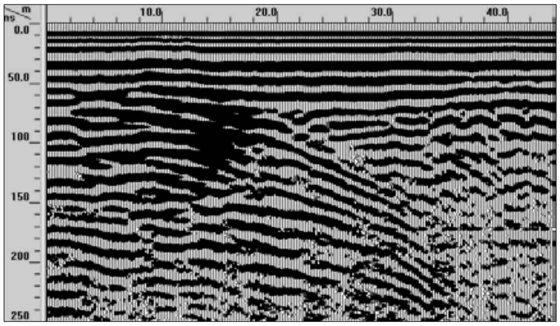

Figure 2. GPR profile highlighting the potential reverse component of the Aqaba fault. These data were collected as part of the MERC project "High resolution marine geophysical imaging of active faults in the Aqaba-Eilat region".

Geological trenches excavated across several faults in Aqaba document that the fault motion is transferred from the Aqaba fault onto five northwest - trending cross-faults that produce active tectonic subsidence at the head of the Gulf (Mansoor, 2002; Slater and Niemi, 2003; Fig. 4). Mapping of alluvial fan and buried soil horizons in trenches excavated on three of the cross faults reveal multiple fault ruptures on the highest scarps and fewer distinct ruptures on the lowest scarp (Mansoor, 2002). The scarp heights range from 25 cm across the youngest Qf_4 surface to 1.3 m across the older Qf_1 and Qf_2 surfaces. These data indicate that scarp heights reflect cumulative slip events. The most recent scarp-forming event fault occurred after A.D. 1045-1278 based on a corrected, calibrated radiocarbon age from charcoal collected from a buried campfire at the base of the scarp (Fig. 3). This likely represents fault motion in either the historical earthquakes of 1212 or 1068.

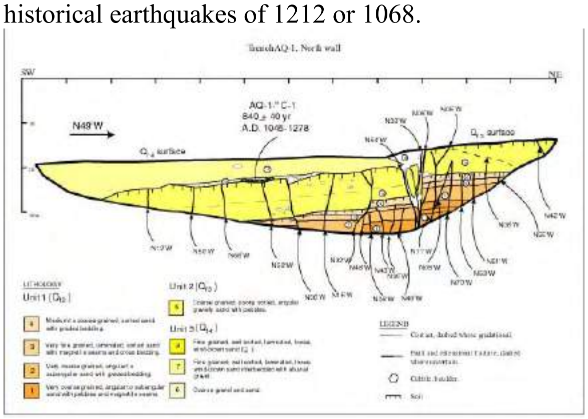

Figure 3. Trench log of the north wall of AQ-1 excvated across the cross fault 4 (Mansoor, 2002).

ARCHAEOSEISMOLOGY IN AQABA

Islamic Ayla

Based both on the historical accounts and the archaeological work of Whitcomb and Parker (*e.g.* 1996), it is clear that earthquakes have played a significant role in the history of the Aqaba region. The exact location of the Aqaba fault remains somewhat uncertain because it has never been exposed in paleoseismic trenches in this heavily urbanization location. Whitcomb (1993; 19) hypothesized that the wadi running across the ancient site of Ayla has its origins in erosion along the structural weakness of the fault itself. Thus, our main objective in investigating the city wall of Ayla was to test this hypothesis and to locate the Aqaba fault.

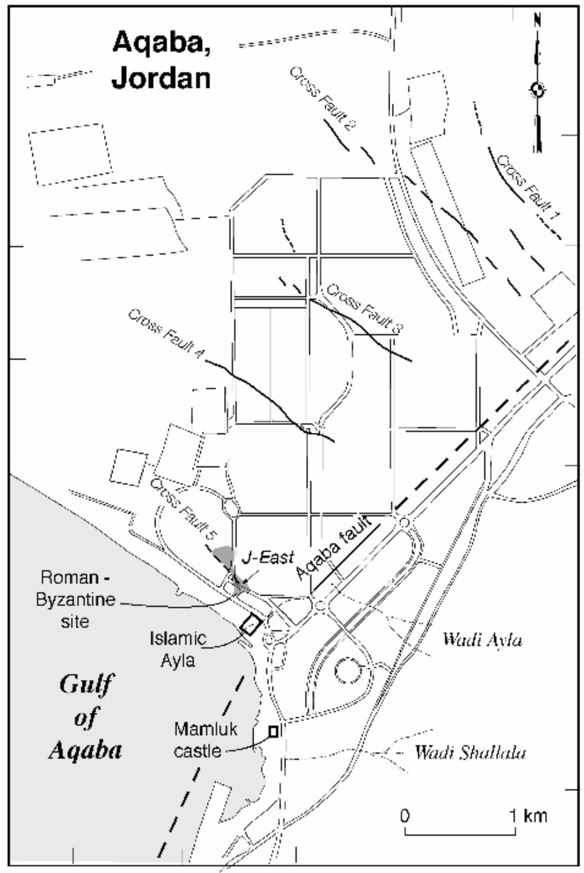

Figure 4. Map of the city of Aqaba showing the location of major archaeological sites. Active cross faults (CF) mapped from aerial photos and discovered in the archaeological excavations of J-east are also shown (Thomas et al., 2007).

The Early Islamic site of Ayla, extensively excavated by Donald Whitcomb of the Oriental Institute at the University of Chicago, is a walled city, circa 250 m southeast of the Byzantine city wall excavated by Parker (1996; 2002), and approximately 850 m north of the Mamluk castle in modern Aqaba (Fig. 4). The city of Islamic Ayla was probably founded under the Caliph 'Uthman ibn 'Affan around 650 A.D. (Whitcomb, 1995; 277). The city seems to have suffered some damage as a result of the 748 A.D. earthquake, and extensive reconstruction with the beginning of the Abbasid period (Whitcomb, 1994; 9). It is described by al-Muqaddasi in the late 10th century, as he described it in reference to the ruins nearby of the Roman/Byzantine site (after Whitcomb, 1997; 359). The town was severely damaged by the earthquake in 1068 A.D. (Ambraseys, 1994; 31). The destruction and loss of life (accounts claim that all but 12 residents who had been out fishing were killed) caused by this earthquake may account for the relative ease with which Baldwin I of Jerusalem took over when he arrived with a small retinue in 1116 A.D. Baldwin I constructed a small fortification (the origin of the current castle?), and a new settlement grew up around this (Whitcomb, 1997; 359). The site of Islamic Ayla was apparently never reoccupied to any significant degree after the time of the Crusaders.

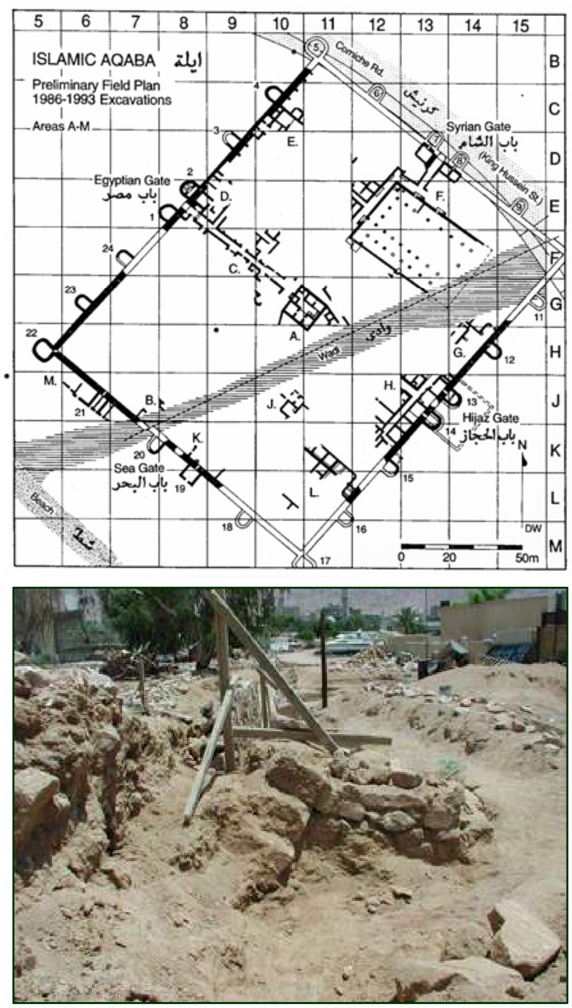

Figure 5. (Top) Site Plan of Early Islamic Ayla, from Whitcomb (1995). (Bottom) Section of the Sea Wall, tilted outward and buttressed in antiquity, with reconstructed wall on original alignment in background, view to SE.

Al-Hamoud and Tal (1998) conducted geotechnical investigations using three boreholes to a depth of 12m on the tell of Islamic Ayla. Archaeological deposits overlie sand and gravels. They noted tilting and sinking of exterior walls that they interpreted as slumping due to horizontal ground acceleration in an earthquake. Similar conclusions were reported by Al-Tarazi and Koryenkov (2007). According to the analyses of Mansoor *et al.* (2004), Ayla lies in an area of high liquefaction susceptibility due to the presence of saturated sands at shallow depth. This means that during seismic shaking, the substrate may lose its ability to bear weight, resulting in collapse of structures. Areas in the city of Aqaba that experienced subsidence in the Nuweiba earthquake of 1995 lie along the beach zone near the ancient site of Ayla (Wust 1997; Malkawi *et al.,* 1999; Al-Tarazi, 2000).

Rucker and Niemi (2005) reported on the results of excavation of the northeast corener tower the walled citadel of Islamic Ayla. In the four trenches excavated, the wall aligns across the entire width of the wadi indicating that no fault offset is present in the NE or SE city wall or through the corner tower in the wadi. Furthermore, the 2001 Department of Antiquities restoration project in the south corner of the site revealed a section of the Sea Wall that was tilted outward (Fig. 5). The outer edge of this section before excavation would have appeared on the ground surface 1.5 to 2m from the alignment of its actual foundation. Interestingly, it appeared to have been buttressed and continued in use in antiquity. This phenomenon, (easily caused by liquefaction and subsidence, not faulting) may provide an explanation for the apparent misalignment in the Sea wall above foundation levels observed by Whitcomb and others.

Byzantine Aila

The Roman Aqaba Project directed by S. Thomas Parker (North Carolina State University) excavated a monumental mudbrick structure heavily damaged by successive earthquake faulting in Aqaba (in excavation Area J-East), between 1994 and 2003. A collaborative study of the excavated evidence from this area identified a sequence of seven earthquakes that have ruptured the fault since the 2nd Century A.D. (Thomas *et al.,* 2007).

Previous excavations of the monumental Byzantine mudbrick structure indicate that a portion of this building collapsed in the earthquake of May 19, 363 A.D. This date is derived from over 100 coins of Constantius II (337-361 A.D.) found beneath a thick layer of collapsed mudbrick walls. Our detailed mapping of the excavated Early Byzantine walls revealed ancient repair work over seismically-induced structural wall failures. The structural repairs of the Church walls indicate that the southwest corner of the building subsided. This damage may have occurred in a minor earthquake (perhaps a significant foreshock) prior to the major earthquake that collapsed the structure. Based on subsidence across the fault location, changes in floor elevations, and layers of collapsed mudbrick, the archaeological data suggest that the site was ruptured in an early 2nd Century earthquake, an early 4th Century earthquake, and the 363 A.D. earthquake. The monumental use of the structure was converted to domestic use in the late 4th to early 5th Century.

Figure 6. Faults across the Byzantine mudbrick building in Aqaba. Person is standing by the wall that is faulted. View toward the SW.

We also have evidence for primary ground rupture for at least four post-date 363 A.D. earthquakes that transect the ruins in the J-East area of Aila. Primary fault rupture is documented in stratigraphic sections and plan maps of walls of various construction age (Fig. 6). Two earthquakes occurred during the Late Byzantine to Umayyad period (sith to eighth Century). There is a hiatus of deposition at this location between the Umayyad and the modern age. The two most recent earthquakes, with 42 and 35 cm of dip slip, occurred some time after the 8th Century and may correlate to the historical earthquakes of 1068 and 1212 A.D. No stratified materials were found at this site that could be used to further refine the timing. Our data suggest significant periods of active seismicity (M 6-7) in the 4th, 7th-8th, and probably in the 11th-13th Centuries. These data clearly show that historical earthquake catalogues are incomplete with regard to some of the less damaging earthquakes that have affected southern Jordan but may have played a significant role in the cultural history of the region. The data also document a long period of quiescence since the last phase of intense earthquake activity along the southern Dead Sea transform and highlight the elevated potential earthquake hazard in the region.

GEOLOGY FROM AQABA TO PETRA

The mountains east of Aqaba and for a distance of 50 km northeast are Precambrian igneous rocks of the Aqaba Granite Complex (Rashdan, 1988). These igneous rocks are composed of granite, monzogranite, granodiorite, and quartz diorite that developed during the Pan-Arrican orogeny. A series of dikes with widely varying compositions from diabase to felsite cross cut the granitic rocks.

Nonconformably overlying the Aqaba Granite Complex are Paleozoic rocks of the Ram Group (Fig. 7). Cambrian arkosic sandstones and conglomerates derived from the weathered granitic rocks (Salib Formation) form the basal unit. These rocks grade into massive quartzose sandstones of Cambrian to Silurian age (Umm Ishrin and Disi Formations). Outcrops of Lower Paleozoic sandstone are present 50 km northeast of Aqaba along the eastern mountain range. Erosion of the sandstone supplies the sand which has formed extensive dune field within Wadi ‘Arabah to the north.

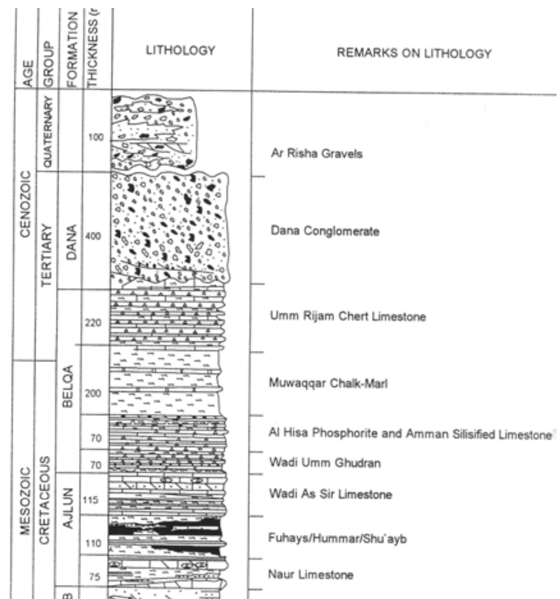

Figure 7. Generalized graphic log of the lithostratigraphic units exposed in Southern Jordan (Barjous, 2003).

The road to Amman crosses the Aqaba Complex rocks within the canyon of Wadi Yutim along part of the King's Highway—the *Via Nova Traiana* commissioned by Trajan in 111-114 A.D. The walls of the canyon expose the cross-cutting late phases of dike intrusion during the latest Precambrian. Pleistocene terraces line the course of the wadi.

Near the turn-off for Wadi Rum, the valley opens and the contact between the Aqaba Complex and overlying sedimentary sequence is easily discerned. The nonconformity represents an erosional peneplain that is tilted to the east (Abed *et al.,* 1998).

North of Wadi Rum the region of Ras En Naqab is a spectacular area of scenic beauty. The NW-SE trending fault escarpment separates Lower Cretaceous varicolored sandstone and Upper Cretaceous carbonates in the north from the sandstone highlands in the south (Abed *et al.,* 1998). The recent highway improvements in this area expose outcrops of faulted bedrock.

PETRA

Petra, the "Rose City" was the capital of the Nabataeans during the Hellenistic and into the Roman periods. In the Siq of the Petra, you will first pass through the white Disi Sandstone and then the underlying thick red Umm Ishrin sandstone into which most of the monuments were carved (Abed *et al*., 1998). "Following the course of Wadi Musa, the city-center was laid out on either side of the colonnaded street on an elongated plan between the theater in the east and Qasr al Bint in the west. Petra basin boasts over 800 individual monuments that were mostly carved in the Cambrian sandstone by the technical and artistic genius of the Nabataeans" (Barjous, 2003). Some of the most famous antiquities at Petra include al Khazneh (the Treasury), Qasr al-Bint (the free-standing, two-storey building), the Roman Amphitheater, the Great Temple, the Temple of the Winged Lion, and the Petra Church.

Several earthquakes are likely to have caused damage at Petra since it's founding. Josephus Flavius in his *Jewish Wars* describes an earthquake in 31 B.C. that "killed an infinite number of cattle and thirty thousand people" in Palestine (Guidoboni, 1994: 173). Evidence from this early occupation period is scanty because of later monumental construction.

There is evidence of massive destruction in Petra at the Temple of the Winged Lions, at the Great Temple, and other monuments dated to the beginning of the 2nd century A.D. Much scholarly debate has focused on the interpretation of the destruction in light of sparse and rather enigmatic documentary evidence for the Trajanic annexation of Nabataea ca. 106 A.D. The lack of historical text leaves open the possibility of multiple interpretations for the destruction horizons. Coins and milestones suggest Arabia was "acquired" rather than gained by military force. Corroborating evidence for a 2nd C. earthquake in the southern Levant has been documented at Nabataean sites in the Negev, Wadi 'Arabah (Arava Valley), and at Aqaba. The coincidence of an earthquake with a documented political transition makes unequivocal interpretation of the archaeological record extremely difficult (Niemi *et al.,* 2006).

Undeniably, Petra sustained significant damage in the May 19, 363 earthquake that affected the region from north of Lake Tiberias to Aqaba in the south. Russell (1980) and Guidoboni (1994: 264-267) provide convincing literary data for the earthquake. Furthermore, coins from 358-361 beneath collapse at the Petra site of Ez-Zantur (Stucky *et al.,* 1990) and Aqaba (Parker, 1999) confirm damage at both sites in the earthquake.

Figure 8. Collapsed columns of the Great Temple at Petra viewed toward the east. The collapse likely dates to late antiquity sometime after the 6th century.

In the Byzantine period, the Urn tomb was modified into a 5th century church. Other churches were constructed through the 6th and 7th centuries as Petra thrived as a Byzantine center. Many Hellenistic- and Roman-era Nabataean building stones and architectural elements are reused in this construction phase. Excavators of the Petra garden and pool complex just east of the Great Temple (Bedal *et al.,* 2007) note that the final destruction there probably occurred in the 6th century, perhaps they hypothesized, by the 551 A.D. However, the source rupture of this earthquake is the Lebanese coast (Elias *et al.,* 2007).

Scrolls found in the Petra Church provide an unprecedented record of Late Byzantine Petra (Feima *et al.,* 2001). The church was destroyed in a fire at the end of the 6th or the beginning of the 7th century. The fire carbonized scrolls that were being stored in the church. The last recorded date on the scrolls is 597 A.D. It is possible that the earthquake that destroyed

Aereopolis (east of the Dead Sea) based on a dedicatory inscription found there that states "Restored in 492 (597-598 C.E.) after the earthquake" (Zayadine, 1971), also caused damage in Petra.

After the fire and into the 7th century A.D., the church ceased to function as an ecclesiastical building, materials were gutted, and the shell of the structure was converted to a domestic complex. Feima *et al.* (2001) noted evidence for two earthquakes in the later phases of the Petra Church—one in the 7th Century and one in the medieval to Ottoman period—at which time no columns remained standing.

REFERENCES CITED

Abed, A.M., Jarrar, G., and Atallah, M., 1998, Geology of Jordan—An overview: 6th Jordanian Geological Conference 5-8 October, 1998, University of Jordan, Amman, Jordan, 12 p.

Al-Homoud A.S. and Tal A.B., 1998, Geotechnical study for evaluating stability and restoration work at the 1,000 year old archaeological site of Ayla, Gulf of Aqaba, Kingdom of Jordan: *Environmental and Engineering Geoscience*, v. 4, p. 103-114.

Al-Tarazi, E., 2000, The major Gulf of Aqaba earthquake, 22 November 1995—maximum intensity distribution: *Natural Hazards*, v. 22, p. 11-27.

Al-Tarazi, E., and Korjenov, A.M., 2007, Archaeoseismological investigation of the ancient Ayla site in the city of Aqaba, Jordan: *Natural Hazards*, v. 42, no. 1, p. 47-66.

Ambraseys N. N., Melville, C.P. and Adams, R.D., 1994, *The Seismicity of Egypt, Arabia, and the Red Sea*.Cambridge University Press, Cambridge, 181 p.

Barjous, M.O., 2003, *The Geology of Petra and Wadi Al Lahyana Area, Map Sheets No. 3050-I and 3050-IV*, National Resources Authority, Geology Directorate, Amman, Jordan, 93 p. Map scale 1:50,000.

Bedal, L.-A., Gleason, K.L., Schryver, J.G., 2007, The Petra garden and pool complex, 2003-2005: *Annual of the Department of Antiquities of Jordan*, v. 51, p. 151-176.

Elas, A., *et al.,* 2007, Active thrusting offshore Mount Lebanon: Source of the tsunamigenic A.D. 551 Beirut-Tripoli earthquake: *Geology*, v. 35, no. 8, p. 755–758.

Feima, Z.T., Kanellopoulos, C., Waliszewki, T., and Schick, R., 2001, *The Petra Church*, P.M. Bikai (ed.), American Center of Oriental Research, Amman, Jordan, 446 p.

Garfunkel, Z., Zak, I., and Freund, R., 1981, Active faulting in the Dead Sea Rift: *Tectonophysics*, v. 80, p. 1-26.

Garfunkel, Z., 1981, Internal structure of the Dead Sea leaky transform (rift) in relation to plate kinematics: *Tectonophysics*, v. 80, p. 81-108.

Guidoboni, E., 1994, *Catalogue of ancient earthquakes in the Mediterranean area up to the 10th century*. Roma, Italy: Istituto Nazionale di Geofisica, 504 p.

Malkawi, A.H., Abdulla, F., and Barakat, A.B., 1999, The Earthquake of November 22, 1995: *Earthquake Spectra,* v. 15, no. 3, p. 711-724.

Mansoor, N.M., 2002, A GIS-based assessment of active faults and liquefaction potential of the city of Aqaba, Jordan: M.S. Thesis, Geosciences Dept., UMKC, 258 p.

Mansoor, N.M., Niemi, T.M., and Misra, A., 2004, A GIS-based assessment of liquefaction potential of the city of Aqaba, Jordan: *Environmental and Engineering Geoscience*, v. 10, no. 4, p. 297-320.

Niemi, T.M., and Smith, A.M., II, 1999, Initial results of the southeastern Wadi Araba, Jordan geoarchaeological study: Implications for shifts in Late Quaternary aridity: *Geoarchaeology*, v. 14, no. 8, p. 791-820.

Niemi, T.M., Thomas, R., and Parker, S.T., 2006, A 2nd century earthquake at the time of the Roman annexation of Nabataea?: *Geological Society of America* annual meeting, Philadelphia, PA, Oct. 22-25, 2006.

Parker, S.T., 1996, The Roman Aqaba Project: Preliminary Report of the 1994 Season, *Annual of the Department of Antiquities of Jordan*. Amman.

Parker, S.T., 1999, Brief notice on a possible early 4th century church at Aqaba, Jordan: *Journal of Roman Archaeology, v.* 12, p. 372–376.

Parker, S.T., 2002, The Roman Aqaba Project: Preliminary Report of the 2000 Season. *Annual of the Department of Antiquities*, Amman

Rashdan, M., 1988, *The regional geology of the Aqaba-Wadi Araba area*, Map Sheets No. 3049 III and 2949 II: National Resources Authority, Geology Directorate, Amman, Jordan, 87 p. Map scale 1:50,000.

Reches, Z., 1987, Mechanical aspects of pull-apart basins and push-up swells with application to the Dead Sea transform: *Tectonophysics*, v. 141, p. 75-88.

Rucker, J.D., and Niemi, T.M., 2005, New excavations of the city wall at Islamic Ayla in Aqaba, Jordan: *Annual of the Department of Antiquities of Jordan*, v. 49, p. 501-508.

Russell, K.W., 1980, The earthquake of May 19, A.D. 363: *Bulletin of the American School of Oriental Research,* v. 238, p. 47–64.

Slater, L., and Niemi, T.M., 2003, Detection of active faults along the Dead Sea Transform using ground penetrating radar and implications for seismic hazards within the city of Aqaba, Jordan: *Tectonophysics,* v. 368, p. 33-50.

Stucky, R.A. *et al*., 1990, Schweizer Ausgrabungen in Ez Zantur, Petra Vorbericht der Kampagne 1988: *Annual of the Department of Antiquities of Jordan*, v. 34, p. 249-283.

Thomas, R., Niemi, T.M., and Parker, S.T., 2007, Structural damage from earthquakes in the 2nd-9th Century at the archaeological site of Aila in Aqaba, Jordan: *Bulletin of the American School of Oriental Research*, v. 346, p. 59-77.

Whitcomb, D., 1993, *Oriental Institute Annual Report* 1992-1993/

____, 1994a, Water and Recent Excavations at Aqaba, *The Oriental Institute News and Notes*. University of Chicago.

____, 1994b, A Street and the Beach at Ayla: The Fall Season of Excavations at Aqaba. 1992, *Annual of the Department of Antiquities of Jordan*. V. 39, p. 499-507.

____, 1995, The *misr* of Ayla: New Evidence for the Early Islamic City, *Studies in the History and Archaeology of Jordan V, Amman: Department of Antiquities.*

____, 1997, The Town and Name of 'Aqaba: An Inquiry into the Settlement History from an Archaeological Perspective*, Studies in the History and Archaeology of Jordan* v. 6, Amman: Department of Antiquities.

Wust, H., 1997, *The November 22, 1995, Nuweiba Earthquake, Gulf of Elat (Aqaba): Post Seismic Analysis of Failure Features and Seismic Hazard Implications*: Geological Survey of Israel, Report GSI 3-97, Jerusalem, Israel.

Zayadine, F., 1971, Un séisme a Rabbat Moab (Jordanie) d'apres une inscription Grecque du VIe S., *Berytus*, v. 20, p. 139-141.

A r a v a v a l l e y

22.2.2009

Fie l d l e a d e r

A r i m a t m o n

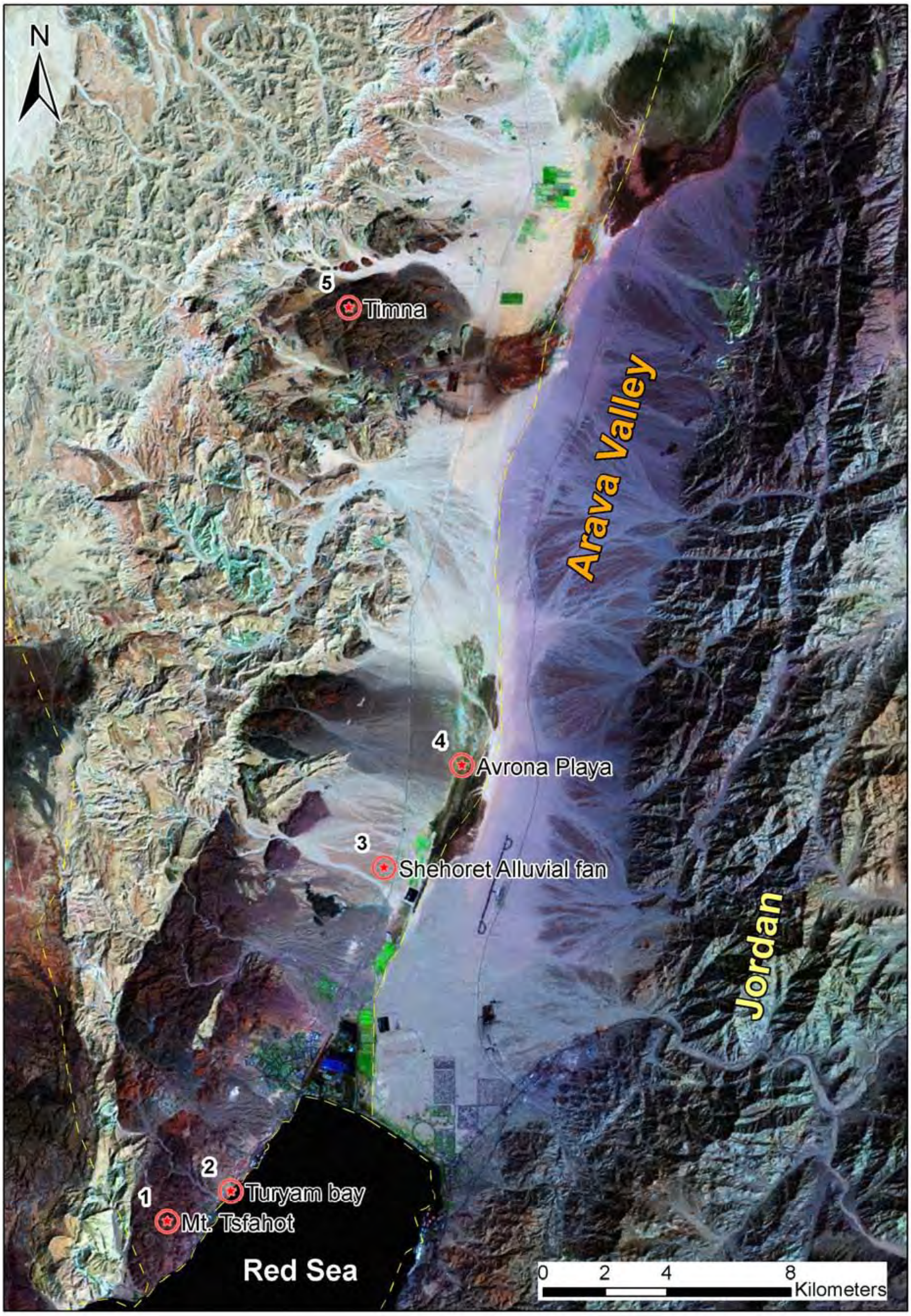
N
5
Timna
Arava Valley
4
Avrona Playa
3
Shehoret Alluvial fan
Jordan
2
Turyam bay
1
Mt. Tsfahot
Red Sea
0 2 4 8
Kilometers


N
Machtesh Ramon
Arava Valley
Paran Valley
Petra
6
Central Arava
Jordan
5
Timna
0 4 8 16
Kilometers

The structure of the western margin of the Dead Sea rift, southern Arava Valley

(modified after Garfunkel et al., 1974, ' Raham conglomerate – new evidence for Neogene tectonism in the southern part of the Dead Sea Rift) paper attached

The Red Sea Rift splits in the N into the Suez Rift and the Dead Sea Rift (Fig. 1). The southern part of the latter is occupied by the Gulf of Elat (Aqaba). A thick marine Neogene series developed in the Suez Rift attests to its already advanced development in Miocene, and probably in older, times (Hume, 1906; Said, 1962; Robson, 1971). Marine Miocene rocks are also known from the southern tip of the Gulf of Elat (Hume, 1906; Omara, 1959; Bramkamp *et al.*, 1963; Goldberg, (unpub. thesis, Hebrew University of Jerusalem) 1957; see Fig. 1), but these do not bear any direct evidence on the age of the tectonic depression which comprises the Dead Sea Rift. Neogene sediments were not clearly identified nor described from the southern part of the Dead Sea Rift. This led to the belief that the Gulf of Elat, which is much deeper than the Gulf of Suez and bears abundant evidence of young tectonism, was shaped by Quaternary movements only. The southernmost Neogene basin within the Dead Sea Rift, located more than 100 km N of the Gulf of Elat, is filled with continental sediments of the Hazeva Formation (Bentor & Vroman, 1957; Garfunkel & Horowitz, 1966).

This work describes a newly discovered group of Neogene sediments around the northern part of the Gulf of Elat, herein called the Raham Conglomerate, which bears direct evidence on the Neogene existence of the southern part of the Dead Sea Rift.

The Raham Conglomerate was deposited subsequent to, and as a result of, the creation of a considerable topographic and structural relief in the Elat region. The retreating Middle (and Late?) Eocene seas left a very subdued relief here and an almost tabular structure, later considerably modified by tectonic movements and by erosion, mainly related to the formation of the Dead Sea Rift. The formation of the deformed Raham Conglomerate is related herein to the early stages of the formation of the Rift Valley during the Neogene.

The existence of a considerable topographic and structural relief when the Conglomerate was formed is indicated by the coarseness of the conglomerates and the nature of the clast-

The occurrence of clasts from different parts of the section requires that they were all exposed side by side, which could result only from tectonic uplifting and subsequent stripping of the overlying sediments. In particular the occurrence of clasts of Precambrian rocks in Nahal Taba indicates that the basement rocks were exposed at least at the same topographic elevation as the Eocene rocks which underlie the Conglomerate. Therefore, S of Nahal Taba the structural relief was at least 1200 m, which is approximately the thickness of the sedimentary cover in this region. If much of the structural relief was achieved by flexures, as it is now, then the structural relief must have been considerably larger, perhaps exceeding 2 km. Analogously, a lesser, though still considerable relief, is also indicated near Ras Burqa.

Precambrian rocks are now exposed W of the northern part of the Gulf of Elat in a narrow strip, due to uplifting along the margins of the rift valley. The older outcrops could not have been larger, and rocks similar to the clasts in the Raham Conglomerate are exposed there. It is therefore assumed that the development of the border structures of the rift in this region was well under way when the Raham Conglomerate was deposited, possibly as a syntectonic sediment.

The angular unconformities at the base of the Raham Conglomerate suggest still older tectonism, but since the various outcrops are probably not strictly contemporaneous, an older and distinct phase cannot be demonstrated.

Later movements deformed the Conglomerate, and erosion stripped the rock formations which supplied the clasts of the Conglomerate from most of the area. In particular Senonian to Eocene rocks, which were still abundant in the Elat region when the Raham Conglomerate was formed, are now virtually completely eroded, except in few structural lows. It is most probable that considerable volumes of the Raham Conglomerate itself were also eroded.

The bulk of the Conglomerate is probably fluviatile and lacustrine, but the occurrence of marine beds indicates that an arm of the sea, conveniently termed the 'ancestral' or 'proto' Gulf of Elat, reached as far N as the Elat region. This further corroborates the conclusion that the depression of the Dead Sea Rift was already well outlined when the Raham Conglomerate was deposited. This old Gulf probably did not communicate with the Mediterranean, but only with the Red Sea. Marine Neogene sediments are well developed at the southern end of the Gulf of Elat (see Fig. 1, and Omara, 1959; Bramkamp *et al.*, 1963; Goldberg, 1957, see Introduction above), but they do not clearly prove the existence of a Neogene Gulf. The few fossil occurrences and the tectonic position indicate a Neogene age for the Raham Conglomerate.

Additional information can be derived from consideration of the relations of the Raham Conglomerate with continental sediments preserved on the plateau W of the Gulf of Elat (Fig. 1).

These sediments belong to the higher parts of the Hatzeva Formation and contain conglomerates of extremely well-rounded pebbles, mainly of chert and quartzites, of the type known as the 'cover conglomerate' (Bentor & Vroman, 1957; Garfunkel & Horowitz, 1966). These conglomerates were transported over distances exceeding 150–200 km, and in the N interfinger with marine sediments of Late Miocene or earliest Pliocene age (Reiss & Gvirtzman, 1966).

The conglomerates in the higher parts of the Hazeva Formation are probably only broadly contemporaneous, but they do seem to record a definite episode when a well-integrated drainage system crossed the entire Negev and debauched into the Mediterranean in the Beer Sheba region.

For the present purpose the following observations are important:

(a) The 'cover conglomerate' was transported across the outcrops of the Raham Conglomerate west of Elat (Fig. 1).

(b) The 'cover conglomerate' was deposited on rocks of the Judea Group or on down-faulted younger rocks; the field relations indicate that by that time the Eocene rocks had already been virtually completely eroded away from the region west of Elat, and the Senonian rocks were also largely eroded.

(c) The virtual total absence of clasts of local derivation, and the great distances of transport of the clasts of the 'cover conglomerate' indicate a generally subdued, plateau-like landscape. In fact, the region N of Sheikh Atiya still largely retained this physiography.

These features suggest that the Raham Conglomerate, except perhaps the uppermost parts of the section near Ras Burqa, is older than the 'cover conglomerate' in this region, and that a period of extensive erosion intervened between the two. Thus the Raham Conglomerate may be of Middle Miocene or even older age.

It should be stressed that the very characteristic clast assemblage of the 'cover conglomerate' was not found in any of the outcrops of the Raham Conglomerate or anywhere else in the rift valley within a distance of 150 km N of Elat. It seems that the interior of the rift valley in the Elat region was already separated by a watershed from the drainage of the plateau W of it, similar to the present situation.

The Raham Conglomerate is probably roughly equivalent to the basal conglomerate and lower parts of the Hazeva Formation of the Central Arava and Northern Negev, which are older than the 'cover conglomerate' (Bentor & Vroman, 1957). This is suggested not only by the relations in the Elat region discussed above, but also by:

(a) general lithologic similarity;

(b) similar tectonic position, namely deposition in the first morphotectonic or topographic depressions to be formed along the borders of the Dead Sea Rift, and probably also inside the rift valley.

A new formational name is suggested herein for the southern conglomerates because they were deposited in a separate basin or in several basins which were related to the Gulf of Elat. On the other hand, the Hazeva Formation was related to a northward flowing drainage system and to a basin in the Central Arava. Thus it seems that the two groups of sediments record somewhat different histories.

It seems that the Raham Conglomerate is also generally correlative with the 'Untere Syntektonische Konglomerate' of southern Jordan which occurs in similar structural circumstances, and possibly also with an outcrop of marine Neogene beds at Gebel Hureij, all of which were described by Bender (1968).

Summarizing, the Raham Conglomerate records a Middle Miocene or older phase of deposition which was related to early movements in the southern half of the Dead Sea Rift. A morpho-tectonic depression was already developed and it was partly occupied by the 'proto' Gulf of Elat, which communicated with the Red Sea. The structural relief in some parts of the border structures of the rift exceeded 1.2 km, and probably even 2 km.

The major erosion of the rift margins which ensued in response to the deepening of the rift valley had not yet occurred when the Raham Conglomerate was formed, and the cover of Eocene rocks was still largely preserved in the Elat region. The deposition of the Raham Conglomerate in fact records part of this erosion, which was already very advanced by the time of the deposition of the 'cover conglomerate' (Latest Miocene or Early Pliocene) of the Hazeva Formation.

Later tectonism greatly deformed the Raham Conglomerate and eventually shaped the present form of the rift valley.

Plate arrangement in the eastern Mediterranean region

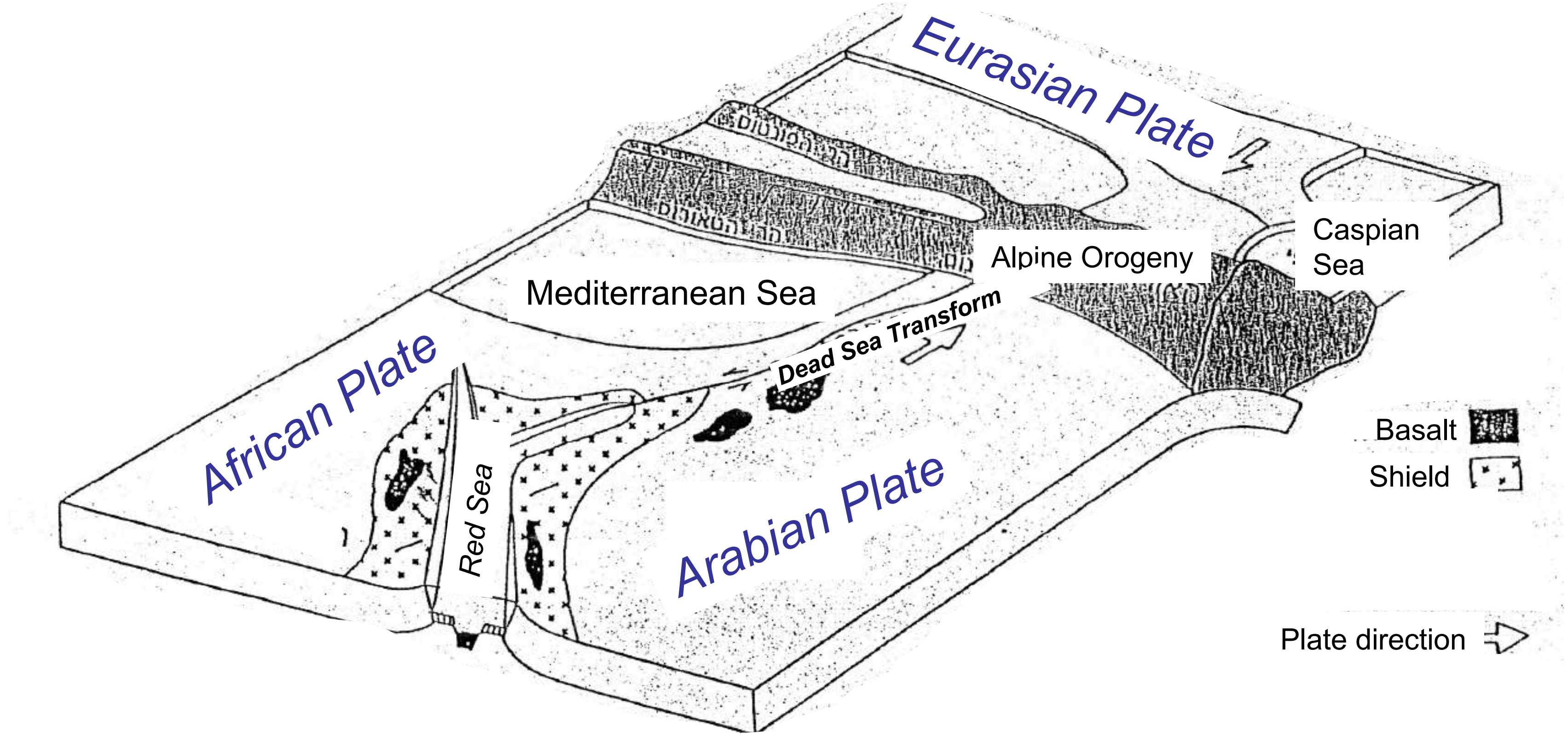

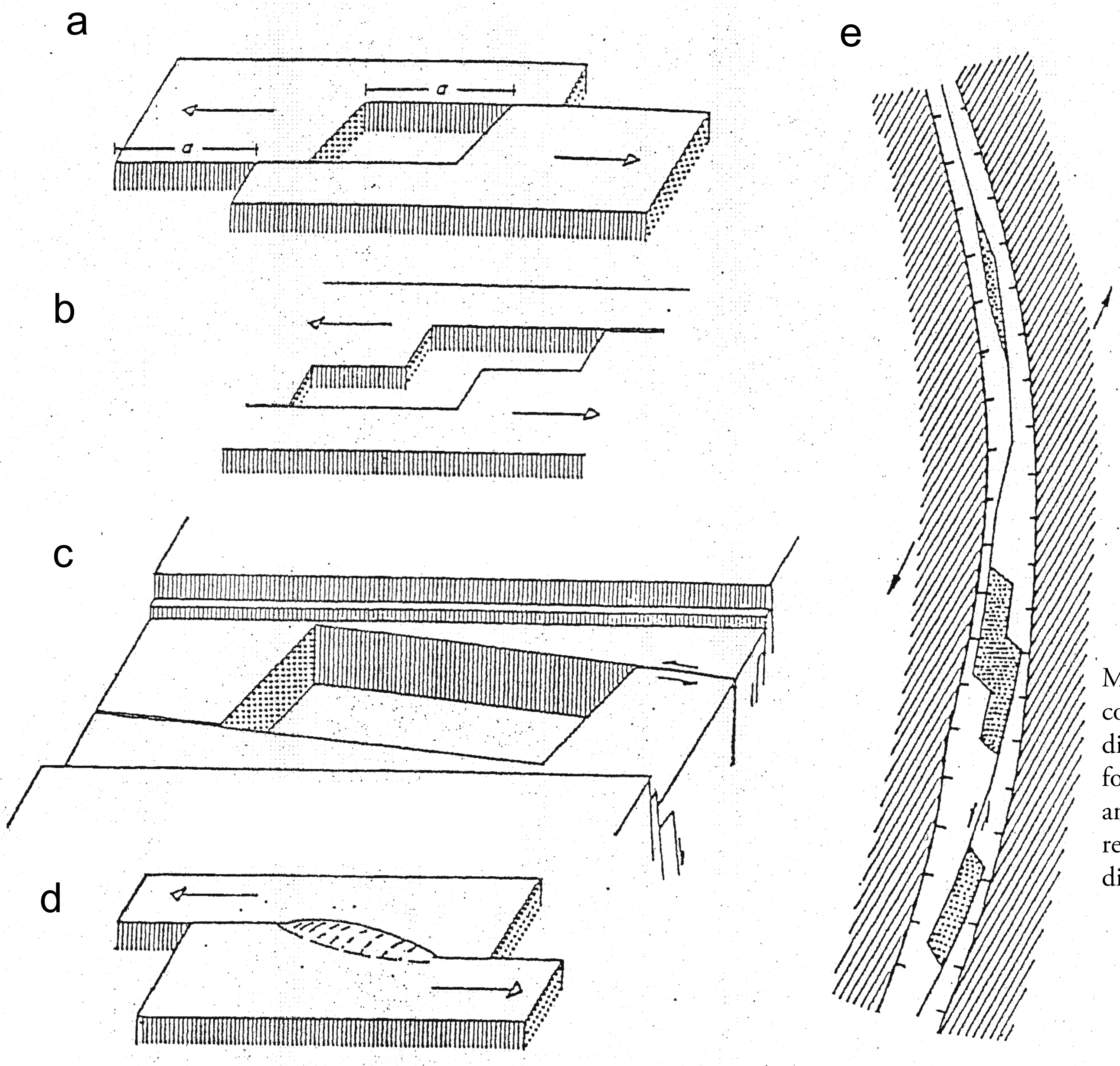

Garfunkel, 1981

Motion along the Dead Sea fault is composed of lateral and normal displacement. This combination forms deep rhomb shaped grabens and push ups within a rift valley as a result of shift in the plate boundary direction.

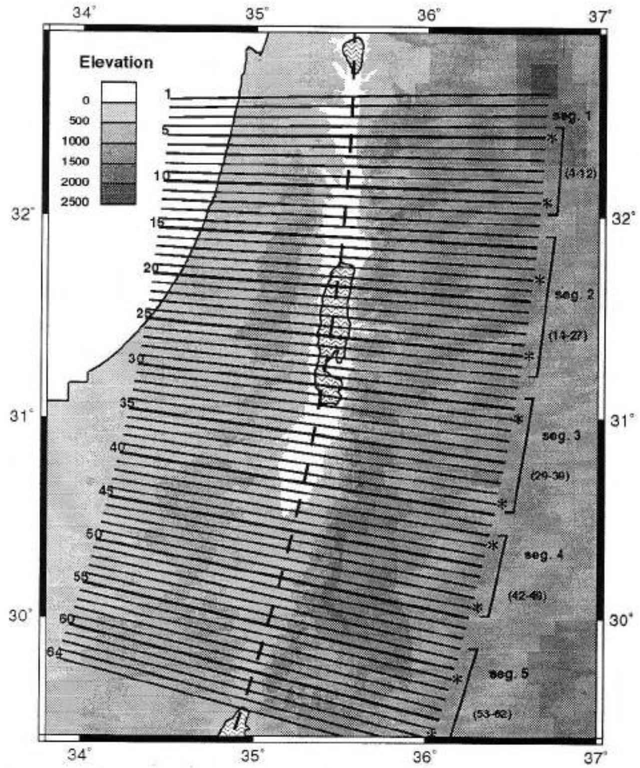

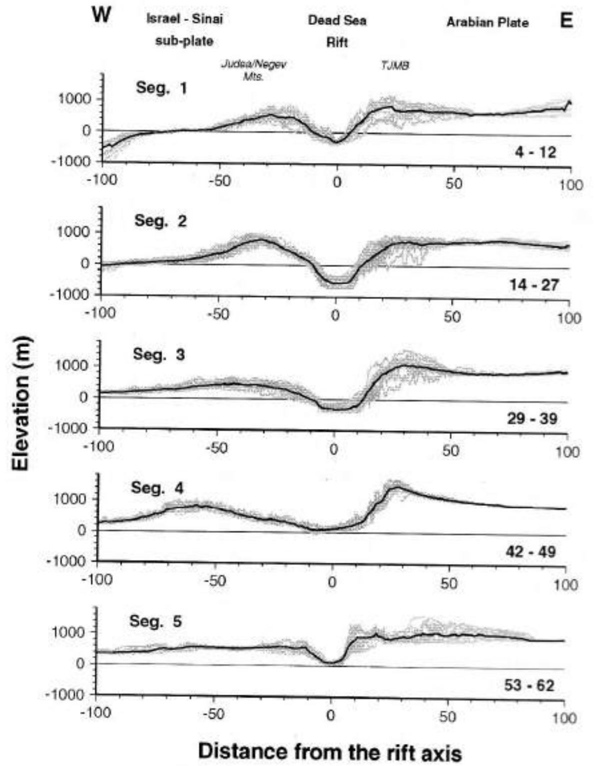

Wdowinski and Zilberman, 1997

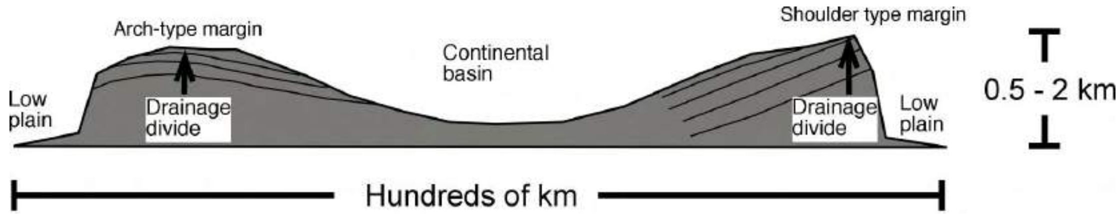

Generalized continental margin geometry modified from Ollier (1984). *Shoulder-type margins* are those where the uplift axis is located at the edge of the uplifted domain. Along these margins, the drainage divide is coincident with the top of the escarpment. *Arch-type margins* are those where the uplift axis is located inland from the edge of the uplifted domain. Along these margins, the drainage divide is separated from the top of the escarpment (Matmon et al., 2002).

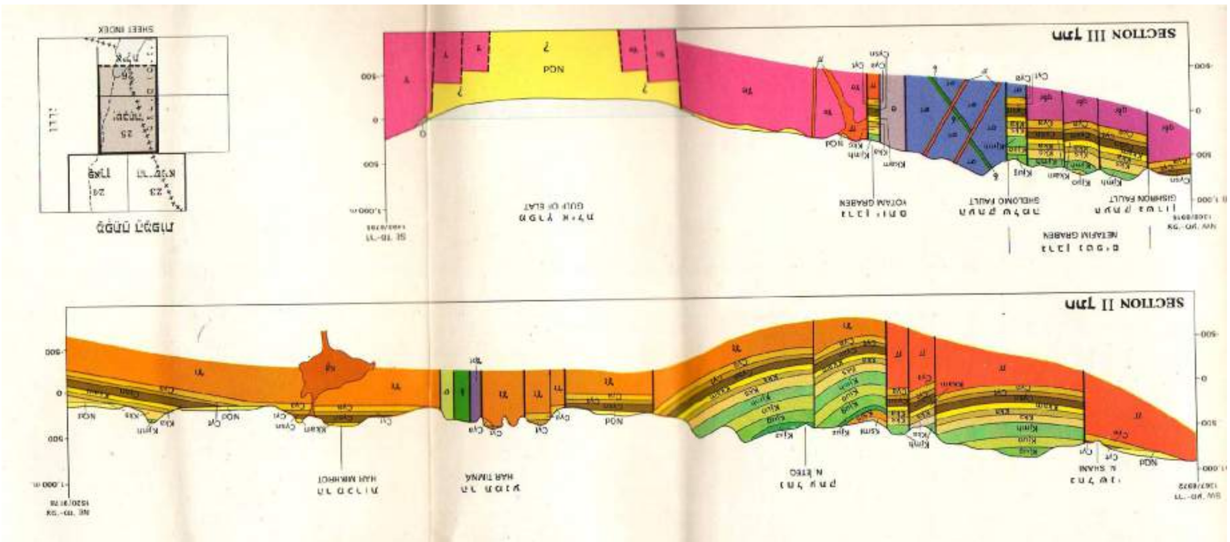
SECTION III
SECTION II
GULF OF ELAT
SHELOMO FAULT
NETAFIM GRABEN
YOTAM GRABEN
GISHRON FAULT

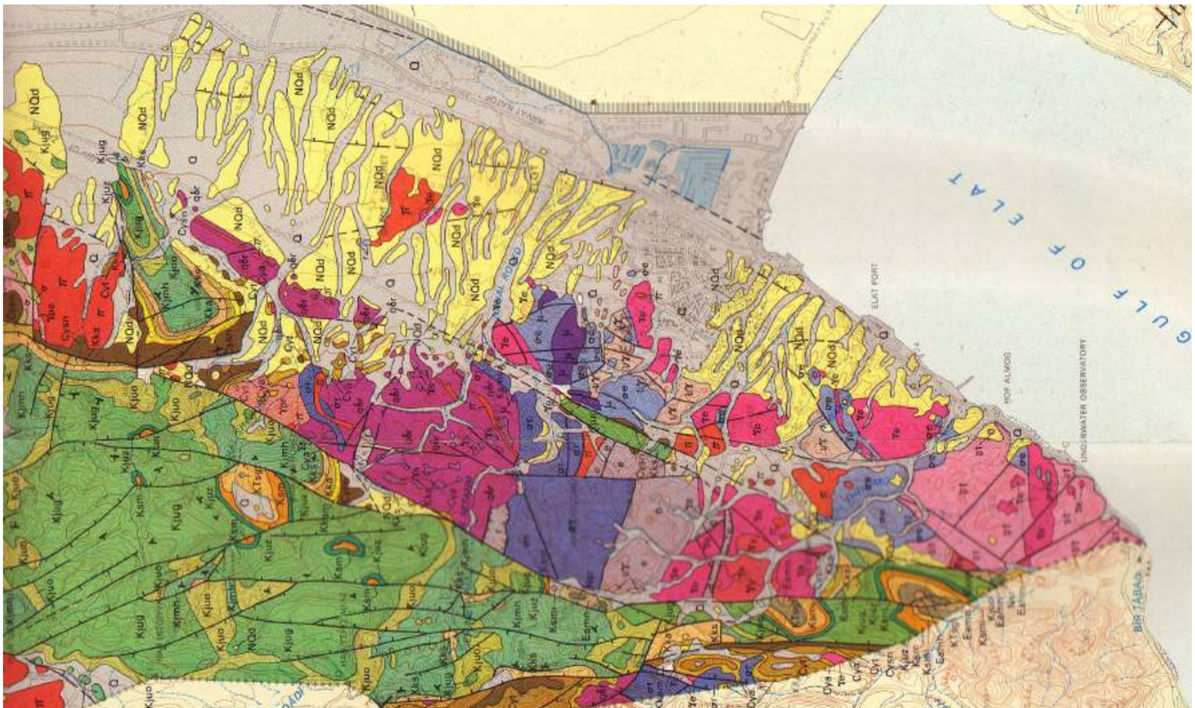
GULF OF ELAT
ELAT PORT
HOF ALMOG
UNDERWATER OBSERVATORY

Geodetic and Geophysical Background of the Arava Valley

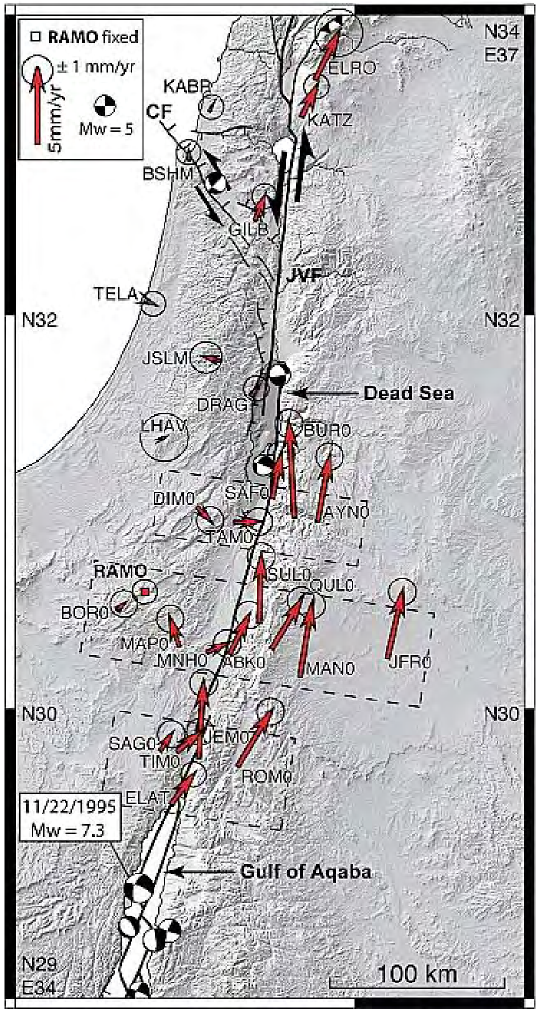

Figure 1: Tectonic map and horizontal velocity field plotted relative to site RAMO. Also shown focal mechanisms of events with ML > 5 that occurred since 1976 (USGS (http://www.seismology.harvard.edu) and GII (http://www.gii.co.il) databases). Le Beon et al., 2008.

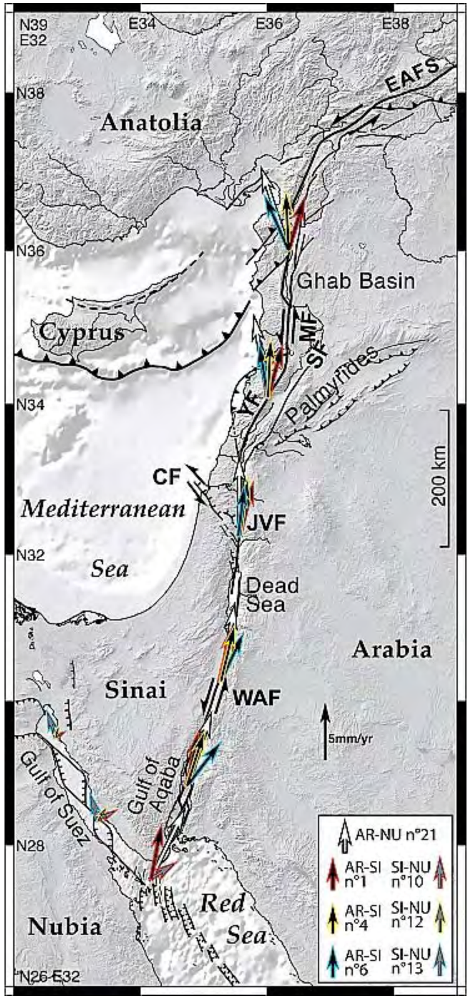

Figure 2: Regional kinematics predicted by selected Euler vectors. AR, Arabia; NU, Nubia; SI, Sinai. Pole numbers refer to Tables 4, 5a, and 5b. EAFS, East Anatolian fault system; WAF, Wadi Araba fault; JVF, Jordan Valley fault; CF, Carmel fault; YF, Yammouneh fault; SF, Serghaya fault; MF, Missyaf fault. Le Beon et al., 2008.

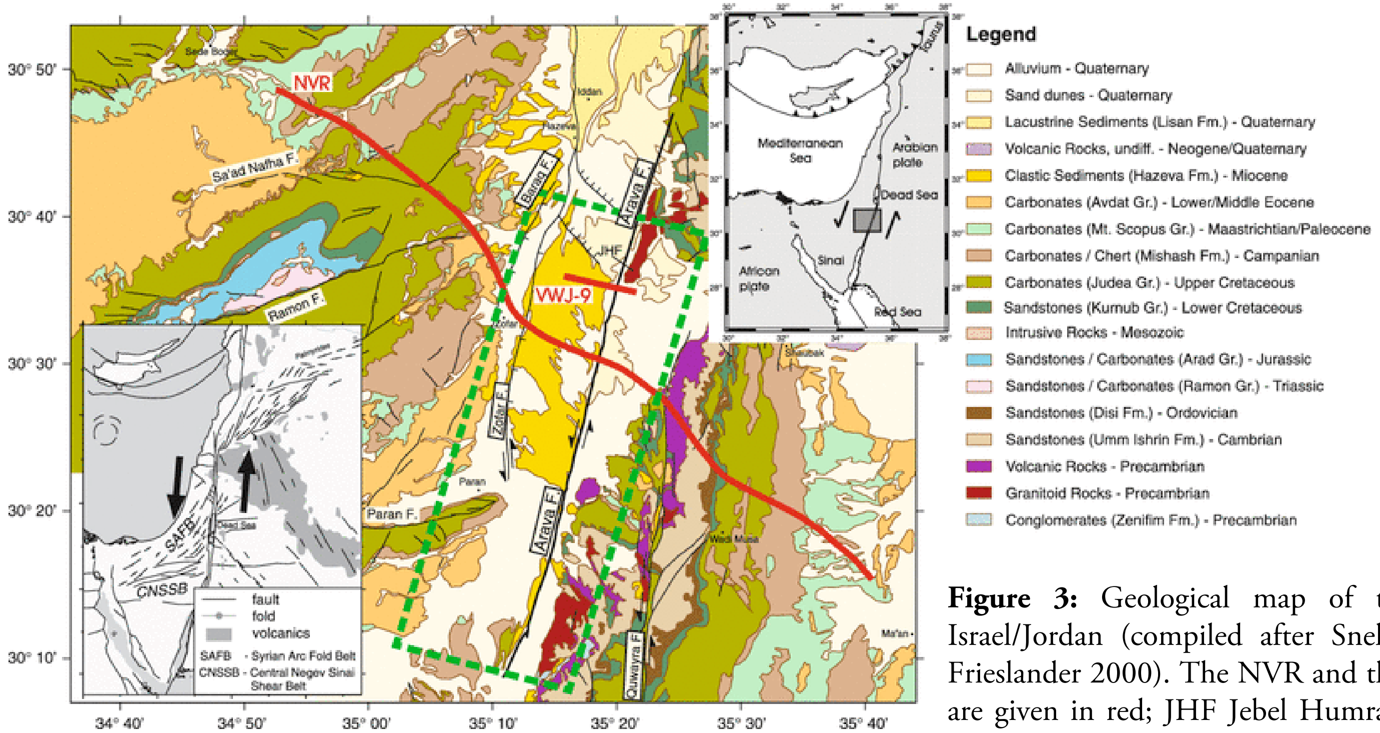

Figure 3: Geological map of the central Arava/Araba Valley in Israel/Jordan (compiled after Sneh et al. 1998; Bender et al. 1968; Frieslander 2000). The NVR and the VWJ-9 common depth point lines are given in red; JHF Jebel Humrat Fiddan. The right inset shows the tectonic setting of the area and indicates the left lateral displacement of 105 km. The left inset shows information on some major tectonic elements in the Dead Sea region (after Sneh et al. 1998). The green dashed box indicates the area of subsequent figures. Kesten et al., 2008.

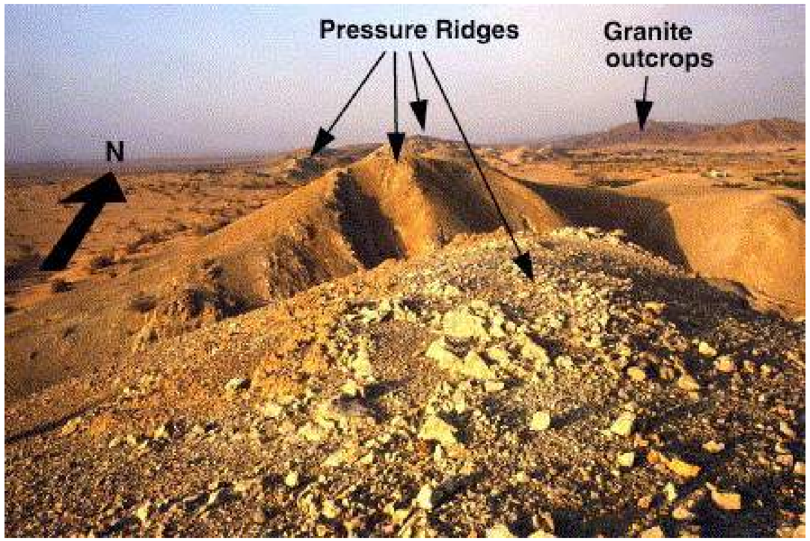

Figure 4: View of the pressure ridges in the northern part of Haberland et al.'s (2007) study area. View toward the North.

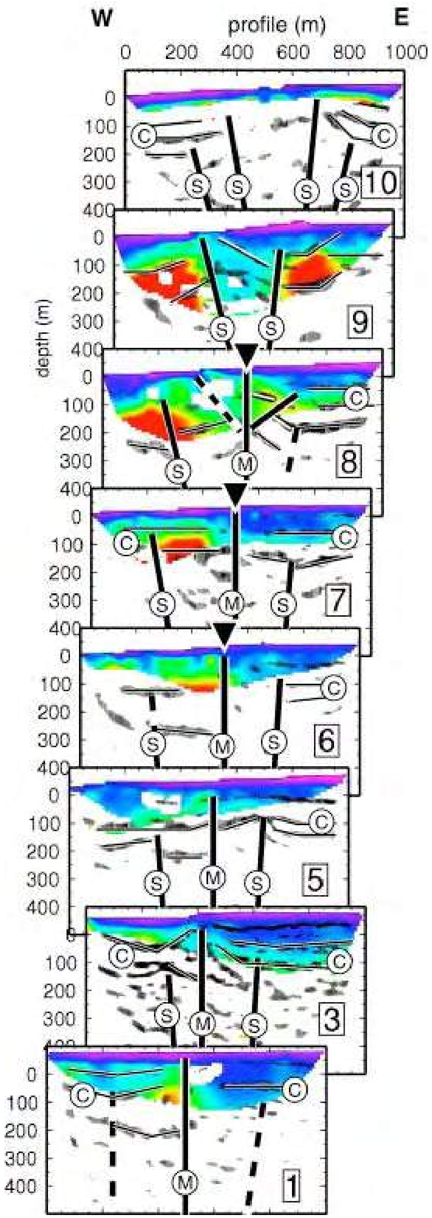

Figure 5: (left) Migrated reflection seismic images (black wiggles) overlaid on the tomography (color coded) together with our geological interpretation. Black thick lines indicate inferred faults, dashed lines indicate less well constrained faults. M), S), and C) indicate the main fault, secondary/flanking faults, and sedimentary cover at the two sides, respectively. Inverted triangles indicate the position of guided wave observations from (Haberland et al., 2003).
(right) A) Summary of all interpreted sections along the fault (perspective view from the South). The main fault is indicated by the red area. B) Possible reconstruction of the fault structure based on the seismic results. A few subparallel faults form the WAF system in the study area; to the North the pressure ridge structure dominates. Covering sediments are omitted.
Haberland et al., 2007.

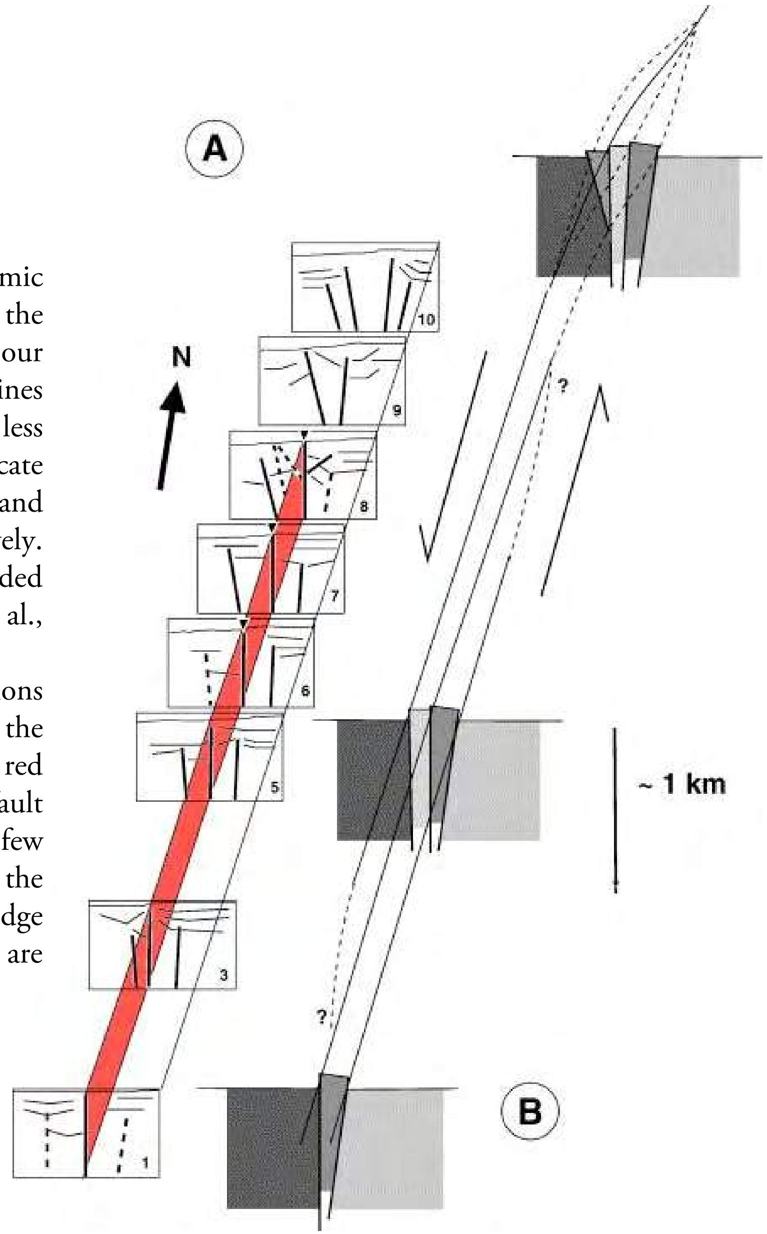

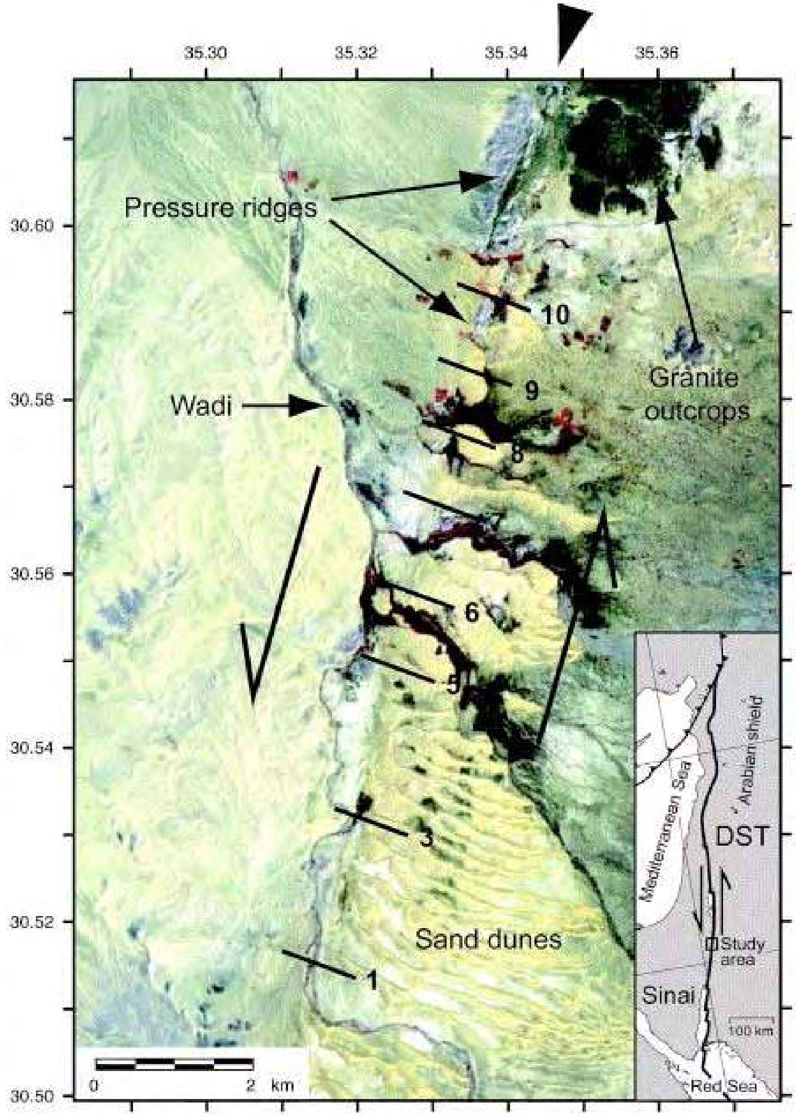

Figure 6: Position of CSA-2 seismic lines overlayed on an ASTER satellite image of the study area. Large arrowheads mark the course of the Wadi Araba fault (WAF). The inset shows the principal geotectonic situation in the Middle East. Haberand et al., 2007.

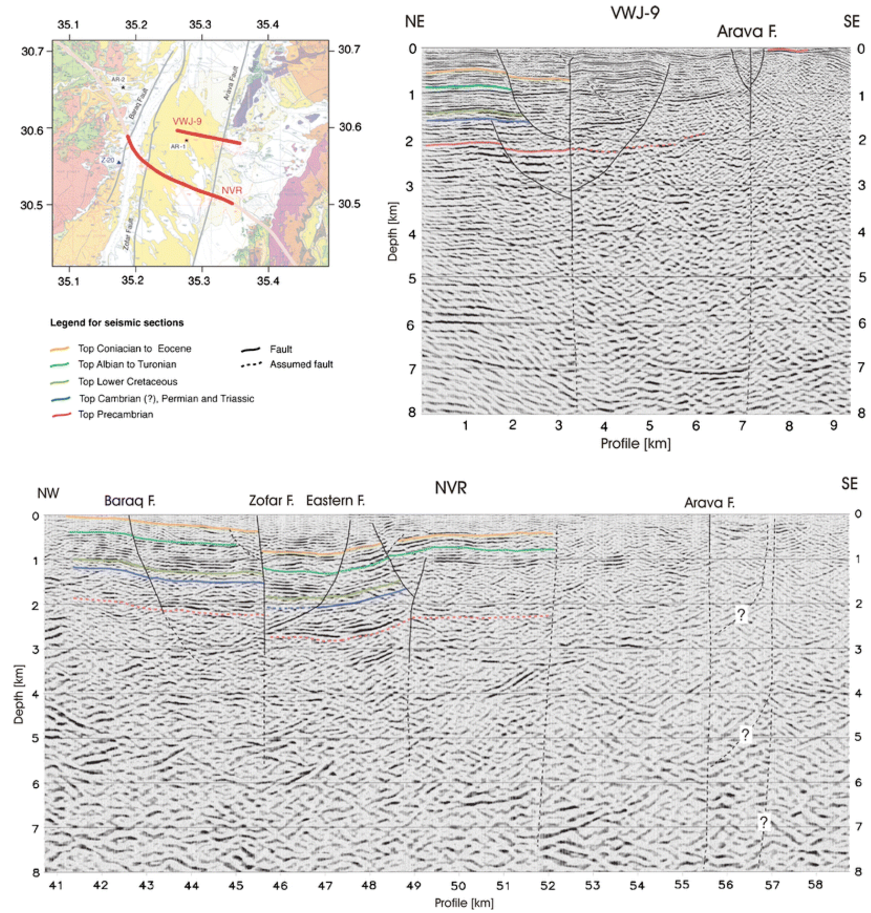

Figure 7: Near-surface structure as seen in seismic reflection data. a Location of seismic profiles NVR and VWJ-9; Z-20: Zofar-20 well; AR-1 and AR-2: outcrops of Arava/Araba Formation. b Depth migrated shallow seismic reflection profile VWJ-9 (Kesten 2004). c Upper central part of the depth migrated NVR profile, only the range indicated in full red is shown (see Fig. 2a, profile km 40.5–58.5). Kesten et al., 2008

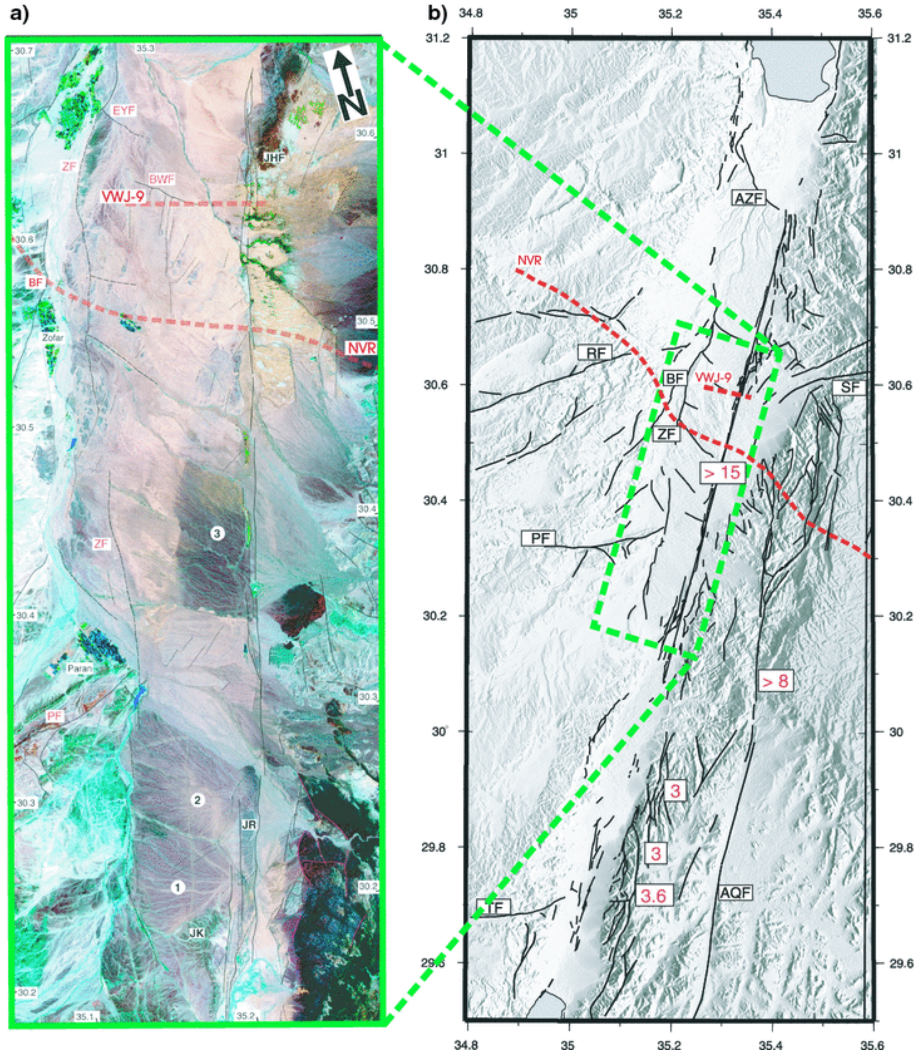

Figure 8: An ASTER scene of the central Arava/Araba Valley taken on April 6, 2001. Three types of lineaments can be distinguished: (1) Solid lines represent lineaments that are clearly recognized as faults (by displaced geological units, offset alluvial fans or clear 'doglegs' of streams); (2) Dashed lines are used for lineaments that were identified as faults in other, mainly shallow seismic studies (e.g. Frieslander 2000); (3) Dotted lines are lineaments whose origin could not be clarified for lack of geological or geophysical information. EYF En Yahav Fault, BWF Buweirida Fault, ZF Zofar Fault, BF Baraq Fault, PF Paran Fault, JHF Jebel Humrat Fidan, JR Jebel Er Risha, JK Jebel El Khureij and numbers 1–3 indicate alluvial fans; b Fault map of the southern Dead Sea Transform, derived from the interpretation of ASTER satellite images (Kesten 2004 and this study) over the shaded relief map. The red numbers indicate the minimum amount of left-lateral strike-slip displacement along the respective faults in kilometres. AQF Al Quwayra Fault, AZF Amaziahu Fault, BF Baraq Fault, PF Paran Fault, RF Ramon Fault, SF Salawan Fault, TF Themed Fault and ZF Zofar Fault. Here, the nomenclature of Frieslander (2000) and Calvo and Bartov (2001) is used.

Kesten et al., 2008

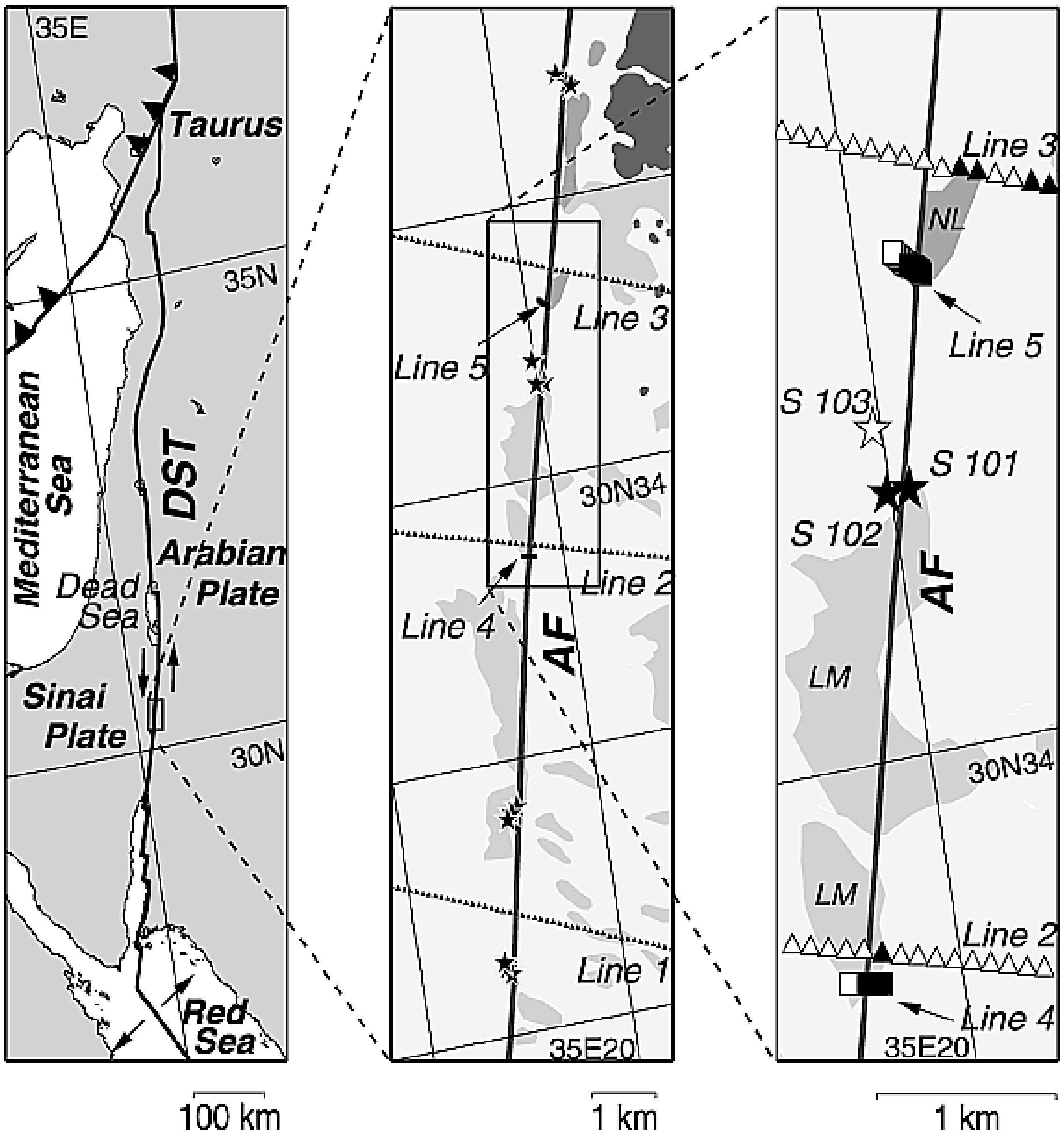

Figure 9: (left) Sketch showing the tectonic setting of the Middle East. (middle) Site map of the active seismic experiment at the Arava Fault (AF) as part of the Dead Sea Transform (DST). Fault trace (dark shaded line) as inferred beneath superficial deposits. Shots are denoted by stars. Vertical sensors on lines 2 and 3 (spacing 100 m) are shown by triangles, and three-component sensors along lines 4 and 5 (spacing 10 m) are shown by squares. (right) Close-up of the region displayed in the middle panel. Solid symbols (stars, triangles, and squares as before) indicate shots generating and receivers observing guided waves; open symbols indicate shots and receivers without such generation or observation, respectively. Geology adopted from Rabb'a [1994] (NL, Na'ur limestone; LM, Neogene marl).

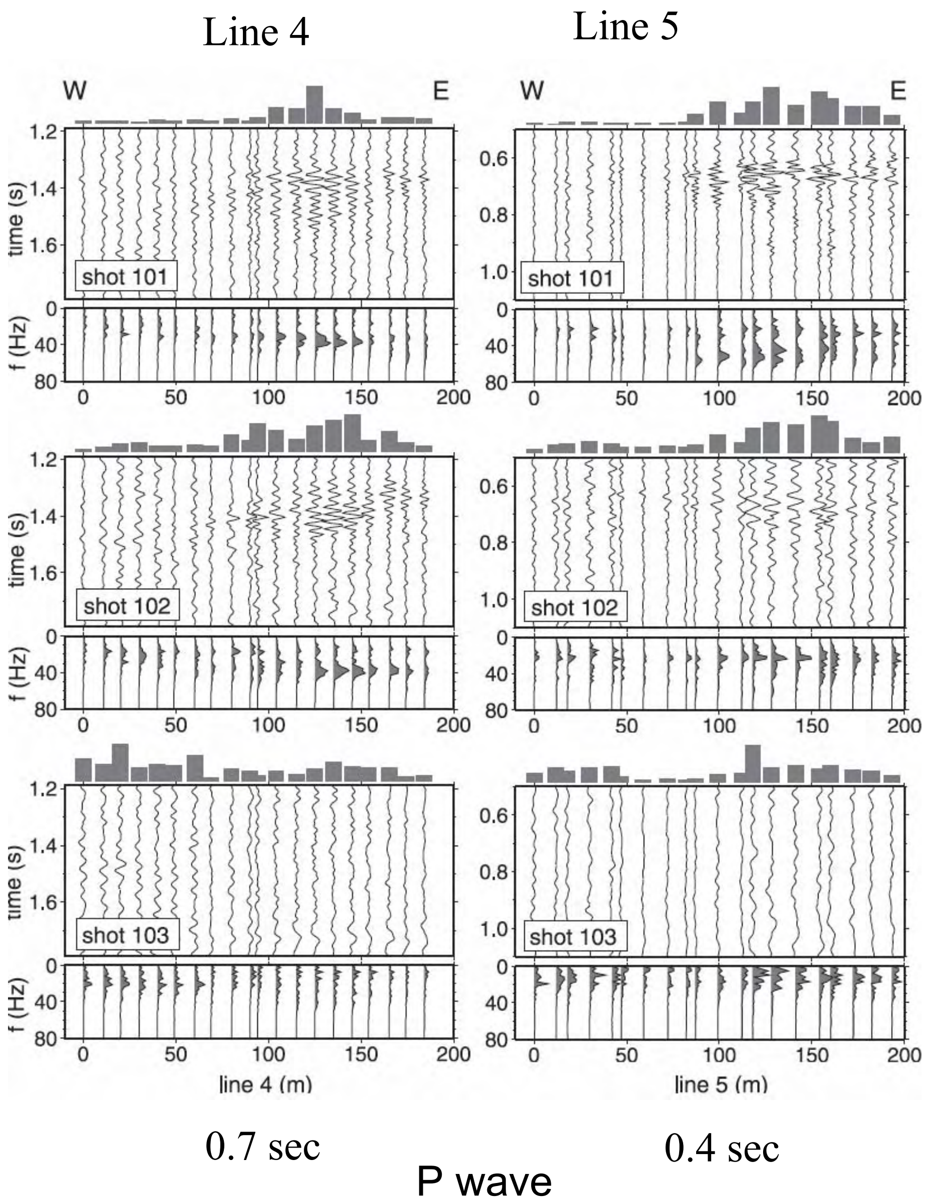

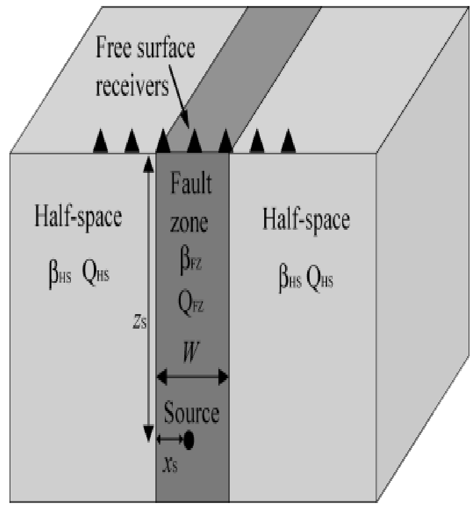

Figure 10: (top) Schematic showing experimental layout. (left) Observations on receiver line 4 (left) and line 5 (right) for the three shots 101 (top), 102 (middle), and 103 (bottom). For each gather, normalized maximum energy (bars, top, within time windows of 1.2 to 1.6 and 0.6 to 0.8 s, respectively), time series (middle), and spectra (bottom) for each trace are shown. Note the high-frequency wave trains from shots 101 and 102 on eastern traces of both lines between 1.3 and 1.6 s (line 4, left) and 0.6 and 0.8 s (line5, right), but no such phase for shot 103 (and all other shots; see text). For positions, refer to map above. Shown are unfiltered vertical component data containing presumed guided waves. P wave onsets (not shown) arrive at around 0.7 s (line 4, left) and 0.4 (line 5, right). Haberland et al., 2003.

References

Haberland C., Agnon , A., El-Kelani , R., Maercklin, N., Qabbani , I., Rumpker, G., Ryberg, T., Scherbaum, F., Weber M., 2003. Modeling of seismic guided waves at the Dead Sea Transform, Jour. Geophys. Res., 108, 2342.

Haberland, Ch., Maercklin, N., Kesten, D., Ryberg, T., Janssen, Ch., Agnon, A., Weber, M., Schulze, A., Qabbani, I., El-Kelani, R., 2007. Shallow architecture of the Wadi Araba fault (Dead Sea Transform) from high-resolution seismic investigations, Tectonophys., 432, 37-50.

Kesten, D., Weber, M., Haberland, Ch., Janssen, Ch., **Agnon, A.**, Bartov, Y., Rabba, I., The DESERT Group, 2008. Combining satellite and seismic images to analyse the shallow structure of the Dead Sea Transform near the DESERT transect, Int J Earth Sci (Geol Rundsch), 97, 153-169.

Le Beon, M., Klinger, Y., Amrat, A. Q., **Agnon**, **A.**, Dorbath, L. , Baer, G., Ruegg, J-C., Charade, O., Mayyas, O., 2008. Slip rate and locking depth from GPS profiles across the southern Dead Sea Transform, J. Geophys. Res., 113, B11403, doi:10.1029/2007JB005280.

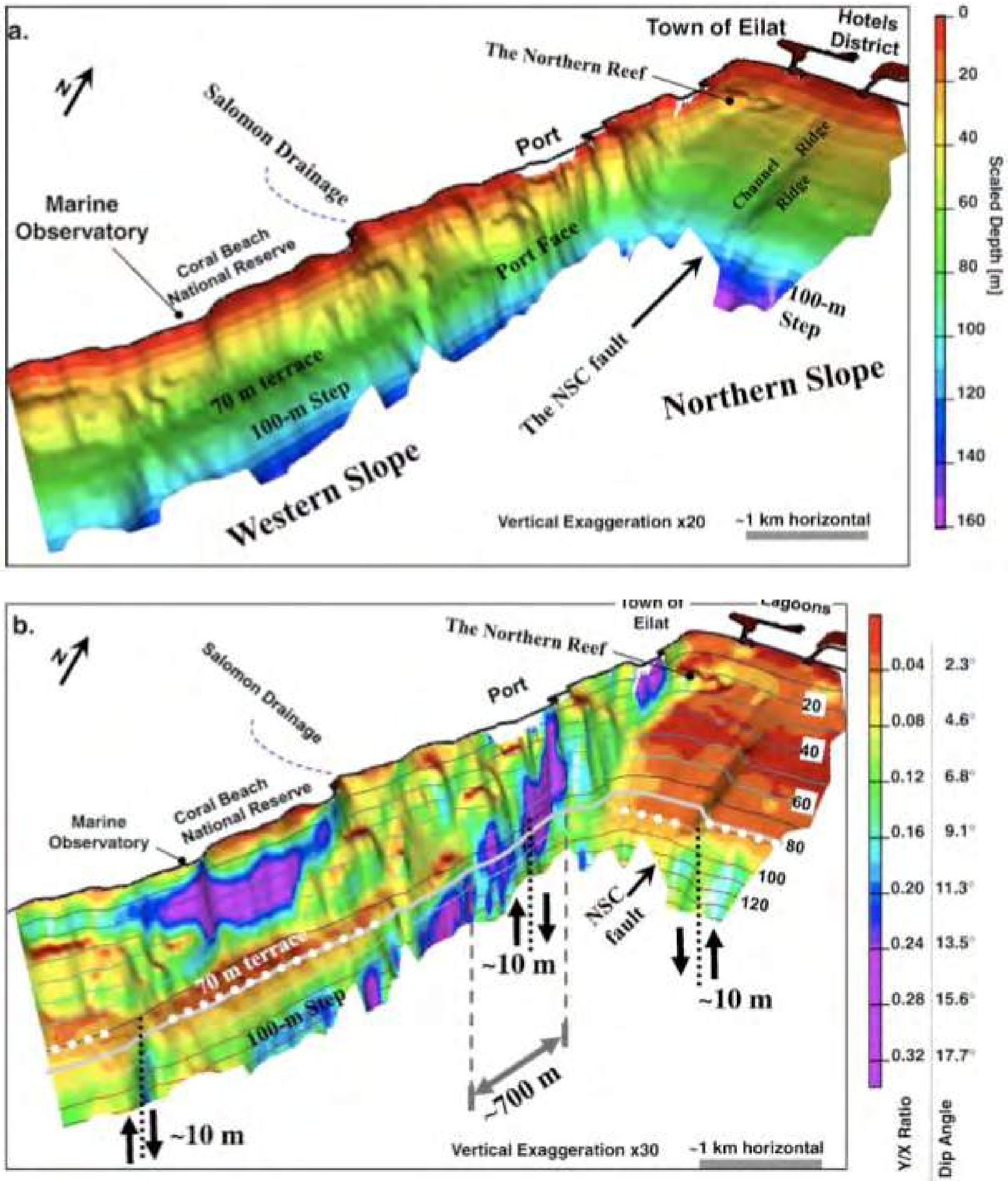

Northern Gulf of Eilat

Figure 1: 3D shaded relief depiction of our bathymetric map viewed from the south east and above. Black line marks the coast line. a. The shaded relief is colored according to approximately-scaled water depth (with water velocity of 1540 m/s), and is vertically exaggerated × 20. Features and locations discussed in the text are noted. The NSC fault trace asses below the gentle step between the ridge and channel (labeled). b. The shaded relief is color coded by the gradient of the bathymetry, overlaid by depth contours, and vertically exaggerated × 30. Terraces are apparent in red, while steep faces are purple. Apparent vertical offsets of the 100-m Step (see also Fig. 3) are roughly estimated by the changes in depth of the 2.3° contour (dashed with white circles), and noted with their sense and order-of-magnitude size (dashed lines and arrows). A gap of about 700 m in the 100-m Step below the port (the "Port Face") is noted in grey. Makovsky et al., 2008.

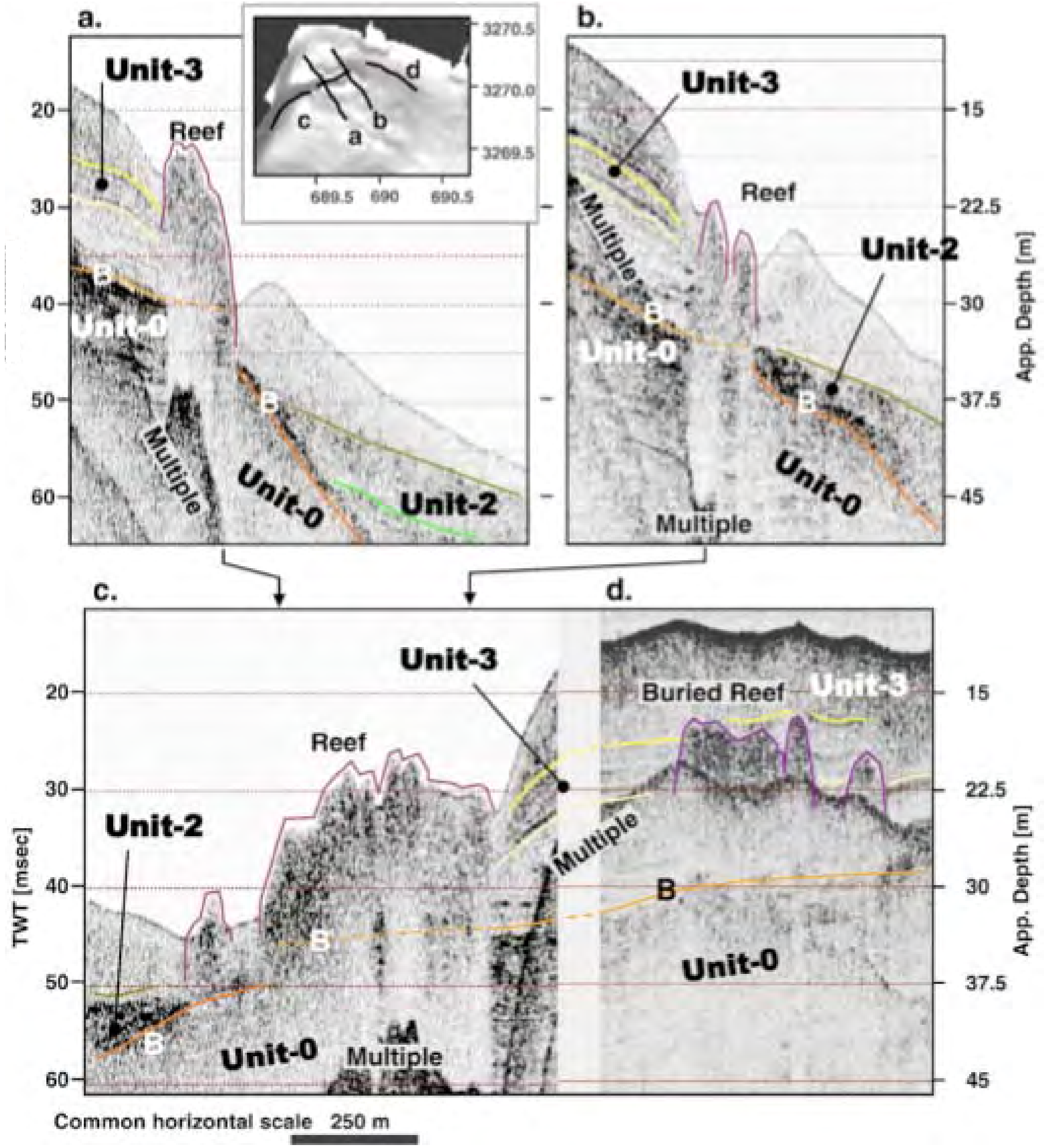

Figure 2: Four Chirp time sections across (a, b), and along (c, d), the Northern Reef. The section amplitudes are corrected by exponential gain, enhancing the internal reflectivity patterns and multiples. The profiles traces are overlaid on the shaded relief of the bathymetry and colored by in the inset map (top middle). Arrows between the sections show the intersections of profile (a) and (b) with profile (c). The sections are overlaid with colored interpretations of the basal surface (B) at the top of Unit-0 (orange), retrograde sedimentary wedges of Unit-2 (greens), reefs (purple), and Unit-3 coastal ramp layers (yellows). The reefs prevent acoustic penetration, appearing to cast a light shade beneath them. The buried reef seems somewhat shallower than the exposed reef, but that is probably an artifact of the higher seismic velocity in the burying sediments being higher than in the water. Note the flat tops of the reef in section (c) representing probably fossil reef tables. The first layers of Unit-3 above the basal surface (sections a, b) approach the reef uniformly not appearing to 'sense' its presence. Stratigraphically higher layers of Unit-3 dip where approaching the reef, probably because the sediments flow was blocked by the reef. Corresponding layers of Unit-3 cover the reef farther to the east. Makovsky et al., 2008.

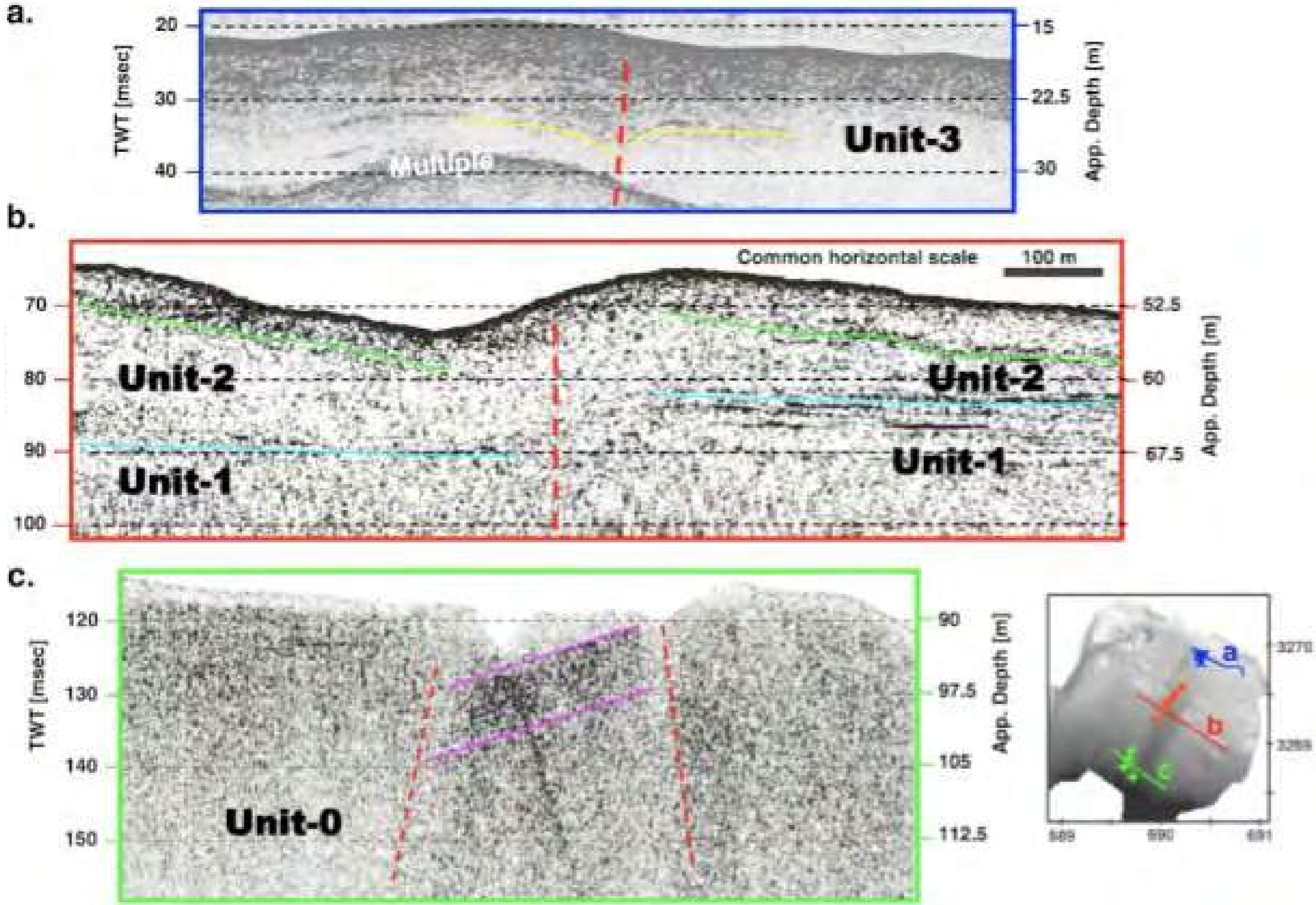

Figure 3: Three about 1-km long time sections across the NSC fault. Each section represents a different apparent style of faulting of the NSC fracture system. The profiles displayed, and locations at which each style of faulting is observed are marked with matching colors on the inset map. The different deformation styles are reminiscent of the near-surface appearance of a strike-slip fault. Interpretation of marker horizons is color-coded as in previous figures. The purple horizons marked in (c) are not correlated with any of the other units, and probably represent deeper horizons of Unit-1. Note that while the yellow horizon in (a) is not clearly offset, just bent inwards, the light blue horizon in (b) is offset by about 5 m across the interpreted fault trace. Due to the retrograde nature of the sedimentation (e.g. Fig. 6) section (a) images younger sediments than section (b), suggesting a differential offset with age (Makovsky et al., 2008).

Figure 4: A high resolution bathymetric map produced (see text and Fig. 2b for details) from the dense Echo Sounder survey measurements (see Fig. 1b for location). a. A depth contour map of the Echo Sounder bathymetry (contour spacing of 5 m) overlain on a shaded relief depiction of this map. The map is oriented approximately along the trend of NSC fault bathymetric step (azimuth 23.5), and is centered on its approximate trace (dashed white line). The 65-m Reef appears as a sub-linear, 1 to 2 m high, bump on the seafloor lit on one side and shaded in the other. The reef is truncated and shifted left laterally where it crosses the trace of the NSC fault. b. Progressive reconstructions of the 65-m reef by shifting the western (left) side of the shaded relief depiction of the map in (a) northwards (upwards in a right lateral sense) by changing amounts (noted on each panel) with respect to a fixed eastern (right) side. A thin dotted line marks the contact between the two sides, along which the western panel is shifted. Best continuity of the 65-m Reef is obtained when shifting the western panel by 30 m. Some continuity is obtained also when the shift is 20, and 40 m. This test suggest that 30 ± 10 m left lateral slip was accommodated by the NSC fault since the formation and drowning of the 65-m Reef. c. A 3D-shaded-relief depiction of the map in (a) viewed from the south west. Vertical exaggeration is × 6. The 65-m reef is truncated and shifted both 30 ± 10 m left laterally and 10 ± 1 m down to the west where it crosses the seafloor step that marks the NSC (marked in white). A thin veneer of sediments covers the 65-m reef farther to the west. No significant progradation is observed in the depth of the reef's top, suggesting that most offset occurred after the reef stopped evolving (Makovsky et al., 2008).

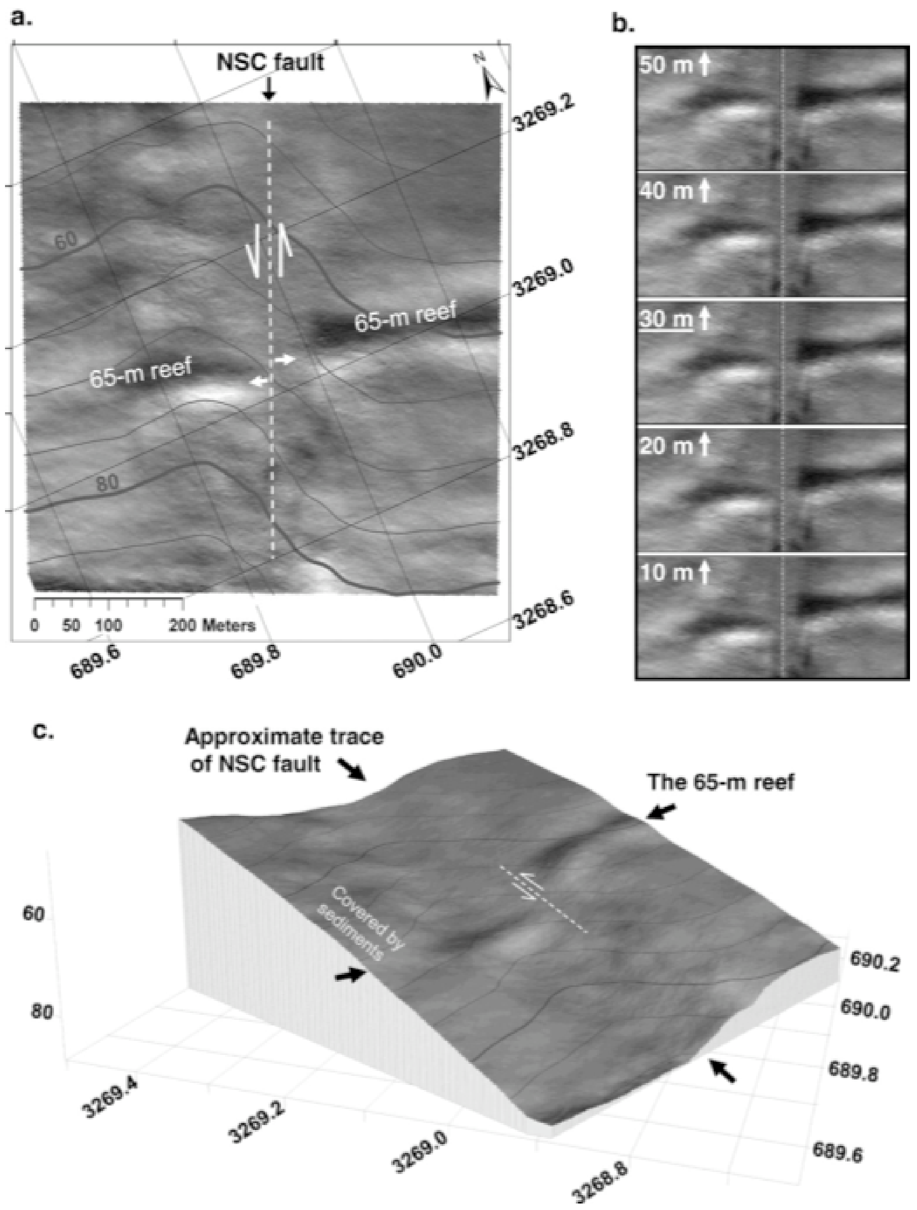

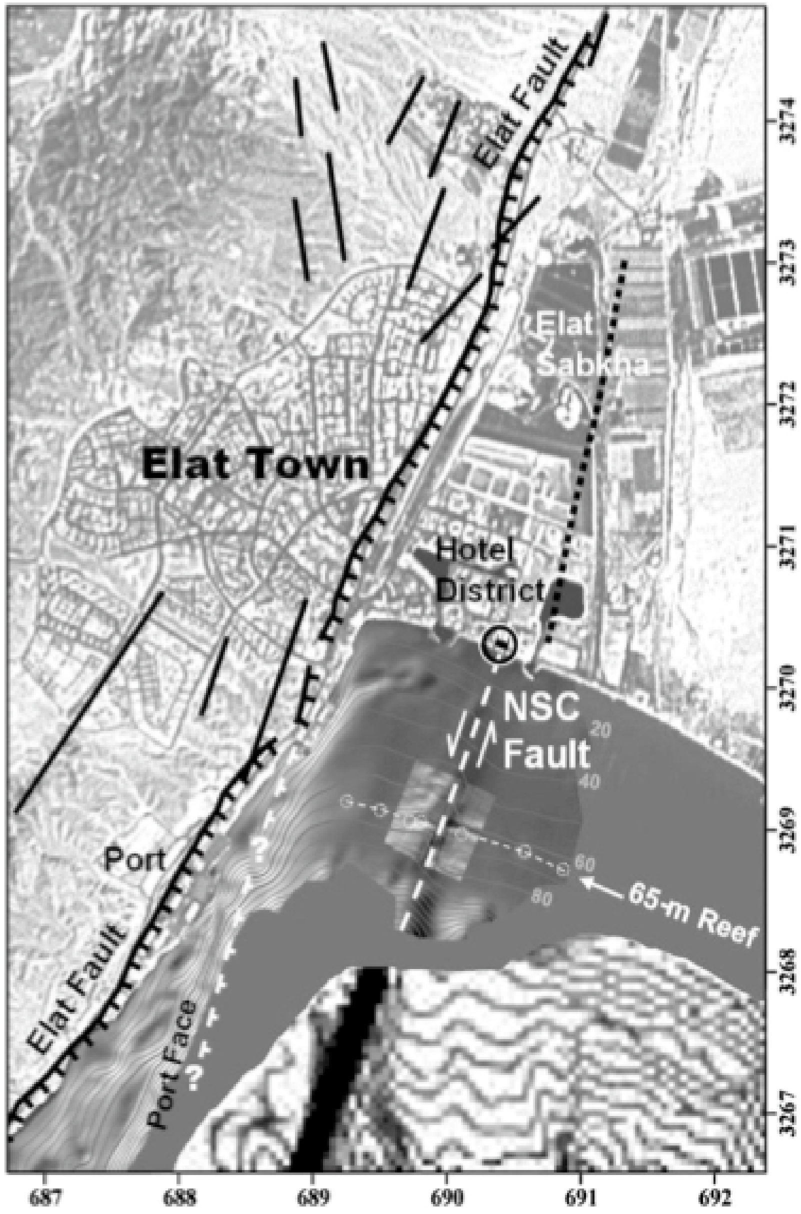

Figure 5: A map incorporating the results presented in this paper in the regional tectonicand civil context. A LANDSAT image of Elat and vicinity overlaid with 10 m bathymetric contours, and shaded relief depictions of the Chirp and Echo Sounder bathymetric maps. Also overlaid are the faults traces of Fig. 1b (black lines), and Ehrhardt et al. (2005) bathymetry (bright area in the bottom). The thick black line is Ehrhardt et al. (2005) interpreted fault. The location on the north coast where Frieslander (2000) imaged a sub-vertical fault is noted with a black bar (surrounded by a black circle), representing the range of uncertainty in the exact surface impingement of this fault. The eastern (right) side of this bar represents the projection of the fault's trend from about 100 ms (about 100 m depth). The locations where the 65-m Reef was imaged on our Chirp sub- bottom profile (dotted circles), and conceptual lines connecting these locations (thin dashed lines), are marked as on the inset of Fig. 6. The NSC fault is a major fault that crosses the Northern Slope approximately along the elongated bathymetric step (e.g. Fig. 4), offsets the 65-m Reef, and project into Elat hotel district and Elat Sabkha approximately where the sub-horizontal fault is imaged by Frieslander (2000). This trend of the NSC fault is approximately parallel with the trend of the Avrona fault 15 km to the north where it impinges southward into the Avrona Sabkha. The Elat fault, defined by Garfunkel (1970) as a predominantly normal fault, may be splaying south- ward along the Port Face and accommodating a significant down to the east slip Makovsky et al., 2008.

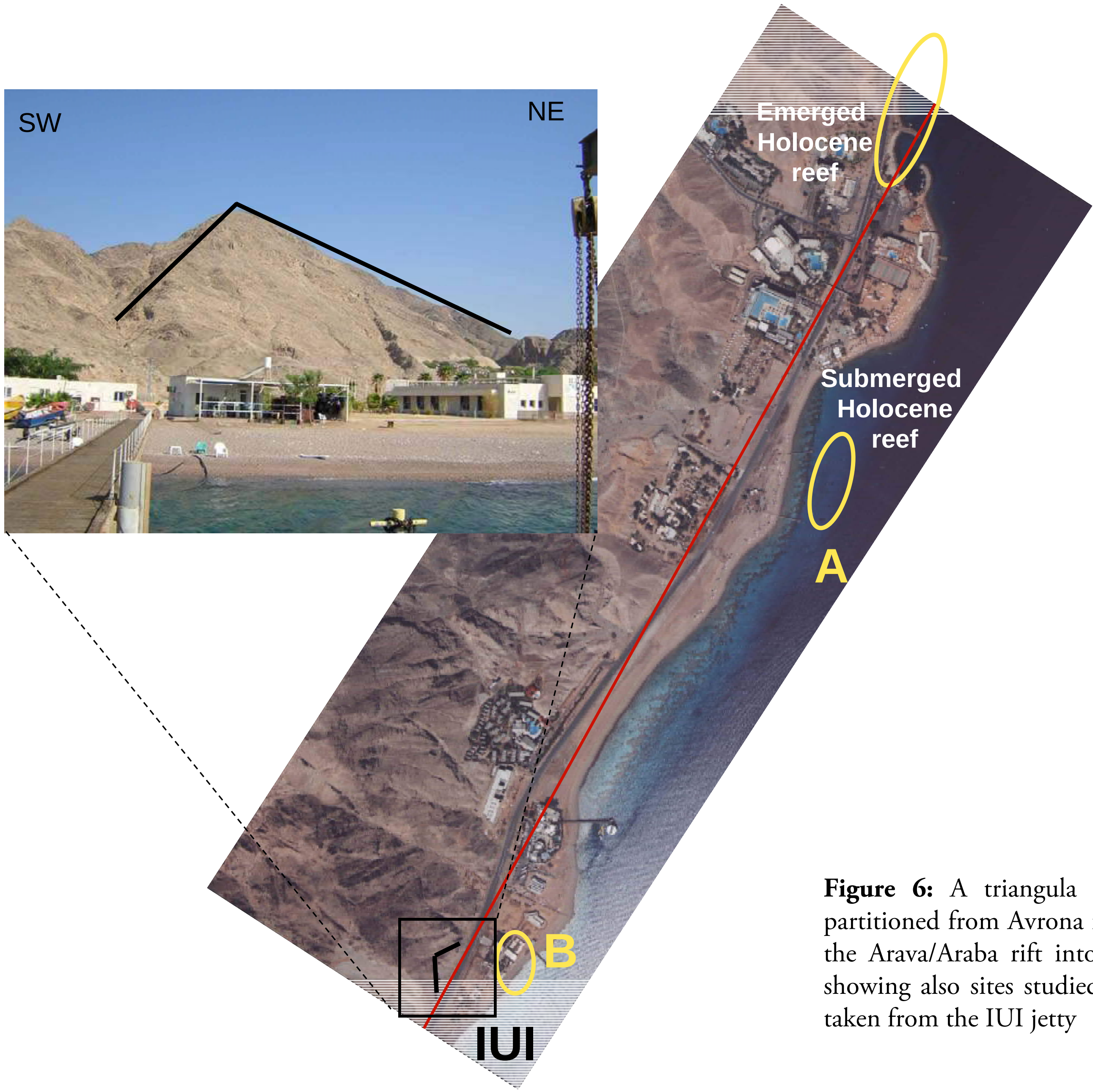

Figure 6: A triangula facet of Elat's fault - a normal fault partitioned from Avrona fault segment - the southern extension of the Arava/Araba rift into the Gulf of Elat-Aqaba. A: Airphoto showing also sites studied by Shaked et al. (2002, 2005). photo taken from the IUI jetty

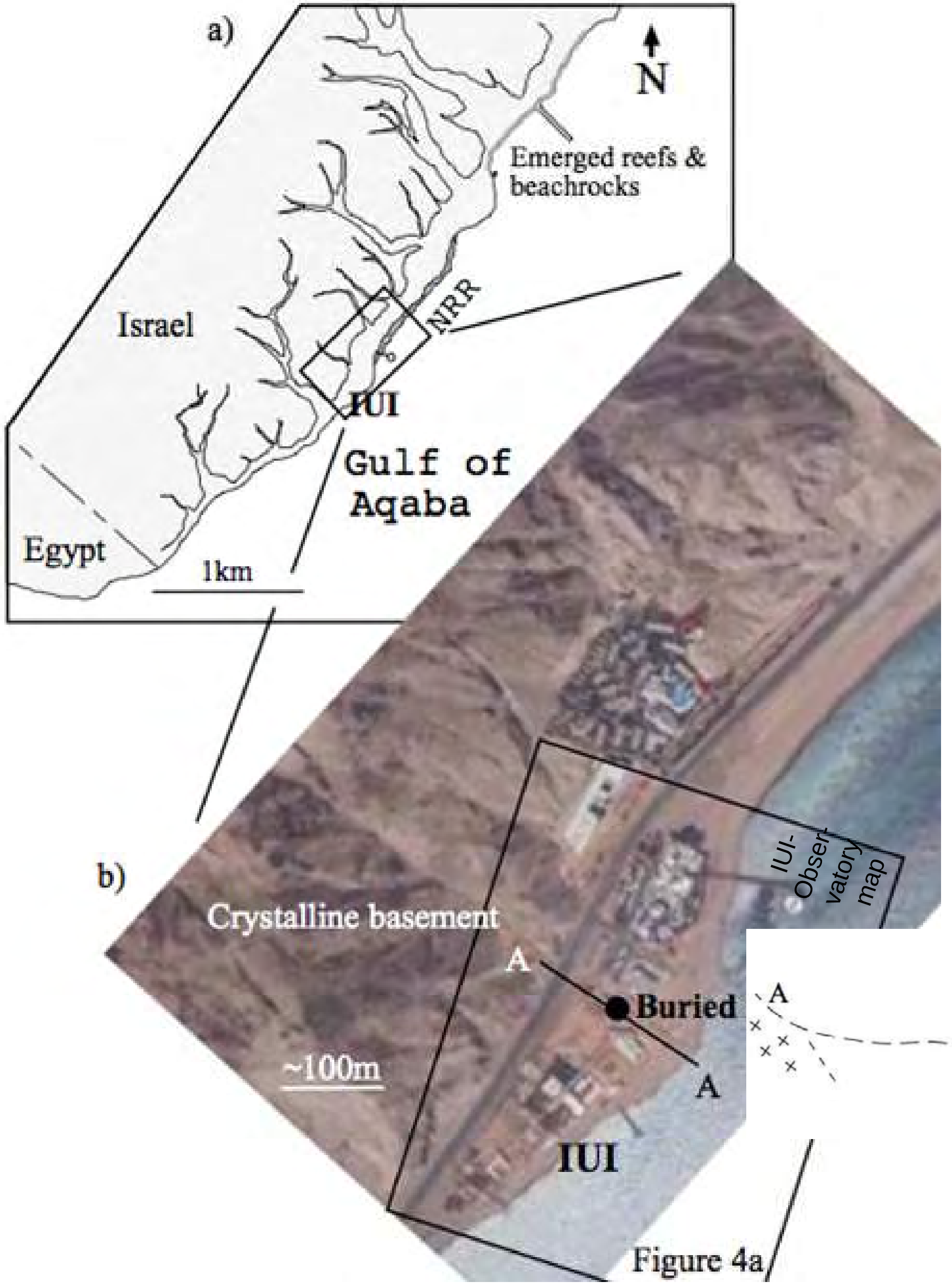

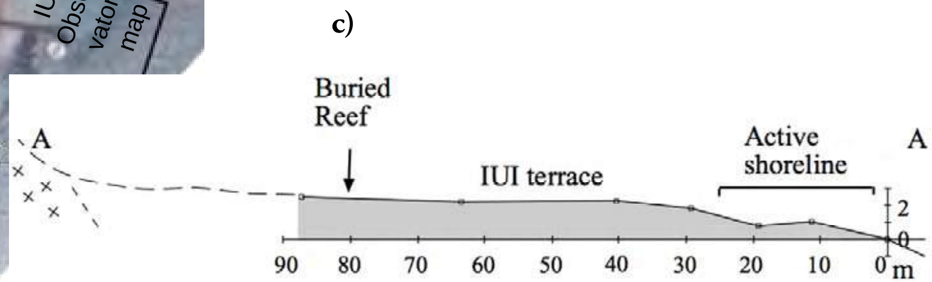

Figure 7: The IUI shoreline: a) Outline of the shore near the IUI showing the drainage patterns, location of the IUI and the modern nature reserve reef (NRR), and the emerged reefs that constrains the Holocene sea level. b) Aerial photo of the IUI beach with the location of the pits and boreholes that exposed the buried reef marked as a black circle. The box marks the area mapped in the next figure. c)Topographic profile across the IUI terrace at its widest part (A-A). Grey marks the length of the northern sediment trench. Shaked, 2002.

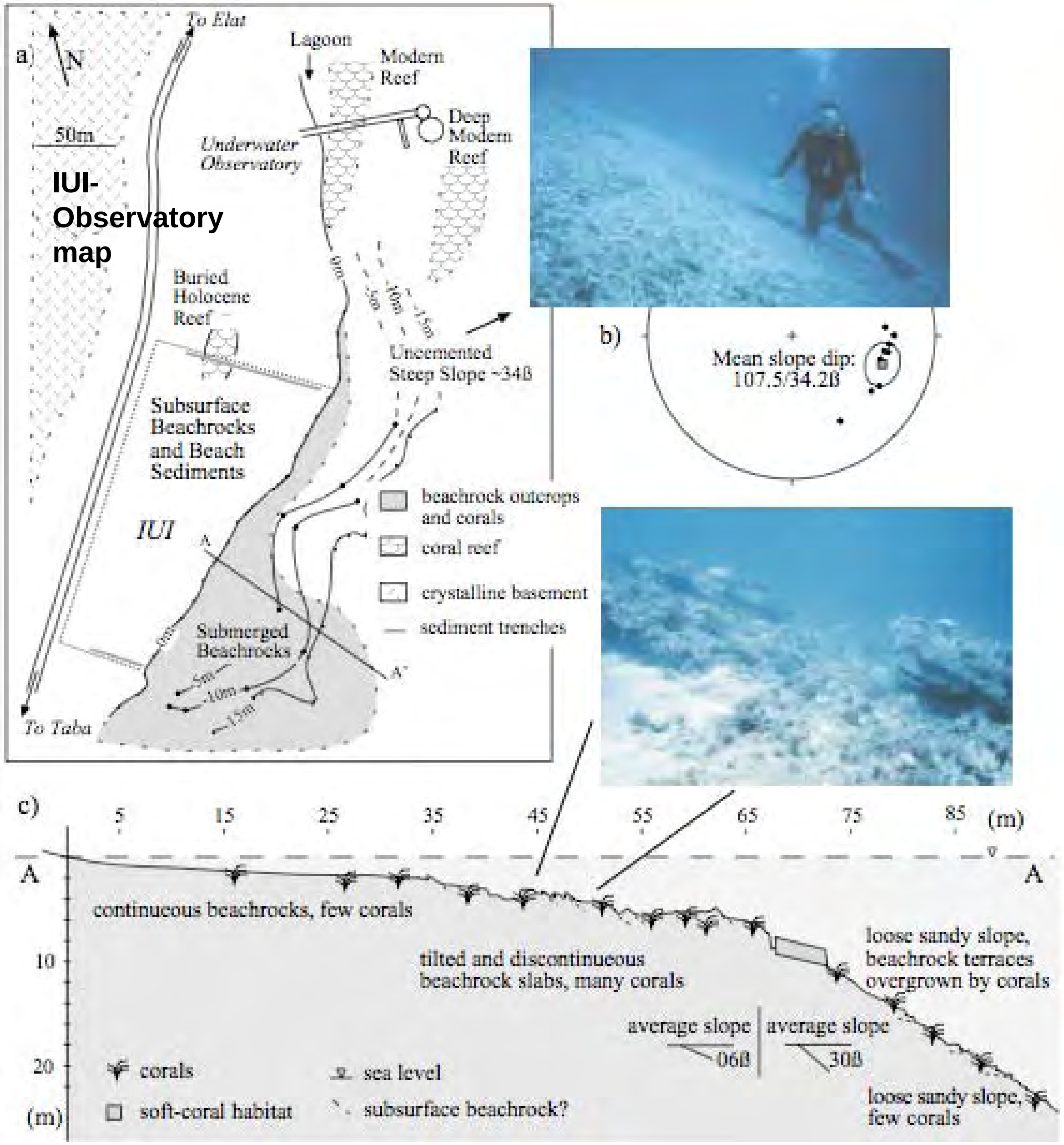

Figure 8: a) Geomorphic map of the shallow slope off-shore from the IUI. b) The north- facing slope of unconsolidated material, its average dip 34°. Note the air bubbles above the diver, indicating vertical. c) A cross section off the south-facing slope and photo from the shallow part showing tilted beachrock strips overgrown by corals. Shaked, 2002.

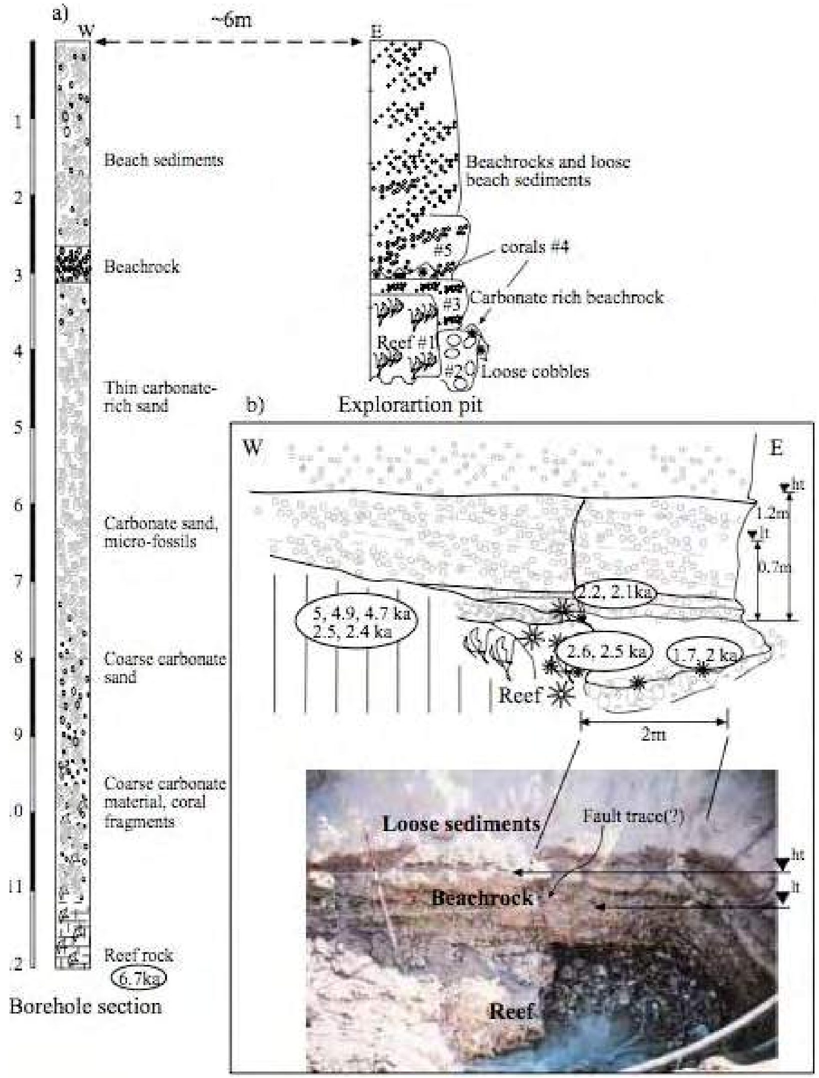

Figure 9: (top) Stratigraphy of the IUI buried reef: a) Log of borehole (left) and ~6m E of it stratigraphic section at the research pit. b) Cross section (north wall) and photograph of the buried reef at the IUI research pit. lt= low tide mark; ht= high tide mark. Shaked, 2002.

Figure 10: (right and bottom) Samples from the buried reef. a) The edge of the reef front structure comprising a large Lobophylia (2.8ka) covered by carbonate rich clastic sediment and overgrown by a small Astreopora and Gyrosmilia. b) and c) Microscope photos of the Gyrosmilia that overgrows the reef front (2.3ka). d) A delicate Acropora overgrowing a granite cobble east of the reef structure. Many similar corals were found at the site. The perfect preservation of every detail of the coral indicates that it has never been transported or exposed to erosion. Shaked, 2002.

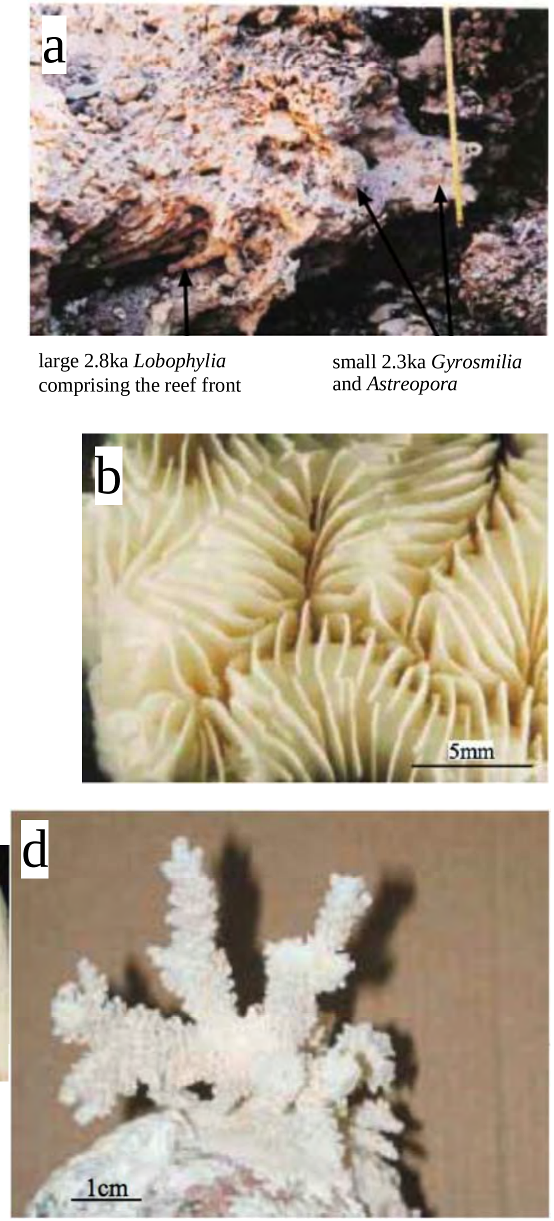

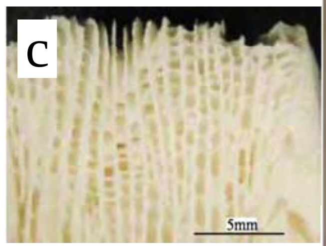

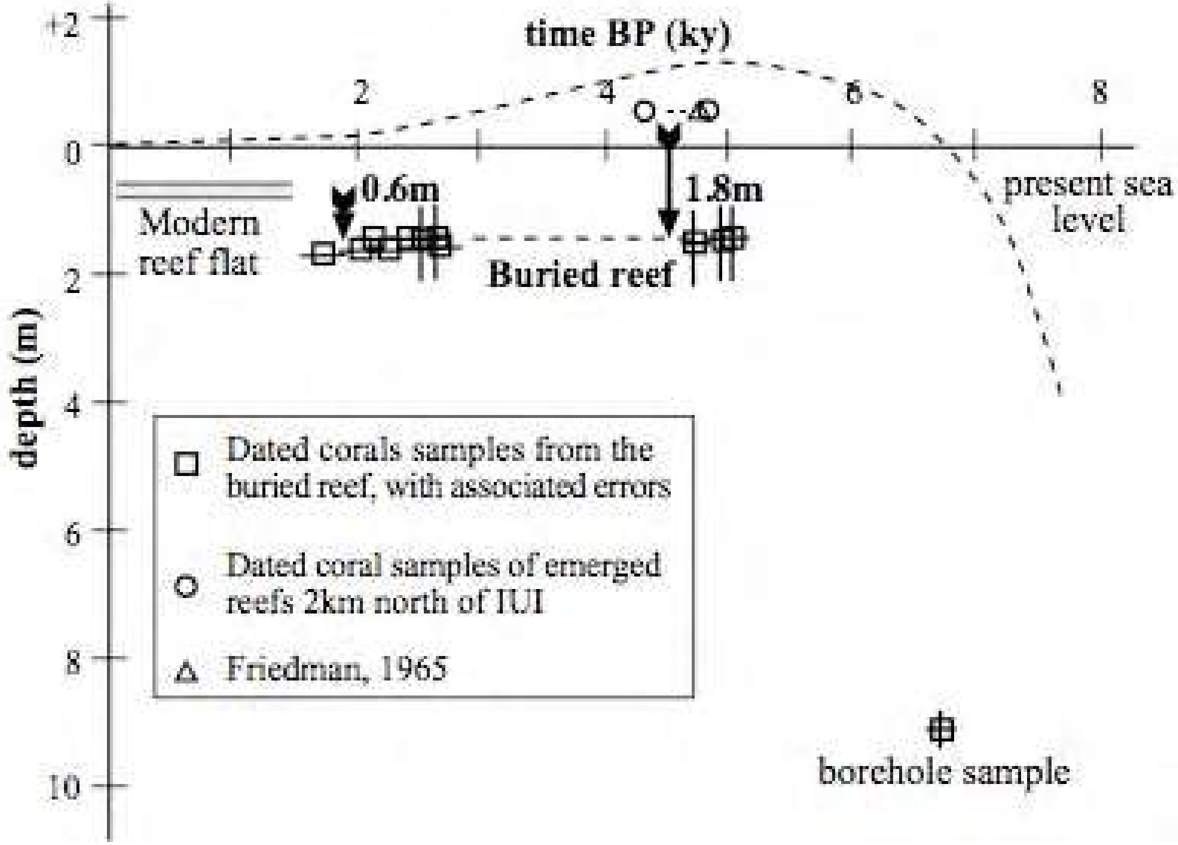

Figure 11: Elevation versus age of coral samples from the buried reef (squares) and emerged reef outcrops ~2km to the north (circles and triangles). The emerged outcrops represent the in-situ position of ~5ka reefs around the Gulf of Aqaba. The length of the arrows is the estimated down faulting of the buried reef relative to emerged Holocene reefs, and to the modern reef of Elat (gray bar). Shaked, 2002; Shaked et al., 2004.

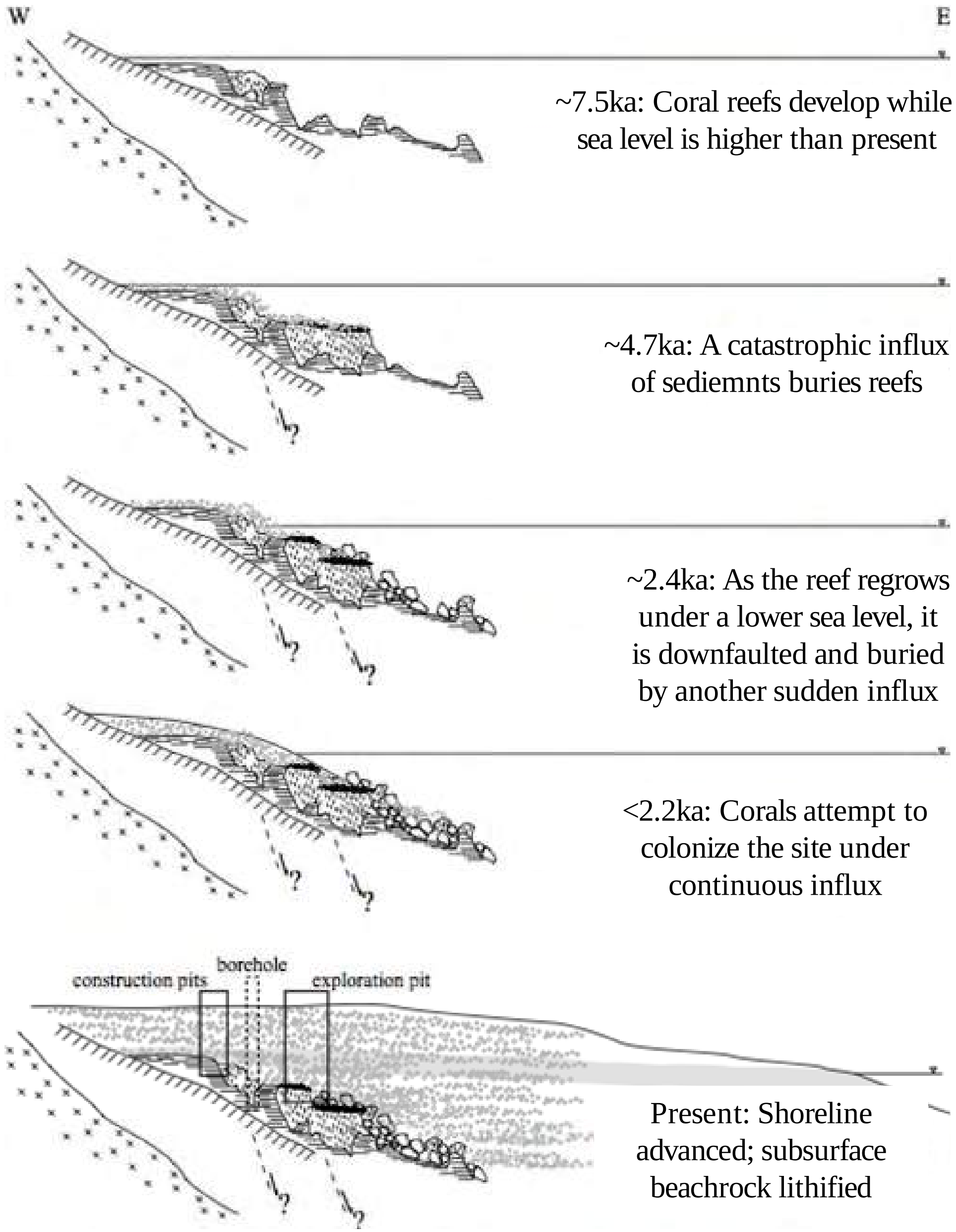

Figure 12: Illustration (not to scale) of reconstructed events at the IUI buried reef site. Boxes at present-day section denote the stratigraphy found at construction pits and the exploration pit. The dashed box of the borehole stratigraphy is in reality normal to the section and only shows the older reef beneath lagoon sediments.

Shaked, 2002

References

Makovsky, Y., Wunch, A., Ariely, R., Shaked, Y., Rivlin, A., Shemesh, A., Ben-Avraham, Z., Agnon, A., 2008. Quaternary transform kinematics constrained by sequence stratigraphy and submerged coastline features: The Gulf of Aqaba, Earth Planet. Sci. Lett., 271, 109-122.

Shaked, Y., 2002. Neotectonics and eustasy at the Gulf of Elat-Aqaba. PhD Thesis, Hebrew Univ., Jerusalem,

Shaked, Y., Marco, S., Lazar, B., Stein, M., Cohen, C., Sass, E., Agnon, A., 2002. Late Holocene shorelines at the Gulf of Aqaba: Migrating shorelines under conditions of tectonic and sea level stability, Eur. Geophys. Soc. Stephan Mueller Spec. Publ. Ser., 2, 1–10.

Shaked, Y., Agnon, A., Lazar, B., Marco, S., Avner, U., Stein, M., 2004. Large earthquakes kill coral reefs at the north-west Gulf of Aqaba, Terra Nova, 16: 133-138.

Shaked Y, Lazar B, Marco S, Stein, M., Tchernov, D., Agnon, A., 2005. Evolution of fringing reefs: space and time constraints from the Gulf of Aqaba Coral Reefs 24: 165-172.

Late Quaternary Seismicity of The Southern Arava Valley, The Dead Sea Fault

Rivka Amit[1*], Yehouda Enzel[2*], Porat Naomi[1*], Yariv Hamiel[1*], Ezra Zilberman[1]

[1]Geological Survey of Israel

[2]The Hebrew University of Jerusalem

rivka@gsi.gov.il

*Field guide

Late Quaternary paleoseismicity of the southern Arava was deduced from offsets on faults detected in trenches, in a fault zone that is 6 km wide and 40 km long, extending through the rift valley from the north-western coast of the Gulf of Elat (Aqaba) to the north-east (Amit *et al.,* 1995; Amit *et al.,* 2002; Zilberman *et al.,* 2005). The fault zone may be subdivided into three subzones: a central sub-zone, 5 km wide, trending northeast, characterized by sinistral faults expressed by push-ups and pull-aparts, and two marginal zones characterized by normal faults that trend northwest and north–northeast on both sides of the rift valley (Fig. 1). Amit *et al.* (2002) reported 20 different paleo-earthquakes between 45-1 Kyr BP in the southern Arava segment. The cumulative normal slip versus time that was calculated from these data shows that a constant slip rate of 0.5 mm/year can account for the total normal slip. The lower-than-average amount of normal slip per event recorded during the last 16 Kyr (12 events, average slip of 0.65m per event) is compensated by the shorter recurrence interval in that period (1,500 years), as compared to the earlier period of 45-16 Kyr (8 events, average slip of 1.4m, and a recurrence interval of 3,000 years) (Fig. 2). The difference in slip per event between the two periods is statistically significant ($p< 0.002$ in the Mann-Whitney test, where p is the probability that the two samples are drawn from the same population).

Assuming an average slip rate of 5 mm/year for the left lateral motion along the DSF, the average cumulative normal slip rate in the southern Arava of 0.5 mm/year suggests that normal faulting is only ~10% of the total strike-slip motion in the last 45 Kyr. This is supported by the calculated rate for small and large earthquakes along the DSF in modern times (Hofstetter *et al.,* 2003; Salamon *et al.,* 2003), and by the amount of transverse extension along the fault (e.g. Joffe and Garfunkel, 1987). Similar dip slip to strike slip ratio was observed in the north-eastern Sea of Galilee basin (Marco *et al.,* 2005).

The transformation of displacement detected in trenches across faults to earthquake magnitude was calculated using the regressions presented by Wells and Coppersmith (1994). The calculated magnitudes for all paleo-earthquakes in the Arava segment are in the range of $5.9<M_w<7.1$, with average magnitude of $M_w6.5$ for 16-1 Kyr, and 6.8 for 45-16 Kyr BP. Due to the nature and inaccuracy of the displacement-magnitude relation (Wells and Coppersmith, 1994), we assume an error in magnitude of ±0.6 (~10%) for all paleo-events. The earthquake catalogues that are based on historical records report a single large earthquake (M>6) that occurred in the year of 1068 AD in the southern Arava (e.g., Guidoboni and Comastri, 2005; Zilberman *et al.,* 2005), which is included in the above mentioned record. Due to the remoteness of this desert area in ancient times it is hard to find a reliable historic evidence for earlier events. Fig. 3 shows the calculated frequency-magnitude relation for the Southern Arava segment using the instrumental and paleo-seismic records. The instrumental record includes 123 events and was divided to magnitudes between 2-2.9, 3-3.9, and 4-4.9. The instrumental data were taken from the Geophysical Institute of Israel earthquake catalogue (www.gii.gov.il). As the catalogue is complete for earthquakes with $M_L \geq 2$ only since 1983, we used instrumental data that were recorded between the years of 1983 and 2007. We found that the data points as retrieved from paleo-seismic record for the Southern Arava segment lie on the linear extrapolation of the frequency-magnitude relation of the instrumental record, with a calculated *b*-value (the slope of the frequency-magnitude relations) of 1. This value is in agreement with *b*=0.96 that was found for the DSF in Israel using instrumental data only (Shapira and Hofstetter, 2002).

The marginal fault zone – Nahal Shehoret

The alluvial fan of *Nahal* Shehoret is dissected by sub-parallel normal faults arranged in a domino structure. The displaced alluvial surfaces are of Holocene and Pleistocene ages (Fig 4). The domino structure has a surficial expression of shallow saddles scattered across the alluvial surfaces and arranged along straight lineaments directed north - south. Eight trenches were excavated from west to east across several fault scarps in this zone. The faults were trenched from west to east. To the west, faults displace alluvial surfaces of Middle Pleistocene age and to the east faults displace Upper Pleistocene and Holocene alluvial surfaces and Holocene playa deposits. The total vertical displacements on these normal faults ranges from 7.5 m at trench T-6 (Fig. 5), where a fault displaces an Upper Pleistocene alluvial surface, to 0.5 m at trench T-15, where a fault displaces a Holocene alluvial surface. All of the faults are multiple-event fault types except the youngest Holocene fault, which is a single-event type (Table 1). The oldest fault, exposed in trench T-8 (Fig. 1), is oriented NNW and was active after 80ka; based on the catenary relationship it was determined that its activity ceased at most 40ka ago. The fault with the youngest activity is exposed in trenches T-5,T-6,T-17 and T-16. All these trenches were excavated across a N-S lineament of about 3.5 km long. The orientation of this lineament contrasts with the NNW orientation of the fault line exposed in trench T-8 (Amit et al., 2002)

Trench T-17 (Fig. 4)

Trench, T-17, was excavated on the continuation of the fault line exposed in trench T-6 (Fig. 6). The total amount of displacement which is 100 m north to trench T-6 reaches 3.4 m. The normal fault is characterize by an angular unconformity associated with faulting accompanied by

back tilting and followed by normal drag along the fault plane. The tilted of the brittle materials mainly resulted in the opening of tension fissures related to the normal fault between the tilted blocks. Three dicrete colluvil wedges (Fig 6; C1-C3) were deposited as a result of three faulting events post 63.9± 10.9 ka, the age of the surface on which the Reg soil developed across the tilted blocks. The age of the faulting event related to the deposition of unit C1 can not be precisely determined by OSL. This difficulty is because of poor bleaching of the sediment as a result of rapid burial of the collapsed soil material from the hanging wall and soil material dragged toward the fault on the down faulted block. There for the OSL age of wedge C1, composed of colluvial material represents the age of surface Qa1 and not the age of the faulting event. This event displace the surface by 1.5 m, occurred after 63.9± 10.9 ka, the age of the surface. A soil developed in unit C1 during an interval of 7-10 ky. The estimated of the time to form the soil is used to bracket the timing of the first tectonic event detected in this trench to between 7-10ky before the second tectonic event 36 ± 4.5 ka; thus the first event occurred at 45±2 ka. Colluvial unit C2 was dated at 36 ±4.5 ka A third small event occurred later; according to the very weak soil profile developed in the colluvium, the event might have occurred during the past 10ky. The two events are related to the major faulting activity detected in trench T-6. Later displacements were smaller, up to 0.4 m, as also evident in other trenches on this lineament .
A similar trend is also discernible in trench T-15, which was excavated on the same fault line as trench T-17 and T-6 (Table 1). In this case, faulting displaced a Holocene surface. Only one event with a displacement amount of 0.5 m is evident. Based on the relative age dating of soils, it occurred during the Holocene (about 8ka).

The westernmost part of the marginal fault zone was active until 80 ka (Fig. 1,4; trench T-8). The next set of fault trace ~0.5 km to the east was active between 37 and 5 ka, during the late Pleistocene and the middle Holocene (trenches T-10, T-15, T-6). At least two branches represented by trenches T-10 and T-17 were active together. A clear trend of decreasing with time in the amount of displacement is evident across this fult zone. An important observation is that the amount of displacement and number of faulting events vary along a single fault trace.

The central fault zone - Avrona Playa

The central part of the Elat fault zone is characterized by extension and compression structural features, such as grabens and push-up ridges. Flower structures typical of strike-slip faults are clearly defined in the subsurface. Two environments were chosen for paleoseismic analysis. One is a Holocene alluvial fan of Nahal Shehoret that is crossed by a graben structure (Fig. 7). The other, located to the east, is the Avrona playa, across which push-ups, pull-apart and normal faults occur (Fig. 8).

The youngest surface ruptures in the southern Arava valley were detected in the Avrona playa area (Fig. 1). The playa forms one of several en-echelon tectonic basins bounded by subparallel left-stepping faults. It is a 10 km long and 0.5-2 km wide basin that is crossed diagonally by the Elat fault zone in a NNE direction. The playa area at present forms a broad elevated elongated ridge. Its relief is composed of low longitudinal sub-ridges (0.5-4 m high and up to 5 km long) and shallow braided channels flowing along and across these ridges. Wadi Avrona and Wadi Raham drain the playa toward the Gulf of Elat through the Elat coastal sabkha. A detailed analysis of the tectonic history, which deformed the Avrona playa, and changed it from a closed basin with internal drainage system to an open basin, is presented in Amit et al. (1999) (Fig. 8,9). The paleoseismic data is summarized briefly next.

A 2 km long by 1 m high fault scarp dissects a transitional, non-sterile, vegetated playa zone composed of sand to sandy-loam sediment. This fault was evaluated to be the youngest in the playa area. A trench excavated at this site exposes a multiple-event normal fault with one main fault plane (Fig. 10). Five partially preserved colluvial units were identified adjacent to the fault plane (Fig. 10, units I-V). Each wedge merges with a fluvial unit on the down-faulted block. Continues fluvial erosion on the down faulted block removed most of the colluvial material, leaving only the upper most part of each colluvial wedge. The variation in the pedogenic features in the colluvial units indicates that each wedge formed during different time period. According to the age of unit 3, which overlies the colluvial units, and unit 1a at the base of the section, five tectonic events occurred between 14,200± 300 and 3700± 300 years ago. Each of these events was accompanied by displacements of at least 0.5 m. The deposition of unit 3 marks the beginning of at least 2000 years of quiescence. During this period, fluvial sediments were deposited mainly on the down faulted block. Fluvial activity along the fault scarp decreased over the last 3000 yr. Toward the end of this period, fluvio-eolian sand sheets were deposited over the entire playa area and cover the fault trace. At this stage a soil was developed continuously across the inactive faulted area. Tectonic activity along this fault was renewed sometime between 700 and 1000 years ago, as indicated by a vertical surface displacement of about 1 m (the petrosalic horizon, detected in unit 5a, of the Salorthid soil was used as a stratigraphic maker for the measurement of the displacement). The paleoseismological, geophysical and archaeological evidences indicate that this last event was the historical devastating earthquake which occurred in 1068 AD in the eastern Mediterranean region (Fig. 11) (Zilberman et al., 2005). To conclude, at least six surface rupture events have affected the Avrona playa during the last 14,000 years.

Geodetic measurements of the displacement field along and across the DST

The estimated seismic slip rate along the DSF, based on historical earthquakes account for only 1/3 of the total plate motion (Garfunkel et al., 1981), and the 20th century seismicity accounts for only 10% of the geologic slip (Salamon et al., 1996). These estimations indicate that either a strong earthquake along the DST is overdue or that the missing slip is aseismic. A first direct evidence for creep along the DSF was reported by Finzi (2005). In this study, aseismic slip was detected by Interferometric Synthetic Aperture Radar (InSAR) measurements of surface deformation along the Arava segment within Yotvata, Zofar and Avrona fault step-over zones. However, no creep was detected between these zones. Finzi (2005) suggested that 30-50% of the total slip was released aseismically during the years 1995-2000. However, due to the fact that the look angle of InSAR satellites is almost perpendicular to the direction of the DSF, it makes it very difficult, almost impossible, to measure interseismic surface deformation along the DSF using InSAR observations.

Several attempts were made to geodetically measure the displacement field along and across the DST in Israel. A network of far-field permanent GPS receivers revealed about 3.7 mm/yr left-lateral movement across the DST, but suggested that the fault itself is locked (*Wdowinski et al.,* 2004). Analysis of two campaign GPS measurements in Israel in 1996 and 2002, led *Ostrovsky* (2001) to estimate the present rate of plate movement along the central DST to be 7.5mm/yr. Recent detailed GPS measurements across the Arava segment (southern DST) suggested left-lateral motion on the order of 5mm/yr and a locking depth of 12km (*Le Beon et al.*, 2008). Still, all recent GPS observations along the DST lack near-fault measurements and therefore are unable to resolve the depth or the rate of shallow creep motions. Figure 12 presents the location of new campaign sites along a dense profile (200-1000 m apart) and across the geologically mapped Arava fault zone .

References

Amit, R., E. Zilberman, N. Porat, Y. Enzel (1999). Relief inversion in the Avrona playa as evidence of large-magnitude historical earthquakes, southern Arava Valley, Dead Sea Rift. Quaternary Research 52, 76-91.

Amit, R., Harrison, J.B.J., Enzel, Y., 1995. Use of soils and colluvial deposits in analyzing tectonic events – the southern Arava valley, Israel. Geomorphology, v.12, 91-107

Amit, R., E. Zilberman, Y. Enzel, and N. Porat (2002). Paleoseismic evidence for time dependency of seismic response on a fault system in the southern Arava valley, Dead Sea rift, Israel, *Geol. Soc. Am. Bull.* 114, 192-206.

Finzi, Y., 2005. Current deformation in the southern Dead Sea Transform: Radar interferometry measurements and their tectonic implications. Geological Survey of Israel report, GSI/24/04, 74 p.

Garfunkel, Z., I, Zak, and R., Freund, 1981, Active faulting in the Dead Sea rift, *Tectonophysics,* 80, 1-26.

Guidoboni, E., and A. Comastri (2005). *Catalogue of earthquakes and tsunamis in the Mediterranean area from the 11th to the 15th Century.* INGV-SGA, Italy.

Hamiel, Y., R., Amit, Z.B., Begin, S., Marco, O., Katz, A., Salamon, E., Zilberman, N., Porat (in press), The seismicity along the Dead Sea fault during the last 60,000 years. BSSA

Hofstetter, A., H.K. Thio, and G. Shamir (2003). Source mechanisms of the 22/11/1995 Gulf of Aqaba earthquake and its aftershock sequence, *J. Seism.* 7, 99– 114.

Joffe, S., and Z. Garfunkel (1987). Plate kinematics of the circum Red Sea- a re-evaluation, *Tectonophysics* 141, 5-22.

Le Beon, M., Y. Klinger, A.Q. Amrat, A. Agnon, L. Dorbath, G. Baer, J-C Ruegg, O. Charade, O. Mayyas, 2008. Slip rate and locking-depth from GPS profiles across the southern Dead Sea Transform, *J. Geophys. Res.,* 113.

Marco, S., T.K. Rockwell, A. Heimann, U. Frieslander, and A. Agnon (2005). Late Holocene slip of the Dead Sea Transform revealed in 3D palaeoseismic trenches on the Jordan Gorge segment, *Earth Planet. Sci. Lett.* 234, 189-205.

Ostrovsky, E., 2001. The G1 GPS geodetic-geodynamic reference network: Final processing results. Israel Journal of Earth Sciences, v. 50, 29 - 38

Salamon, A., A. Hofstetter, Z. Garfunkel, and H. Ron (1996), Seismicity of the Eastern Mediterranean region: Perspective from the Sinai subplate, *Tectonophysics*, *263*, 293-305.

Salamon, A., A. Hofstetter, Z. Garfunkel, and H. Ron (2003). Seismotectonics of the Sinai subplate - The eastern Mediterranean region, *Geophys. J. Int.* 155, 149-173.

Shapira, A., and A. Hofstetter (2002). Seismicity parameters of seismogenic zones, *Geophy. Inst. Israel report,* 592/230/02.

Wells, D.L., and K.J. Coppersmith (1994). New empirical relationships among magnitudes, rupture length, rupture width, rupture area, and surface displacement, *Bull. Seismol. Soc. Am.* 84, 974-1002.

Wdowinski, S., Bock, Y., Baer, G., Prawirodirdjo, L., Bechor, N., Naaman, S., Knafo, R., Forrai, Y, Melzer, Y., 2004. GPS measurements of current crustal movements along the Dead Sea Fault. JGR, v. 109, B05403, doi:10.1029/2003JB002640

Zilberman, E., R. Amit, N. Porat, Y. Enzel, and U. Avner (2005). Surface ruptures induced by the devastating 1068 AD earthquake in the southern Arava valley. Dead Sea Rift, Israel, *Tectonophysics* 408, 79-99.

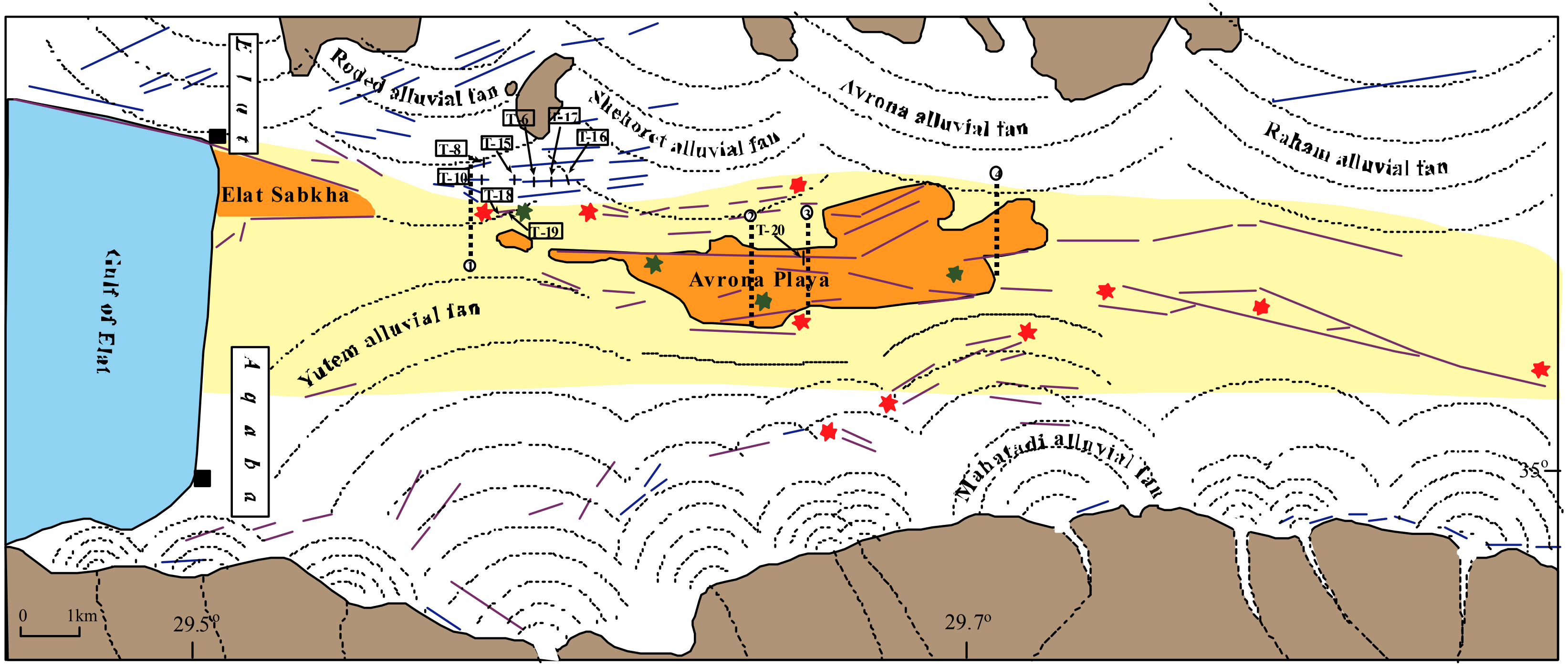

Figure 1: Map of the southern Arava Valley showing the main morphological and morphotectonic elements of the southern Arava Valley. Notice marginal (white color) and central fault zone (Yellow color), the distribution of the trenches across the selected fault lines and the location of seismic lines.

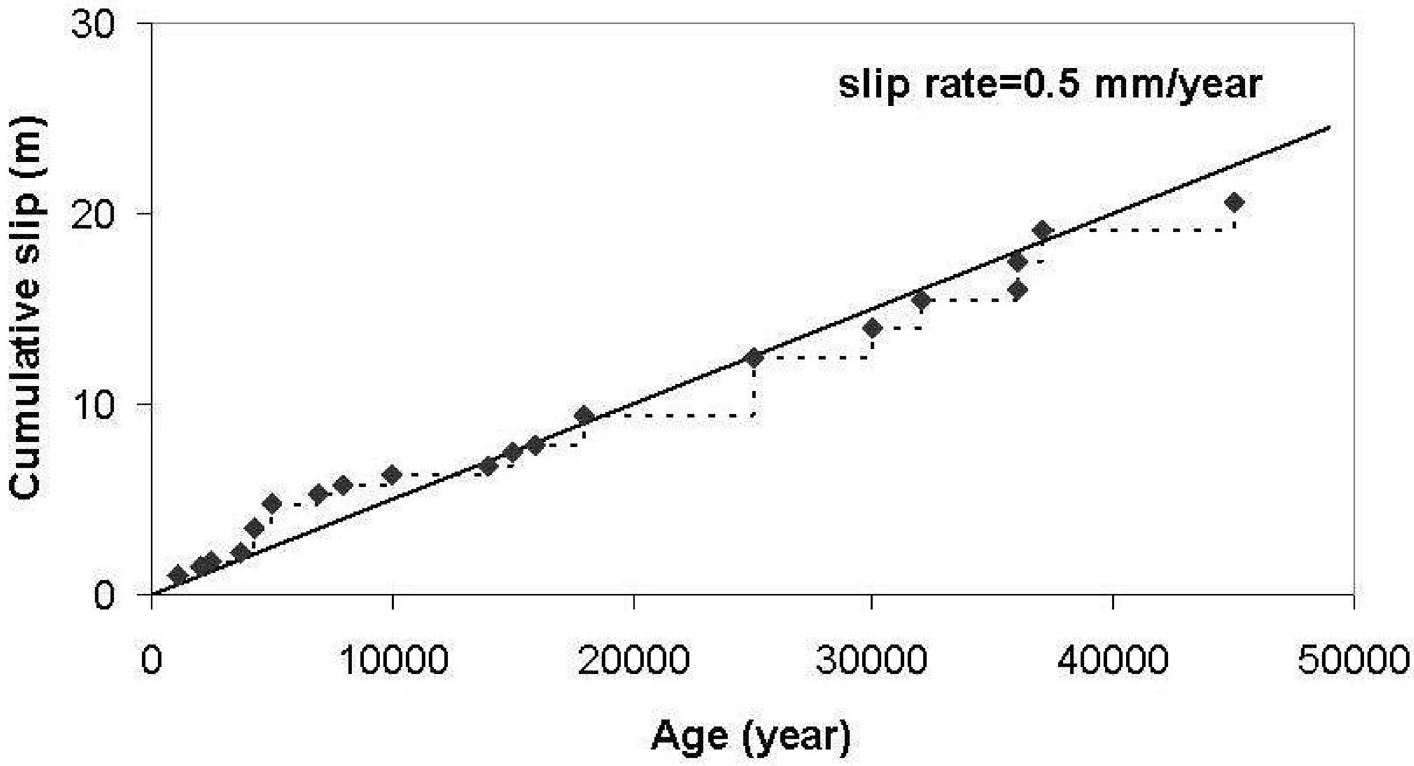

Figure 2: Cumulative normal slip versus time from the southern Arava paleo-seismic data (diamonds). The black line illustrates a slip rate of 0.5 mm/year.

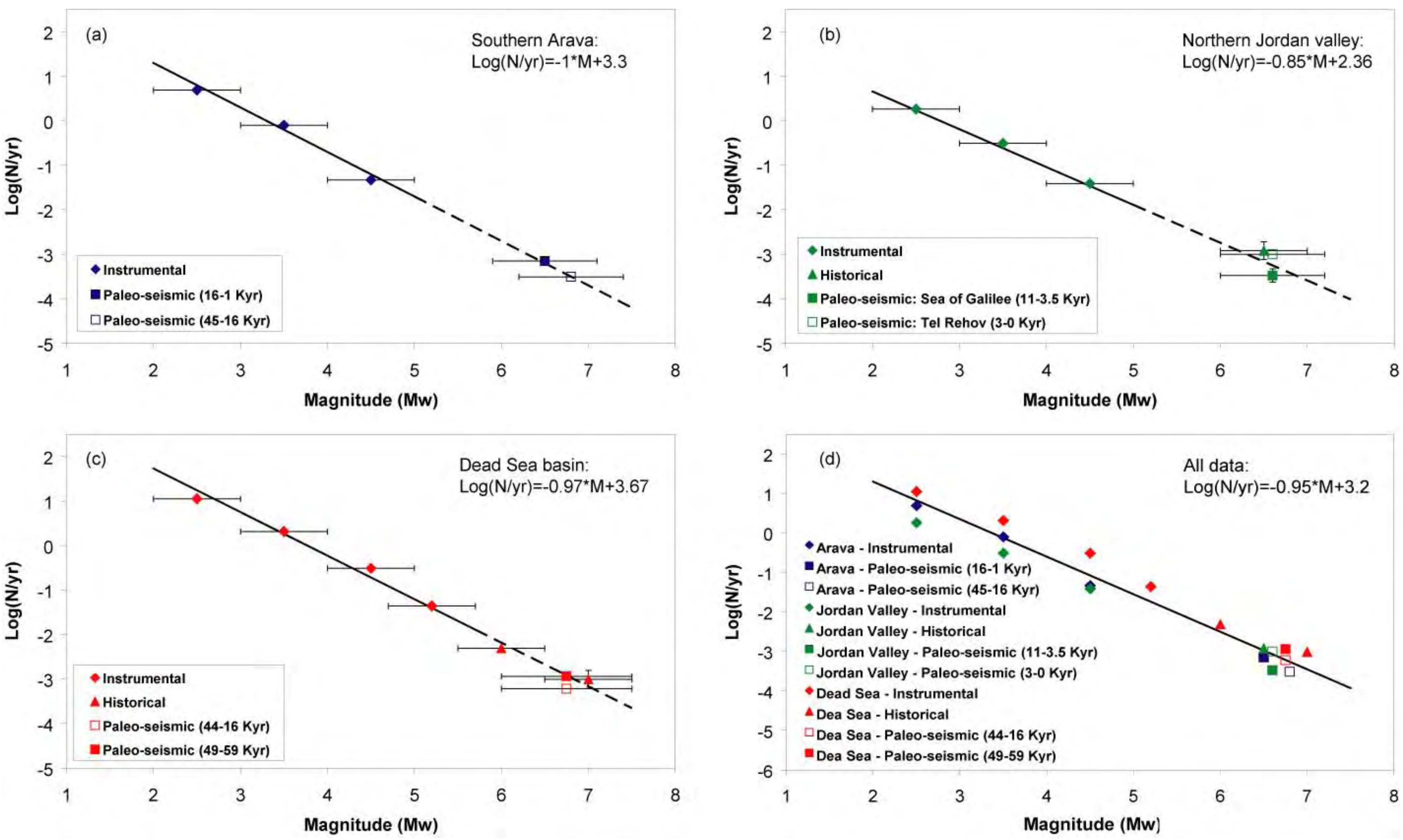

Figure 3: Frequency-magnitude relations for the southern Arava Valley segment (a), the northern Jordan Valley segment (b), the Dead Sea basin (c), and all three segments together (d), using instrumental (diamonds), historical (triangles), and paleo-seismic (squares) records. Black lines denote the regression curves for the instrumental record only (in a-c), and dashed lines denote its extrapolation. Black line in (d) denotes the best fitted model for all data. Note that *b*-value (the slope of the curve) of 0.95 can explain the whole data range for all three segments. (Hamiel et al., in press BSSA)

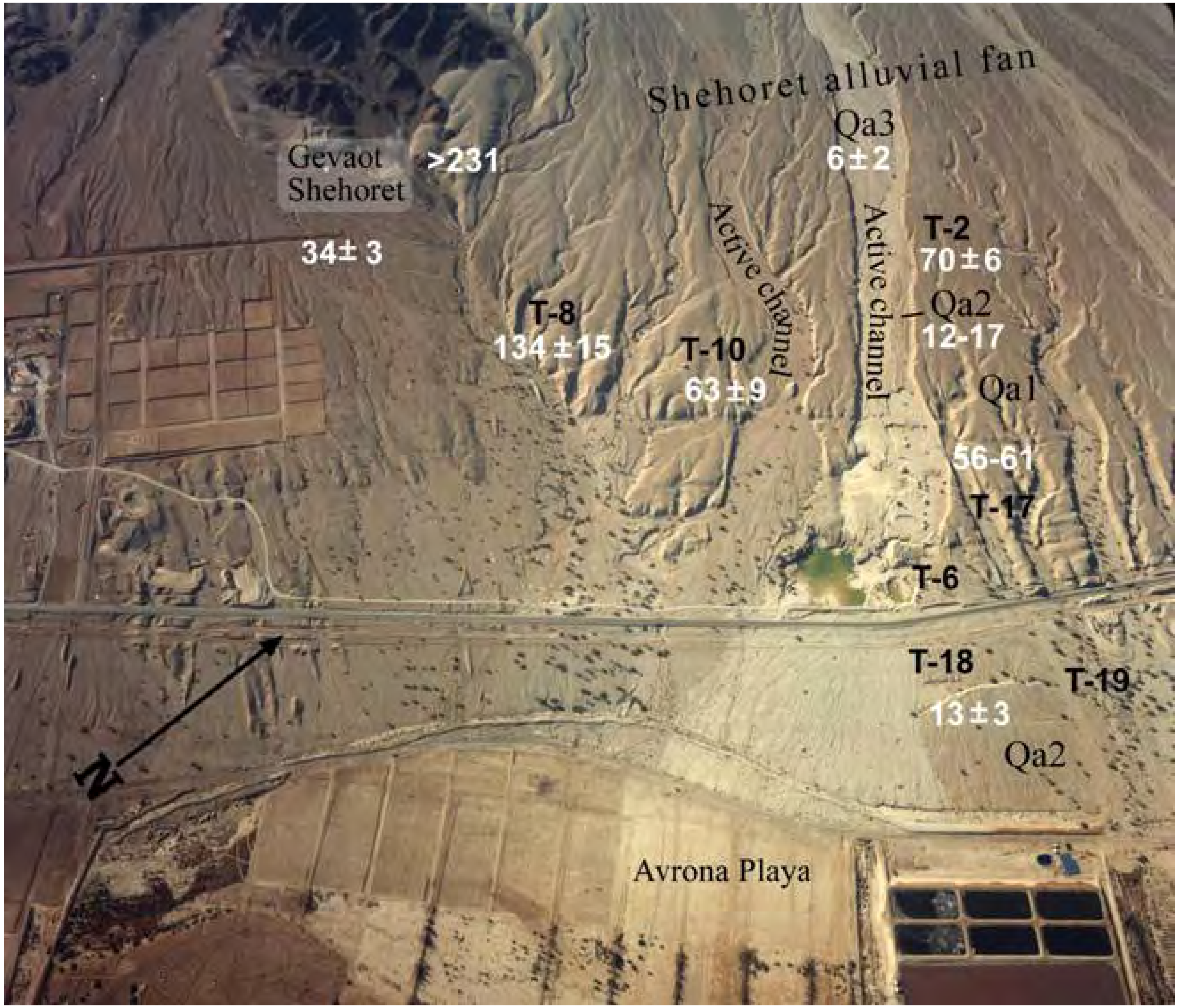

Figure 4: Arial photo of Shehoret alluvial fan. Notice the dated surfaces by OSL ages, trenches location and numbers.

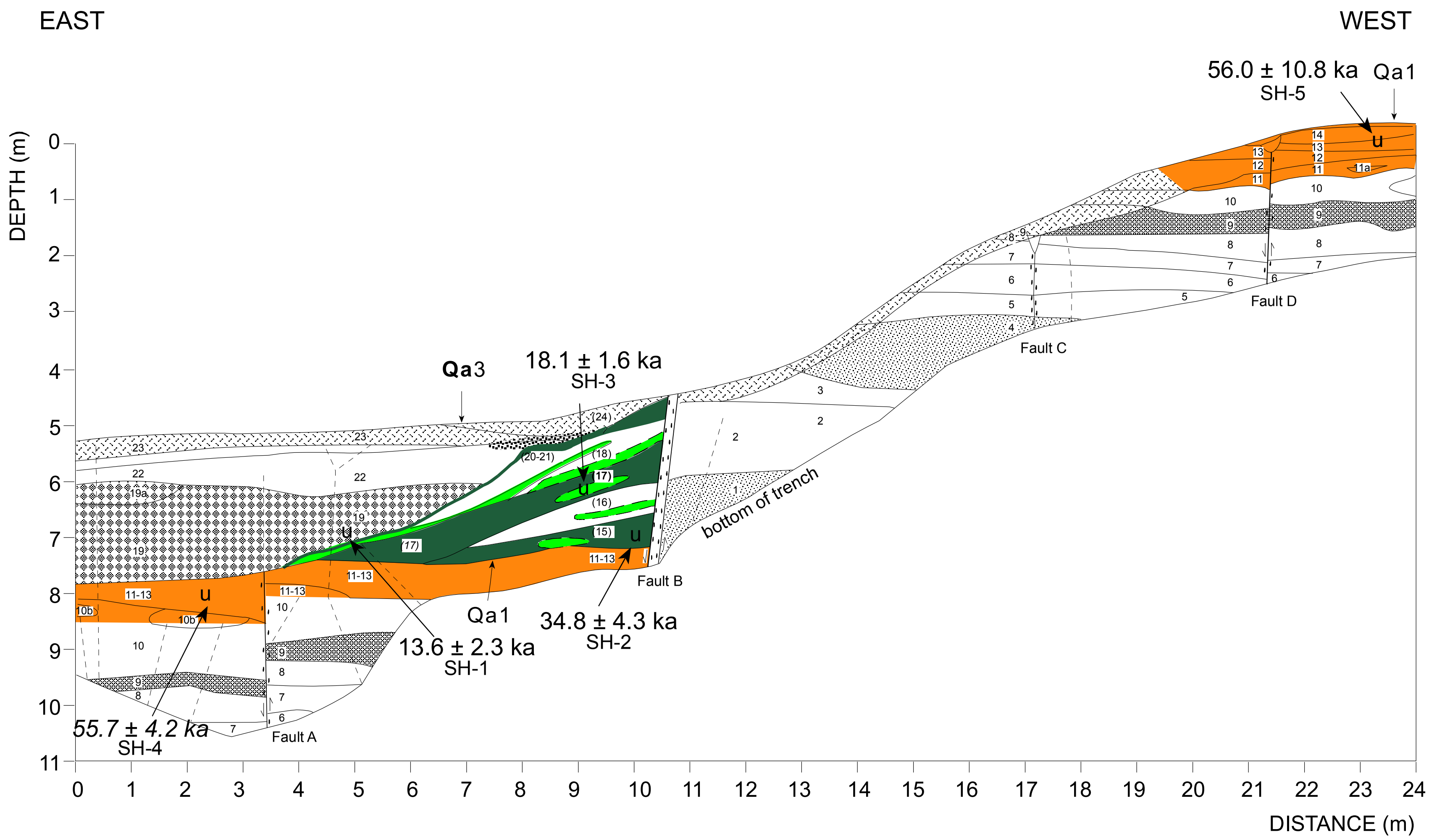

Figure 5: Log of the southern wall of trench T-6 across one of the faults that cross the marginal fault zone.

~ 1 m vertical displacement; Mw ~ 6.6

1.2 ± 0.3 ky

Last earthquake 1068 AD

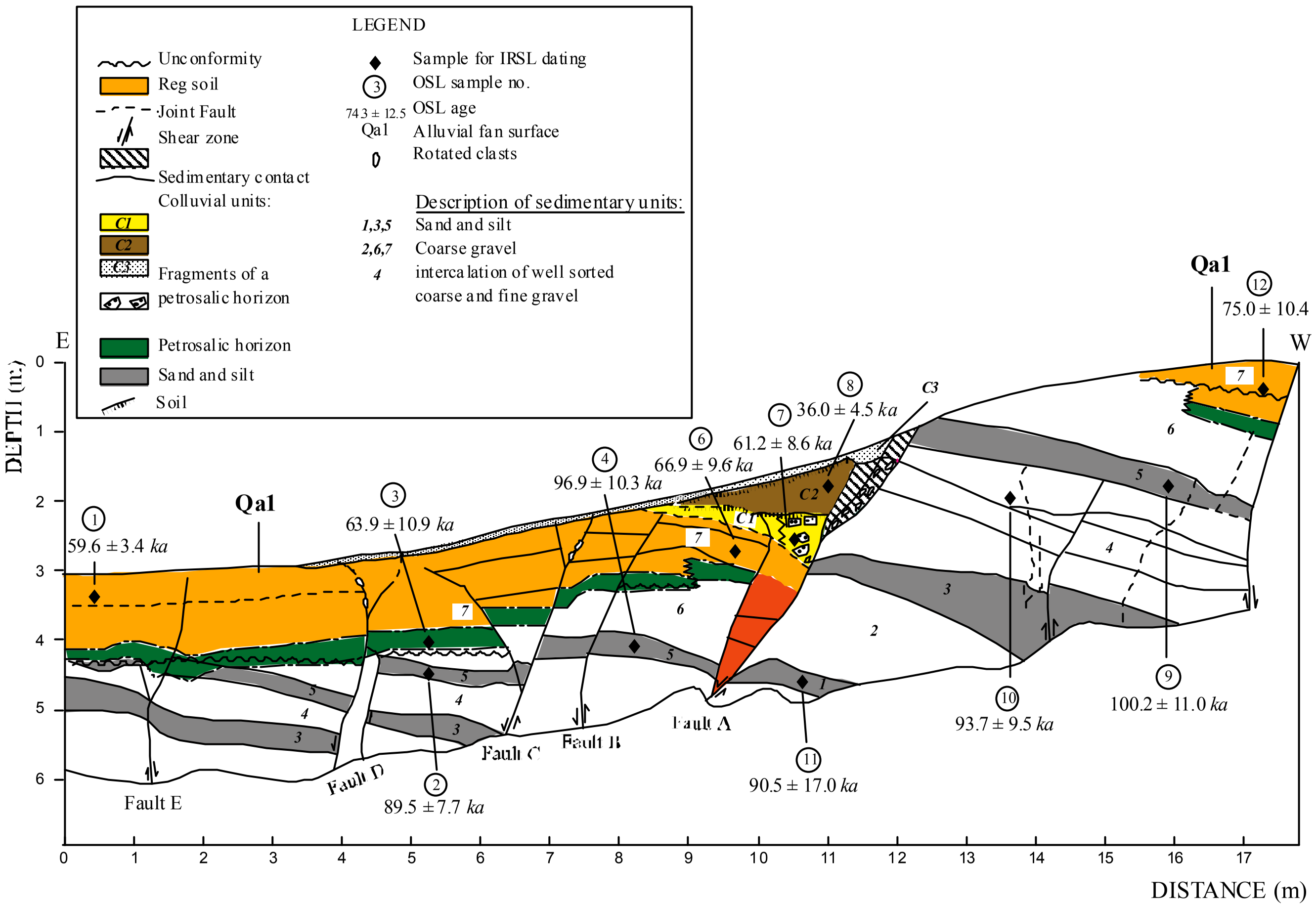

Figure 6: Log of the southern wall of trench T-17 across a fault scarp in the Avrona playa.

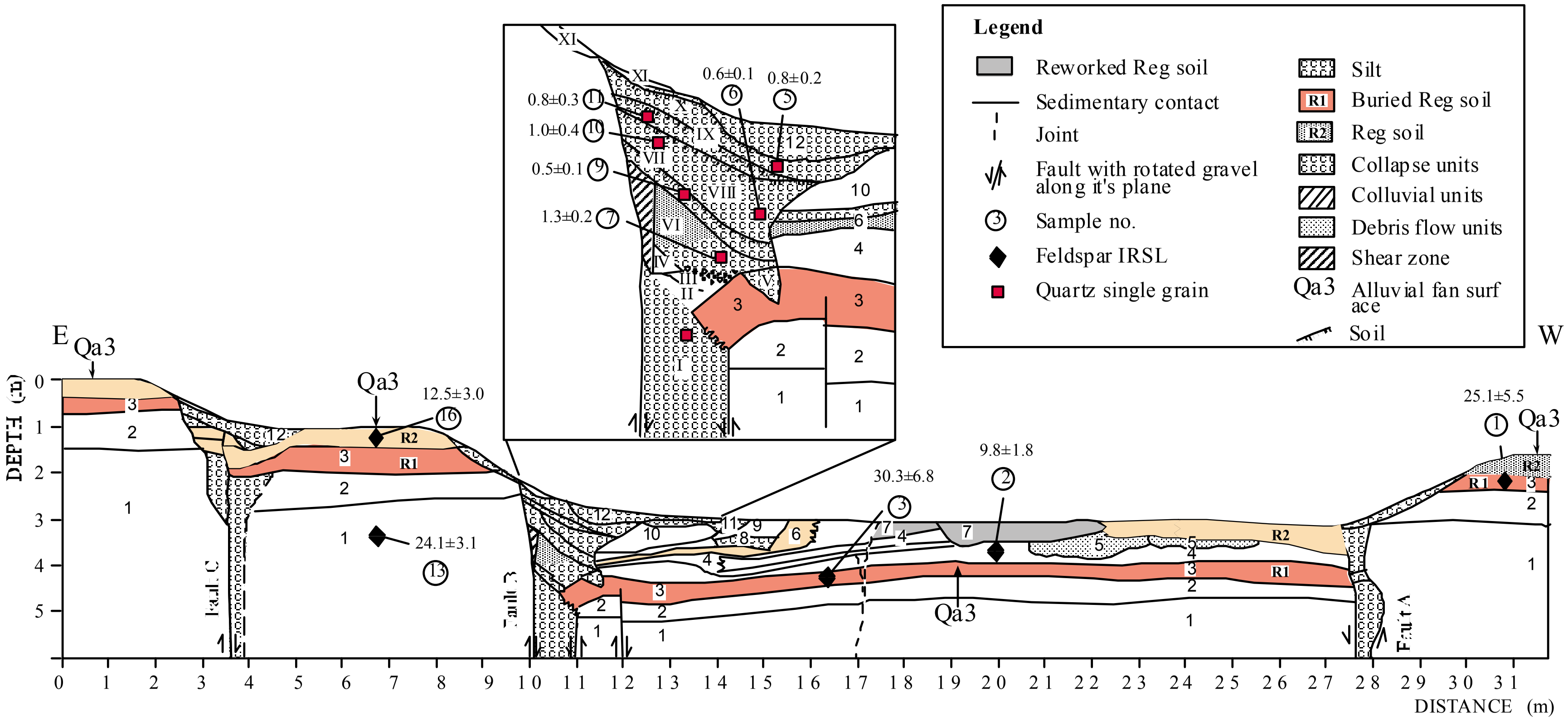

Figure 7: Log of the southern wall of trench T-18, showing a graben structure located in the central fault zone. The box shows details of area adjacent to fault B.

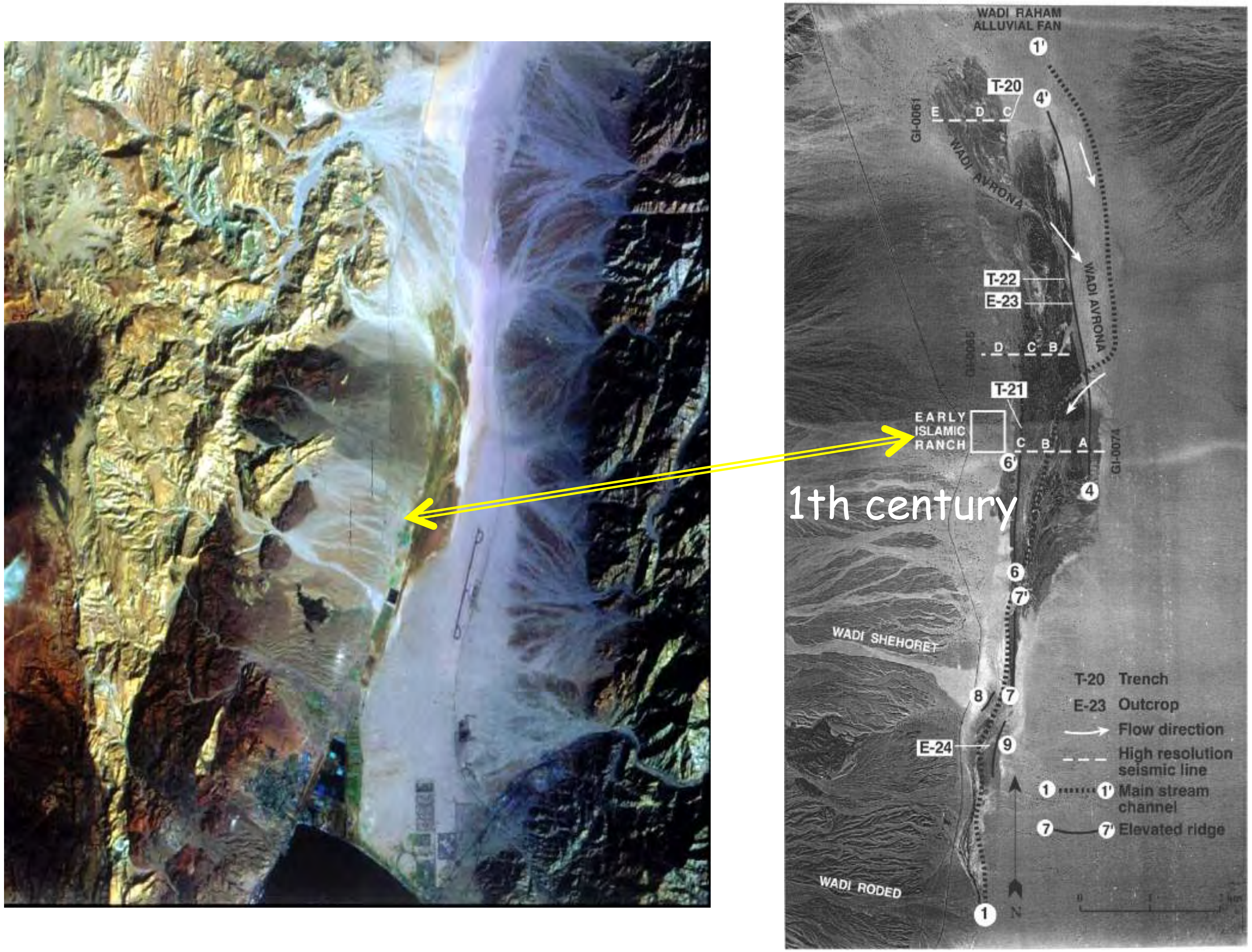

Figure 8: Air photos of the Avrona Playa showing the traces of photogrametric topographic profiles (circles) and the sites of the trenches and exposures (rectangles). The straight lineament that bounds and crosses the playa (dark area) represents a NNE-trending fault of the Avrona Shear Zone. This fault was trenched in T-20. The dark area bounded by straight lineaments corresponds to the uplifted sterile playa sediment. The light-tone areas mark the wide braided Wadi Avrona stream, which occupies a structural depression in the north and splits into several narrow and shallow streams within the playa area. The main faults are designated A-E; geophysical lines are labeled GI-0061, GI-0065 and GI-0074

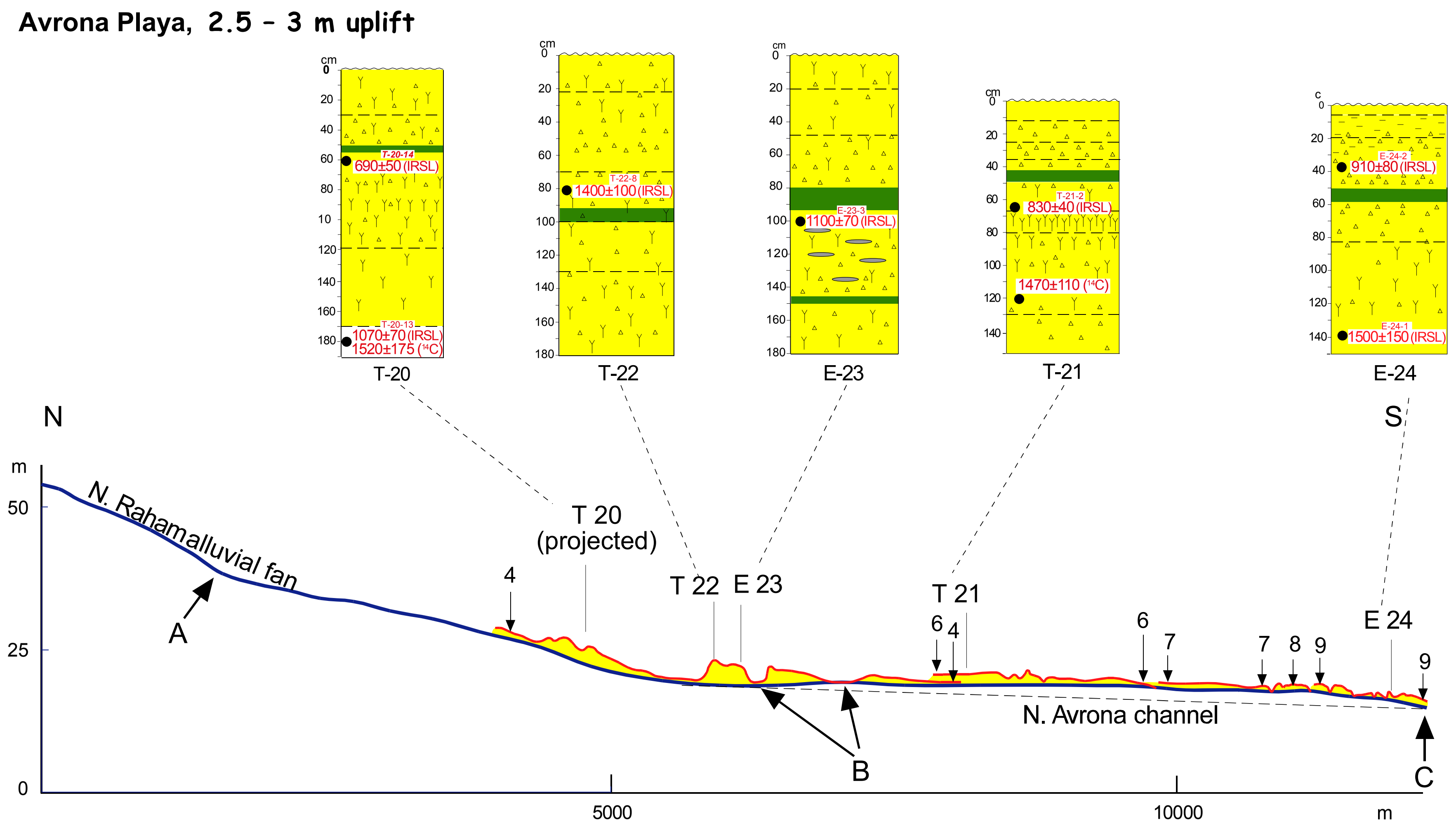

Figure 9: Composite topographic profiles of Wadi Avrona stream channel and the elevated sub-ridge across the playa area. Notice the nick point at A, where the stream crosses the fault that displaces the alluvial fan and the convex profile of the stream channel between points B and C, where the stream crosses the elevated ridge. Numbers refer to segments of the profiles. The soil and sedimentary profiles represent the upper 1.5 m of the elevated playa deposits showing similarity throughout the tectonically deformed area. Notice the petrosalic horizon which serves as a chrono-stratigraphic marker for correlating the elevated playa surface.

~ 1 m vertical displacement; Mw ~ 6.6

1.2 ± 0.3 ky

Last earthquake 1068 AD

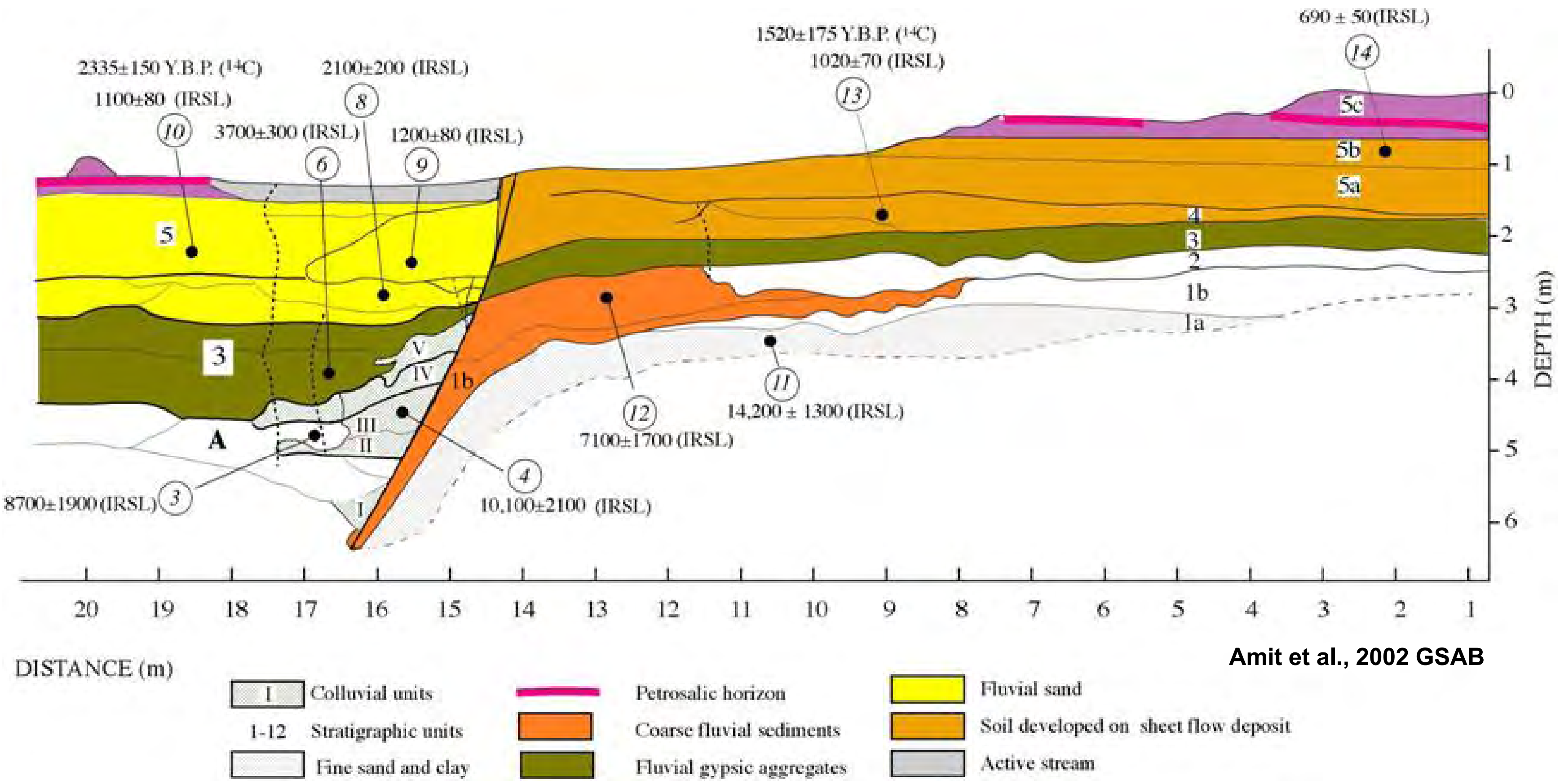

Figure 10: Log of the southern wall of trench T-20 across a fault scarp in the Avrona playa.

Avrona early Islamic farm - Qanat irrigation system

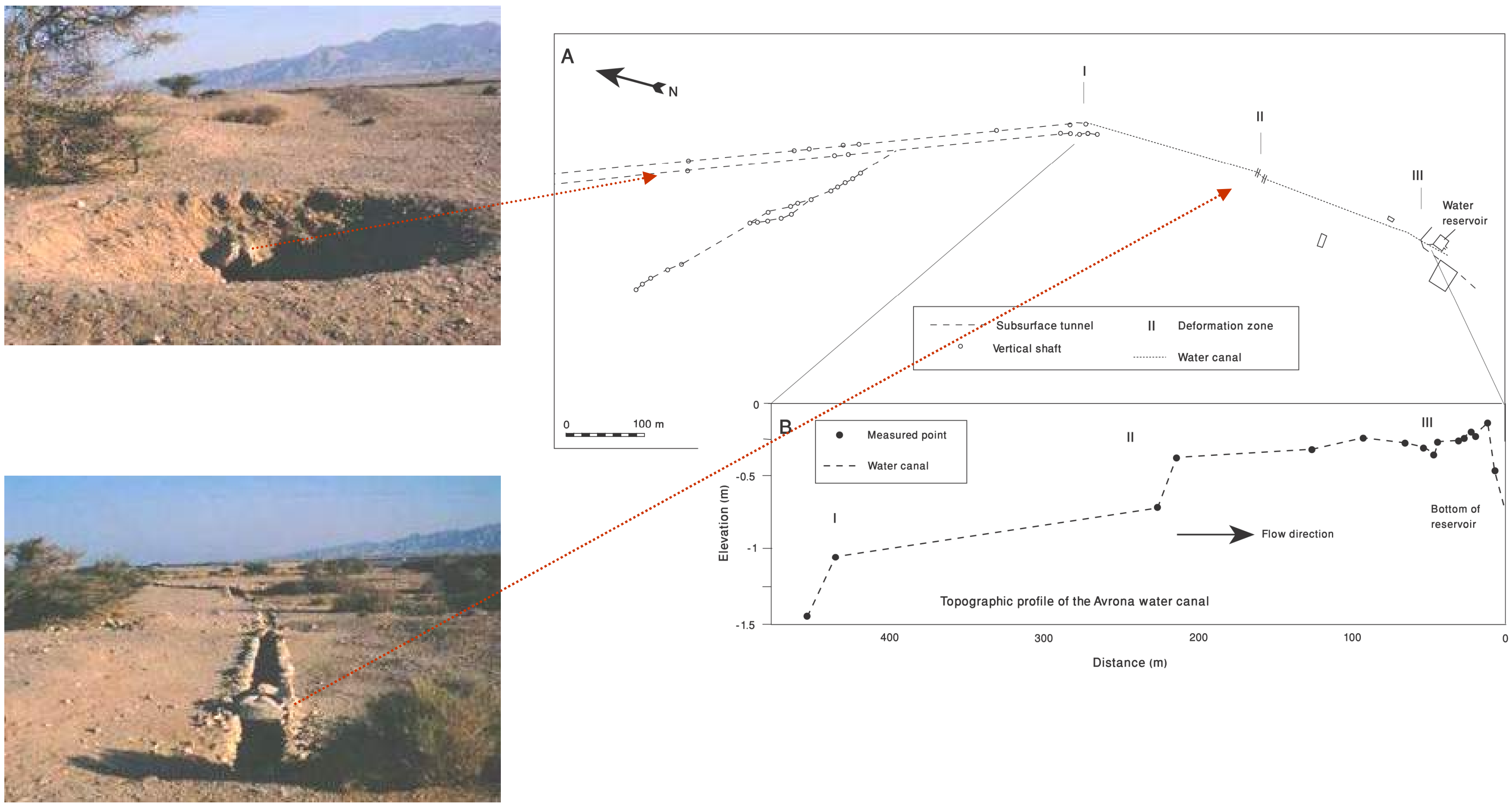

Figure 11: Topographic profile of the water canal in the Avrona Islamic farm. The profiles were measured by EDM total station.

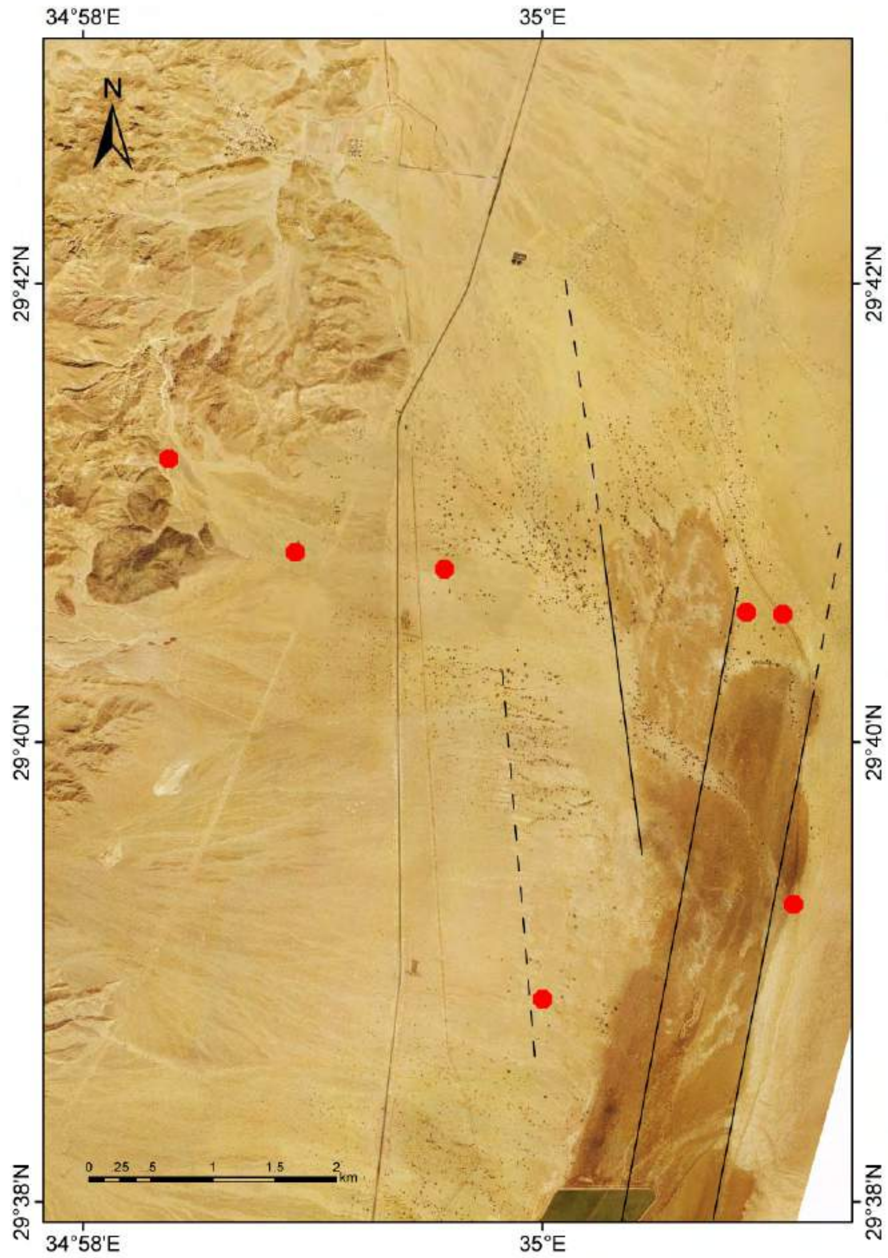

Figure 12: Red dote: location of GPS measurement

Table 1: Eilat fault zone data

<table>
<tr><th>Segment</th><th>Trench site</th><th>Event</th><th>Age, ka</th><th>Displacement, m</th><th>Cumulative displacement, m</th><th>Magnitude (M)</th><th>Reccurrence, kyr (average)</th><th colspan="2">Slip rate mm/yr (average)</th><th>Time start point, ka</th><th>Dating methods</th></tr>
<tr><td rowspan="17">Marginal fault zone</td><td>T-8</td><td>1</td><td>84±6</td><td>3.5</td><td>3.5</td><td>7.0</td><td>—</td><td colspan="2">—</td><td>—</td><td>OSL</td></tr>
<tr><td rowspan="4">T-10</td><td>1</td><td>25±15</td><td>3</td><td rowspan="4">4</td><td>6.9</td><td rowspan="4">5±2</td><td colspan="2" rowspan="4">0.2</td><td rowspan="4">25</td><td rowspan="4">Soils and
SLOPEAGE model</td></tr>
<tr><td>2</td><td>15±5</td><td>0.7</td><td>6.5</td></tr>
<tr><td>3</td><td>10±5</td><td>0.2</td><td>6.1</td></tr>
<tr><td>4</td><td>5±1.5</td><td>0.1</td><td>5.9</td></tr>
<tr><td rowspan="7">T-6</td><td>1</td><td>37±3.7</td><td>1.6</td><td rowspan="7">7.6</td><td>6.7</td><td rowspan="7">3.8±0.6</td><td rowspan="4">0.3</td><td rowspan="7">0.25</td><td rowspan="7">37</td><td rowspan="7">OSL, Soils
SLOPEAGE model</td></tr>
<tr><td>2</td><td>32±3.4</td><td>1.5</td><td>6.7</td></tr>
<tr><td>3</td><td>30±3</td><td>1.6</td><td>6.7</td></tr>
<tr><td>4</td><td>18±1.6</td><td>1.5</td><td>6.7</td></tr>
<tr><td>5</td><td>16±1.6</td><td>0.4</td><td>6.3</td><td rowspan="3">0.2</td></tr>
<tr><td>6</td><td>14±1.4</td><td>0.5</td><td>6.4</td></tr>
<tr><td>7</td><td>10±5</td><td>0.5</td><td>6.4</td></tr>
<tr><td rowspan="3">T-17</td><td>1</td><td>45±2</td><td>1.5</td><td rowspan="3">3.4</td><td>6.7</td><td rowspan="3">6.6±1.4</td><td rowspan="2">0.3</td><td rowspan="3">0.2</td><td rowspan="3">45</td><td rowspan="3">OSL, Soils
SLOPEAGE model</td></tr>
<tr><td>2</td><td>36±4.5</td><td>1.5</td><td>6.7</td></tr>
<tr><td>3</td><td>5±2</td><td>0.4</td><td>6.3</td><td>0.1</td></tr>
<tr><td>T-16</td><td>1</td><td>36±9</td><td>0.5</td><td>Active channel</td><td>6.4</td><td>—</td><td colspan="2">—</td><td>—</td><td>OSL</td></tr>
<tr><td>T-15</td><td>1</td><td>8±2</td><td>0.5</td><td>0.5</td><td>6.4</td><td>8±2</td><td colspan="2">0.1</td><td>8</td><td>Soils</td></tr>
<tr><td rowspan="13">Central fault zone</td><td rowspan="9">T-18</td><td>1</td><td>10±2</td><td>0.5</td><td rowspan="9">4</td><td>6.4</td><td rowspan="9">1±0.4</td><td colspan="2" rowspan="9">0.3</td><td rowspan="9">10</td><td rowspan="9">OSL, Soils
SLOPEAGE model</td></tr>
<tr><td>2</td><td>8±2</td><td>0.2</td><td>6.1</td></tr>
<tr><td>3</td><td>7±2</td><td>0.2</td><td>6.1</td></tr>
<tr><td>4</td><td>4.5±2</td><td>1.3</td><td>6.7</td></tr>
<tr><td>5</td><td>2.5±1</td><td>0.2</td><td>6.1</td></tr>
<tr><td>6</td><td>2±1</td><td>0.5</td><td>6.4</td></tr>
<tr><td>7</td><td>1.5±0.5</td><td>0.5</td><td>6.4</td></tr>
<tr><td>8</td><td>1±0.5</td><td>0.3</td><td>6.2</td></tr>
<tr><td>9</td><td>1±0.5</td><td>0.3</td><td>6.2</td></tr>
<tr><td>T-19</td><td>1</td><td>4.1±0.8</td><td>1</td><td>Active channel</td><td>6.6</td><td>—</td><td colspan="2">—</td><td>—</td><td>OSL, Soils</td></tr>
<tr><td rowspan="3">T-20</td><td>1</td><td>7.1±1.7</td><td>0.5</td><td rowspan="3">2</td><td>6.4</td><td rowspan="3">2±0.3</td><td colspan="2" rowspan="3">0.3</td><td rowspan="3">10</td><td rowspan="3">OSL, ^{14}C, Soils</td></tr>
<tr><td>2</td><td>3.7±0.3</td><td>0.5</td><td>6.4</td></tr>
<tr><td>3</td><td>1.1±0.1</td><td>1</td><td>6.6</td></tr>
</table>

Landscape development in an hyper arid sandstone environment along the margins of the Dead Sea fault: implications from dated rock falls

Ari Matmon[1*], Yony Shaked[1], Amotz Agnon[1], Naomi Porat[2], Yehouda Enzel[1], Robert Finkel[3], Nathaniel Lifton[4], and Boaretto Elisabetta[5]

[1]Institute of Earth Sciences, The Hebrew University of Jerusalem

[2]Geological Survey of Israel

[3]Lawrence Livermore National Laboratories

[4]Geosciences Department, University of Arizona, Tucson

[5]Weizmann Institute of Science

arimatmon@cc.huji.ac.il

*Field guide

In this study we explored the spatial and temporal relations between boulders and their original in-situ locations on sandstone bedrock cliffs. This was accomplished by combining field observations with dating methods using cosmogenic isotopes (^{10}Be and ^{14}C) and optically stimulated luminescence (OSL). Our conclusions bear both on the landscape evolution and cliff retreat process in the hyper-arid region of Timna and on the methodology of estimating exposure ages using cosmogenic isotopes.

Geological and morphological setting

Timna is located at the western margin of the southern Arava Valley, a hyper-arid region extending from the Dead Sea basin to the Gulf of Aqaba (Fig. 1). Timna is an uplifted core of late Precambrian igneous rocks (Druckman et al., 1993) overlain by Cambrian and lower Cretaceous clastic sediments. It is a bowl-shaped valley, about 8 km in diameter, and is surrounded by cliffs of upper Cretaceous limestone and dolomite rising up to 600 m above the valley floor.

Landscape development in the Timna area is controlled by the tectonic activity along the southern section of the DSF (Hannan Ginat, personal communication). Erosional truncation of the upper Cretaceous carbonate cap rocks during the Oligocene and Miocene exposed the more erodable lower Cretaceous sandstone. As the southern Arava Valley developed into a topographic base level, the sandstone was eroded and transported towards that base level, the Timna Valley was incised, and the Precambrian basement and Cambrian sediments were exposed at the base of the Timna Valley.

The Cambrian sandstone in Timna reaches a thickness of about 100 m (Druckman et al., 1993) and forms cliffs that dominate the landscape. Within the Cambrian sandstone terrain, erosion is dominated both by detachment of massive boulders from the sandstone cliffs and by slow weathering of the cliff faces, as evident from 0.1 m-scale cavities (tafoni). Generally, boulders detached from sandstone cliffs are found in piles, and are usually coated with varnish. In many locations, the cliff face and the faces on the boulders match perfectly both in detail and overall morphology. Some of these boulders can be accurately traced to their original position on the cliff from which they were detached (Fig. 2).

We concentrated on three boulder sites in the Timna area (Figs. 1 and 3). The first, the Lower Valley, contains two boulder piles (one close to the source sandstone cliff face, which we call the "Closer Pile", and one farther away, the "Farther Pile") detached from a cliff that rises 10-14 m above the valley floor. The boulders at this site were deposited at the mouth of the Lower Valley (30X60 m), creating a dam, and causing upstream accumulation of sandy sediments on the valley floor. The second site, the Upper Valley, contains several boulder piles. We concentrated on a single boulder pile detached from a nearby 10 m cliff. At both locations boulders are not significantly affected by erosion and perfectly match the cliff faces (Fig. 2). Unlike the first two sites that contain unweathered boulder piles, the third site we examined contains three weathered boulders that are located at distances of 20, 14, and 4 meters from the source cliff.

Results

We recognize three discrete rock fall events, at 31 ka, 15ka, and 4ka (Figs. 4 and 5). In this hyper arid region the most plausible triggering mechanism for rock fall events is strong ground acceleration caused by earthquakes generated by the nearby Dead Sea fault (DSF). Our record, however, under represents the regional earthquake record implying that ongoing development of detachment cracks prior to the triggering event is slower than the earthquake cycle.

Cliff retreat rates calculated using the timing of rock fall events and estimated thickness of rock removed in each event range between 0.14 m ky^{-1} and 2 m ky^{-1} (Fig. 8) When only full cycles are considered, we derive a more realistic range of 0.4 m ky^{-1} to 0.7 m ky^{-1}. These rates are an order of magnitude faster than the calculated rate of surface lowering in the area. We conclude that sandstone cliffs at Timna retreat through episodic rock fall events that preserve the sharp, imposing, landscape characteristic to this region and that ongoing weathering of the cliff faces is minor.

A 10%-20% difference in the ^{10}Be concentrations in samples from matching boulder and cliff faces that have an identical exposure histories and are located only a few meters apart, indicate that cosmogenic nuclide production rates are sensitive to shielding and vary spatially over short distances. However, the uncertainties associated with age calculations for boulder and matching cliff face pairs yielded ages that are similar within 1 . The use of external constraints, in the form of field relations and OSL dating helped to establish each pair's age. The agreement between calculated ^{14}C and ^{10}Be ages indicates that the accumulation of ^{10}Be at depth by the capture of slow deep-penetrating muons was properly accounted for in the study.

Rock falls and earthquakes

Many processes, including tectonic, climatic, and environmental factors can cause rockslides (Wieczorek et al., 1996). Many of these factors can be eliminated in the case of rockslides in Timna. Snowmelt, freeze and thaw effects, ground water seepage, and tree root wedging can be ruled out due to the hot and hyper-arid conditions in the area. Although rain storms and the resulting expansion of clay and salt particles in cracks is a plausible mechanism, we would expect boulders to detach one at a time rather than in groups that form large piles as is the case in Timna. Furthermore, the frequency of clay and salt wetting events is not high enough to generate proper stress in the fractures to allow boulder release. Several observations, mainly the large size of the boulders (many of the boulders have at least one dimension longer then 5 meters) and the agreement in ages of boulder piles in the sampling locations suggest that each pile of boulders was detached from its source cliff in a single event. The proximity of Timna to the DSF, where >M6 earthquakes are common, suggests that ground shaking due to seismic events is the most likely cause for the Timna boulder slides.

Rock falls are sensitive recorders of strong ground motion resulting from earthquakes (Bull and Menges, 1977). Synchronous rock falls may indicate the occurrence of past earthquakes and rock fall timing may constrain earthquake recurrence intervals and magnitude. The relation between seismic events and the formation of boulders in rock falls is well established. A worldwide correlation between landslide size and distribution and variables such as earthquake magnitude and the specific ground-motion characteristics was determined by Keefer, (1984). A coseismic lichenometry model was developed in New Zealand following the discovery that lichens growing on rocky hill slopes recorded synchronous pulses of rock falls generated by historical earthquakes. The lichenometry model was used to date boulders and rock falls associated with earthquakes (Bull, 1996a,b; Bull et al., 1994; Kong, 1994; Smirnova and Nikonov, 1990).

Current measurements in the southern Arava Valley along the DSF system show no seismic activity (Shapira, 1997). However, historical evidence documents several large seismic events (Ambraseys, 1994; Amiran, 1994; Fig. 6). Paleoseismic studies in the southern Arava Valley suggest that late Pleistocene earthquakes ranged in magnitude between 6.7 and 7.1 and the average recurrence interval was 2.8±0.7 ky (Amit et al., 2002). These studies indicate that Holocene earthquakes were more frequent, with an average recurrence interval of 1.2±0.3 ky, but with smaller magnitudes that ranged between M5.9 and M6.7. Several studies in the northern Arava Valley also suggest frequent Holocene and late Pleistocene seismic activity (Amit et al., 1996; Ambraseys, 1994; Ken-Tor et al., 2001; Migowski et al., 2004; Enzel et al., 1996; Gluck et al., 1999).

The time interval between the three boulder forming events recorded in this study is much longer than the recurrence interval of >M6 earthquakes in the region. However, this discrepancy does not rule out seismic motion as the mechanism for the boulder formation. We suggest that the interval between boulder forming events represents the time that is necessary for fractures to develop to the point of minimum friction between boulders and bedrock (Fig. 7). During this time, earthquakes occur and gradually enhance the opening of fractures that surround boulders. Once these fractures are sufficiently developed, the next major earthquake releases the boulders. The spacing between the fractures determines the thickness of collapsed wall during each rock fall event and the level of sandstone lithification determines the resistance of the fresh exposed rock to weathering. Continued study of additional rock piles at Timna may help better constrain the temporal frequency of rock fall events, and improve the correlation between rock falls and earthquakes.

Conclusions

The combined ages of boulders from the three investigated sites suggest that they were deposited in three events at 31 ka, 15 ka, and 4 ka. The most likely mechanism for boulder formation in this tectonically active hyper-arid region is by tectonically induced ground motion. Paleoseismic studies in the area suggest a recurrence interval of 1000-2000 yr for earthquakes >M6. The cosmogenic and OSL age dating of the boulders suggests that boulder-formation events do not occur as frequently as >6M earthquakes occur in this area Therefore, it is apparent that boulder falls in the study area do not represent a full seismic record. We suggest that boulder formation events occur during earthquakes only after blocks of rock are sufficiently separated from bedrock by large and well-developed cracks. These cracks allow the detachment of the boulders when the next earthquake occurs.

Cliff retreat rates determined from the rock falls in Timna range between 0.14 and 2 m ky^{-1}. A more constrained range of 0.4 to 0.7 m ky^{-1} is calculated from the complete collapse cycles. These retreat rates are similar to those calculated in other arid regions. Field observations suggest that the retreat occurs mainly during rock fall events and that continuous weathering of the rock faces is less important. Since cliff retreat rates in Timna are an order of magnitude larger than the calculated rate of surface lowering, as calculated in the Lower Valley site, the sharp and imposing landscape characteristic to this region is preserved.

References

Ambraseys, N.N., C.P. Melville, R.D. Adams, The seismicity of Egypt, Arabia, and the Red Sea - A historical review, Cambridge University Press, Cambridge, UK, (1994), 181 p.

Amiran, D., Earthquakes in Israel, Qadmoniot 29 (1994) 53-61.

Amit, R., E. Zilberman, Y. Enzel, N. Porat, Paleoseismic evidence for time dependency of seismic response on a fault system in the southern Arava Valley, Dead Sea rift, Israel, Geol. Soc. Am. Bull. 114 (2002) 192-206.

Amit, R. J.B.J. Harrison, Y. Enzel, N. Porat, Soils as a tool for estimating ages of Quaternary fault scarps in a hyper arid environment - the southern Arava Valley, the Dead Sea rift, Israel, Catena 28 (1996) 21-45.

Bull, W.B., C.M. Menges, Geomorphic evidence for Holocene faulting in the central Mojave Desert, California, GSA, Abstr. Programs 9 (1977) 915.

Bull, W.B., Dating San-Andreas faults with lichenometry, Geology 24 (1996a) 111-114.

Bull, W.B., Prehistoric earthquakes on the Alpine Fault, New Zealand, J. Geophys. Res. 101 (1996b) 6037-6050.

Bull, W.B., P.N. J. Ki, F. Kong, T. Moutoux, W.M. Phillips, Lichen dating of coseismic landslide hazards in alpine mountains, Geomorphology 10 (1994) 253-264.

Druckman,Y., T. Weissbrod, Z. Garfunkel, Geological map of Israel, scale 1:100,000, sheets 25,26, Yotvata and Elat, (1993) Geol Surv. Isr.

Enzel, Y., R. Amit, N. Porat, E. Zilberman, J.B.J. Harrison, Estimating the ages of fault scarps in the Arava, Israel, Tectonophys. 253 (1996) 305-317.

Gluck, D., Y. Enzel, A. Heimann, Late Pleistocene and Holocene earthquakes at the southwestern margin of the Dead Sea Basin, Israel, EOS, Trans. Am. Geophys. Union 80 (1999) Suppl. 1024.

Keefer, D.K., Landslides caused by earthquakes, Geol. Soc. Am. Bull. 95 (1984) 406-421.

Ken-Tor, R., A. Agnon, Y. Enzel, M. Stien, S. Marco, J.F.W. Negendank, High resolution geological record of historic earthquakes in the Dead Sea basin, J. Geophys. Res. 106 (2001) 2221-2234.

Kong, F., Analysis of lichen size data for dating and describing prehistorical seismic shaking, M.S. thesis, University of Arizona, Tucson, (1994).

Migowski, C., A. Agnon, R. Bookman (Ken-Tor), J.F.W. Negendank, M. Stein, Recurrence pattern of Holocene earthquakes along the Dead Sea Transform revealed by varve-counting and radiocarbon dating of lacustrine sediments, Earth Planet. Sci. Lett. 222 (2004) 301-314.

Shapira, A., Seismicity pattern of the Dead Sea transform - A review, Dead Sea, Israel, in: 13th GIF meeting on the Dead Sea rift as a unique global site, Proc., (1997), 160 p.

Smirnova, T.Y., A. Nikonov, A revised lichenometric method and its application dating great past earthquakes, Arctic and Alpine Res. 22 (1990) 375-388.

Wieczorek, G.F., J.B. Snyder, R.B. Waitt, M.M. Morrissey, R.A. Uhrhammer, E.L. Harp, R.D. Norris, M.I. Bursik, L.G. Finewood, Unusual July 10, 1996, rack fall at Happy Isles, Yosemite National Park, California, Geol. Soc. Am. Bull. 112 (1996) 75-85.

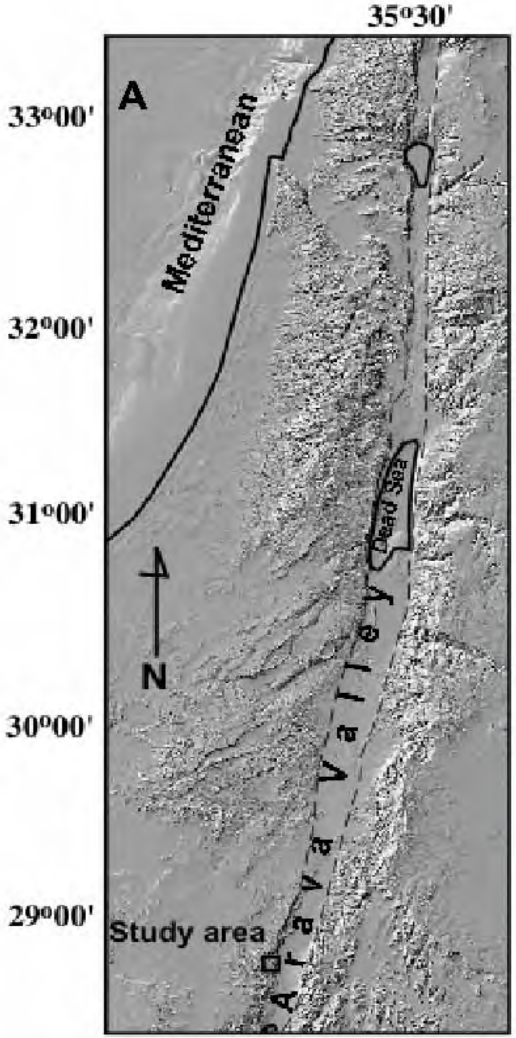

Study area location. A. DEM of Dead Sea fault (DSF) region. B. Aerial photo of the study area.

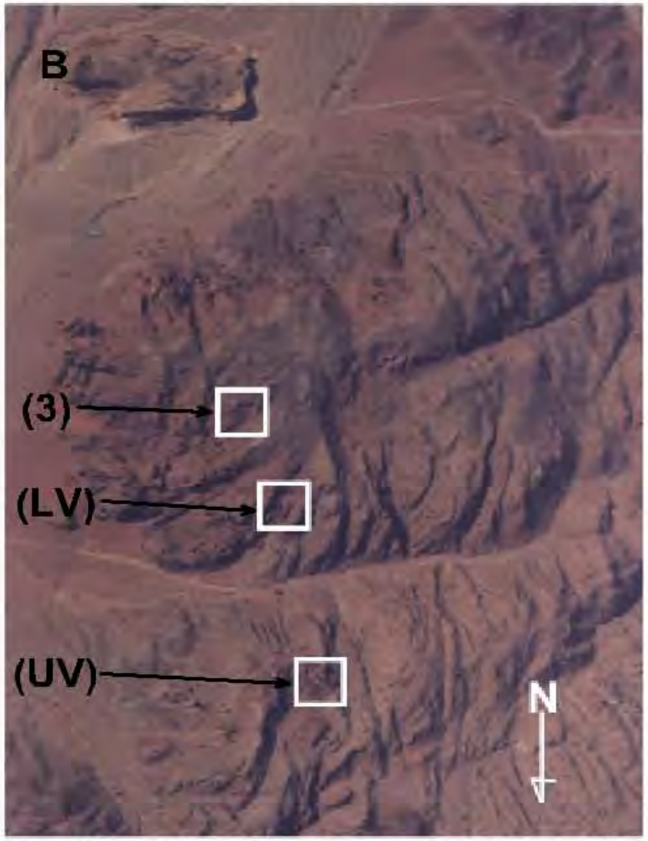

Open white squares indicate sampling sites

Timna is located at the western margin of the southern Arava Valley, a hyper-arid region extending from the Dead Sea basin to the Gulf of Aqaba. Timna is an uplifted core of late Precambrian igneous rocks [Druckman et al., 1993] overlain by Cambrian and lower Cretaceous clastic sediments. Within the Cambrian sandstone terrain, erosion is dominated by detachment of massive boulders from the sandstone cliffs and by slow weathering of the cliff faces, as evident from 0.1 m-scale cavities (tafoni).

Figure 1

A. Small quartzite pebbles on the boulder face can be matched to cavities on the cliff face and vice versa. B. The relief of fracture ribs is apparent on a sampled boulder. Both examples indicate insignificant erosion of boulders since detachment.

Figure 2

We assume a relatively simple, two stage, cosmogenic nuclide accumulation history of the sampled boulders and cliff faces in Timna: the first stage, prior to detachment, when each sampled boulder and its source cliff were identically shielded and accumulated similar amounts of cosmogenic nuclides, and the second stage, after detachment,when cosmogenic nuclides accumulated at surface production rates which were reduced differently for the boulder and the cliff face because of differences in topographic shielding and geometry. Cosmogenic nuclide concentrations can be interpreted in terms of the exposure age of the boulders and cliff faces:

$$N_{measured} = \frac{P_{eff}}{\lambda}(1-e^{-\lambda t}) + (N_{inherited})e^{-\lambda t} \qquad (1)$$

We estimated the pre-detachment accumulation of ^{10}Be, produced at depth mainly by muons, following Granger and Muzikar [2001]:

$$N_{Be} = \frac{B_0}{\frac{1}{\tau_{Be}} + \frac{E\rho}{L_0}} + \frac{B_1}{\frac{1}{\tau_{Be}} + \frac{E\rho}{L_1}} + \frac{B_2}{\frac{1}{\tau_{Be}} + \frac{E\rho}{L_2}} + \frac{B_3}{\frac{1}{\tau_{Be}} + \frac{E\rho}{L_3}} \qquad (2)$$

where B_i is the production in atoms g^{-1} yr^{-1}, L_i is the attenuation length in g cm^{-2} (B_1=0.0055, B_2=0.0137, and B_3=0.0187. L_0 = 165 g cm^{-2}, L_1 = 738 g cm^{-2}, L_2 = 2688 g cm^{-2}, and L_3 = 4360 g cm^{-2}. r = 2.2 g cm^{-3}), E is the surface lowering rate in cm yr^{-1}, ρ is the rock density in g cm^{-3}, and τ_{Be} is the mean life of ^{10}Be (2.18+/-0.09 My). In both the Upper and Lower Valley sites, the source cliff face rises ~10 m above the sample. Therefore, we calculated the accumulation of ^{10}Be at depth assuming steady erosion rate of the upper surface and a minimum depth of 10 m.

Production by nucleons is insignificant at depths of 10 meters and more. Therefore, the first term in equation (2) is insignificant. Sea level, high-latitude (SLHL) production of ^{10}Be by muons is calculated to be 0.116 atoms g^{-1} yr^{-1} for negative muons and 0.026 atoms g^{-1} yr^{-1} for fast muons [Granger and Smith, 2000]. Production rates are scaled for local atmospheric shielding using an atmospheric attenuation length of 240 g cm^{-2}. A resulting scaling factor of 1.19 is determined from the average barometric pressure in the Timna area. The production rate at a depth of 10 m is calculated using [Granger and Muzikar, 2001]. We estimate the predetachment accumulation at 17.41.4)X10^3 atoms (g quartz) $^{-1}$. The similarity in ^{10}Be and ^{14}C ages from boulder Timna 2 indicates that our estimate is good.

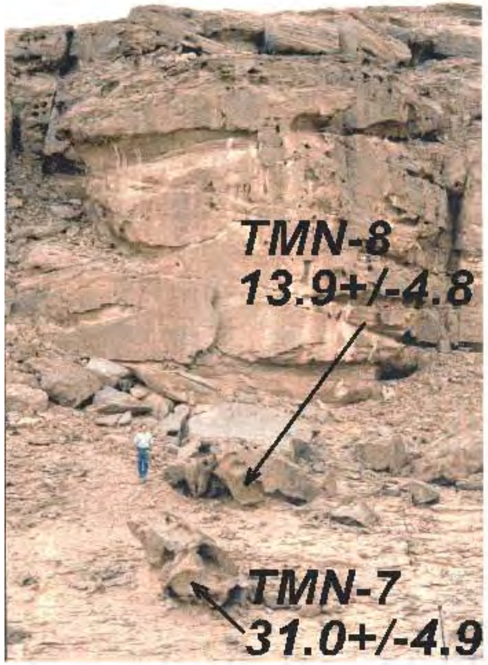

We concentrated on three boulder sites in the Timna area . The first, the Lower Valley, contains two boulder piles detached from a cliff that rises 10-14 m above the valley floor. The boulders at this site were deposited at the mouth of the Lower Valley (30X60 m), creating a dam, and causing upstream accumulation of sandy sediments on the valley floor. At the second site, the Upper Valley, we concentrated on a single boulder pile detached from a nearby 10 m cliff. At the third site we examined three weathered boulders that are located at distances of 20, 14, and 4 meters from the source cliff.

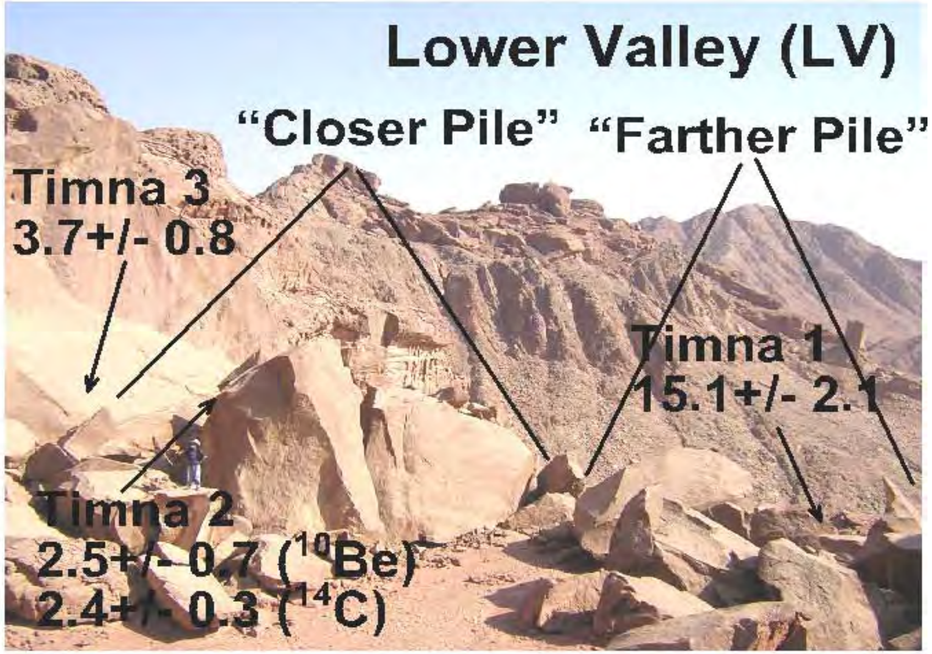

(all ages are in ky)

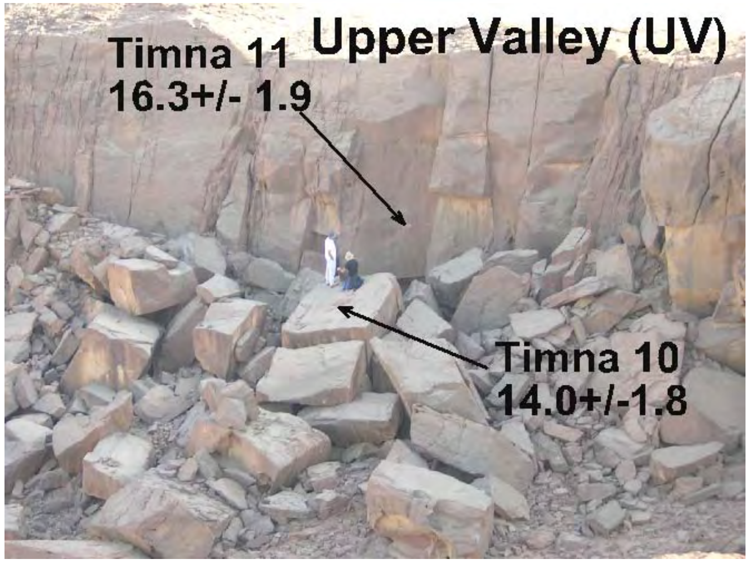

Figure 3

Cosmogenic ^{10}Be and ^{14}C results for boulders and cliff face samples from Timna Valley

Sample Name	Measured ^{10}Be (10^3 atoms g^{-1})	Un-corrected ^{10}Be age[a] (ka)	Measured ^{14}C (10^3 atoms g^{-1})	Total scaling factor[b]	^{10}Be Erosion rate (mm ky^{-1})[a]	^{10}Be Peff (atoms g^{-1} yr^{-1})[c]	Corrected ^{10}Be age[d] (ka)	^{14}C age[e] (ka)
] [][[								
Timna 1	55.3±3.3	18.4±2.2		0.46		2.52	15.1±2.1	
Timna 2	28.3±2.3	10.4±1.3	32.9±4.0	0.80		4.33	2.5±0.7	2.4±0.3
Timna 3	34.1±2.7	11.8±1.5		0.84		4.53	3.7±0.8	
] [][[								
Timna 10	49.2±2.0	17.6±1.9		0.42		2.28	14.0±1.8	
Timna 11	54.6±2.0	17.7±1.9		0.42		2.30	16.3±1.9	
] [][[								
Timna 20	239.3±8.0			1	20.7±2.2			
Timna 21	180.2±6.3			1	27.9±2.9			

[a] Model un-corrected ages and erosion rates were calculated using a SLHL ^{10}Be production rate of 5.37 atoms g^{-1} yr^{-1} [Schaller et al., 2001]. SLHL production rate was scaled for latitude and altitude using Lal [1991] for nucleonic production, Granger and Smith [2000] for muonic production, and Pigati and Lifton [2004] for paleomagnetic intensity variations. Site surface production rate of 5.42 atoms g^{-1} yr^{-1} was calculated. Attenuation of muons in the atmosphere was scaled to the sites elevation using a factor of 1.19. Sample density: 2.2 g cm^{-3}.

[b] Total scaling factor includes: (1) topographic shielding factor which was measured for each sample in 8 major directions and calculated using Dunne et al. [1999]. Following Masarik and Weiler [2003], boulder geometry factor was calculated for boulder sample Timna 2 (6%) and boulder sample Timna 10 (2%).

[c] ^{10}Be Peff calculated by multiplying site's surface production rate (5.42 atoms g^{-1} yr^{-1}) by the total scaling factor.

[d] Corrected age calculated considering the pre-detachment production of ^{10}Be at depth mainly by muons (17.4+/-1.4 atoms g^{-1}; see text for explanation), and using ^{10}Be Peff. Cosmogenic age uncertainties include analytical errors and a 10% uncertainty in production rate.

[e] Age calculated using a sea level, high latitude production rate of 16.1+/-0.2 atoms g^{-1} yr^{-1} and a spallogenic/ muogenic ratio of 0.83:0.17 [Heisenger et al., 2002].

Sample	Location	Depth (m)	K (%)	U (ppm)	Th (ppm)	ext. ! (∝Gy/a)	Ext. _ (∝Gy/a)	Cosm. (∝Gy/a)	Ext. ∀ +cosm. (∝Gy/a)[2]	De (Gy)[1]	# of aliquots[3]	Dose rate (∝Gy/a)[4]	Age (ka)
TMN-1	Pit – 1 (Lower Valley, Farther pile)	0.15	1.5	1.4	8.5	1429	914	253		11.1±2.3	17/18	2607±49	4.3±0.9
TMN-2	Pit – 1 (Lower Valley, Farther pile)	0.3	1.3	0.9	6.6	1208			1146	14.9±1.7	10/16	2361±119	6.3±0.8
TMN-3	Pit – 2 (Lower Valley, Closer pile)	0.1	2.4	1.4	7.5	2047	1088	264		11.0±2.0	9/13	3409±53	3.2±0.6
TMN-4	Pit – 2 (Lower Valley, Closer pile)	0.5	2.3	1.4	7.6	1980			1463	18.0±3.5	18/33	3453±151	5.2±1.0
TMN-5	Modern sediment (Lower Valley)	0								0.3±0.5		~ 3000	0.1
TMN-7	Boulder – (Third site, 20 meters from cliff)	1.2	1.1	0.7	4.7	963			848	57±8.5	10/12	1817±88	31.0±4.9
TMN-8	Boulder – (Third site, 14 meters from cliff)	2.7	2.5	1.0	6.5	2030			1045	40±14	10/12	3084±109	13.9±4.8

Notes: [1]De was measured on the 88-125 ∝m fraction of quartz grains using a Single Aliquot Regenerative Dose (SAR) protocol.
[2]∀and cosmic radiation were measured in the field or calculated from radioisotope contents and the cosmic dose estimated from burial depth. Because of the high dose rates the ages are not sensitive to the estimated cosmic dose.
[3]The number of aliquots used for De calculations out of the measured aliquots.
[4]Including an _ dose contribution of 8-10 ∝Gy/a.

Samples Timna 20 and Timna 21 were collected from the upper surface above the Lower Valley. Assuming steady rate erosion, these samples yield an average erosion rate of 24.3+/-3.6 mm ky^{-1}.

Figure 4

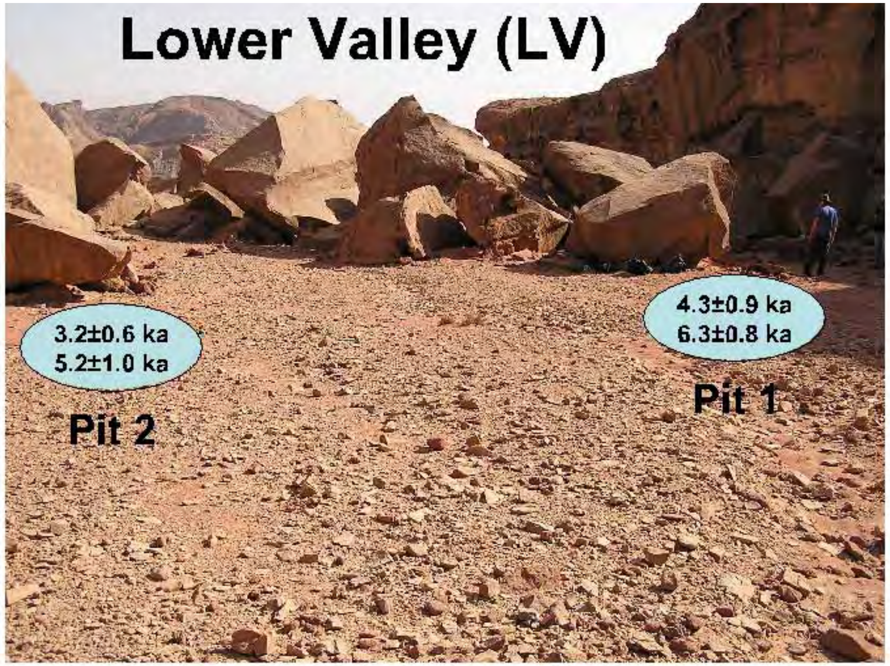

Samples for OSL dating were collected from the Lower Valley site and from the third site. Two shallow pits were dug in the sediments that accumulated upstream of the boulders in the Lower Valley site: Pit-1 behind the "Farther Pile" and pit-2 behind the "Closer Pile". The pits were dug down to bedrock. Samples were collected at depths ranging from 0.15 to 0.5 m. In the third site, samples were collected from beneath each one of the boulders.

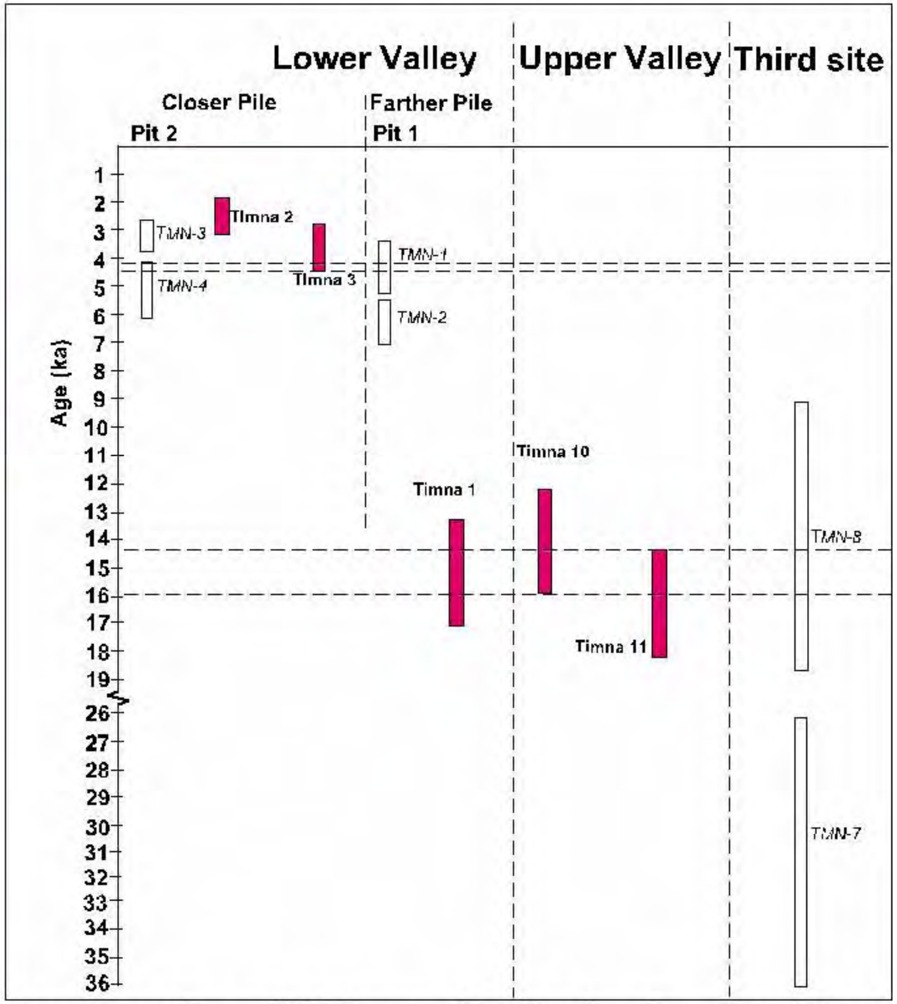

Cosmogenic and OSL age distribution from boulders, cliff faces and sediment in the three studied sites in Timna.

Figure 5

Many processes, including tectonic, climatic, and environmental factors can cause rockfalls [Wieczorek et al., 1996]. Most can be eliminated inTimna. Snowmelt, freeze and thaw effects, ground water seepage, and tree root wedging can be ruled out due to the hot and hyper-arid conditions in the area. The frequency of rain storms and the resulting expansion of clay and salt particles in cracks is too low to generate proper stress and allow boulder release. Several observations, mainly the large size of the boulders and the age clustering of boulder piles in the sampling locations suggest that each pile of boulders was detached from its source cliff in a single event. The proximity of Timna to the DSF, where >M6 earthquakes are common, suggests that ground shaking due to seismic events is the most likely cause for the Timna boulder slides.

Figure 6

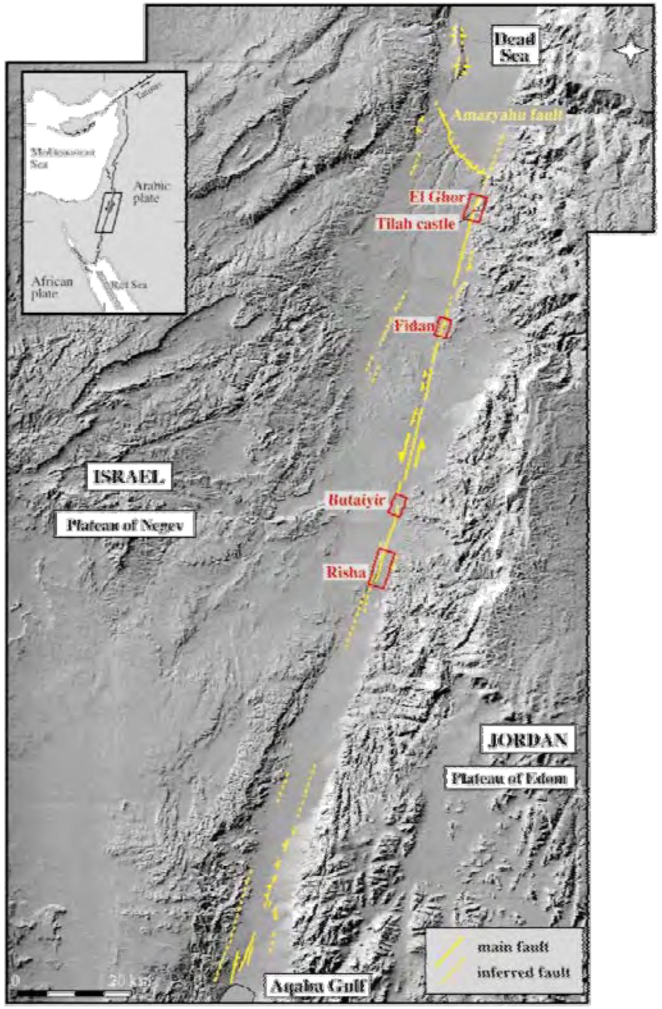

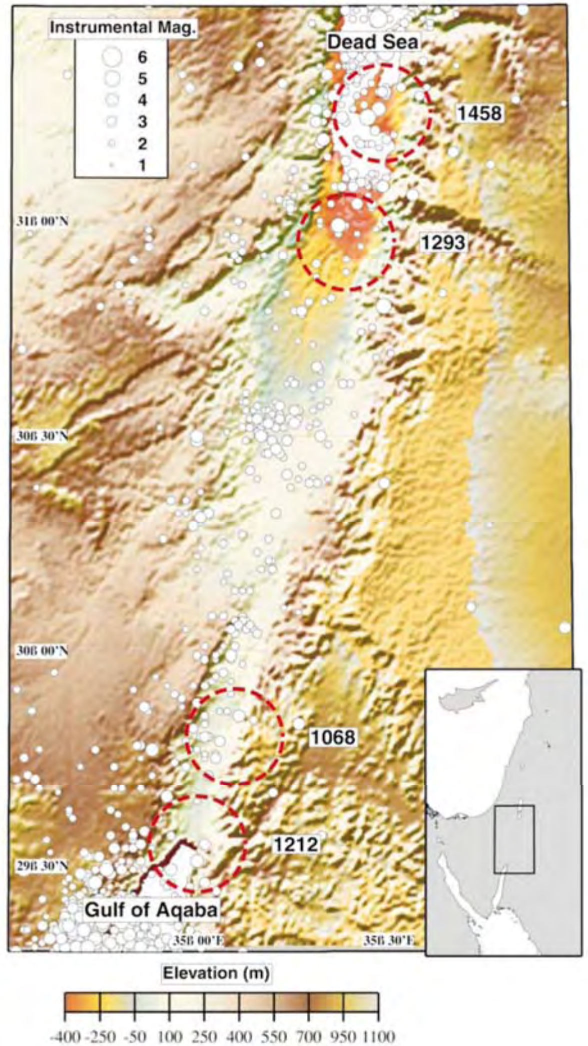

Recurrence intervals:
Klinger et al., (2000): 200 years for earthquakes Mw 7-7.2 (or larger earthquakes with longer intervals (e.g. Mw 7.6 every 6000 years).
Amit et al., (2002): Late Pleistocene: 2800+/-700 (Mw 6.7-7); Holocene: 1200+/-300 (Mw 5.9-6.7).
4 historical large earthquakes (Ambraseys et al., 1994):Two in the south (1068, 1212) and two in the north (1293, 1458).

The combined ages of boulders from the three investigated sites suggest that they were deposited in three events at 31 ka, 15 ka, and 4 ka. Paleoseismic studies in the area suggest a recurrence interval of 1000-2000 yr for earthquakes >M6. Therefore, it is apparent that boulder falls in the study area do not represent a full seismic record. This under representation implies that the on-going development of detachment cracks prior to triggering events is slower than the earthquake cycle and controls boulder formation or that boulder piles are formed only during big and rare earthquakes.

Figure 7

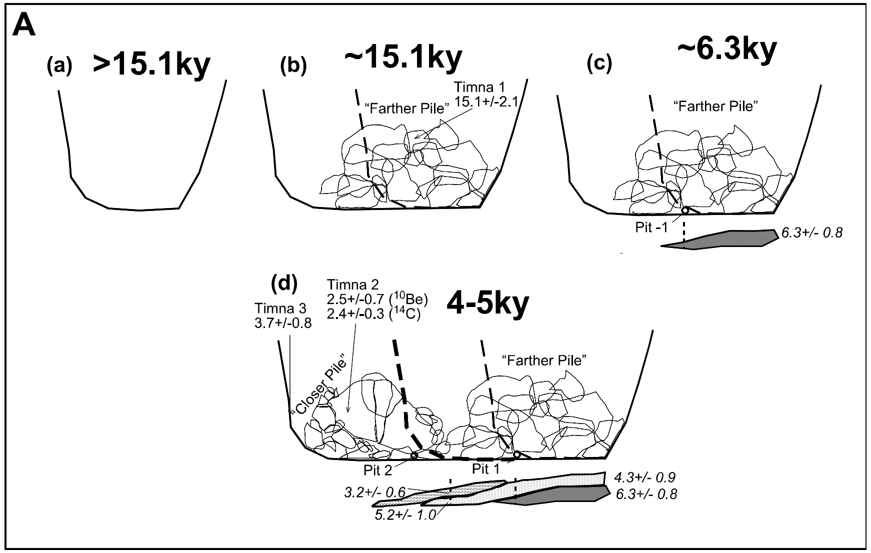

Cliff retreat rates determined from rock falls in Timna range between 0.14 and 2 m ky^{-1}. A more constrained range of 0.4 to 0.7 m ky^{-1} is calculated from the complete collapse cycles. Similar cliff retreat rates that range between 0.1 and 0.85 m ky^{-1} were calculated in other arid environments [e.g. Schumm and Chorley, 1966; Yair and Gerson, 1974; Mayer, 1979; Cole and Mayer, 1982].

In Timna, rates of cliff retreat are faster by an order of magnitude than the rate that the upper surfaces are lowered by weathering. Even though cliffs retreat through the episodic process of rock fall events while the upper surface weathers continuously, over time the difference in rates maintains the sharp morphology of Timna and vertical slopes (cliffs) do not roll back to become more gentle and rounded slopes.

Cliff retreat obviously initiated when voids large enough opened and enabled the collapse process to begin. This space opening was first accomplished through incision of stream channels through the sandstone following the development of the Arava Valley topographical base level. Assuming the range of cliff retreat rates calculated in this study, the 30 m wide Lower Valley opened approximately 40 - 70 ka. This range of ages determines the time at which the upstream-moving signal of the lowering base level of the DSF reached the Lower Valley site.

Figure 8

Reconstructing active rift margin tectonics using cosmogenic exposure age dating of desert pavements: Quaternary subsidence along the western margin of the Dead Sea Rift

Benny Guralnik[1]*, Ari Matmon[1]*, Yoav Avni[2], David Fink[3]

[1]Institute of Earth Sciences, The Hebrew University of Jerusalem
[2]Geological Survey of Israel
[3] Australian Nuclear Science and Technology Organization (ANSTO), Australia

arimatmon@cc.huji.ac.il

*Field guide

Fragmentation of drainage basins, their rearrangement, stream divergence, and consequent full drainage reversal occur in response to tectonic forcing such as subsidence of continental rift valleys and uplift of rift shoulders. We present new cosmogenic data from the Negev Desert, southern Israel, that shed light on the relations between the tectonic history of the western margins of the southern Dead Sea Rift (DSR) and drainage basin evolution since the Pliocene. In the Pliocene, a north-oriented river system drained the central Negev into the Dead Sea basin, collecting tributaries that originated east of the DSR and flowed westward (fig. 1). Tectonic deformation along the western margin of the DSR that began in the Pliocene caused regional eastward tilting and reversal of these tributaries by the early Pleistocene. Zero regional gradients which prevailed during the reversal stage, were accompanied by the accumulation of red beds and lake deposits, currently found on progressively lower elevations towards the rift, recording the Quaternary subsidence. To constrain the breakdown history of the Pliocene drainage system and reconstruct the Quaternary subsidence, we sampled mature desert pavement from 14 abandoned alluvial surfaces associated with the Plio-Pleistocene deposits. Seven samples were collected from the highest windgaps along major water divides, in which remnants of the early Pleistocene surface are preserved. Five of these samples yielded exposure ages that range between 1.9 Ma and 1.5 Ma (fig. 2). These ages bracket the collapse of the Pliocene drainage basin and suggest the eastward migration of this process. Seven other samples which yielded ages that range between 1.3 Ma and 0.5 Ma were collected from alluvial terraces inset into the early Pleistocene surface. They indicate stages of incision of the present drainage system. Under conditions of long-term hyperaridity and the absence of soil and vegetation desert pavement chert clasts are continuously exposed at the surface and do not erode. Thus, their cosmogenic isotope concentration may reflect changes in production rate due to elevation changes during exposure. By interpreting the cosmogenic isotope concentrations measured in the our easternmost samples as partially being produced at higher elevations we infer a minimum, and reasonable subsidence rate of ~130 m/Ma since 1.3 Ma (fig. 5). The detection of such a slight change in elevation is enabled due to the unique condition of continuous exposure and no erosion of the chert clasts in the desert pavement.

Introduction

The present study focuses on the western margin of the Dead Sea Rift (fig. 1), in which the unique combination of hyperaridity, considerable subsidence during the Plio-Pleistocene (0.5 – 0.7 Km; Avni et al, 2000a), and the continuous exposure and extremely low erosion of desert pavement clasts (<0.2 m/Ma; Matmon et al, 2008) present a case-study for detecting a cosmogenic signal of tectonic activity.

Although basin fragmentation may occur even within a cratonic provenance (Chorowicz and Fabre, 1997), rift-induced modification of topography results in dramatic regional-scale flow reversals, as was reported from the Corinth–Patras Rift (Zelilidis, 2000), the Rio Grande Rift (Mack et al, 2006), Tasman Rift (Ollier, 1995), and East African Rift (Summerfield, 1991). Flow reversal was observed also in transform zones such as the East Anatolian Fault Zone (Boulton and Whittaker, 2008), and even in the glacial environments of the West Antarctic Rift system (Van der Wateren and Cloetingh, 1999, and references therein; Bart, 2004). Most commonly, paleo-flow directions are reconstructed by the inspection of windgaps, which are dry paleo-valleys that represent now-abandoned water courses (Keller et al., 1999; Burbank and Anderson, 2001). The time scale for river reversal has been recently demonstrated on the Palaeo-Nyabarongo River system, which switched from drainage into the East African Rift towards drainage away from it within approximately 300 – 350 Ka (Holzforster and Schmidt, 2007). A tectonic model for the drainage reversal induced by the Dead Sea leaky transform (traditionally referred to as "rift"; Garfunkel, 1981) was proposed by Wdowinski and Zilberman (1996), while specific drainage reversals have been reported from many locations along it (Kafri and Heimann, 1994; Matmon et al, 1999; Zilberman and Avni, 2006; Avni and Zilberman, 2007; Garfunkel and Horowitz, 1966; Ben David et al, 2002; Ginat et al, 1998; Ginat et al, 2000; Avni et al, 2000a).

The Negev Desert (10,000 km^2 at 29°–31°N, fig.1) is part of the larger Saharo-Arabian desert belt, and is currently among the driest places on Earth (Amit et al, 2006). Its Neogene history was dominated by the 18-14 Ma sinistral transform boundary between the present African and Arabian plates (Bartov et al, 1980; Garfunkel, 1981). During the Miocene, a >650 m thick section of the fluviatile Hazeva formation was deposited all over the Negev by westward-flowing rivers which originated hundreds of Km east of the transform and drained into the Mediterranean (Calvo and Bartov, 2001). The activity of this drainage system terminated at the latest ~6 Ma (Steinitz and Bartov, 1991; Steinitz et al, 2000). This termination coincides with the change in the plate's motion direction, which caused extension and initiated the development of the Dead Sea Rift as a deep inland drainage basin at ~5 Ma (Garfunkel, 1981). This tectonic phase was followed by the collapse of the Miocene fluvial system, rift margin uplift, erosion of most of the Miocene sedimentary deposits, and the development of a N-S main water-divide along the western margins of the Dead Sea rift (Wdowinski and Zilberman, 1996).

By the early Pliocene, a new north-oriented river network known as the paleo-Paran drained most of the southern and central Negev into the Dead Sea basin. The sediments deposited by the paleo Paran drainage basin (the Arava formation) originated from the northern Sinai as well as from the Trans-Jordan Mountains (the "Edom Channel"; Ginat, 1998). Smaller westward-oriented paleo-rivers were identified as well (Avni, 1998; Avni et al, 2000a) (fig. 1). Although never directly dated, an age of 2-4 Ma was attributed to the Arava formation (Avni et al, 2000a).

During the Pliocene-Pleistocene transition, a simultaneous uplift of ~200 m of the Negev Highlands with the subsidence of ~500 – 700 m in the central Arava Valley, caused a gentle eastward tilting of a ~60 Km-wide strip about an axis roughly coinciding with the main channel of the Paleo-Paran. The proximity of the tilt axis to the paleo Paran channel is suggested by the location of the current active Paran channel only 1 – 3 Km east of its ancestor and <20 m below it (Avni et al, 2000a). In the vicinity of Mt. Zenifim (a local Plio-Pleistocene uplift axis), the axis of rotation is shifted to the east, and may be identified with the Paran Plains (fig. 1). The eastward tilting caused the fragmentation of the paleo Paran system into several smaller drainage systems (Paran, Hayyon, Neqarot, and Quraya) and relicts of the once westward-flowing rivers are found today at progressively lower elevations toward the east (Ginat et al, 1998; Avni et al, 2000a). During the period of stream reversal, as the regional gradients approached zero, a syntectonic sedimentary unit termed the Zehiha formation was deposited upon the stagnated channels (Ginat et al, 2002), masking the previous basin boundaries and promoting its break-up (Avni et al, 2000a). The resemblance of the fauna and hominid artifacts found in the Zehiha formation to those of 'Ubediya (Tschernov, 1987), assigned it an early Pleistocene age of ~1.4 Ma (Ginat et al, 2003). Although the tectonic framework of the Plio-Pleistocene is relatively well established, the fluvial deposits associated with this period lacked direct dating, limiting the understanding of the relationship between the tectonic and fluvial processes accompanying the subsidence of one of the most studied rift margins in the world.

Tectonic scenarios

The original elevations of the Pliocene Arava deposits along the presently reversed channels can be reconstructed by assuming a westward paleo-gradient similar to that of the present day Paran and Hiyyon channels (~4.5‰), and extrapolating it from the tilting axis (where no elevation change occurred) to the east (Ginat et al, 2000; Avni et al, 2000a). With these reconstructions, the cosmogenic concentrations at these sites can be subjected to two "end-member" interpretations (fig. 4). In the "pre-DP subsidence" scenario (fig. 4), the pavements developed after the surfaces reached their final (stable) elevation. Thus, the cosmogenic concentration should reflect nothing but age and may point at the period (~400 ky) it took the paleo Paran system to completely disintegrate. The main weakness of the "pre-DP subsidence" scenario is that it forces the zero-gradient stage to be ≥ 1.9 Ma (equal or older than the oldest desert pavement sample PS-6). This is in contradiction to the assigned age of ~1.4 Ma of the deposits of lake Zihor and the associated red beds, which have been related with the fluvial stagnation during the gradient reversal (Ginat et al, 2002; 2003).

Alternatively, in the "post-DP subsidence" scenario (fig. 4), desert pavements were developed during the drainage reversal phase and at significantly higher elevations. A signal of subsidence postdating terrace abandonment should therefore be present in their cosmogenic concentrations, making their true abandonment ages slightly younger than simple exposure ages, based on a relationship derived below.

Denoting uplift and erosion rates (U, ε) and the reciprocals of atmospheric and rock attenuation lengths (M, μ), we expand Craig and Poreda's original model (1986) to account for an unstable nuclide, by including its disintegration constant (λ) in the "effective irradiation time", T (Lal, 1991):

$$T(U,\varepsilon) = \left(\lambda + MU + \mu\varepsilon\right)^{-1} \tag{1}$$

The ratio of the measured concentration in a sample (N) to the calculated in-situ production rate (P), must then satisfy the equation:

$$N/P = T(U,\varepsilon)\left(1 - \exp\left(-t/T(U,\varepsilon)\right)\right) \tag{2}$$

where t is the true exposure age, which can be expressed as

$$t = -T(U,\varepsilon)^{-1}\ln\left(1-(N/P)\cdot T(U,\varepsilon)\right) \tag{3.1}$$

Since erosion of chert clasts in the Negev in desert pavements can be neglected equation (3.1) becomes:

$$t = -(\lambda + MU)\ln\left(1-(N/P)\cdot(\lambda + MU)^{-1}\right) \tag{3.2}$$

The dependence between t and U for an observed N/P value, given by equation (3.2), may be represented by a curve which hereafter will be referred to as N/P plot (fig. 5). In such N/P plots simple exposure ages are obtained at the intersection of the N/P curve with $U = 0$ and for a fixed N/P ratio, there is a negative trend between exposure age and subsidence rate, one being on the expense of the other. The thin solid red and blue lines in figure 4 correspond to the observed N/P ratios at sites ES and EZ, respectively. The color band around the N/P curve represents the confidence interval due to the analytic uncertainty in N only. At this confidence interval, the observed N/P ratios of samples EZ ($1.082 \pm 0.005 \times 10^6$) and ES ($1.041 \pm 0.016 \times 10^6$) do not overlap, which means that the age of ES is significantly younger than that of EZ. This fact supports the geologic field relations: site EZ is situated on an uplifted and abandoned surface of the Edom Channel; it pre-dates the zero-gradient stage. On the other hand, desert pavement at site ES developed on top of the Zehiha formation, and post-dates the zero-gradient surface Based on known rates of carbonate precipitation and soil formation, the time required to deposit the 15 m thick sequence of the Zehiha formation which separates both sampled surfaces was estimated to 50 – 150 Ky, (Ginat et al, 2003).

Since equation (3.2) is a solution of a differential equation, for any given point in the $U-t$ space, the tectonic rate U represents an averaged tectonic rate over the entire exposure age indicated by t. As a first-order approximation, constant tectonic rates may be assumed. Points 1 and 2 in figure 5 mark such combinations of age and constant subsidence rate (1.56 Ma at 10 m/My for EZ, 1.38 Ma at 142 m/My for ES). The product yields the estimated amount of subsidence since the Pleistocene (17 m at EZ and 195 m at ES). While the subsidence and the age shift for site EZ are negligible, the simple exposure age of ES shifts by about 100 Ky to 1.38 Ma, implying an age difference of 0.19 Ma between EZ and ES, corresponding to the time it took to deposit the Zehiha formation.

These averaged rates calculated above may significantly differ from instantaneous rates. Field evidence from the Negev suggests that the rapid tectonic activity that shaped the present basins during early Pleistocene diminished with time (Avni et al, 2000a). The cosmogenic concentrations at ES due to random monotonous subsidence histories (starting at 450 m asl, and ending today at 255 m asl) are simulated. Only those subsidence histories that produced the observed concentration at ES (within the analytic uncertainty in N and 5% uncertainty in P) are presented in figure 6. Despite the significant scatter, a trend of a diminishing tectonic activity with time is noticeable.

References

Amit, R., Enzel, Y., Sharon D., 2006. Permanent Quaternary hyperaridity in the Negev, Israel, resulting from regional tectonics blocking Mediterranean frontal systems. Geology 34, 509–512.

Avni, Y., 1998. Paleogeography and tectonics of the central Negev and the Dead Sea Rift western margin during the late Neogene and Quaternary. Geol. Surv. Isr. Rep. GSI/24/98, 231 pp. (in Hebrew, English abstr.)

Avni, Y., Bartov, Y., Garfunkel, Z., Ginat, H., 2000. The evolution of the Paran drainage basin and its relation to the Plio-Pleistocene history of the Arava Rift western margin, Israel. Isr. J. Earth Sci. 49, 215–238.

Avni, Y., Zilberman, E. 2007. Landscape evolution triggered by neotectonics in the Sede Zin region, central Negev, Israel. Isr. J. Earth Sci. 55, 189–208.

Bart, P.J., 2004. West-directed flow of the West Antarctic Ice Sheet across Eastern Basin, Ross Sea during the Quaternary. Earth Planet. Sci. Lett. 228, 425–438.

Bartov, Y., Steinitz, G., Eyal, M., Eyal, Y., 1980. Sinistral movement along the Gulf of Aqaba—its age and relation to the opening of the Red Sea, Nature 285, 220–221.

Ben-David, R., Eyal, Y., Zilberman, E., Bowman, D., 2002. Fluvial systems response to rift margin tectonics: Makhtesh Ramon area, southern Israel. Geomorphology 45, 147–163.

Boulton, S.J., Whittaker, A.C., 2008. Quantifying the slip rates, spatial distribution and evolution of active normal faults from geomorphic analysis: Field examples from an oblique-extensional graben, southern Turkey. Geomorphology, doi:10.1016/j.geomorph.2008.09.007

Burbank, D.W., Anderson, R.S., 2001. Tectonic Geomorphology. Blackwell Science, Oxford, U.K. 274 pp.

Calvo, R., Bartov, Y. 2001. Hazeva Group, southern Israel: New observations, and their implications for its stratigraphy, paleogeography, and tectono-sedimentary regime. Isr. J. Earth Sci. 50, 71–99.

Chorowicz, J., Fabre, J., 1997. Organization of drainage networks from space imagery in the Taneztouft Plateau Western Sahara: implications for the recent intracratonic deformation. Geomorphology 212, 139–151.

Garfunkel, Z., 1981. Internal structure of the Dead Sea leaky transform (rift) in relation to plate kinematics. Tectonophysics 80, 81–108.

Garfunkel, Z., Horowitz, A. 1966. The Upper Tertiary and Quaternary morphology of the Negev, Israel. Isr. J. Earth Sci. 15, 101–117.

Ginat, H., Enzel Y., Avni, Y., 1998. Translocated Plio-Pleistocene drainage systems along the Arava fault of the Dead Sea transform. Tectonophysics 284, 151–160.

Ginat, H., Zilberman, E., Avni, Y., 2000. Tectonic and paleogeographic significance of the Edom River, a Pliocene stream that crossed the Dead Sea Rift valley. Isr. J. Earth Sci. 49, 159–177.

Ginat, H., Zilberman, E., Saragusti, I., 2003. Early pleistocene lake deposits and Lower Paleolithic finds in Nahal (wadi) Zihor, Southern Negev desert, Israel. Quat. Res. 59, 445–458.

Holzforster, F., Schmidt, U., 2007. Anatomy of a river drainage reversal in the Neogene Kivu–Nile Rift. Quat. Sci. Rev. 26, 1771–1789.

Kafri, U., Heimann, A., 1994. Reversal of the palaeodrainage system in the sea of Galilee area as an indicator of the formation timing of the Dead Sea rift valley base level in northern Israel. Palaeog., Palaeocl., Palaeoec. 109, 101–109.

Keller, E.A., Gurrola, L., Tiernay, T.E., 1999. Geomorphic criteria to determine direction lateral propagation of reverse faulting and folding. Geology 27, 515–518.

Lal, D., 1991. Cosmic ray labeling of erosion surfaces: in situ nuclide production rates and erosion models. Earth Planet. Sci. Lett. 104, 424–439.

Mack, G.H., Seager, W.R., Leeder, M.R., Perez-Arlucea, M., Salyards, S.L., 2006. Pliocene and Quaternary history of the Rio Grande, the axial river of the southern Rio Grande rift, New Mexico, USA, Earth Sci. Rev. 79 (1-2), 141–162.

Matmon, A., Enzel, Y., Zilberman E., Heimann A., 1999. Late Pliocene and Pleistocene reversal of drainage systems in northern Israel: tectonic implications. Geomorphology 28, 43–59

Matmon, A., Simhai, O., Amit, R., Haviv, I., Enzel, Y., Porat, N., McDonald, E.V., Benedetti, L., Finkel, R.C., 2009. Desert pavement–coated surfaces in extreme deserts present the longest-lived landforms on Earth. Geol. Soc. Am. Bull., doi: 10.1130/B26422.1.

Ollier, C.D., 1995. Tectonics and landscape evolution in southeast Australia. Geomorphology 12, 37–44.

Reconstructing active rift margin tectonics using cosmogenic exposure age dating of desert pavements: Quaternary subsidence along the western margin of the Dead Sea Rift

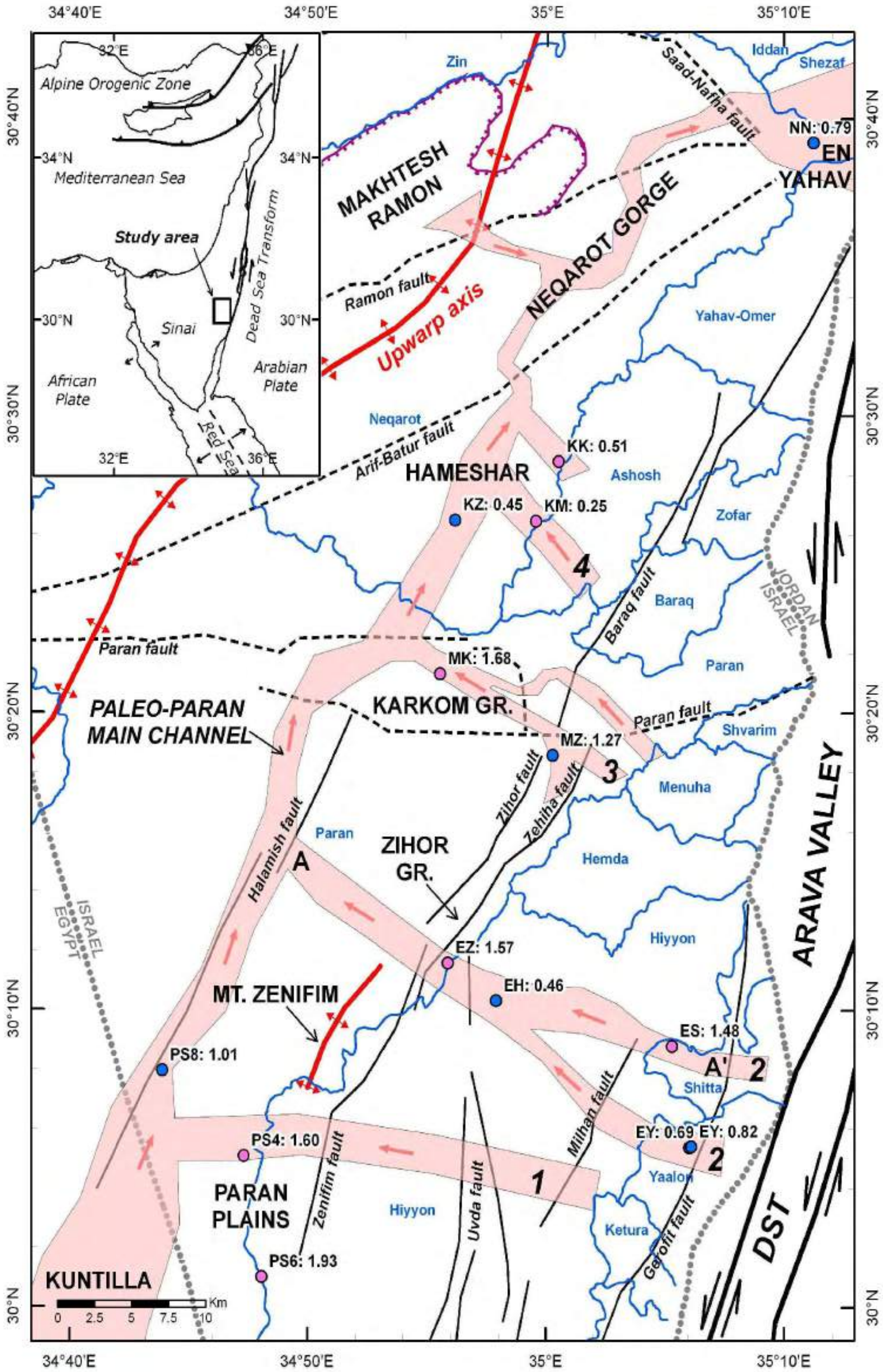

Figure 1: Study area. Present-day drainage basins are outlined in blue, faults in black, Plio-Pleistocene upwarp axes in red. Reconstructed paleo-Paran drainage is outlined in pink (arrows indicate flow direction), major tributaries are numbered: 1 – Zenifim, 2 – Edom, 3 – Menuha, 4 – Kippa. Sample locations and their simple exposure ages are indicated by small circles, pink for watergap samples, blue for stream inset samples. A-A' is the cross section locations. Sources: Ginat (1997), Avni (1998), Ginat et al (2000), Avni et al (2000)

A: Block tilting and rotation model (after Garfunkel, 1970)

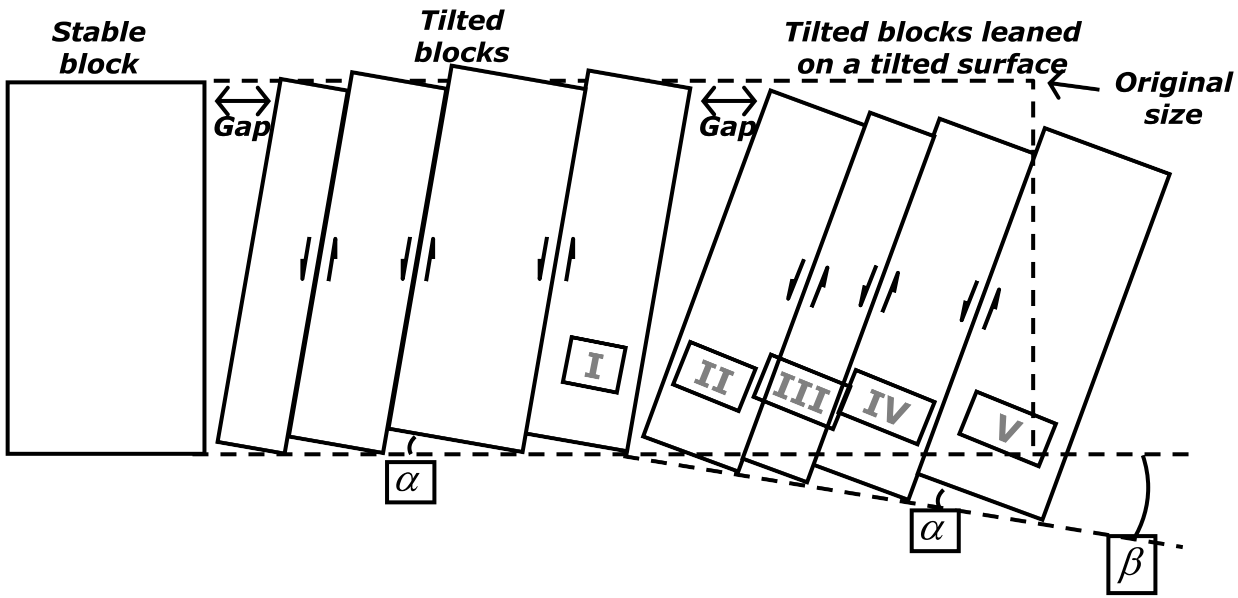

B: Elevation of Edom channel outcrops modeled with block rotation

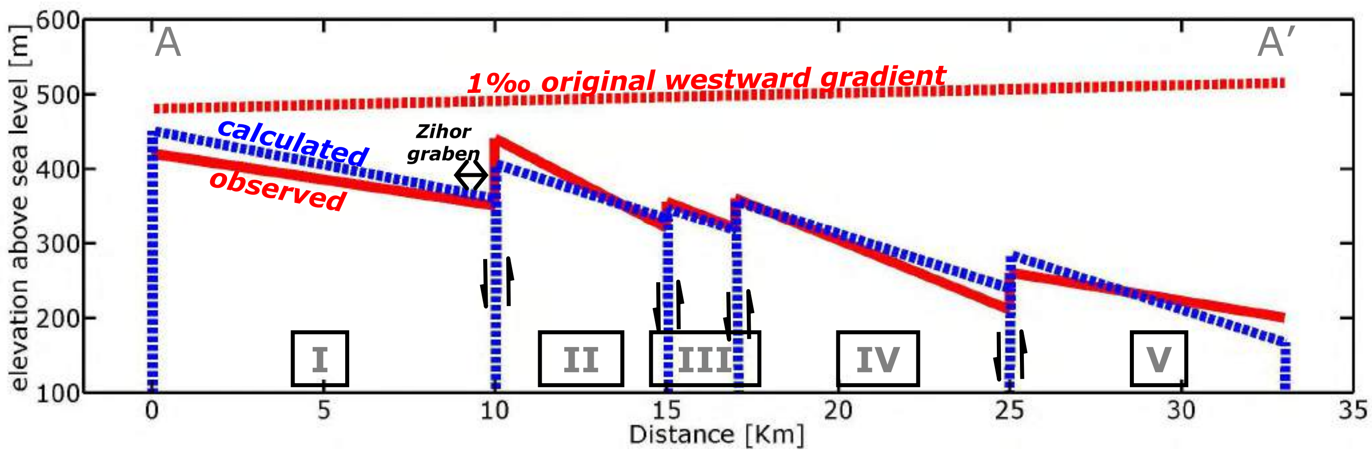

Figure 2: A – Block rotation model: regional rotation (by an angle of β for blocks II-V), is superimposed on local rotation (by an angle of α and common to all blocks), no vertical exaggeration. B – Observed and modeled elevations of the Edom channel facies along transect A-A' (see figure 1), vertical exaggeration of ~20. The model uses a pre-reversal gradient of 1‰, block height of 2 Km, subvertical faults (dipping >80°), α=0.3° and β=0.6°; calculated elevations reproduce actual heights of outcrops within a precision of 30 m.

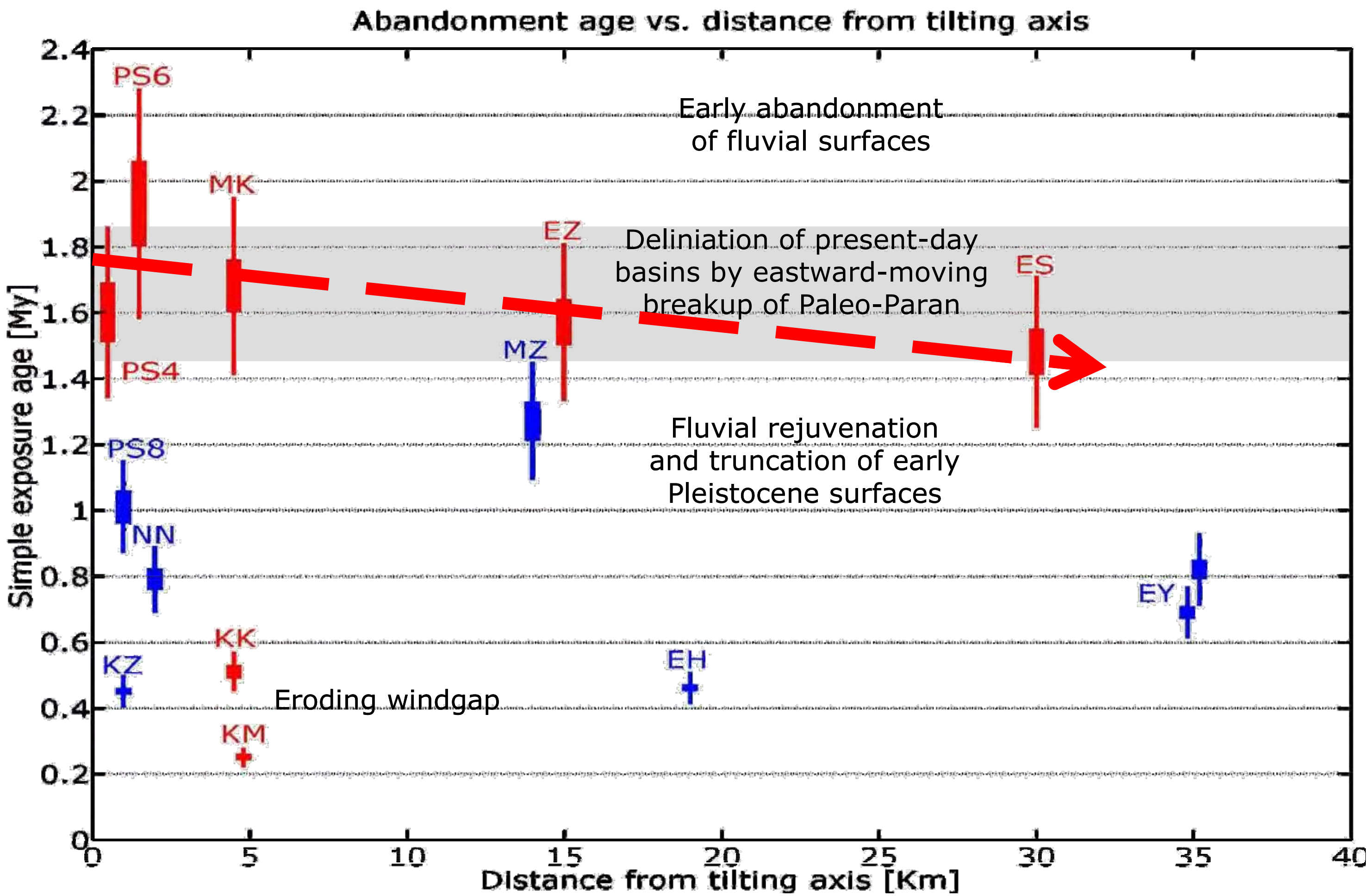

Figure 3: Simple exposure ages of desert-pavements at major windgaps (red) and on inset surfaces (blue), plotted against site distance from the Quaternary tilt axis. Random errors are indicated by thick bars, systematic uncertainty of 10% about the production rate by thin bars. Excluding the anomalously young windgaps of the Meshar (KK and KM), average windgap age is 1.65 ± 0.20 Ma. Red dashed line suggests that the basin breakup propagated in an eastward direction.

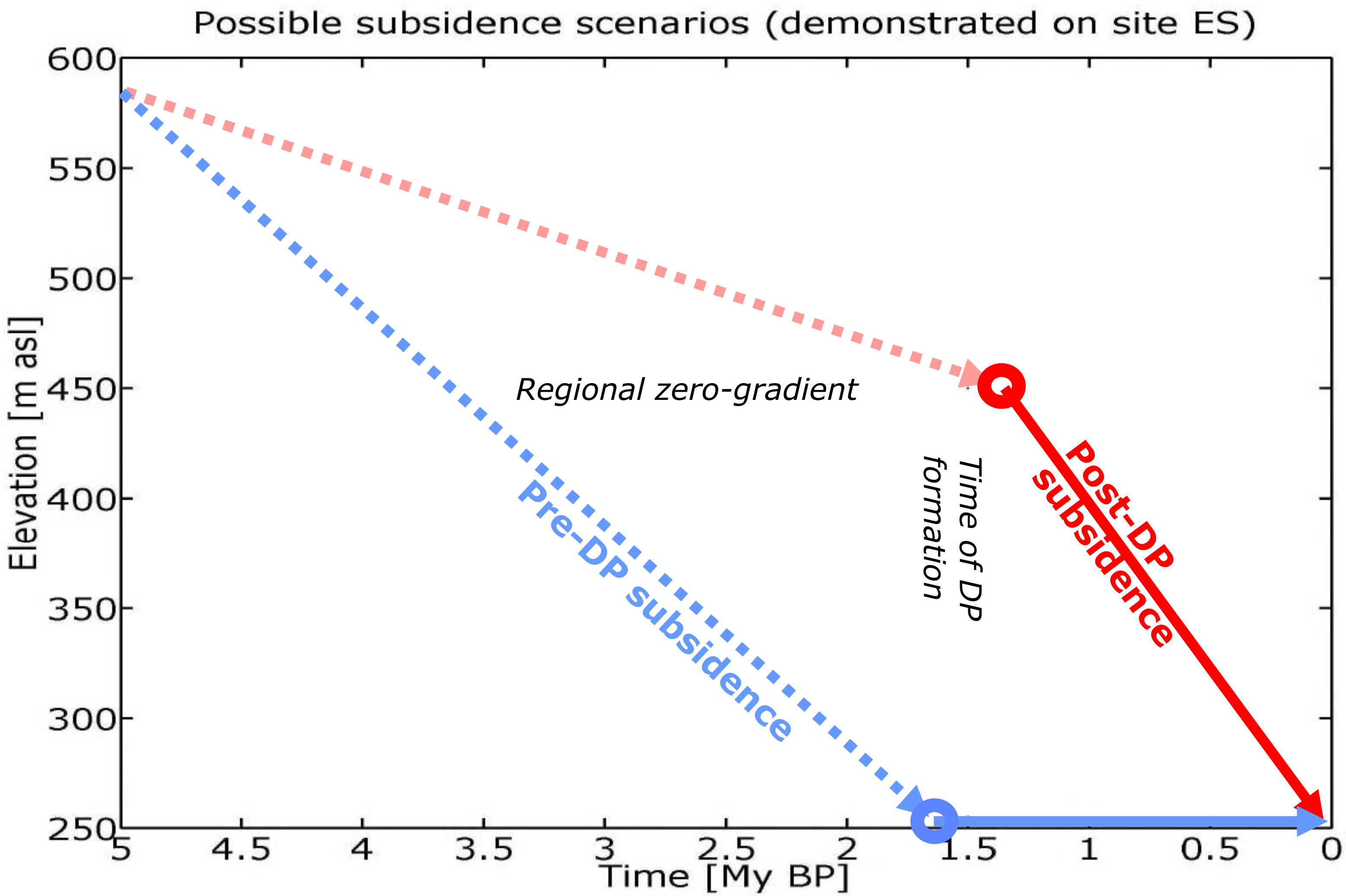

Figure 4: Desert Pavement (DP) development scenarios. Grey areas represent the elevation of regional zero gradient and age of Desert Pavement formation. Blue line represents the “Pre-DP subsidence” scenario, in which the pavements are formed at their present elevation and record age only. Red line represents the “Post-DP subsidence” scenario, in which the pavements are formed at a higher elevation and include a mixed signal of age and subsidence.

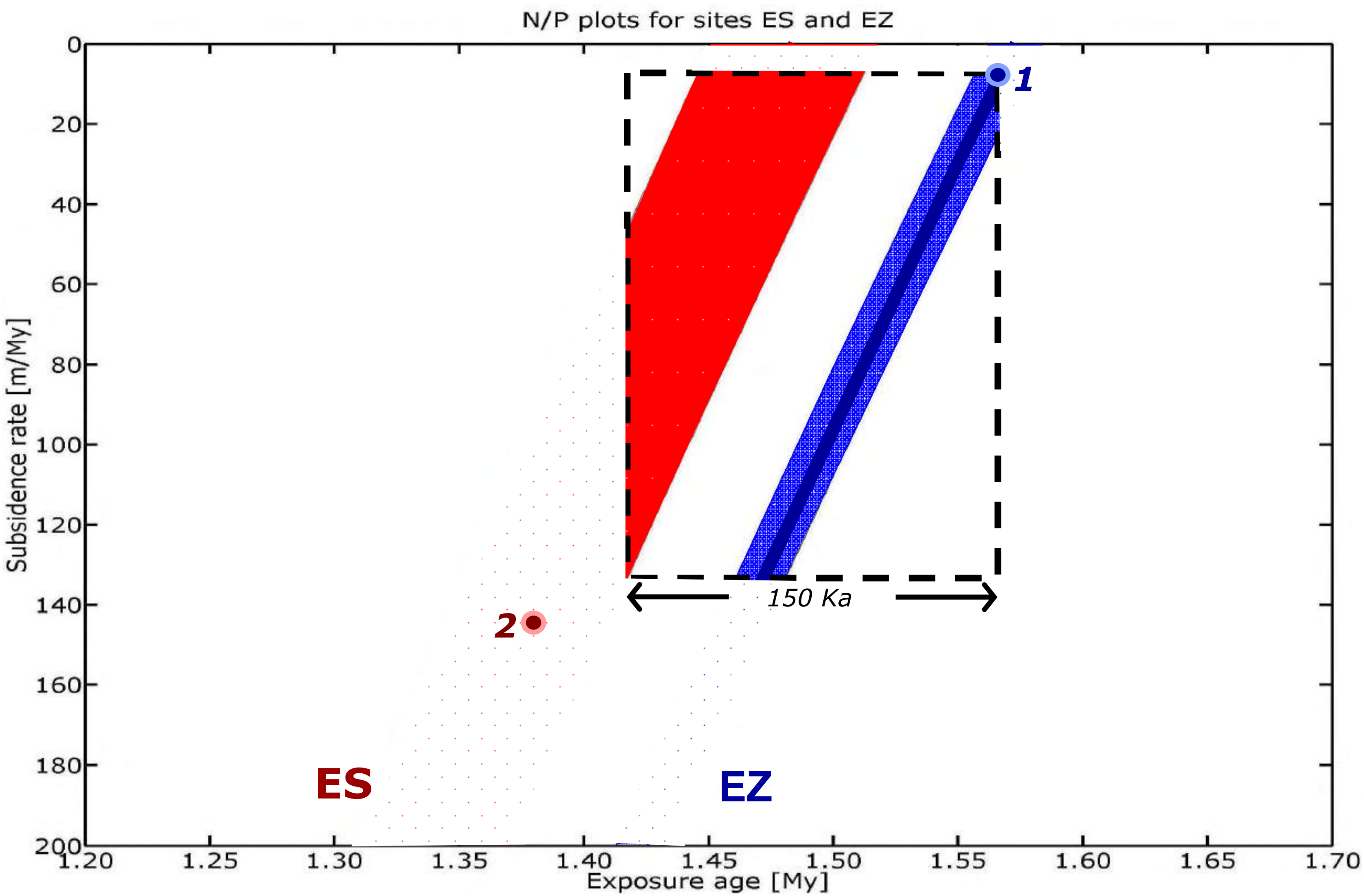

Figure 5: N/P plot: the continuous lines represent all possible combinations of constant uplift rate and true exposure age for a given sample. Simple exposure ages are given by the intersection of the curves with the U=0 line. Red and blue dots represent the corrected age assuming continuous subsidence at a constant rate.

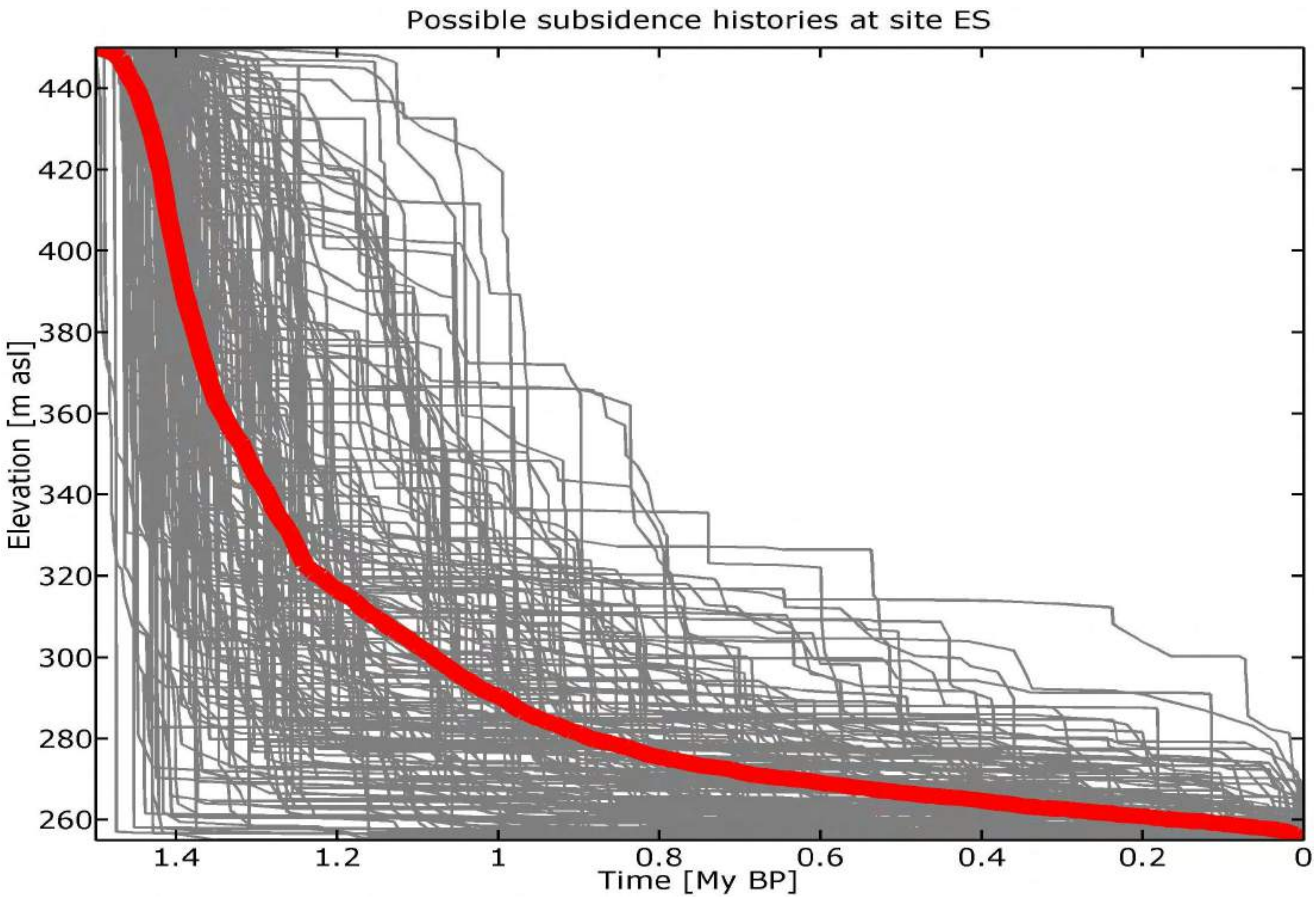

Figure 6: Plot of all possible subsidence histories at site ES, assuming <150 Ka for the deposition of Zehiha formation. Shown are histories which produced N/P values within the analytic uncertainty in N and a 5% uncertainty in P. The red line is an averaged history.

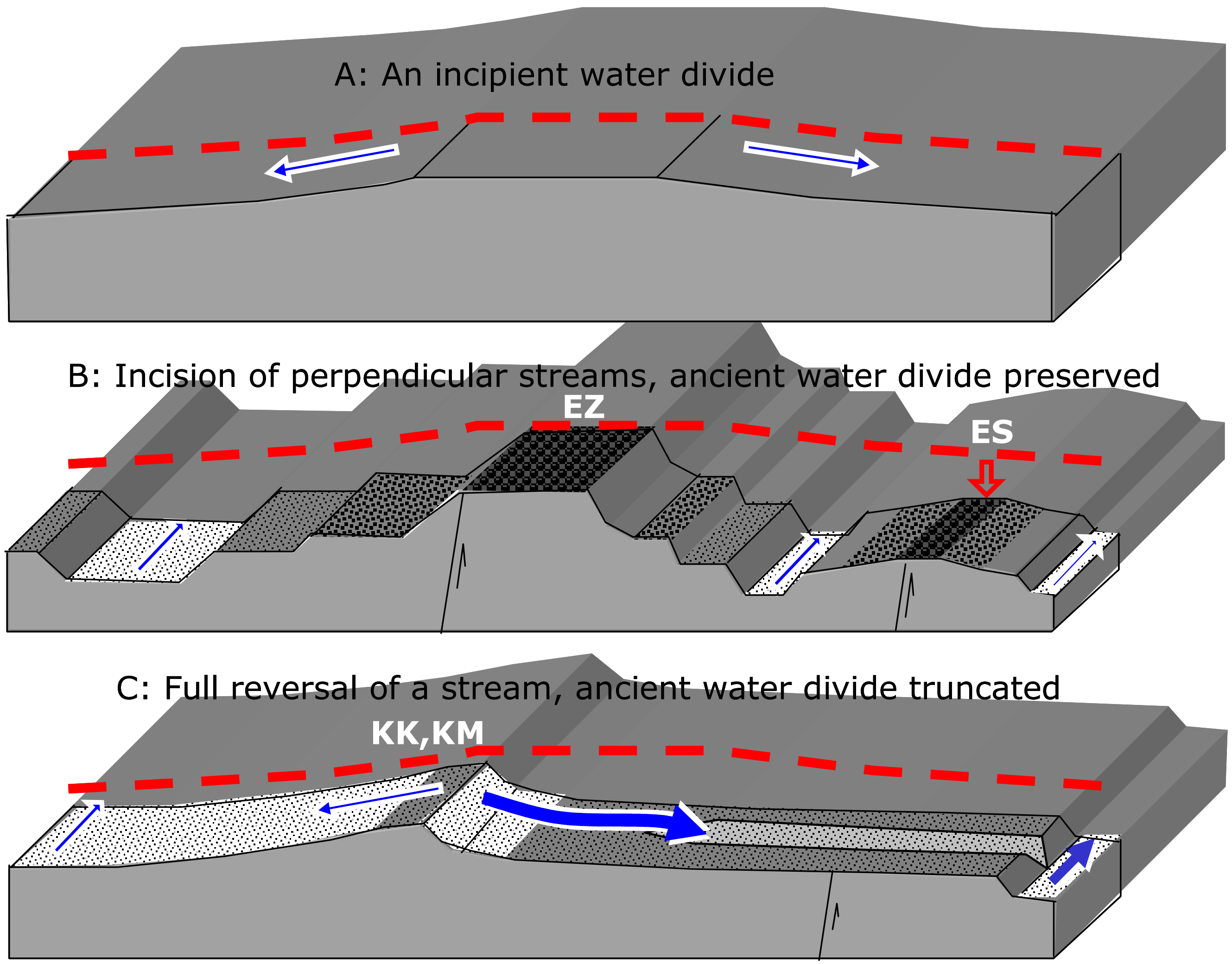

Figure 7: Scenarios for preservation or destruction of surfaces dating a basin's breakup. A – emergence of a new water divide and development of desert pavement in the windgap. B – emergence of a drainage network parallel to the water divide; drainage off the wingap is minimal, and the original abandoned surfaces are preserved. C – emergence of drainage networks away from the windgap causes its truncation and backward migration of the water divide.

Judean Mountains

23.2.2009

Field leader

Elisa Kagan

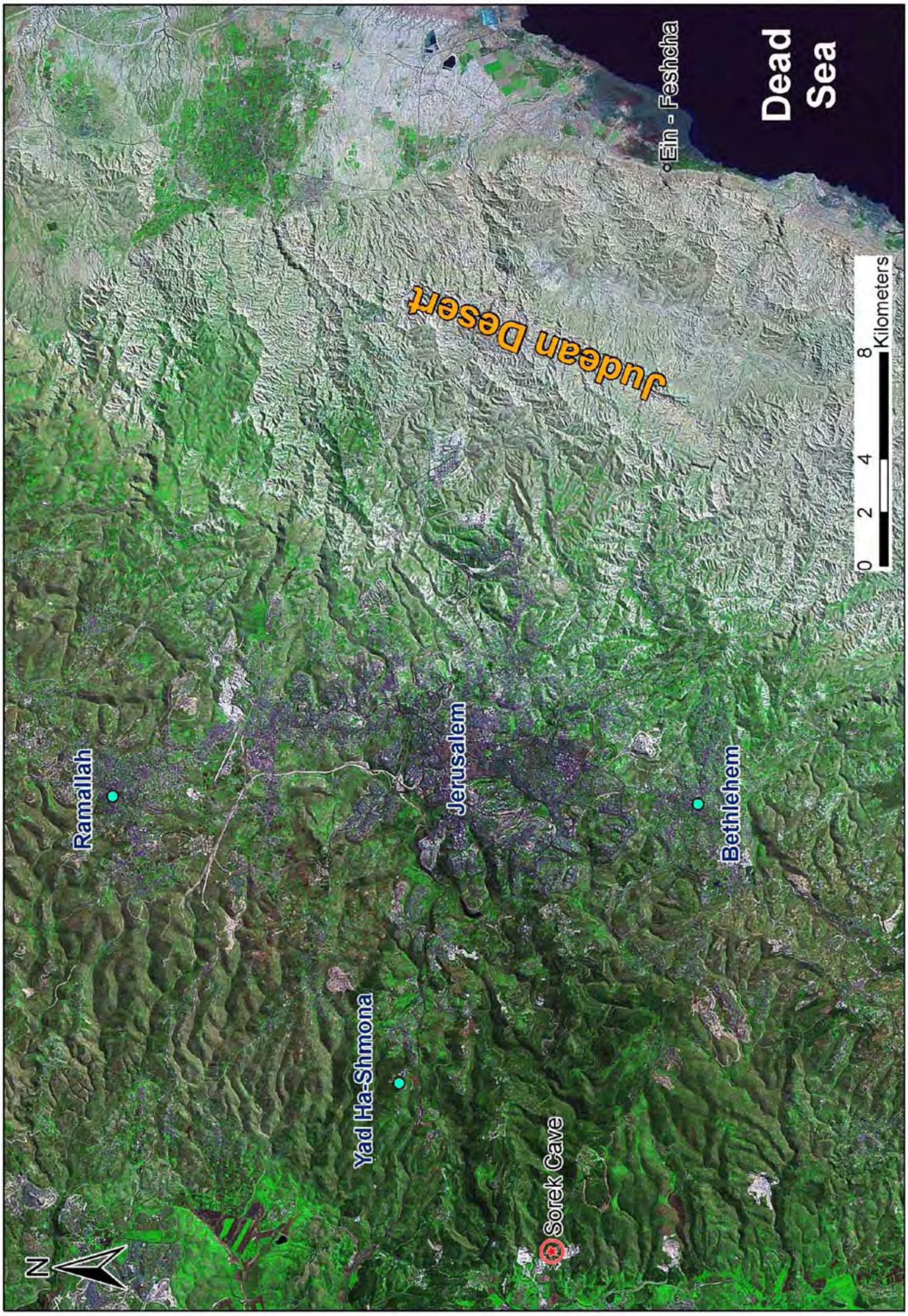

Dead Sea
Ein - Feshcha
Judean Desert
0 2 4 8
Kilometers
Ramallah
Jerusalem
Bethlehem
Yad Ha-Shmona
Sorek Cave
N

Speleoseismology in the Soreq Cave: The first dated ultra-long record of strong earthquakes

Kagan Elisa[1,2*] Miryam Bar-Matthews[2*], Avner Ayalon[2*] Amotz Agnon[1*]

[1] Institute of Earth Sciences, The Hebrew University of Jerusalem
[2]Geological Survey of Israel

elisa.kagan@mail.huji.ac.il

*field guide

Research of past earthquakes, typically retrieving records from soft sediment deformations, can benefit from the study of rockfalls and damaged deposits in caves. Dating of damaged speleothems and deposits overgrowing rockfalls constrains the dates of earthquakes. We have compiled a long-term (~200 kyr) paleoseismic record at the Soreq and nearby Har-Tuv caves, near Jerusalem. The study caves, located 40 km west of the Dead Sea Transform, record earthquake damage from Dead Sea Transform ruptures and, possibly, smaller local intraplate events. The caves were discovered by quarrying activity at 1968, before which they were entirely closed.

In the Soreq Cave, we will see a large variety and quantity of speleoseismites. We will see collapsed cave ceilings, fallen stalactites, fallen columns, stalagmites with their tops severed, and cracks (Fig. 1). Many of these damaged cave deposits are covered in post-collapse regrowth, be it a thin film of calcite, flowstone, or stalagmites, which constrain damage age. Also, the crack network will be seen, through which most of the water entering the cave seeps.

Non-seismic sources of collapse, such as ice-movements, ground subsidence, and cave-bears, problematic elsewhere, were considered and refuted. Neither ice cover, nor perma-frost, has occurred in this region during the investigated period. Ground subsidence does not pose a problem since the cave floors are solid carbonate rock. The caves have only non-natural recent openings; therefore pre-1960's animal or anthropogenic effects are not a possibility. The study caves offer an excellent opportunity for paleoseismic research as they contain a large amount of damaged deposits. The two study caves present the opportunity to correlate between two nearby sites.

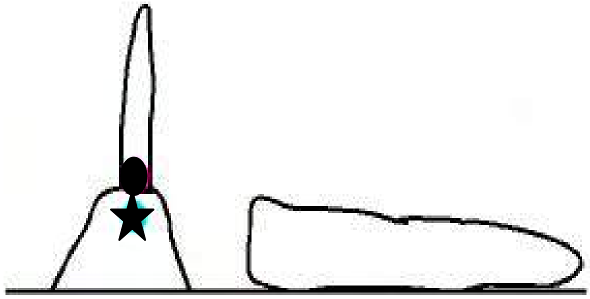

Fig 1a

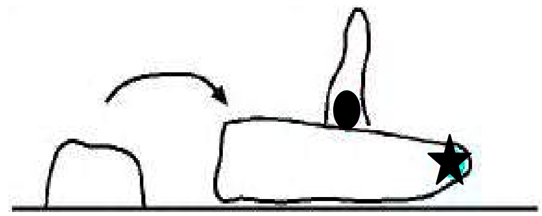

Fig 1b

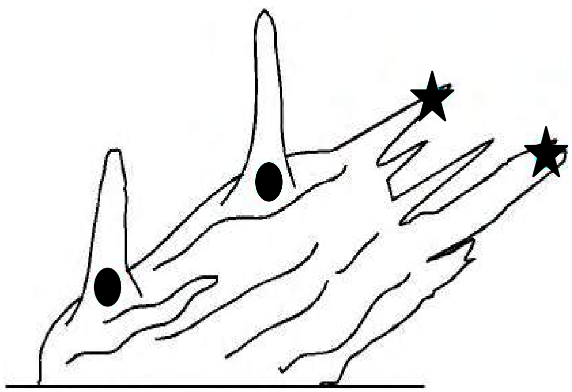

Fig 1c

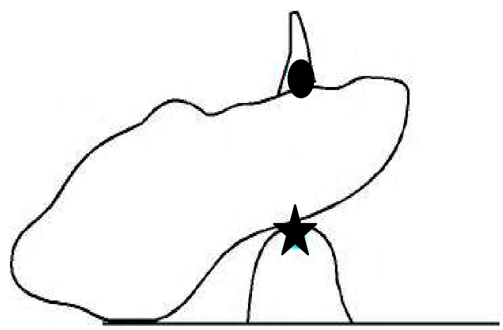

Fig 1d

Figure 1: Some of the types of speleoseismites to be seen in the Soreq Cave. Stars denote pre-earthquake age, circles denote post-earthquake age. 1a-Severed stalagmite and post-break stalagmite regrowth. 1b- Severed stalagmite and post-break stalagmite regrowth off the pre-earthquake location. 1c- Collapsed group of stalactites with post-collapse stalagmite regrowth. 1d-Collapsed block covering previously active stalagmite, with new stalagmite regrowth on block.

The Soreq and Har-Tuv caves were mapped at considerable resolution and the detailed maps demonstrate dominant EW and NW-SE orientation of fractures, and dominant EW and NS orientation of collapsed speleothems (Fig. 2). The prevailing orientations of collapsed speleothems are equivalent to directions of ground motion during the passage of surface waves emitted from the Dead Sea transform. These preferential orientations of collapse strongly support a seismic source of collapse. We identified "new generations" of speleothem growth on top of collapses. This post-collapse precipitation constrains ages of collapse. The unconformities between the collapses and the in-situ regrowth were recognized, and termed paleoseismic "contacts" or "horizons". Laminae above and below the unconformity were separated and dated by the $^{230}Th/^{234}U$ mass spectrometry method at the MC-ICP-MS at the Geological Survey of Israel. The pre-seismic and post-seismic dates of a collapse bracket the period within which the earthquake occurred. The closer in age the pre-seismic and post-seismic deposits are, the better constrained is the earthquakes age. When dating post-seismic regrowth on collapsed bedrock (and not collapsed speleothem), only the post-seismic age is available. We also drilled cores into the flowstone floor and discovered laminae that embed fallen small stalactites (soda-straw formations) (Gilli et al., 1999). We dated the laminae that embed the fallen stalactites, which give the age of the seismic event. We also compared the oxygen stable isotopic record (^{18}O) of the laminae adjacent to the tectonic unconformities with the extensive well-dated stable isotope record of Soreq Cave speleothems, as was reconstructed for the last 185 kyr by Bar-Matthews et al. (2000) and Ayalon et al. (2002). This stable isotope comparison technique improves and corroborates the U/Th ages. It also helps us to rule out climatic events as sources for rockfalls.

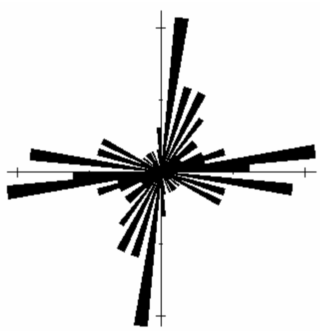

Figure 2: Rose diagram (intervals of 5°) depicting the orientations of the long axes of fallen speleothems in the Soreq Cave. Sixty fallen speleothem orientations were measured and incorportated into this diagram. Dominant EW and NS orientations are evident.

Seventy damaged speleothems were sampled and dated from which about twenty separate events were defined. The Holocene events observed in the cave correlate with lacustrine seismites dated in cores from the Dead Sea and with historically or archeologically recorded earthquakes: 185±30 yr BP correlates with an earthquake in the 1830's, 250±30 yr BP correlates with an earthquake that took place in 1759. Both dates refer to post-earthquake dripping, and we do not have positive evidence for large ground accelerations (yet these dates may correspond to crack opening responding to stress redistribution). 4400 ±400 yr BP may correlate with an archaeologically recorded earthquake from Tel Ai at ~4.7 ka (Karcz et al., 1977) and 4.6 ±0.9 ka marginal DST fault displacement (Gluck, 2001). It also correlates with a breccia layer from the Dead Sea (Migowski et al., 2004; Agnon et al., 2006). All cave events have lacustrine counterparts, but many lacustrine events do not correlate with cave events. This may suggest that the cave filters out the smaller events and records only the larger events (Kagan et al., 2005, 2007).

For the period correlating to the Last Glacial paleo-Dead Sea Lisan Fm (75 to 20 ky) we identified ~6 events, three to four (~ 38, 40, 53, and 70 ka) of which correlate with lacustrine soft sediment deformation in all studied Lisan paleoseismic sites and additional two events (~ 47, 26 ka) which correlate with only some Lisan sites (Kagan et al., 2007). Cave-recorded events older than 75 ka (at approximately 75, 85, 108, 119, 128, 133, 150, 155, 180 ka) are at present the only dated paleoseismic record for this period in the central Dead Sea region and present a promising breakthrough in long-term paleoseismic research.

The karstic paleoseismic record supports the lacustrine seismite evidence, and the long dating range of calcite cave deposits and their potential for recording seismic events can vastly increase the length of the seismic record and are valuable for seismic hazard assessment.

References:

Agnon, A., Migowski, C., and Marco, S., 2006. Intraclast breccia layers in laminated sequences: recorders of paleo-earthquakes, in Enzel, Y., Agnon, A., and Stein, M., eds., New Frontiers in Dead Sea Paleoenvironmental Research, Geological Society of America Special Paper 401, p. 195-214.

Ayalon, A., Bar-Matthews, M. and Kaufman, A., 2002. Climatic conditions during marine isotopic stage 6 in the Eastern Mediterranean region as evident from the isotopic composition of speleothems: Soreq Cave, Israel. Geology, 30, 303-306.

Bar-Matthews, M., Ayalon, A., Kaufman, A., 2000. Timing and hydrological conditions of sapropel events in the Eastern Mediterranean, as evident from speleothems, Soreq cave, Israel. Chem. Geol., 169,145-156.

Gilli E, Levret A, Sollogoub P, et al., 1999. Research on the February 18, 1996 earthquake in the caves of Saint-Paul-de-Fenouillet area, (eastern Pyrenees, France), Geodynamica Acta 12, 143-158.

Gluck, D., 2001. The landscape evolution of the southwestern Dead Sea Basin and the paleoseismic record of the southwestern marginal fault of the Dead Sea Basin and of the Carmel Fault during the Late Pleistocene and the Holocene: Jerusalem, The Hebrew University.

Kagan, E.J, Agnon, A., Bar-Matthews, M., 2005. Dateing large, infrequent earthquakes by damaged cave deposits. Geology 33, 261-264.

Kagan, E.J, Stein, M., Bar-Matthews, M., Agnon, A., 2007. A Tale of Two Cataclysmic-Earthquakes: 39 and 52 kyr BP, Dead Sea Transform, Israel; a Multi-archive Study. AGU, Fall Meeting 2007, San Francisco, Session T12.

Karcz, I., Kafri, U. Meshel, Z., 1977. Archaeological evidence for subrecent seismic activity along the Dead Sea-Jordan rift, Nature 269, 234 – 235.

Migowski, C., Agnon, A., Bookman, R., Negendank, J. F. W., and Stein, M., 2004, Recurrence pattern of Holocene earthquakes along the Dead Sea transform revealed by varve-counting and radiocarbon dating of lacustrine sediments: Earth and Planetary Science letters 222, 301-314.